Master's thesis

NTNU
Norwegian University of Science and Technology
Faculty of Engineering
Department of Civil and Environmental Engineering

Halvard Eiesland

Numerical Simulation of Monopile Vibratory and Impact Installation in Saturated Sand

Master's thesis in Civil and Environmental Engineering
Supervisor: Prof. Gudmund Eiksund (NTNU)
Co-supervisor: Dr Steven Bayton (NGI) and Dr Jörgen Johansson (NGI)

June 2021

NTNU
Norwegian University of Science and Technology

Halvard Eiesland

Numerical Simulation of Monopile Vibratory and Impact Installation in Saturated Sand

Master's thesis in Civil and Environmental Engineering
Supervisor: Prof. Gudmund Eiksund (NTNU)
Co-supervisor: Dr Steven Bayton (NGI) and Dr Jörgen Johansson (NGI)
June 2021

Norwegian University of Science and Technology
Faculty of Engineering
Department of Civil and Environmental Engineering

NTNU
Norwegian University of
Science and Technology

Preface

This master's thesis is written as part of the Civil and Environmental Engineering Master's Degree Programme at the Norwegian University of Science and Technology (NTNU) in Trondheim. It is written in relation with the geotechnical engineering course TBA4900 during the spring of 2021, with a scope of 30 credits. The topic for the thesis was suggested by main supervisor Prof. Gudmund Eiksund at NTNU. The study is carried out in collaboration with supervisors at NTNU and the Norwegian Geotechnical Institute (NGI).

Trondheim, 10.06.2021

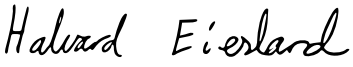

Halvard Eiesland

Acknowledgement

The main supervisor of this study has been Prof. Gudmund Eiksund at NTNU, to whom I would like to express my sincere gratitude for the guidance I have received. Dr Steven Bayton and Dr Jörgen Johansson at NGI have been co-supervising this study and have provided valuable suggestions and shared their knowledge throughout the process. The collaboration with you have been highly appreciated.

I would like to thank Prof. Gustav Grimstad and Prof. Steinar Nordal at NTNU for providing valuable comments and suggestions in conjunction with the thesis.

H.E.

Abstract

Installation of offshore monopiles by vibratory driving is suggested to have several advantages compared to the conventional impact driving method. However, there are uncertainties related to the prediction of axial and lateral bearing capacity of vibratory driven piles. Enhanced knowledge regarding soil behaviour during pile driving with this installation method may grant improved prediction of the bearing capacity of the pile after installation. Ultimately, this may lead to better utilisation of the vibratory installation method with its suggested advantages.

Numerical simulations of vibratory and impact driving of a monopile in saturated sand is performed in PLAXIS 2D. The pile is wished-in-place at final depth, and a vertical, dynamic load is applied to the top of the pile. The possibly different soil behaviour during driving, and after consolidation, is compared for the two simulated installation methods. In addition, the effect of driving frequency and initial soil density on the soil behaviour is investigated for the vibratory installation method. The reliability of the results is evaluated, however, neither the numerical modelling decisions nor the obtained results are verified by data from pile installations in the field with vibratory and impact driving. Hence, the assessments of the results are mainly conceptual.

The results show a clear difference in soil behaviour during simulation of vibratory pile driving compared to impact driving, while the final settlement of the pile is close to similar for both methods. The vertical displacement rate of the top of the pile is considerably higher during vibratory driving. Excess pore pressure build-up is seen for both driving methods, however, the build-up at the centre of the embedded pile length, near the exterior pile wall, develops at a significantly higher rate during vibratory driving. The relative reduction of the estimated secant shear modulus from the first to the last loading cycle is, in the aforementioned point in the soil, considerably higher during vibratory driving compared to impact driving. However, 1 m further out from the pile wall the relative reductions are close to similar for both driving methods. Indications of cyclic mobility is seen in the point near the exterior pile wall during impact driving already during the first loading cycle, with a relatively large increase of effective mean stress in pressure. The SANISAND material model used does not implement cap hardening. Hence, the simulated soil behaviour may under-predict the plastic strains along the pile wall during impact driving. Only slight cyclic mobility is indicated in the same point of the soil during vibratory driving and occurs only after several loading cycles. The excess pore pressure and effective mean stress in the soil at the centre of the embedded pile length, near the

exterior pile wall, seem to approach a steady-state during vibratory driving at 23.33 Hz with 38.9 loading cycles, i.e. 1.667 s.

It may be particularly interesting that the results indicate a close to similar stress state in the soil after consolidation in the comparison of the two installation methods, regardless of the considerably different soil behaviour simulated during driving. This may imply a relatively similar bearing capacity of the pile after the simulated pile driving for both methods. This is, however, limited to the two points in the soil investigated. Recommendations for further work may include the verification of a numerical model and obtained results to grant enhanced knowledge of the relation between observed soil behaviour during vibratory driving and the state after consolidation.

The different numerical simulations of vibratory driving suggest a lower rate of vertical displacement of the top of the pile at the lower frequencies with associated smaller load amplitudes. In a point at the centre of the embedded pile length, near the exterior pile wall, the results from the simulated lower frequencies indicate a lower rate of excess pore pressure build-up and a higher ratio of secant shear modulus between the first and last loading cycle. The same tendencies are seen for the simulated lower driving frequency of which the load amplitude remains the same. The results suggest a larger degree of soil liquefaction in the aforementioned point near the exterior pile wall for the looser soil.

Sammendrag (Norwegian)

Installasjon av offshore monopeler ved bruk av vibrolodd er antydet å ha flere fordeler sammenlignet med den konvensjonelle metoden ved bruk av fallodd. Det er usikkerhet knyttet til anslag av aksiell og lateral bæreevne av peler installert med vibrolodd. Økt kunnskap knyttet til jordens oppførsel under peleramming med denne metoden kan føre til forbedrede anslag av pelens bæreevne etter installasjon. På sikt kan dette føre til bedre utnyttelse av denne installasjonsmetoden for peler og introdusere de antydede fordelene som medfølger.

Numeriske simuleringer av en monopel påført last fra vibro- og fallodd i mettet sand er utført i PLAXIS 2D. Pelen er modellert ved endelig dybde, og en vertikal, dynamisk last er påført toppen av pelen. Den mulige forskjellen i jordens oppførsel under pelerammingen, og etter konsolidering, er sammenlignet for de to simulerte installasjonsmetodene. I tillegg er effekten på jordens oppførsel ved ulik frekvens til vibroloddet og initiell tetthet i sanden ved installasjon med vibrolodd vurdert. Påliteligheten av resultatene er evaluert, men hverken valgene foretatt ved modelleringen eller resultatene som er oppnådd har blitt verifisert mot data fra feltundersøkelser ved bruk av vibrolodd og fallodd. Derfor er vurderingene av resultatene hovedsakelig konseptuelle.

Resultatene viser en klar forskjell på jordens oppførsel under simuleringen av vibrolodd sammenlignet med fallodd, samtidig som den endelige setningen av pelen er tilnærmet lik for begge installasjonsmetodene. Hastigheten til den vertikale relative forskyvningen ved toppen av pelen er betydelig høyre under den simulerte lastpåføringen med vibrolodd. Poreovertrykk bygges opp for begge installasjonsmetodene, men ved halve pelens lengde under jorden, nær utside pelevegg, bygges dette opp betydelig raskere ved simuleringen av vibrolodd. Den relative reduksjonen av den estimerte sekant skjærmodulen fra første til siste lastsyklus er, for ovennevnte punkt i jorden, betydelig større ved simuleringen av vibrolodd. Derimot er den relative reduksjonen 1 m lenger ut fra peleveggen tilnærmet lik for begge rammemetodene. Indikasjoner på syklisk mobilitet er sett i punktet nær utside pelevegg ved simulering av fallodd allerede ved første lastsyklus, med en relativt stor økning av effektiv middelspenning i trykk. SANISAND-modellen som er brukt implementerer ikke en øvre grense for konstant spenningsforhold mellom deviatorspenning og effektiv middelspenning i trykk som gir plastiske tøyninger. Dette kan medføre at den simulerte jordoppførselen underestimerer plastiske tøyninger langs peleveggen ved simuleringen av fallodd. Kun en liten grad av syklisk mobilitet antydes i samme punkt i jorden ved simulering av vibrolodd og oppstår først etter flere lastsykler. Poreovertrykket og effektiv

middelspenning oppnår tilsynelatende en stabil tilstand i jorden ved halve pelens lengde under jorden, nær utside pelevegg, i løpet av de 38.9 simulerte lastsyklene med vibrolodd ved en frekvens på 23.33 Hz, som tilsvarer en total vibreringstid på 1.667 s.

Særlig interessant kan det være at resultatene viser en tilnærmet lik spenningstilstand i jorden etter konsolidering i sammenligningen mellom de to installasjonsmetodene, uavhengig av den betydelige forskjellen i simulert oppførsel av jorden under selve peleramming. Dette kan antyde en relativt lik bæreevne av pelen etter begge simulerte metodene av peleramming. Dette er derimot begrenset til de to punktene i jorden som er undersøkt. Anbefalinger for videre arbeid kan inkludere verifisering av en numerisk modell og de oppnådde resultatene for å forbedre kunnskapen om forholdet mellom den observerte oppførselen av jorden under peleramming med vibrolodd og dens tilstand etter konsolidering.

De ulike numeriske simuleringene med vibrolodd antyder en lavere hastighet for vertikal relativ forskyvning ved toppen av pelen ved simulering av de lavere frekvensene med de tilknyttede mindre lastamplitudene. I et punkt ved halve pelens lengde under jorden, nær utside pelevegg, antyder resultatene fra de simulerte lavere frekvensene en lavere hastighet for oppbygging av poreovertrykk og et høyere forhold av sekant skjærmodul mellom første og siste lastsyklus. De samme tendensene er antydet for simuleringen med lavere frekvens hvorav lastamplituden er uendret. Resultatene antyder en større grad av likvifisering av jorden i det ovennevnte punktet nær utside pelevegg for den løsere sanden.

Contents

List of Figures

List of Tables

List of Abbreviations

CPT	Cone Penetration Test
CSL	Critical State Line
CSSM	Critical State Soil Mechanics
DIC	Digital Image Correlation
e.g.	exempli gratia (Latin) / for example (English)
FE	Finite Element
FEA	Finite Element Analysis
i.e.	id est (Latin) / that is (English)
NGI	Norwegian Geotechnical Institute
NTNU	Norwegian University of Science and Technology
OWT	Offshore Wind Turbine
PIV	Particle Image Velocimetry
SANISAND	Simple Anisotropic Sand constitutive models
UDSM	User-defined Soil Model
vs.	versus (Latin) / against (English)
w.r.t	with respect to
2D	Two-dimensional
3D	Three-dimensional

List of Symbols

Note that not all symbols are included in the following lists. This particularly applies to the symbols describing the SANISAND material model in Section 5.2, Chapter 5. However, a description of each symbol should be made when introduced the first time.

Greek letters

$\boldsymbol{\alpha_c}$	Centrifugal acceleration
$\boldsymbol{\alpha_{distr}}$	Factor of load distribution along pile shaft
$\boldsymbol{\alpha, \beta}$	Rayleigh damping coefficients
$\boldsymbol{\beta_{angle}}$	Angle of plasticity
$\boldsymbol{\beta_{friction}}$	Factor for side friction of pile wall
$\boldsymbol{\gamma}$	Specific weight
$\boldsymbol{\gamma_c}$	Cyclic shear strain amplitude
$\boldsymbol{\gamma_{c,t}}$	Cyclic threshold shear strain amplitude
$\boldsymbol{\gamma_{sand,sat}, \gamma_{sand,unsat}}$	Saturated and unsaturated specific weight of sand
$\boldsymbol{\gamma_w}$	Specific weight of water
$\boldsymbol{\gamma_{xy}}$	Cartesian shear strain
$\boldsymbol{\delta_N}$	Stiffness index at cycle N
$\boldsymbol{\delta t}$	Time step for dynamic calculation
$\boldsymbol{\varepsilon^e}$	Elastic normal strain
$\boldsymbol{\varepsilon^p}$	Plastic normal strain
$\boldsymbol{\varepsilon_v}$	Volumetric strain
$\boldsymbol{\varepsilon_q}$	Deviatoric strain
$\boldsymbol{\varepsilon_1}$	Major principal strain
$\boldsymbol{\varepsilon_2}$	Intermediate principal strain
$\boldsymbol{\varepsilon_3}$	Minor principal strain

$\boldsymbol{\Delta\varepsilon^e}$	Change of elastic normal strains
$\boldsymbol{d\varepsilon_q^e}$	Incremental elastic deviatoric strain
$\boldsymbol{d\varepsilon_v^e}$	Incremental elastic volumetric strain
$\boldsymbol{d\varepsilon_q^p}$	Incremental plastic deviatoric strain
$\boldsymbol{d\varepsilon_v^p}$	Incremental plastic volumetric strain
$\boldsymbol{\eta}$	Deviatoric and effective mean stress ratio
$\boldsymbol{\eta_F}$	Force transfer ratio between hammer and pile for rigid system
$\boldsymbol{\eta_{hammer}}$	Efficiency of impact hammer
$\boldsymbol{\eta_{init}}$	Initial deviatoric and effective mean stress ratio
$\boldsymbol{d\eta}$	Incremental deviatoric and effective mean stress ratio
$\boldsymbol{\lambda}$	Hysteretic damping
$\boldsymbol{\mu_{mass}}$	Mass ratio between vibratory hammer components and pile
$\boldsymbol{\nu}$	Poisson's ratio
$\boldsymbol{\xi_1, \xi_2}$	First and second target damping ratio for Rayleigh damping
$\boldsymbol{\pi}$	Constant equal to 3.14159...
$\boldsymbol{\rho}$	Density
$\boldsymbol{\sigma'}$	Effective normal stress
$\boldsymbol{\sigma_v^A}$	Vertical stress amplitude
$\boldsymbol{\sigma_{v,vib,p}^A}$	Vertical stress amplitude subjected to the top of the pile during vibratory driving
$\boldsymbol{\sigma_{v,impact,p}^A}$	Vertical stress amplitude subjected to the top of the pile during impact driving
$\boldsymbol{\Delta\sigma}$	Change of normal stress
$\boldsymbol{\sigma_1}$, $\boldsymbol{\sigma'_1}$	Total and effective major principal stress
$\boldsymbol{\sigma_2}$, $\boldsymbol{\sigma'_2}$	Total and effective intermediate principal stress
$\boldsymbol{\sigma_3}$, $\boldsymbol{\sigma'_3}$	Total and effective minor principal stress
$\boldsymbol{\sigma'_{xx}}$	Effective Cartesian stress in x-direction
$\boldsymbol{\sigma'_{yy}}$	Effective Cartesian stress in y-direction
$\boldsymbol{\sigma'_{zz}}$	Effective Cartesian stress in z-direction
$\boldsymbol{\sigma_{xy}}$	Cartesian shear stress
$\boldsymbol{\tau}$	Shear stress

τ_c	Cyclic shear stress amplitude
$\tau_{c,N}$	Cyclic shear stress amplitude during cycle N
$\tau_{c,1}$	Cyclic shear stress amplitude during first cycle
τ_f	Shear stress at failure
φ	Friction angle
φ_c,φ_e	Friction angle in triaxial compression and extension respectively
φ'	Effective friction angle
ω	Angular frequency
ω_1, ω_2	First and second target angular frequency for Rayleigh damping

Latin letters

A	Area
A_{displ}	Displacement amplitude
A_{pile}	Cross section area of pile
A_{shaft}	Area of internal and external pile shaft
a	Attraction
a_c	Centrifugal acceleration of rotating mass
a_{vert}	Vertical acceleration
a_y	Acceleration in y-direction
c	Cohesion
$D_{inner,pile}$	Inner diameter of pile
$D_{outer,pile}$	Outer diameter of pile
D_r	Relative density
D_{10}, D_{50}, D_{60}	Grain size diameter of which 10%, 50% or 60% of the grains are smaller than
d	Dilatancy
e	Void ratio
e_{init}	Initial void ratio
e_{min}, e_{max}	Minimum and maximum void ratio
E	Elastic modulus

$\boldsymbol{\Delta E_{hyst}}$	Energy loss during a given cycle
$\boldsymbol{E_{k,ram}}$	Kinetic energy of ram
$\boldsymbol{E_{pile}}$	Elastic modulus of pile
$\boldsymbol{E_{p,ram}}$	Potential energy of ram
$\boldsymbol{E_{spring}}$	Elastic modulus of elastomer pads
$\boldsymbol{E^{i}_{k,ram}}$	Kinetic energy of ram the moment before impact
$\boldsymbol{E^{i}_{pile}}$	Necessary energy to subject pile at each blow of impact hammer
$\boldsymbol{E^{i}_{pile,sim.}}$	Estimated energy subjected to top of the pile at each blow of impact hammer, in preliminary simulations
$\boldsymbol{E'}$	Effective elastic modulus
$\boldsymbol{F_b}$	Force from buoyancy
$\boldsymbol{F_{ecc,c}}$	Centrifugal force of eccentric mass
$\boldsymbol{F_v}$	Vertical force
$\boldsymbol{F_{v,vib}}$	Vertical force generated by eccentric moments of a vibratory hammer
$\boldsymbol{F^{A}_{v,impact,p}}$	Amplitude of vertical force from impact hammer subjected to the top of the pile
$\boldsymbol{F^{A}_{v,vib}}$	Amplitude of vertical force generated by eccentric moments of a vibratory hammer
$\boldsymbol{F^{A}_{v,vib,p}}$	Amplitude of vertical force from vibratory hammer subjected to the top of the pile
$\boldsymbol{f}$	Frequency
$\boldsymbol{G}$	Elastic shear modulus
$\boldsymbol{G_{max}}$	Maximum elastic shear modulus during a given cycle
$\boldsymbol{G_s}$	Secant elastic shear modulus
$\boldsymbol{G_{s,N}}$	Secant elastic shear modulus during cycle number N
$\boldsymbol{G_{s,1}}$	Secant elastic shear modulus during first cycle
$\boldsymbol{g}$	Gravitational acceleration
$\boldsymbol{H_{ram}}$	Height of ram above point of impact
$\boldsymbol{I}$	Intensity
$\boldsymbol{K}$	Elastic bulk modulus
$\boldsymbol{L_{embedded,pile}}$	Embedded pile length
$\boldsymbol{L_{spring}}$	Length of elastomer pads

$L_{total,pile}$	Total pile length
$L_{w,pile}$	Length of pile submerged in water
M_{ecc}	Eccentric moment
$M_{ecc,sum}$	Sum of eccentric moments
M_c	Inclination of critical line in $p' - q$ space for triaxial compression
M_e	Inclination of critical line in $p' - q$ space for triaxial extension
m_{cl}	Mass of clamps
m_{dyn}	Dynamic mass, sum of m_{eb}, m_{cl} and m_p
m_{eb}	Mass of exciter block
m_{ecc}	Eccentric mass
m_{ib}	Mass of isolator block
$m_{impact,static}$	Static mass of impact hammer
m_p	Mass of pile
m_{ram}	Mass of impact hammer ram
m_{vib}	Vibratory mass, sum of m_{ib} and m_{eb}
N_q	Toe bearing capacity factor
P	Power
p_{atm}	Atmospheric pressure
p_{excess}	Excess pore pressure
p'	Effective mean stress
p'_v	Effective vertical stress from overlying soil
$p'_{v,average}$	Average effective vertical stress from overlying soil
dp'	Incremental effective mean stress
Q_{shaft}	Contribution from shaft resistance on pile axial bearing capacity
Q_{toe}	Contribution from toe resistance on pile axial bearing capacity
Q_u	Axial bearing capacity of pile in compression
q	Deviatoric stress
dq	Incremental deviatoric stress
R_{inter}	Interface strength reduction factor
r_{ecc}	Eccentric radius
$s_{elastic}$	Elastic settlement of pile
$s_{plastic}$	Plastic settlement of pile

s_{total}	Total settlement of pile
T	Uplift force from vibratory hammer carrier system
t	Time
$t_{wall,pile}$	Thickness of pile wall
U_c	Uniformity coefficient
u	Pore pressure
u_y	Displacement in y-direction
v_c	Longitudinal compression wave velocity in a bar of elastic material
$\mathrm{v}_{c,pile}$	Longitudinal compression wave velocity in pile
v_p	Primary wave velocity
v_{ram}	Velocity of ram
v_s	Secondary wave velocity
v_{ram}^i	Velocity of ram the moment before impact
W_p	Weight of pile

Chapter 1

Introduction

1.1 Background and Motivation

Wind turbines are installed, both on- and offshore, in order to utilise the renewable source of energy in wind. In a press release, the European Commission (EC) proposes an increase of the offshore wind capacity in Europe from 12 GW in 2020 to 300 GW by 2050, being part of the goal to become climate neutral by 2050 (EC, 2020). For the installation of offshore wind turbines (OWTs) there are several foundation types available, amongst others gravity based, monopile and suction bucket foundations (Arshad and O'Kelly, 2013). Monopiles have been the most used foundation type for OWTs the last years, of which 70% of the installed foundations for OWTs were monopiles in 2019 (WindEurope, 2020) and 80.5% in 2020 (WindEurope, 2021).

The process of installing a monopile into the soil may be referred to as pile driving, and impact hammering is currently the conventional pile driving method. This method applies energy to the top of the pile by impacts of a ram, in order to cause the pile to penetrate the soil. Several impacts are performed until the pile has reached the desired depth. Impact driving an offshore pile might emit underwater noise that may be harmful or cause behavioural disturbance for marine wildlife (see e.g. Madsen et al. (2006), Bailey et al. (2010)). Several countries are part of agreements regarding regulations of underwater noise emission in general, of which some of the suggested measures are to (Erbe, 2013):

- Investigate alternative foundation types, e.g. alternatives to piles for OWTs foundation
- Investigate both location and timing at which the noise emission may occur, e.g. related to seasons of whale breeding
- Soft-start of the work causing noise emission, possibly sending a warning to the animals in the area
- Replace, either fully or partly, impact pile driving with vibratory pile driving
- Use bubble curtains during impact pile driving

- Reduce power of the noise emission source, or temporarily shut down the work, if animals are observed within a given zone surrounding the source of noise

Introducing noise mitigation measures due to the noise emission from impact pile driving may increase the total installation costs. Erbe (2013) states that almost every European country requires the use of bubble curtains in order to reduce the noise emission during impact pile driving.

Vibratory driving is an alternative method of driving a pile into the soil, of which a vertical, sinusoidal force is applied to the pile. This method is suggested to emit less noise during pile driving (Erbe, 2013). Saleem (2011) suggests, with reference to an interview with Starre and Boor in 2011 (*Vibratory Hammers*, 2011), several advantages of vibratory pile driving compared to impact driving, in addition to reduced noise emission:

- No pile diameter limitations, since vibratory hammers can be joined together to be able to handle larger pile diameters if needed
- Faster pile driving
- Lower pile installation costs due to the faster pile driving and less energy required
- Easier pile handling upon driving due to possibility of direct clamping the pile with the vibratory hammer
- Vibratory hammers may, in addition to install piles, be used to extract piles
- Lower noise emission during driving

The suggested advantages may give incentives towards a transition from the use of impact driving to vibratory driving when installing piles as foundation for OWTs. However, there are uncertainties related to the use of vibratory pile driving on structural elements. During impact pile driving, evaluating the end of driving (EOD) data may provide information to estimate its axial bearing capacity. Predicting the soil behaviour due to vibratory pile driving is one of the challenges regarding this installation method. The possibility of having large shear stiffness reduction during vibratory pile driving introduces challenges regarding evaluating the pile penetration data to estimate its bearing capacity after installation (Holeyman, 2002). Therefore some vibratory driven piles may be impact driven the last metres, in order to evaluate its axial bearing capacity based on EOD. However, this combined method of pile installation does not fully utilise the advantage of vibratory driving, e.g. in terms of reducing underwater noise emission during offshore pile driving. Enhanced knowledge regarding soil behaviour during vibratory pile driving may grant better prediction of the pile bearing capacity after installation, possibly both axially by EOD and laterally, hence introduce this installation method and its suggested advantages to a larger degree.

1.2 Objectives

The objective of the thesis is to investigate the difference in soil behaviour of a fully saturated sand both during, and after, vibratory and impact driving of an offshore monopile to be used as a foundation for a wind turbine. In addition, the effect of driving frequency and load amplitude during vibratory pile driving is investigated. The effect of initial void ratio on soil behaviour during vibratory driving is also briefly investigated. Being able to realistically simulate vibratory pile driving may allow prediction of the soil behaviour during driving, hence possibly better prediction of bearing capacity after installation. This may ultimately lead to better utilisation of this pile installation method and its suggested advantages.

1.3 Approach

The objectives are to be approached by investigating results obtained from numerical simulations of the aforementioned pile driving methods, using a soil material model appropriate to simulate cyclic loading on sands. PLAXIS 2D is a two-dimensional (2D) Finite Element (FE) software and is used for the simulations. In addition to compare the results from different simulations with each other, the results may also be compared to suggested soil and pile behaviour in the literature to evaluate whether the results could be assumed realistic or not.

1.4 Research Questions

Based on the objectives and approach the thesis aims at answering the following research questions:

1. May the numerical simulations provide indications of different soil behaviour during vibratory driving compared to impact driving? To be evaluated in terms of excess pore pressure build-up and shear modulus degradation.
2. May the numerical simulations provide indications of different soil states after consolidation for vibratory driving compared to impact driving? To be evaluated in terms of stress state and void ratio.
3. How does the simulated soil behaviour during vibratory driving depend on driving parameters such as frequency and load amplitude, and initial void ratio of the soil? To be evaluated in terms of excess pore pressure build-up and shear modulus degradation.
4. Are the results obtained indicating a close to real soil behaviour? Is the SANISAND material model, version by Dafalias and Manzari (2004), an appropriate material model to simulate vibratory and impact pile driving in PLAXIS 2D?

1.5 Limitations

Several limitations are introduced regarding the numerical simulations:

- The full process of pile driving is not simulated. The pile is wished-in-place, and a dynamic load is applied to the top of the pile. Hence, effects on soil behaviour due to soil displacements during full installation is not included. In addition, only a short time of dynamic loading is simulated.
- Possible fatigue damage in the pile is not considered when selecting pile driving parameters.
- Only one set of calibrated input parameters of the SANISAND material model is used for the simulations.
- Only one set of dimensions for the monopile is modelled in PLAXIS, hence possible effects on the soil behaviour due to different pile sizes or pile material is not investigated.
- The selections of parameters and geometries for the simulations are in many cases not unambiguous, and approximations or simplifications may be necessary.
- The results of the numerical simulations are not verified by field investigations. This is partly due to the relatively small amount of investigations of vibratory pile driving regarding the soil behaviour during driving. Hence, the results have an amount of uncertainty related to how the real soil behaviour may be compared to the simulated behaviour.

1.6 Reference Made to Preliminary Study

A preliminary study was carried out by the author during the autumn of 2020, in relation to the course TBA4510 at NTNU, Trondheim in Norway. The scope of the course is 7.5 credits. The preliminary study is presented in the unpublished work of the project thesis with the title *Vibratory Driven Pile Installation*, by Eiesland (2020). Therefore, some paragraphs and statements, possibly with several modifications, are adopted from the project thesis. This particularly applies to:

- Chapter 3 in general
  - and in particular Section 3.3 regarding longitudinal compression wave velocity in a pile
- Chapter 4
  - Section 4.3 regarding behaviour of non-cohesive soils subjected to cyclic shear loading

- Chapter 6
  - Section 6.1.2 regarding modelling of the pile
  - Section 6.1.3 regarding modelling of the soil
  - Section 6.1.8 regarding estimation of axial bearing capacity of pile
  - Section 6.2 regarding the presented phases of the numerical simulations and calculation parameters

1.7 Structure of the Thesis

The thesis consists of 8 chapters. Chapter 1 gives an introduction to the study, presenting the motivation along with the objectives, approach and limitations. Chapter 2 gives a general introduction to the monopile structural element and the two pile driving methods being investigated in the thesis, namely vibratory and impact driving. Chapter 3 briefly presents theory regarding wave propagation, which may be induced during pile driving. Chapter 4 discuss the suggested behaviour of sand subjected to shear loading, which the soil may be subjected to during pile driving. Chapter 5 gives an introduction to the soil material models used for the numerical simulations. Chapter 6 gives a relatively detailed presentation of the numerical model and calculation parameters for a total of 7 different simulations, with the aim to allow replication of the simulations. Chapter 7 presents the results along with the interpretations and the discussion. Chapter 8 presents the conclusions, with a try to answer the aforementioned research questions, based on the interpretations and discussion in Chapter 7. Suggestions for further work is presented in Chapter 8.

Chapter 2

Monopiles, Impact Driving and Vibratory Driving

This section aims at giving a brief introduction to monopiles, and a general review of the two pile driving methods impact and vibratory driving.

2.1 Monopiles

A monopile is a structural element of which the prefix *mono* indicates that it is one single pile supporting a structure, in contrast to pile groups. Figure 2.1 shows an example of an offshore wind turbine (OWT) with a monopile foundation. The transition piece is the connection between the monopile and the tower with the wind turbine mounted on top. The part of the pile at the transition piece may be referred to as the top of the pile while the bottom part of the pile may be termed pile toe. Monopiles supporting OWTs are subjected to both axial and lateral loading, of which the latter may be cyclic loading from, amongst others, both waves and wind. The axial loading may be suggested to be mainly from the self weight of the pile and structure.

Monopiles often have a relatively large diameter with respect to its length, and are hollow, open-ended, with the following design parameters regarding dimensions: outer diameter ($D_{outer,pile}$), wall thickness ($t_{wall,pile}$), total length ($L_{total,pile}$) and embedded length ($L_{embedded,pile}$). Open-ended piles are often considered small-displacement piles, with respect to the relatively small soil displacements induced during penetration of the pile. In contrast, displacement piles induce relatively large soil displacements, and may be the case for closed-ended pile. Non-displacement piles may imply the pile being drilled or that soil is removed before the pile is installed.

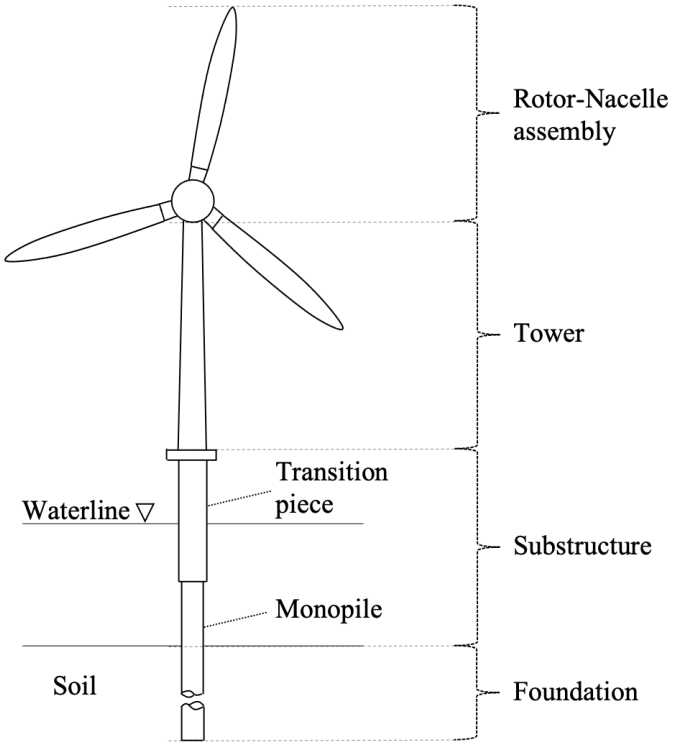

Figure 2.1: Offshore wind turbine with monopile foundation. Redrawn, with modifications, after Ko (2020).

2.2 Impact Driven Installation

The principle of impact pile driving is to transfer kinetic energy from the ram to the top of the pile. Several impacts of the ram is performed until desired depth of the pile is reached.

Components and Energy Equations of an Impact Hammer
Figure 2.2 shows the general components of an impact hammer. Single-acting impact hammers lifts the ram, increasing its potential energy, before it is released to impact the anvil (or cushion). The potential energy is transformed to kinetic energy as the velocity of the ram increases, and at impact of the anvil (or cushion), energy is transferred to the top of the pile. Loss of energy may occur, both during the fall of the ram and at the transfer of energy from the ram at impact to the pile.

The potential energy of the ram ($E_{p,ram}$) may be estimated by:

$$E_{p,ram} = m_{ram} \cdot g \cdot H_{ram} \tag{2.1}$$

of which m_{ram} is the mass of the ram, g is the acceleration from the earth's gravity and H_{ram} is the height of the ram above the point of impact. The kinetic energy of the ram

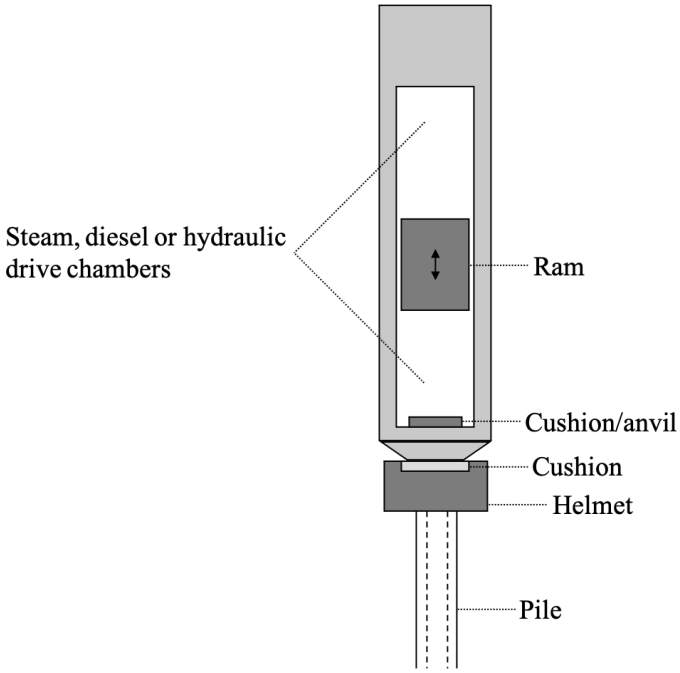

Figure 2.2: Simplified visualisation of the principle of an impact driven hammer. Redrawn, with modifications, after Chung et al. (2013)

($E_{k,ram}$) may be given by:

$$E_{k,ram} = \frac{1}{2} \cdot m_{ram} \cdot \mathrm{v}_{ram}^2 \tag{2.2}$$

of which v_{ram} is the velocity of the ram. The kinetic energy the moment before impact ($E_{k,ram}^i$) may be given by inserting the velocity of the ram the moment before impact (v_{ram}^i) into Equation 2.2, giving:

$$E_{k,ram}^i = \frac{1}{2} \cdot m_{ram} \cdot (\mathrm{v}_{ram}^i)^2 \tag{2.3}$$

Hammer Efficiency Ratio

Due to possible energy loss during free-fall of the ram the potential energy before releasing the ram may not be equal to the kinetic energy the moment before impact. These energy losses may be due to friction occurring by the ram, misalignment of ram or releasing the ram before reaching height H_{ram} (Flynn and McCabe, 2016). Therefore, in order to estimate the energy subjected to the pile, a hammer efficiency may be introduced (Flynn and McCabe, 2016):

$$\eta_{hammer} = \frac{E_{k,ram}^i}{E_{p,ram}} \tag{2.4}$$

of which it is important to note that $E_{k,ram}^i$ is the kinetic energy of the ram the moment before impact and $E_{p,ram}$ is the potential energy of the ram at height H_{ram}, before being

released.

Hammer Selection

There are several different types of impact hammers, and the hydraulic driven impact hammer is the type modelled in the simulation in the thesis. Hydraulic impact hammers may be equipped with velocity measuring devices, measuring the velocity of the ram the moment before impact. This may eliminates the uncertainty regarding energy losses of the ram (Rausche and Klesney, 2007). Further, it is stated that the remaining uncertainty lies in the transition of energy from the hammer to the pile, and in many cases the hammer efficiency for hydraulic hammers with ram velocity measurement may be set to 95 % (Rausche and Klesney, 2007). Hydraulic hammers can be double-acting, lifting the ram by hydraulics and being able to additionally push the ram downwards. This may give an addition to the kinetic energy, compared to the single-acting rams of which the kinetic energy is gained by conversion of potential energy of the falling ram.

The energy subjected to the top of the pile at each blow may cause settlements of the pile into the soil. The total settlement each blow (s_{total}) may be divided into contributions from elastic ($s_{elastic}$) and plastic settlements ($s_{plastic}$):

$$s_{total} = s_{elastic} + s_{plastic} \tag{2.5}$$

of which $s_{elastic}$ may be assumed to be reversed upon load reversal and $s_{plastic}$ is the permanent settlement. If the energy applied to the pile is not sufficiently large, only the elastic settlements may occur. In order to be able to drive the pile to its desired depth, several impacts with plastic settlements needs to be applied to the pile, and the energy needed to be applied at each blow, in order to achieve a permanent settlement of $s_{plastic}$, may be estimated by the so-called impact formula (*Peleveiledningen*, 2019; *Geoteknikk Beregningsmetoder*, 2020):

$$E^i_{pile} = Q_u \cdot s_{plastic} + \frac{1}{2} \cdot Q_u \cdot \alpha_{distr} \cdot \frac{Q_u \cdot L_{total,pile}}{A_{pile} \cdot E_{pile}} \tag{2.6}$$

of which Q_u is the axial bearing capacity of the pile, α_{distr} is a factor of how the load is distributed along the pile. If $\alpha_{distr} = 1.0$ this indicates the bearing capacity is highly dependent on the toe bearing capacity, while $\alpha_{distr} = 0.5$ may indicate large dependency of the shaft bearing capacity. $L_{total,pile}$ is the total length of the pile, A_{pile} is the cross section of the pile and E_{pile} is the elastic modulus of the pile material.

With a hammer efficiency of $\eta_{hammer} = 0.95$, an equilibrium between the energy transferred from the hammer to the pile and and the necessary energy to cause permanent settlement of $s_{plastic}$, each blow, may be introduced:

$$0.95 \cdot E^i_{k,ram} = E^i_{pile} \tag{2.7}$$

Note that if an estimation of the necessary energy subjected to the top of the pile at each blow (E^i_{pile}) is known, then Equation 2.7 allows estimation of either the necessary mass of the ram or velocity the moment before impact by Equation 2.3, given that one of them are known.

2.3 Vibratory Driven Installation

The principle of vibratory pile driving is to reduce the soil resistance by inducing vibrations to the soil due to rapid vertical, cyclic movement of the pile. Jonker (1987) suggests some basic differences between impact and vibratory pile driving, presented in Table 2.1. The difference of the load applied is the lower load amplitude during vibratory driving, but with a higher driving frequency.

Table 2.1: Basic differences between impact and vibratory pile driving (Jonker, 1987)

Impact driving	Vibratory driving
High (peak) force, low frequency hammer	Low force, high frequency hammer
Pile is not rigidly connected to hammer	Pile is rigidly connected to hammer
Continuous[1] energy supply to hammer, intermittent energy supply to soil	Continuous[1] energy supply to hammer, continuous[1] energy supply to soil

The resistance of the soil may be reduced to a certain degree of which the pile penetrates the soil solely by its own weight and the weight of the vibratory hammer. This method is frequently used for driving non-structural piles, and there is an increased interest in being able to vibratory drive also structural piles (DFI, 2015). However, uncertainties regarding how the soil behaves due to the inflicted vibrations, and hence predictions regarding the bearing capacity of the pile, is a restraining factor. Parts of the uncertainties lies within evaluating driving data to predict long term bearing capacity of the pile, since the indications of soil stiffness during driving may deviate from the stiffness after driving. Therefore, enhanced knowledge of the behaviour during and after vibratory driving is desirable.

Components of a Vibratory Hammer

Vibratory hammers are usually either free-hanging or leader-mounted, with respect to how they are supported (Viking, 2002). Free-hanging hammers may be supported by a crane, of which the vibratory hammer is connected to the crane by e.g. steel wires. This support method of the vibratory hammer is the one assumed for the vibratory hammer further in this section, and in the simulations to be presented in the thesis. Figure 2.3a shows a free-hanging vibratory hammer clamped to the top of a pile, and the principle of the same hammer-pile system is shown in Figure 2.3b.

[1]Jonker (1987) uses the word *permanent*, however, *continuous* is assumed as a suitable substitution.

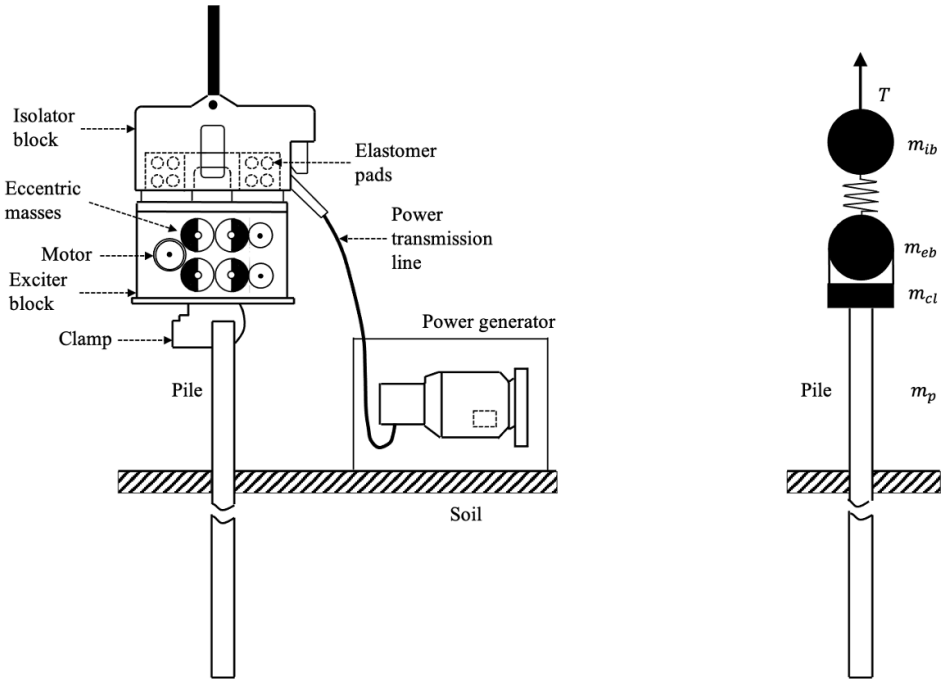

(a) Visualisation of a vibratory pile driver. (b) Mechanism of a vibratory driver.

Figure 2.3: Visualisation and the mechanism of a vibratory driver. Redrawn, with modifications, after Holeyman (2002).

The components and principle of the vibratory hammer shown in Figure 2.3 may be described as follows (Viking, 2002; Holeyman, 2002; Whenham and Holeyman, 2012):

- The suspension force (T) is the possible uplift from the carrier of the vibratory hammer.
- The isolator block, or bias mass, has a mass of m_{ib}. The function of this mass may be two-folded, namely reducing the vibrations produced by the hammer before reaching the carrier and to increase the total mass of the system. The latter may increase the load contribution towards penetration of the pile.
- Elastomer pads are placed between the isolator block and the exciter block to damp vibrations from the exciter block and reduce the natural frequency of the isolator block compared to one of the exciter block.
- The exciter block contains the rotating, eccentric masses, and is the source of the vibrations created during pile driving. The exciter block has a mass of m_{eb}.
- The clamps are the connectors between the exciter block and the pile, creating a rigid connection between these in order to transfer the vertical force to the pile.
- m_p is the mass of the pile being driven into the soil.

Vertical Force of Vibratory Hammer

The vertical vibrations are created by rotating eccentric masses located in the exciter

block (see Figure 2.3a). The eccentric masses have a weight (m_{ecc}) and an eccentric radius (r_{ecc}), of which the eccentric radius may be interpreted as the distance from the centre of rotation to the centre of gravity of the eccentric mass, visualised in Figure 2.4.

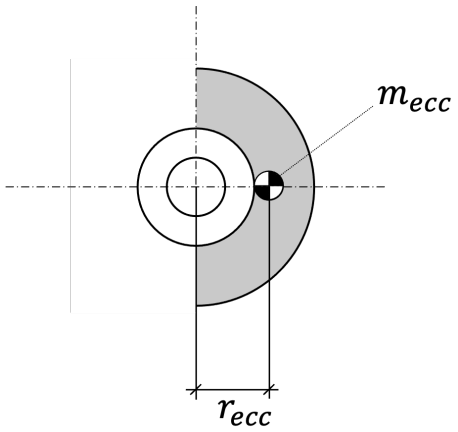

Figure 2.4: Eccentric mass (m_{ecc}), indicated at its centre of gravity, and eccentric radius (r_{ecc}). Redrawn, with modifications, after Viking (2002).

During the rotation of one eccentric mass a centrifugal force ($F_{ecc,c}$) [N] is generated, given by (Viking, 2002):

$$F_{ecc,c} = m_{ecc} \cdot a_c = m_{ecc} \cdot r_{ecc} \cdot \omega^2 = M_{ecc} \cdot \omega^2 \tag{2.8}$$

of which m_{ecc} is the weight of the eccentric mass, a_c is the centrifugal acceleration of the rotating mass, r_{ecc} is the eccentric radius, and ω is its angular frequency. Note the relationship between the eccentric mass and eccentric radius with the the eccentric moment of one eccentric mass (M_{ecc}) [kg· m], given by $M_{ecc} = m_{ecc} \cdot r_{ecc}$.

In order to only have the vertical component of the centrifugal force, the vibratory hammer may be equipped with several eccentric masses of which the rotations are phased in a matter to cancel out the horizontal centrifugal force components while adding together the vertical ones (Jonker and Middendorp, 1988). This principle is visualised for two rotating masses in Figure 2.5.

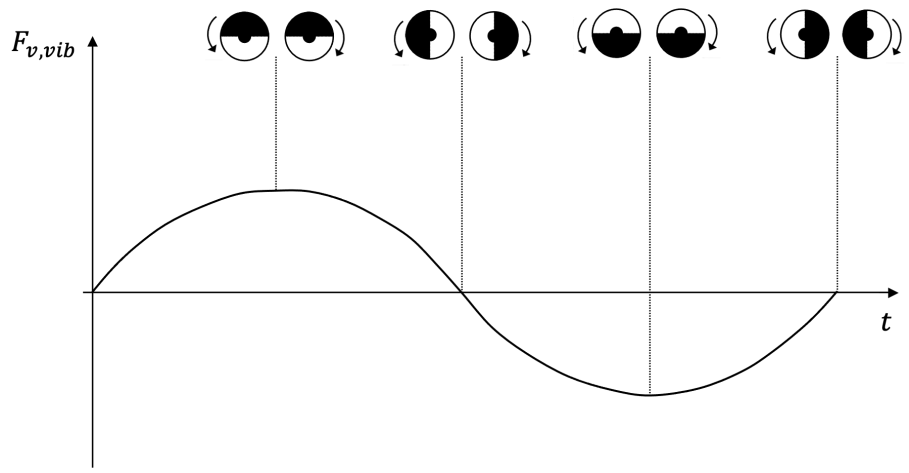

Figure 2.5: Principle of the generation of vertical dynamic load created by a pair of rotating eccentric masses. Vertical force ($F_{v,vib}$) vs. time (t). Redrawn, with modifications, after Jonker (1987) and Jonker and Middendorp (1988). Adopted, with some modifications, from Eiesland (2020)

The continuous vertical force created by the rotating masses may be expressed by a sinusoidal function (Holeyman, 2002):

$$F_{v,vib}(t) = M_{ecc,sum} \cdot \omega^2 \cdot \sin(\omega \cdot t) \tag{2.9}$$

of which $M_{ecc,sum}$ is the sum of eccentric moments from all rotating masses, ω is the angular frequency and t is time. Note that the amplitude ($F^A_{v,vib}$) of the force in Equation 2.9 is given by $M_{ecc,sum} \cdot \omega^2$, since the sinusoidal function ranges between -1 and 1.

Vibratory Driving Frequencies

Vibratory hammers are most often driven by hydraulic power, allowing adjustment of the frequency of the rotating masses during driving (Massarsch et al., 2017). This allows adjustment of the vertical force during driving, due to the relation between frequency and vertical force shown in Equation 2.9. DFI (2015) states that the classification of driving frequencies for vibratory hammers are not unanimously agreed upon, however, suggests driving frequencies in the range of 15-30 Hz to be classified as standard frequency, 30-80 Hz as high frequency and 80-150 Hz as super high frequency.

Some vibratory hammers may have the ability to alter the phase of the eccentric masses during driving, often referred to as variable moment. The eccentric masses may be phased to cancel out all centrifugal force, hence allowing to alter the driving frequency without applying any force to the pile. This allows avoidance of driving in undesirable frequencies, which in some cases may be the frequency creating resonance in the ground during startup or end of driving (DFI, 2015).

Force Transfer Ratio

The vertical, dynamic force induced on top of the pile is not necessarily equal to the force created by the eccentric masses ($F_{v,vib}$). If assuming that the isolator block does not affect the vibrations created by the eccentric masses the hammer-pile system may be modelled by a two-body system consisting of the dynamic part of the vibratory hammer ($m_{vib,dyn} = m_{eb} + m_{cl}$) and the pile ($m_p$), of which $m_{vib,dyn}$ may be assumed rigid, and m_p may be assumed either rigid or elastic (Whenham and Holeyman, 2012). It is in the following assumed that both $m_{vib,dyn}$ and m_p behave as rigid bodies.

Whenham and Holeyman (2012), with reference to Gonin (2006)[2], presents a force transfer ratio (η_F^{rigid}):

$$\eta_F^{rigid} = \left| \frac{F_{v,vib,p}^A}{F_{v,vib}^A} \right| \tag{2.10}$$

of which $F_{v,vib,p}^A$ is the amplitude of the force subjected to the top of the pile and $F_{v,vib}^A$ is the amplitude of the force created by the eccentric moments. Whenham and Holeyman (2012) presents, with reference to Gonin (2006)[3], the following equation by assuming equal vertical acceleration for both $m_{vib,dyn}$ and m_p:

$$\frac{F_{v,vib}^A}{m_{vib,dyn} + m_p} = \frac{F_{v,vib,p}^A}{m_p} \tag{2.11}$$

and introduces the ratio between $m_{vib,dyn}$ and m_p:

$$\mu_{mass} = \frac{m_{vib,dyn}}{m_p} \tag{2.12}$$

and suggests the force transfer ratio in Equation 2.10 to be written by:

$$\eta_F^{rigid} = \frac{1}{1 + \mu_{mass}} \tag{2.13}$$

suggesting the force transfer ratio from the vibratory hammer to the top of the pile to depend on the mass ratio between the dynamic part of the vibratory hammer ($m_{vib,dyn}$) and the pile being driven (m_p).

Vibratory Driving Parameter Selection

Rodger and Littlejohn (1980) suggests a recommended range for a set of vibratory driving parameters based on soil type, pile tip resistance and/or pile weight, as presented in Table 2.2.

[2]Reference not available. Reference is made to Whenham and Holeyman (2012).

[3]Reference not available. Reference is made to Whenham and Holeyman (2012).

Table 2.2: Vibratory driving parameters. Rewritten after Rodger and Littlejohn (1980) with modifications from Holeyman (2002).

Cohesive soils	Dense non-cohesive soils		Loose non-cohesive soils	
All cases	Low pile tip resistance	High pile tip resistance	Heavy piles	Light piles
High acceleration	High acceleration	Low frequency Large displacement amplitude		High acceleration
Predominant side resistance	Predominant side resistance	Predominant end resistance		Predominant side resistance
Requires high acceleration for either shearing or thixotropic[4] transformation	Requires high acceleration for fluidization	Requires high displacement amplitude and low frequency for maximum impact to permit elasto-plastic penetration		Requires high acceleration for fluidization
Recommended parameters				
$f > 40\,\text{Hz}$ a_{vert} : 6-20 g A_{displ} : 1-10 mm	f : 10-40 Hz a_{vert} : 5-15 g A_{displ} : 1-10 mm	f : 4-16 Hz a_{vert} : 3-14 g A_{displ} : 9-20 mm		f : 10-40 Hz a_{vert} : 5-15 g A_{displ} : 1-10 mm

The driving parameters included in Table 2.2 are driving frequency of eccentric masses (f), vertical acceleration (a_{vert}) and one-way displacement amplitude (A_{displ}). The latter two are quantities of the dynamic part of the vibratory hammer, i.e. exciter block and clamps.

[4]Rodger and Littlejohn (1980) states that if the cohesive soil has a certain level of moisture during pile penetration, then thixotropic transformation may be present. Thixotropy may, in general and briefly, be defined as a decrease in viscosity with time and the possible regain of viscosity after loading has ceased (Mewis and Wagner, 2009)

Chapter 3

Theory of Wave Propagation

It is important to distinguish between particle velocity and wave velocity. Particle velocity is the movement of one single particle, while wave velocity is the velocity at which a wave propagates between particles. During vibratory driving the particle velocity of the top of the pile may be considered equal the one for the dynamic mass of the vibratory hammer if the pile is rigidly connected to the hammer through clamps. If the pile itself is assumed rigid the particle velocity is uniform along the pile length, while in cases of which the pile is not assumed rigid the particle velocity may be lower at the pile toe compared to the top of the pile, amongst others depending on the stiffness of the pile and the surrounding soil. Vertical particle movement of the pile during both vibratory and impact driving may induce vertical movement of the surrounding soil due to friction between the pile wall and the soil grains, which may propagate further out form the pile due to friction between adjacent soil grains.

This chapter presents some basic theory regarding different types of wave propagation related to pile driving. Different types of damping are briefly presented.

3.1 Body Waves

Body waves may be characterised by the wave propagation being inside a body (Nordal, 2019). The primary and secondary waves are to be briefly presented.

3.1.1 Primary Waves

Primary waves (P-waves) are compression waves and may be characterised as an alternating push-pull movement between particles (Nordal, 2019). The primary wave velocity is a material property and may for an elastic material be given by (Towhata, 2008; Nordal,

2019):

$$\mathrm{v}_p = \sqrt{\frac{K + \frac{4}{3} \cdot G}{\rho}} = \sqrt{\frac{E(1-\nu)}{\rho(1-2\cdot\nu)(1+\nu)}} \tag{3.1}$$

of which K is bulk modulus, G is shear modulus, ρ is density, E is the elastic modulus and ν is Poisson's ratio. These are material parameters of the medium in which the wave is propagating. K and G relates to E and ν by:

$$K = \frac{E}{3(1-2\cdot\nu)} \tag{3.2}$$

and

$$G = \frac{E}{2(1+\nu)} \tag{3.3}$$

The primary wave velocity of a fully water-saturated soft soil may be assumed close to that of water, which is $\mathrm{v}_p = 1500\,\mathrm{m/s}$, due to the high bulk modulus of water (Towhata, 2008).

During impact pile driving the relatively high load amplitude applied to the top of the pile may lead to a compaction of the pile. This may, at certain places on the pile, cause a rapid expansion of the pile radially. This expansion may be reversed by contraction, depending on whether the material behaves elastic, plastic or a combination of these. If the expansion of the pile diameter is at the part of the pile submerged in water this may lead to propagation of P-waves in the surrounding water, of which may be harmful for underwater marine life. The principle of vibratory driving is to induce a lower load amplitude with an increased number of loading cycles, compared to impact driving. This may reduce the magnitude of pressure of the P-waves, hence, possibly reduce the harm on marine wildlife.

3.1.2 Secondary Waves

Secondary waves (S-waves) are shear waves and may be characterised as oscillation of particles perpendicular to the wave propagation direction (Nordal, 2019). Secondary waves may be generated during pile driving due to friction between the pile wall and the adjacent soil grains, and may propagate further out from the pile wall due to friction between grains. For a linear elastic material in 3D the shear wave velocity may be given by (Nordal, 2019):

$$\mathrm{v}_s = \sqrt{\frac{G}{\rho}} \tag{3.4}$$

Shear waves may not propagate in water due to zero shear modulus, however, shear waves may propagate in water-saturated soils if there are contact between grains.

3.2 Surface Waves

Surface waves propagate on the surface of a body, in contrast to body waves that propagate inside the body (Nordal, 2019). Two surface waves are to be presented, namely Rayleigh waves and Love waves.

3.2.1 Rayleigh Waves

The movement of particles for Rayleigh waves are ellipsoidal (Nordal, 2019), as illustrated in Figure 3.1.

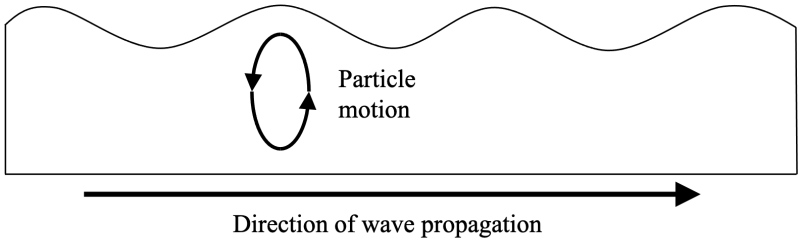

Figure 3.1: Particle motion of Rayleigh waves in an elastic medium. Redrawn, with modifications, after Towhata (2008).

For R-waves with the same wave propagation direction seen in Figure 3.1 the particle motion turns from a counter-clockwise to a clockwise motion at a certain depth (Towhata, 2008).

3.2.2 Love Waves

Another type of surface waves are the Love waves (L-waves), which are shear waves of which the particles move perpendicular to the direction of the wave propagation in the plane of the surface. The wave propagation may be described by a snake-like movement (Nordal, 2019). L-waves may occur on the surface of a soil if the top layer is softer than the lower soil layer (Towhata, 2008).

3.3 Longitudinal Compression Wave Velocity in a Pile

The dynamic loading applied at the top of the pile during pile driving creates compression waves that propagates in the compression load direction. The velocity of the longitudinal compression wave propagation in a bar of elastic material may be given by (Nordal, 2019):

$$\mathrm{v}_c = \sqrt{\frac{E}{\rho}} \tag{3.5}$$

of which E and ρ is respectively the elastic modulus and density of the material. For a pile with $E_{pile} = 200 \cdot 10^9\,\text{Pa}$ and $\rho_{pile} = 7849.1\,\text{kg/m}^3$ the compression wave velocity is calculated to be $\text{v}_{c,pile} = 5047.8\,\text{m/s}$.[5]

During pile driving the compression wave travels from the top of the pile, at which the load is applied, with a downward direction towards the pile toe. The theoretical behaviour of the compression wave when approaching a boundary, e.g. the pile toe or head, depends on the assumption of whether the boundary is assumed fixed, free or a combination of these. At a fixed end the wave is assumed to be reflected as a compression wave while at a free end as a tensile wave (Nordal, 2019). The assumption of the boundary condition may depend on the stiffness of the surrounding soil or if the pile toe is in contact with bedrock. Regardless of the boundary condition the wave is reflected with the same intensity (Nordal, 2019), given by:

$$I = \frac{P}{A} \tag{3.6}$$

of which P [joule/s] is the power of the wave and A [m^2] is the area perpendicular to the direction which the wave is propagating.

3.4 Damping

The amplitude of waves propagating through soils may be gradually reduced due to damping, leading to a loss of energy in the wave. The damping present during wave propagation in soils may be divided into material and geometric damping, of which the latter is related to energy dissipation due to being distributed over a larger area or volume as the wave propagates from the source (Nordal, 2019). Material damping is related to energy loss due to friction between soil grains, deformation of soil structure and the viscosity of any fluid present in the soil structure pores (Ashmawy et al., 1995).

[5]These material parameters are to be used for the pile in the simulations presented later in the thesis, of which ρ relates to specific weight and the gravitational acceleration by $\rho = \gamma/g$.

Chapter 4

Non-cohesive Soils Subjected to Shear Loading

Vertical movement of a pile, both during vibratory and impact driving, induce propagation of shear waves in the soil due to friction between the pile and the surrounding soil. This section briefly presents the term of non-cohesive soils, before discussing these soils subjected to monotonic and cyclic shear loading respectively.

4.1 Non-cohesive Soils

Keaton (2018) describes non-cohesive soils, i.e. cohesionless soils or granular soils, as soils without cohesion contribution to the shear strength, hence only contribution from friction between grains, and that the particles of the soil does not lump together. Sand may be assumed to be a non-cohesive soil, while clay, on the other hand, may be suggested to be a cohesive soil material. E.g. when dried, clay particles may form lumps with a non-zero tensile strength.

Sand may be considered a relatively permeable material. However, if a load is rapidly applied and the sand is investigated during, or right after, the rapid loading the possible change of pore pressure may not have the time to dissipate and the sand may be considered to behave undrained, or partly drained, which may be the case during e.g. earthquake loading (Sawicki and Świdziński, 2007). Dobry et al. (1982) suggests that in the occurrence of earthquakes in saturated fine sands with an assumed undrained condition, the dissipation of the excess pore pressure may in some cases not begin until after the cyclic loading has ended. The load induced on the soil during vibratory pile driving may be considered rapid and may therefore lead to the possibility of increased excess pore water pressure.

4.2 Monotonic Shear Loading

Applying a monotonic shear load on a non-cohesive soil specimen induces relative movement between soil grains. Figure 4.1 shows two different packing of spheres, of which the spheres at both densities represents the same soil grains. Figure 4.1a shows a loose packing and Figure 4.1b a dense packing, and when subjected to shear stress in a drained condition the loose packing will contract and become denser, while the dense packing will dilate and become looser (Wood, 1990).

(a) Loose packing of spheres.

(b) Dense packing of spheres.

Figure 4.1: Loose (a) and dense (b) packing of spheres. Redrawn, with modifications, after Wood (1990).

The initial void ratio is of importance regarding the behaviour of a non-cohesive soil during shear loading, however, during continuous shearing it is suggested that a sand in drained conditions eventually will approach a critical state. Roscoe et al. (1958) defines the critical void ratio of a saturated drained soil sample as the state at which any further shear stress (τ) applied to the sample does not cause any additional change of the void ratio. For a saturated undrained soil sample, the void ratio remains unchanged during any applied shear stress, however, a critical void ratio is eventually obtained due to change of effective mean stress (p') so that the initial void ratio becomes the critical one (Roscoe et al., 1958). These principles are part of the critical state soil mechanics (CSSM) framework of soil behaviour.

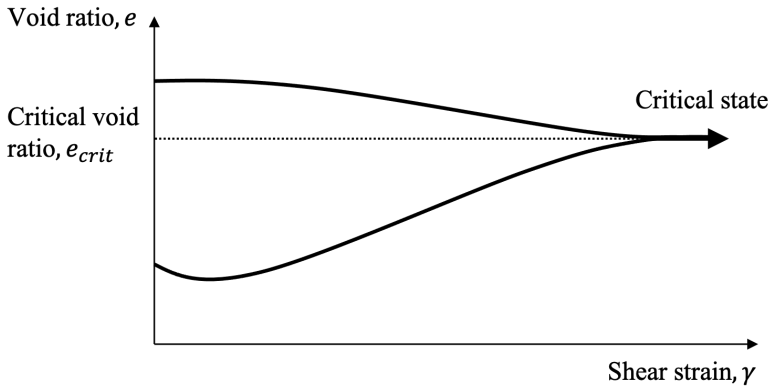

Figure 4.2: Void ratio of a soil sample approaching critical state during continuous shearing at a constant effective mean stress in a drained condition, regardless of initial void ratio. Redrawn, with modifications, after Nordal (2020) with modifications from Dahl and Løyland (2017).

Figure 4.2 shows the change of void ratio of a sand subjected to shear strain in drained conditions, at a constant effective mean stress (p'). Initial contraction may be seen for soil samples of initial void ratios both above and under the critical one when subjected to shear strains. However, whether a soil sample continues to contract or starts dilating (expand) when subjected to further shearing depends on whether the initial void ratio is higher or lower than the critical, seen in Figure 4.2. Wood (1990) states that the critical void ratio of a sand is lower if sheared at a high effective mean stress in pressure than if the same sand is sheared at a lower effective mean stress, hence the critical void ratio depends on effective mean stress.

During rapid loading on sands the behaviour may be undrained, or partly drained, and the possible contraction of the soil may not take place if the liquid in the voids are assumed incompressible. Instead of contraction, this leads to an increased pore pressure (u), which further leads to a reduction of the contact, or effective, normal stresses between soil grains (σ') by the following relation:

$$\sigma' = \sigma - u \tag{4.1}$$

if the total normal stress (σ) is assumed constant during the loading. This may lead to the reduced p' in pressure, eventually causing the current void ratio to become the critical one during continuous undrained loading.

Reduction of the effective normal stresses between soil grains may lead to a reduction of the failure shear strength (τ_f) in the soil, which by Coulomb's law is defined by:

$$\tau_f = c + \sigma' \cdot \tan(\varphi) = (\sigma' + a) \cdot \tan(\varphi) \tag{4.2}$$

of which c is cohesion, φ is the friction angle and a is the attraction. Cohesion and attraction has the following relation:

$$c = a \cdot \tan(\varphi) \tag{4.3}$$

A non-cohesive soil may, by definition, have $c = 0\,\text{kPa}$, which implies that for an increased excess pore pressure due to rapid loading the failure shear strength may approach zero, and the soil may behave like a liquid. The term full liquefaction may be used for the state of the soil if the effective stresses are zero. Poulos et al. (1985) states that the effect of soil liquefaction may occur also for dry sands in certain conditions, due to increased pore pressure of to the air in the voids.

4.3 Cyclic Shear Loading

In contrast to monotonic loading cyclic loading additionally inflicts load reversals on the soil. The soil behaviour may be evaluated by plotting the response in terms of hysteresis loops, which may be used to visualise how the behaviour of the soil may change during cyclic loading, adding the dimension of time to the plot. Figure 4.3 shows an example of a shear stress vs. shear strain hysteresis loop of a soil subjected to cyclic strain-controlled loading (Vucetic, 1994). The figure shows the hysteresis loops for the first cycle and cycle number N, and the shear strain amplitude (γ_c) and the shear stress amplitude (τ_c) is the maximum value of shear strains and stress respectively during each cycle.

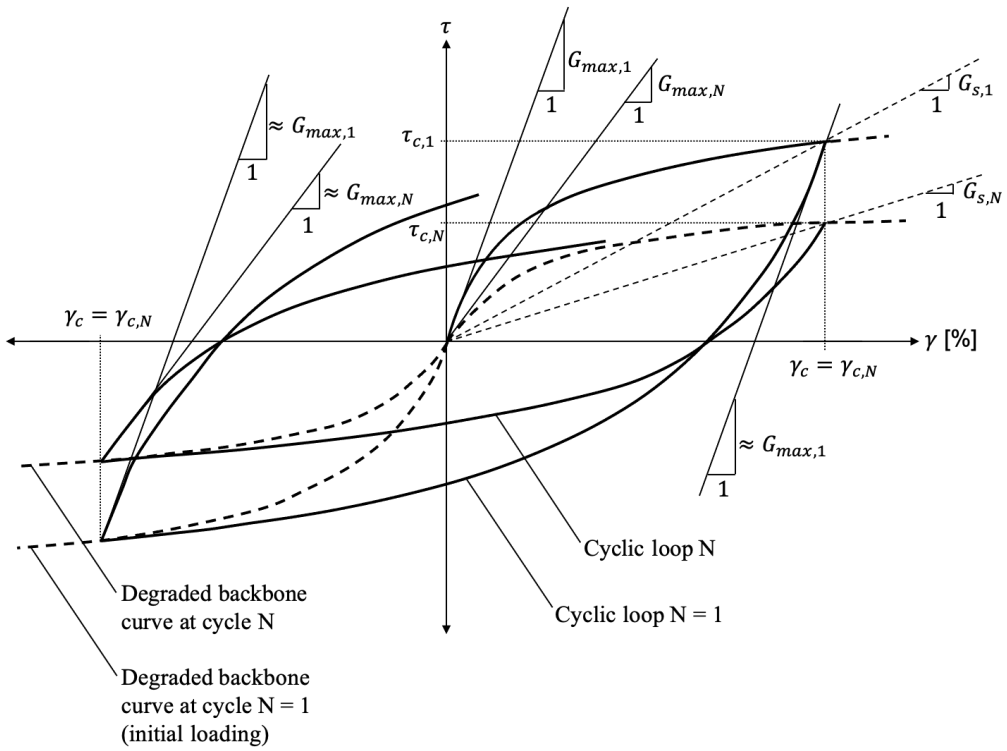

Figure 4.3: Hysteresis loop of soil subjected to cyclic strain-controlled loading. Redrawn, with modifications, after Vucetic (1994) with modifications from Holeyman (2002) and Deckner (2013). Adopted, with some modifications, from Eiesland (2020).

The hysteresis loops in Figure 4.3 shows a non-linear response of the soil during the cyclic loading, and of which the shear modulus, or shear stiffness, (G) reaches its approximate maximum value (G_{max}) for a given cycle at load initiation for the first cycle and at the load reversals. The secant shear modulus (G_s) shown in Figure 4.3 is given by the relation:

$$G_s = \frac{\tau_c}{\gamma_c} \tag{4.4}$$

of which τ_c is the cyclic shear stress amplitude and γ_c is the cyclic shear strain amplitude for a given cycle.

Figure 4.3 shows that the amplitude of the cyclic shear stress is lower at cycle number N compared to the first, and since the cyclic shear strain amplitude is held constant at each cycle (strain-controlled cyclic loading) this imply a reduction of the secant shear modulus. This is often termed cyclic shear modulus degradation. In the case of undrained loading on a saturated non-cohesive soil this degradation may be mainly due to the generation of excess pore pressure, which leads to a reduced shear strength as previously discussed in Section 4.2. The magnitude of shear stiffness degradation may be evaluated by the stiffness index (δ_N) (Idriss et al., 1978)[6] (Vucetic and Mortezaie, 2015):

$$\delta_N = \frac{G_{s,N}}{G_{s,1}} = \frac{\tau_{c,N}/\gamma_c}{\tau_{c,1}/\gamma_c} = \frac{\tau_{c,N}}{\tau_{c,1}} \tag{4.5}$$

of which N is the number of cycles, and parameters denoted 1 indicate values for the first cycle. δ_N equal to 1.0 indicates no degradation, while zero may indicate full liquefaction, at cycle number N.

The plastic response seen in Figure 4.3 implies the presence of energy dissipation in terms of material damping, which for the hysteresis loops may be termed hysteretic damping, given by (Vucetic and Dobry, 1991):

$$\lambda = \frac{1}{2\pi} \cdot \frac{\Delta E_{hyst}}{G_s \cdot \gamma_c^2} \tag{4.6}$$

of which ΔE_{hyst} is the enclosed area of the hysteresis loop, and may be interpreted as the energy loss for the given cycle due to plastic deformations.

When shearing a sand sample it may initially contract before either further contracting or dilating, depending on the initial void ratio compared to its critical void ratio, as previously visualised in Figure 4.2. Rapid, cyclic loading on sand may lead to undrained behaviour and excess pore pressure build-up. Full soil liquefaction may occur if the excess pore pressure is equal to the initial effective stresses. It is suggested that the generation of excess pore pressure in undrained conditions are closely related to the potential volume reduction that may take place if the soil eventually is consolidated (Vucetic, 1994; Holeyman, 2002).

In addition to different degrees of liquefaction, of which may be present both during monotonic and cyclic loading, the term cyclic mobility may be included in order to describe the behaviour of saturated sand subjected to undrained cyclic loading. Cyclic mobility may be described as a state at which the soil subjected to undrained cyclic shear loading regains some of its stiffness due to increased effective stresses (Towhata, 2008). The increase of effective stresses is due to phase transformation from a contractive to dilatant behaviour during the cyclic loading (Towhata, 2008), and may be illustrated in a $p' - q$ plot as seen in Figure 4.4. The figure shows an excerpt of a stress path for a dense sand subjected to undrained cyclic loading of which the effective mean stress is reduced in pressure until reaching phase transformation and some of the effective mean stress may be regained due

[6]Reference not available. Reference is made to Vucetic and Mortezaie (2015).

to dilative behaviour. Further cyclic loading may reduce the effective stress, before some of it again is recovered.

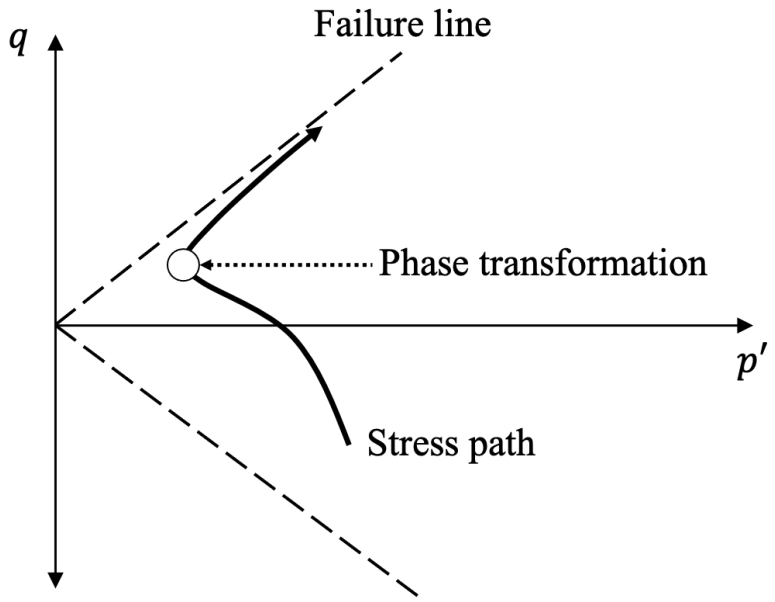

Figure 4.4: Excerpt of the $p' - q$ stress path during undrained cyclic loading on sand, showing phase transformation. Redrawn, with modifications, after Towhata (2008).

Zhang et al. (2007) states that very loose sands may reach full liquefaction ($p' = 0$) without experiencing cyclic mobility, while medium dense sands may fully liquefy in addition to having cyclic mobility, and that dense sands does not fully liquefy. Figure 4.5 shows examples of the suggested stress path in $p' - q$ space during undrained cyclic triaxial testing on initially loose, medium and dense sand. The initially loose sand (Figure 4.5a) approaches full liquefaction, i.e. $p' = 0$, before cyclic mobility is initiated, while the medium sand (Figure 4.5b) experiences cyclic mobility when approaching full liquefaction. The dense sand (Figure 4.5c) does not approach full liquefaction, and could be suggested to exhibit only a slight cyclic mobility.

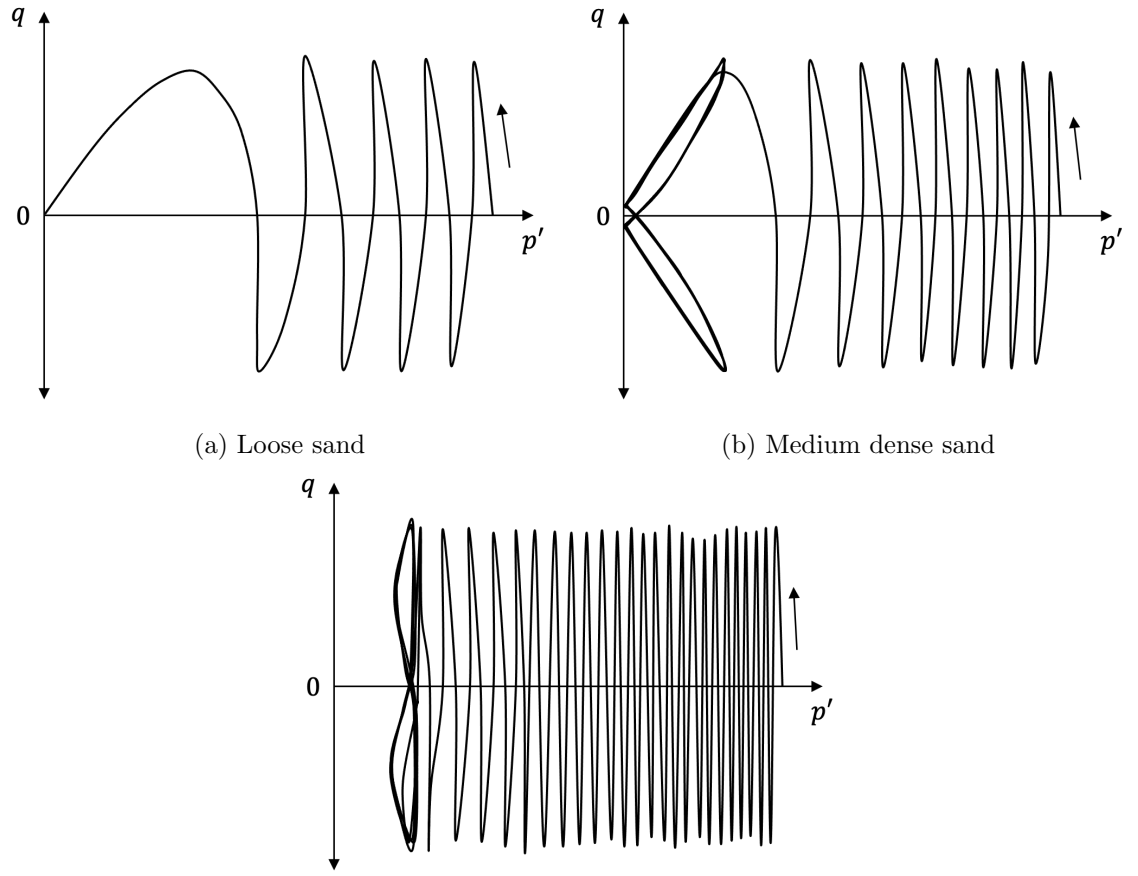

(a) Loose sand

(b) Medium dense sand

(c) Dense sand

Figure 4.5: Examples of $p' - q$ stress paths during undrained cyclic triaxial shear testing on sands at different initial densities. Arrows indicate stress path direction during loading. Redrawn, with modifications, after Zhang et al. (2007)

Prediction of Pore Water Pressure Build-up of Sand

This section as a whole is based on results from cyclic triaxial tests presented by Dobry et al. (1982), investigating pore water pressure build-up and liquefaction prediction of sands during earthquakes. Reference is therefore made to Dobry et al. (1982) for the following paragraphs in this section.

Several strain-controlled cyclic triaxial tests were performed under undrained conditions on a saturated sand. The tests were all isotropically consolidated to a given effective radial stress (σ_3'). The cyclic strain was applied as a sinusoidal function at 1 Hz. 12 tests were performed, varying the effective radial stress (σ_3'), relative density (D_r) and the cyclic shear strain amplitude (γ_c) applied. 10 out of the 12 tests were performed with $\sigma_3' = 95.6\,\text{kPa}$. The relative densities for the soil in the tests were either 45 %, 60 % or 80 %. The cyclic shear strain amplitudes used were $\gamma_c = 3 \cdot 10^{-4}$, $\gamma_c = 1 \cdot 10^{-3}$ and $\gamma_c = 3 \cdot 10^{-3}$.

Shear modulus degradation is measured in terms of the reduction of the ratio $G_s/G_{s,1}$, of which G_s is the secant shear modulus and $G_{s,1}$ is the secant shear modulus at the first cycle. The test results indicate that $G_s/G_{s,1}$ approaches zero for all three relative densities

tested with $\sigma_3' = 95.6\,\text{kPa}$ when applying the cyclic strain of $\gamma_c = 3 \cdot 10^{-3}$. Zero $G_s/G_{s,1}$ is indicated for $D_r = 45\,\%$ after 10 cycles, for $D_r = 60\,\%$ after 50 cycles and for $D_r = 80\,\%$ after 100 cycles. Applying $\gamma_c = 1 \cdot 10^{-3}$, however, indicates $D_r = 45\,\%$ approaching zero after 100 cycles, while after the same number of cycles $D_r = 60\,\%$ is at approximately $G_s/G_{s,1} = 0.3$ and $D_r = 80\,\%$ approximately $G_s/G_{s,1} = 0.8$.

Undrained cyclic triaxial tests were performed on the sand with $D_r = 60\,\%$ and $\gamma_c = 3{\cdot}10^{-4}$ with three different σ_3', being approximately 25.48 kPa, 95.60 kPa and 191.20 kPa. The results indicate the largest shear modulus degradation for $\sigma_3' = 25.48\,\text{kPa}$ and least for $\sigma_3' = 191.20\,\text{kPa}$.

Dobry et al. (1982) states there are indications of a predictable dependency between the cyclic shear strain amplitude and generation of pore water pressure in saturated sands, and that for normal consolidated sands there is a cyclic shear strain amplitude threshold value ($\gamma_{c,t}$) at which $\gamma_c < \gamma_{c,t}$ does not induce any densification of dry sands and no pore pressure buildup for saturated sands. Dobry et al. (1982) states that results from the undrained cyclic strain-controlled triaxial tests performed suggests a value of $\gamma_{c,t} = 1.1 \cdot 10^{-4}$ for 10 cycles, and is suggested to be regardless of the three relative densities tested and σ_3' between $23.9 - 95.6\,\text{kPa}$.

Soil Behaviour During Small Cyclic Strains

It is suggested that there is a threshold value for the cyclic shear strain amplitude at which strains below this value may not generate any extensive excess pore pressures at a small number of cycles, often referred to as the cyclic threshold shear strain ($\gamma_{c,t}$) (Dobry et al., 1982; Vucetic, 1994). However, it is suggested that noticeable excess pore pressure may be generated at a large number of cycles, even with cyclic loading of which $\gamma_c < \gamma_{c,t}$, which may be the case in particular situations of machine vibrations or ocean wave loads on a foundation (Vucetic, 1994). Figure 4.6 shows the principle of secant shear stiffness degradation and hysteretic damping as a function of γ_c for a given number of cycles, suggesting the stiffness degradation being close to zero for very small shear strain amplitudes.

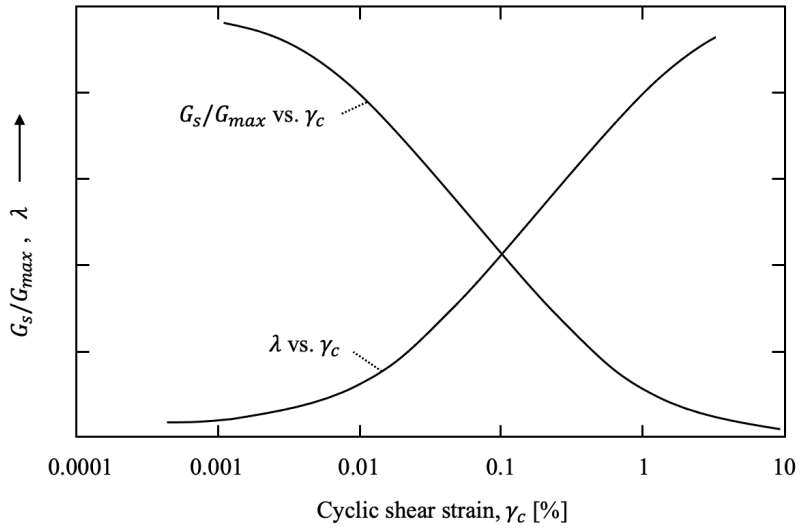

Figure 4.6: Example of plot with G_s/G_{max} and λ respectively vs. γ_c for a given number of cycles. The plot is not in scale. Redrawn, with modifications, after Vucetic and Dobry (1991). Adopted from Eiesland (2020).

Vucetic and Mortezaie (2015) investigate the behaviour of water-saturated sands during undrained strain-controlled cyclic loading with relatively small strains, in the area of a suggested cyclic threshold shear strain equal to $\gamma_{c,t} \approx 1 \cdot 10^{-4}$. Cyclic simple shear strain-controlled tests were performed on Nevada sand, at a frequency of $f = 0.01$ Hz with number of cycles in the range of 5-20. Vucetic and Mortezaie (2015) suggests, for undrained cyclic shear straining of saturated sands, the following soil behaviour with respect to secant shear modulus at cycle N ($G_{s,N}$), pore pressure at the end of cycle N (u_N) and the cyclic shear strain amplitude (γ_c):

- $3 \cdot 10^{-5} < \gamma_c < \gamma_{c,t}$: No change of u_N for increased N. Initial increase of $G_{s,N}$ with increased N, before levelling off or slightly decreasing after reaching a certain N.
- $\gamma_{c,t} < \gamma_c < 1 \cdot 10^{-3} - 1.5 \cdot 10^{-3}$: u_N continuously increases with increased N. $G_{s,N}$ has an initial increase, before decreasing.
- $\gamma_c \geq 1 \cdot 10^{-3} - 1.5 \cdot 10^{-3}$: Relatively large buildup of u_N for increased N. $G_{s,N}$ solely decreases with increased N.

The behaviour listed above is limited to a few tests and within the stated ranges of shear strain amplitudes, however, based on several other previous performed tests the trend in the soil behaviour, perhaps with different ranges for γ_c, is suggested valid in general for undrained loading on saturated sands (Vucetic and Mortezaie, 2015). Note the suggested initial increase of G_s also for shearing with $\gamma_c > \gamma_{t,c}$ to a certain value, however, shear strains of this magnitude, and larger, may induce generation of pore pressure which leads to a greater reduction of G_s than the initial increase (Vucetic and Mortezaie, 2015). Vucetic and Mortezaie (2015) suggests this to be partly explained by increased contact areas between grains, and the formation of new contact points, during loading, and states

this behaviour of sand to be previously recognised by Drnevich and Richart (1970)[7] for a dry sand.

4.4 Review of Experimental Results of Vibratory Pile Driving

This section reviews some experimental results in the literature regarding soil behaviour, and state, due to vibratory pile driving.

Full-scale Lateral Load Tests on Impact and Vibratory Driven Piles in Dense Non-cohesive Soil (Achmus et al., 2020)

The field investigation consisted of installing 6 monopiles near Cuxhaven in Germany in 2014, of which 3 were impact driven and the other 3 vibratory driven. The outer diameter of the piles were 4.3 m, with total length of 21 m and embedded lengths between 18.2-18.7 m. The piles had a wall thickness of 45 mm at the upper 6.2 m followed by a wall thickness of 40 mm in the lower part of the piles. The piles were tested in pairs, with a distance of approximately 26 m between each other, of which one was impact driven and the other vibratory driven. The lateral loading was applied on the pile at between 0.85 m and 1.05 m above ground level. The impact driven piles were installed at 40, 40-75 and 20-50 blows per minute respectively. The installation method for the pile installed at 40-75 impacts per minute is the HiLo Method, which indicates a higher rate of blows per minute while inflicting less energy per impact. The vibratory driven piles were all driven at a frequency of 12 Hz the first 8.5-9.5 m, followed by 22.5 Hz to final depth with the exception of one pile being also driven at 15 Hz. The two vibratory driven piles with driving frequency of 22.5 Hz to final depth had a considerable lower installation time compared to the pile vibrated at both 22.5 Hz and 15 Hz after the first 9.5 m.

Achmus et al. (2020) states that the two pile being vibrated at 22.5 Hz to final depth had a less stiff response to the lateral loading compared to the impact driven piles, while the vibratory driven pile being driven at 22.5 Hz and 15 Hz after the initial 9.5 m also had a less stiff behaviour compared to the impact driven, however, it was stiffer than the other two vibrated piles. Achmus et al. (2020) suggests this is to be explained by the lower amount of loosening of the soil due to the vibrated pile being partly driven at a lower frequency. This pile behaved relatively similar as the impact driven in that pair. Achmus et al. (2020) therefore points at the importance of vibratory driving parameters on the influence of bearing capacity of the pile after installation.

Cone penetration tests (CPTs) were carried out both before and after the pile installations to evaluate possible changes of relative density due to installation method. Achmus et al. (2020) states that the results of these tests indicate a clear connection between alteration

[7]Reference not available. Reference is made to Vucetic and Mortezaie (2015).

of CPT results due to pile installation, in terms of altered relative density, and lateral bearing behaviour. A lower cone resistance was observed for the impact driven piles, however, a larger reduction was observed for the two vibratory driven piles at a frequency of 22.5 Hz from below 8.5-9.5 m depth to final depth.

Small-scale Experiment Investigating Alteration in Relative Density of a Saturated Dense Sand Due to Vibratory Pile Driving at 1g Conditions (Remspecher et al., 2019)

The model-setup was the half cross section of a steel pile, being driven along a, close to frictionless, glass panel to evaluate changes of relative density in the soil. To see and record those changes the Digital Image Correlation (DIC), also known as Particle Image Velocimetry (PIV), method was used. 4 images per second were taken, with a resolution of 0.221 mm/pixel. The model container was 1.70 m by 0.7 m, 0.25 m drainage at the bottom and 1.15 m height above this. Pile dimensions were 20 cm outer diameter and 4 mm wall thickness. A penetration of 10 cm was recorded, and was from depth 20 cm to 30 cm. The hammer operated with a load amplitude of 1670 N with a driving frequency of 23 Hz, and a total static load of 225 N. The soil was a well-graded medium to coarse saturated dense sand with an initial relative density of 76 %.

The results presented by Remspecher et al. (2019) indicate a clear loosening of the soil near both the exterior and interior pile wall, while compaction is seen further out from the exterior pile wall. The loosening was seen in a zone approximately 4 mm from exterior pile wall, while compaction at 40 mm from the 4 mm.

Large-scale Laboratory Test of Vibratory Driven Displacement Piles in Saturated Sand (O'Neill et al., 1990)

The pile was installed by vibratory driving and in addition by impact driving for comparison. The tests were performed with one of the objectives being to investigate the effect vibratory driving parameters on pile driveability and its bearing capacity after installation.

The model set-up was in a pressure chamber to replicate in-situ stresses of the soil. The soil container was a cylinder with diameter of 0.76 m and 2.54 m height. Drainage was allowed through certain drains on the container perimeter, and rubber was installed at the bottom to absorb primary waves induced by the pile during driving. The pile was a closed-ended steel pile with diameter of 102 mm and 5.1 mm wall thickness. The pile was referred to as a displacement pile, indicating relatively large soil displacements during pile driving. This is for instance in contrast with open-ended piles, being considered as small-displacement piles, amongst others depending on pile wall thickness. The vibratory hammer model was capable of operating at frequencies of 5-60 Hz, force amplitude of 57.9 kN, maximum vertical displacement amplitude of 8.6 mm and a maximum eccentric moment of 33.9 Nm. The dry sand was built-in dry with two different relative densities,

65 % and 90 %, followed by water-saturating the sand.

O'Neill et al. (1990) states that a driving frequency of 20 Hz gave the highest rate of penetration for the vibratory driven pile in the different tests conducted for that specific hammer-pile-soil system, regardless of altered soil conditions, eccentric moment and bias weight of vibratory hammer. Vibratory driving required less energy for the sand with relative density of 65 % compared to the impact driving, however, with relative density of 90 % the impact driver required less than the vibratory driver. The vibratory driven pile showed a lower axial, compression, bearing capacity for the medium dense sand compared to the impact driven pile. However, for the dense sand the vibratory pile showed a higher axial, compression bearing capacity compared to the impact driven one. O'Neill et al. (1990) suggests the reason for the latter to be a higher toe bearing for the vibrated pile. Note that the pile in the laboratory test was a displacement pile.

Chapter 5

Soil Material Models

The behaviour of a specific material may be observed in a laboratory by performing different tests on a sample. Material models may be used to model an idealisation, or simplification, of the observed behaviour of a material, in order to be able to focus on the decisive parts of its behaviour (Wood, 1990).

Figure 5.1 shows respectively the observed and idealised stress-strain (σ-ε) behaviour of a low-carbon steel sample in tension (Wood, 1990). This particular idealisation is an example of an elasto-plastic material model, with linear-elasticity and perfect-plasticity.

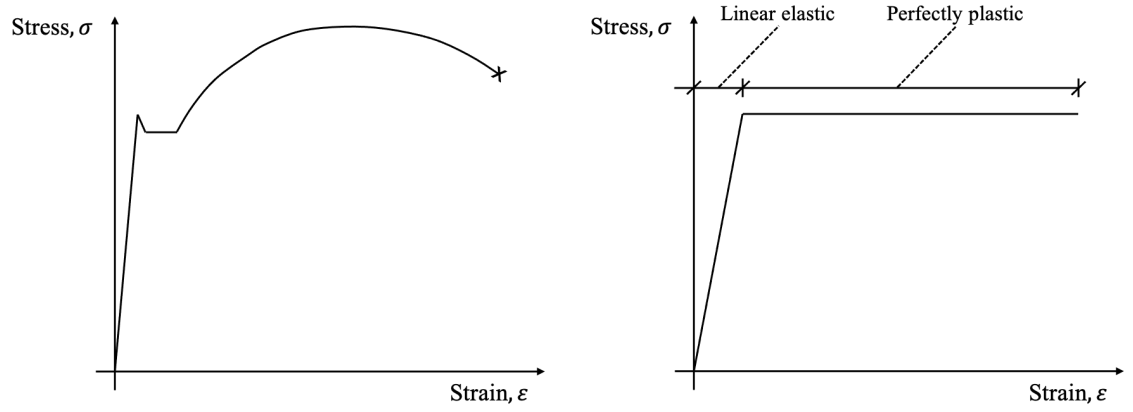

(a) Observed stress-strain relationship.

(b) Idealised stress-strain relationship.

Figure 5.1: Observed and idealised stress-strain curve of a low-carbon steel sample in tension. Redrawn, with modifications, after Wood (1990).

Two material models will be presented in this chapter, namely Mohr-Coulomb and the Simple Anisotropic Sand (SANISAND) constitutive model. These are used to model the soil in the numerical simulations performed in PLAXIS 2D, presented in Chapter 6.

5.1 Mohr-Coulomb

Mohr-Coulomb is a soil model based on elasto-plasticity, of which the total normal strains (ε) may be divided into contribution from elastic normal (ε^e) and plastic normal strains (ε^p):

$$\varepsilon = \varepsilon^e + \varepsilon^p \tag{5.1}$$

Elastic strains are considered reversible, implying that if a sample is loaded and elastic strains occur, these strains are reversed to the initial strain condition during unloading. Dependency between normal stress and elastic normal strains in the linear elastic behaviour may, in the $\sigma - \varepsilon$ space, be described by Hooke's law:

$$\Delta\sigma = \Delta\varepsilon^e \cdot E \tag{5.2}$$

of which $\Delta\sigma$ is change of normal stress, $\Delta\varepsilon^e$ is change of elastic normal strains and E is the elastic modulus of the material. Plastic strains, however, are considered permanent. If a sample is loaded to the magnitude of which plastic strains occur, then the elastic strains are reversed during unloading while the plastic strains remains. This is visualised in Figure 5.2, in the plane of largest principal strain (ε_1) and deviatoric stress (q), of which the latter is defined as the difference between the largest and smallest principal stresses:

$$q = \sigma_1' - \sigma_3' = \sigma_1 - \sigma_3 \tag{5.3}$$

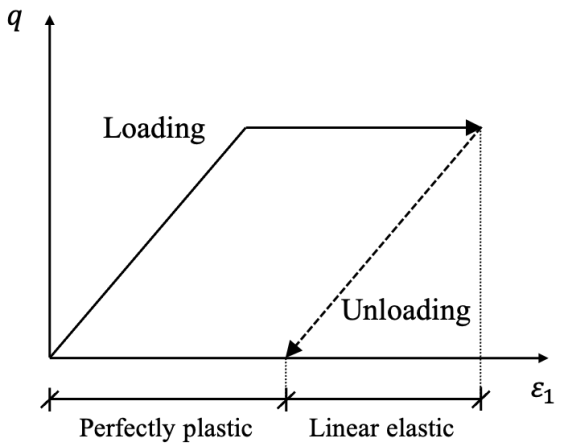

Figure 5.2: Loading and unloading on a linear-elastic and perfectly-plastic soil model. Redrawn, with modifications, after Nordal (2020)

The transition from linear-elasticity to perfect-plasticity for the Mohr-Coulomb material model is determined by the Coulomb criteria for the shear stress at failure (τ_f) for a given

normal effective stress (σ'):

$$\tau_f = c + \sigma' \cdot \tan(\varphi) = (\sigma' + a) \cdot \tan(\varphi) \tag{5.4}$$

of which c is cohesion, φ is the friction angle, a is the attraction, and:

$$c = a \cdot \tan(\varphi) \tag{5.5}$$

shows the relation between cohesion and attraction.

5.2 SANISAND

Manzari and Dafalias (1997) presents a material model based on critical state soil mechanics (CSSM), capable of simulating both monotonic and cyclic behaviour of sands. The material model simulates plasticity by two yield lines in the triaxial space, and surfaces forming shape of a cone for the multiaxial space. CSSM is based on the principle that any soil subjected to shear strains approaches its effective mean stress dependent critical void ratio (Roscoe et al., 1958), as presented in Section 4.2.

SANISAND has been subjected to several developments, and Dafalias and Manzari (2004) incorporates, amongst others, parameters to simulate the dilatant behaviour due to possible changes in the soil fabric. Taiebat and Dafalias (2008) suggests the name Simple Anisotropic Sand (SANISAND) constitutive models for this family of material models, and incorporates cap hardening in addition to the already implemented cone hardening. Cap hardening implements the occurrence of plastic strains at a certain effective mean stress (p'), even if the stress ratio q/p' is constant, for the triaxial stress space. In other words, a cap is introduced to the two yield lines for the triaxial stress space.

The version of SANISAND used in the numerical simulations in Chapter 6 is the one described in Dafalias and Manzari (2004), hence without cap hardening. This SANISAND version is described for the triaxial stress space and the multiaxial stress space in Manzari and Dafalias (1997) and Dafalias and Manzari (2004). The following section presents the equations for SANISAND in the triaxial stress space, followed by a section with an overview of the multiaxial equations.

All the following equations and explanations presented in this chapter describing the SANISAND material model, in both triaxial stress space and multiaxial stress space, are after Dafalias and Manzari (2004) unless else is stated specifically. These equations builds upon formulations presented in Manzari and Dafalias (1997).

5.2.1 Triaxial Stress Space

Formulations for triaxial stress space imply that σ'_1 is the largest principal effective stress, and $\sigma'_2 = \sigma'_3$. The largest principal strain is ε_1, and $\varepsilon_2 = \varepsilon_3$. The triaxial stress space may refer to the $p' - q$ space, of which p' is the effective mean stress and q is the deviatoric stress. For the triaxial stress space p' and q may respectively be defined by:

$$p' = \frac{\sigma'_1 + 2 \cdot \sigma'_3}{3}; \quad q = \sigma'_1 - \sigma'_3 \tag{5.6}$$

and the stress ratio between deviatoric and mean effective stress be introduced as $\eta = \frac{q}{p'}$. The volumetric (ε_v) and deviatoric strains (ε_q) may respectively be defined in the triaxial space by:

$$\varepsilon_v = \varepsilon_1 + 2 \cdot \varepsilon_3; \quad \varepsilon_q = \frac{2}{3} \cdot (\varepsilon_1 - \varepsilon_3) \tag{5.7}$$

The incremental elastic strains ($d\varepsilon_v^e$ and $d\varepsilon_q^e$) are related to incremental effective mean stress (dp') and incremental deviatoric stress (dq) respectively by:

$$d\varepsilon_v^e = \frac{dp}{K}; \quad d\varepsilon_q^e = \frac{dq}{3 \cdot G} \tag{5.8}$$

while the incremental plastic strains ($d\varepsilon_v^p$ and $d\varepsilon_q^p$) are related to dp' and dq respectively by:

$$d\varepsilon_v^p = \mathrm{d} \cdot \left| d\varepsilon_q^p \right|; \quad d\varepsilon_q^p = \frac{d\eta}{H} \tag{5.9}$$

of which K is the bulk modulus, G is the shear modulus, d in Equation 5.9 is the dilatancy, $|d\varepsilon_q^p|$ is the absolute value of $d\varepsilon_q^p$ and H is the plastic hardening modulus.

For the SANISAND model to be presented Dafalias and Manzari (2004) states Richart et al. (1970)[8] and Li and Dafalias (2000) suggests that K and G may be defined as functions of effective mean stress (p') and void ratio (e):

$$K = \frac{2(1+\nu)}{3(1-2\cdot\nu)} \cdot G; \quad G = G_0 \cdot p_{atm} \cdot \frac{(2.97-e)^2}{1+e} \cdot \sqrt{\frac{p'}{p_{atm}}} \tag{5.10}$$

of which ν is Poisson's ratio, G_0 is a material constant and p_{atm} is the atmospheric pressure.

The $p' - q$ stress space in Figure 5.3 visualises the yield-, dilatancy-, critical-, and bounding lines, governing different soil behaviour at different stress states for both triaxial compression and extension.

[8]Reference not available. Reference is made to Dafalias and Manzari (2004).

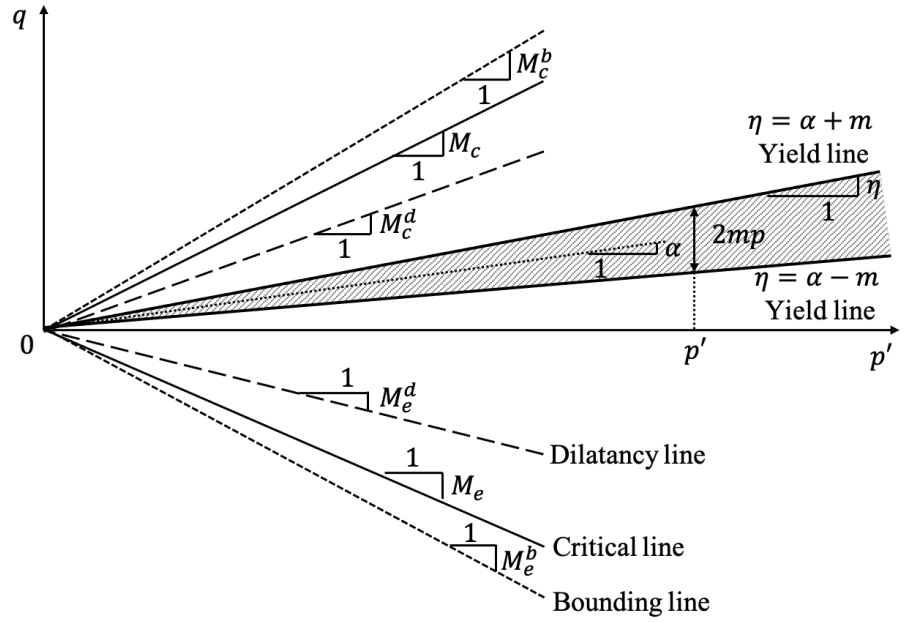

Figure 5.3: SANISAND material model: $p' - q$ stress space with yield, dilatancy, critical and bounding lines indicated. Triaxial compression and extension denoted c and e respectively. Redrawn, with modifications, after Dafalias and Manzari (2004) with modifications after Manzari and Dafalias (1997).

The yield lines in Figure 5.3 are given by:

$$f_{yield} = |\eta - \alpha| - m = 0 \tag{5.11}$$

of which the inclination of the upper and lower yield line are respectively given by:

$$\eta = \alpha + m; \quad \eta = \alpha - m \tag{5.12}$$

Stress states inside the yield lines induce elastic strains, while if the stress path reaches a yield line, i.e. $f_{yield} = 0$ in Equation 5.11, and $d\eta > 0$ at the upper or $d\eta < 0$ at the lower yield line, plastic strains occur and the yield lines are updated in order to satisfy $f_{yield} = 0$. Note that plasticity may only occur for loading at a non-constant stress ratio ($d\eta \neq 0$).[9] SANISAND incorporates both isotropic and kinematic hardening to update the yield lines. Isotropic hardening implements alteration of the size of the area between the upper and lower yield line, by changing the parameter m seen in Figure 5.3. Isotropic hardening may be excluded in the model by setting a constant m (Manzari and Dafalias, 1997). Kinematic hardening changes the direction of the yield lines, i.e. the value of α in Figure 5.3. Kinematic hardening introduces the ability to obtain plastic strains in the soil of a stress state regardless if the sample previously has been in the same stress state. Kinematic hardening is an important feature of the model in order to

[9]Note that if a cap is introduced to the yield lines, as done by Taiebat and Dafalias (2008), plastic strains may occur also for loading at a constant stress ratio ($d\eta = 0$).

simulate accumulation of plastic strains and excess pore pressure build-up during cyclic loading, since isotropic hardening solely increases the elastic area, possibly leading to plastic behaviour only the first few loading cycles (Bardet, 1986).

The plastic hardening modulus (H) for the SANISAND material model is given by:

$$H = h(M_c^b - \eta); \quad H = h(M_e^b + \eta) \tag{5.13}$$

of which M^b is the inclination of the bounding line shown in Figure 5.3 and h is a variable defined by:

$$h = \frac{b_0}{|\eta - \eta_{in}|}; \quad b_0 = G_0 \cdot h_0(1 - c_h \cdot e)(\frac{p}{p_{atm}})^{-1/2} \tag{5.14}$$

of which η_{in} is the initial stress ratio and h_0 and c_h are part of the input parameters for a given sand.

Figure 5.3 shows the dilatancy lines with inclination M^d, and whether the soil dilates (d < 0), contracts (d > 0) or has zero change of volume (d $= 0$) is decided by d in the following equations:

$$\mathrm{d} = A_d(M_c^d - \eta); \quad \mathrm{d} = A_d(M_e^d + \eta) \tag{5.15}$$

of which A_d is a state variable, and M^d is denoted c and e for triaxial compression and extension respectively. Note that a stress state outside the lines of M^d gives (d < 0), hence dilation.

Figure 5.3 shows the inclinations for the critical state lines for compression (M_c) and extension (M_e). The critical state line at triaxial compression is defined by the critical state stress ratio:

$$M_c = \frac{q_c}{p'_c} \tag{5.16}$$

of which q_c and p'_c are the critical deviatoric and effective mean stress respectively. A parameter c is introduced as the ratio between the critical state line in compression and extension (Dafalias and Manzari, 2004) (Mašín, 2015):

$$c = \frac{M_e}{M_c} \tag{5.17}$$

Dafalias and Manzari (2004), with reference to Li and Wang (1998), suggests the following relation between the critical void ratio (e_c) and the critical effective mean stress (p'_c):

$$e_c = e_0 - \lambda_c(\frac{p'_c}{p_{atm}})^{\xi} \tag{5.18}$$

of which e_0 is the void ratio on the critical state line for $p' = 0$, and λ_c and ξ are both critical state parameters.

The dilatancy line (M^d) and bounding line (M^b) are defined as exponential functions suggested by Li and Dafalias (2000):

$$M^d = M \cdot e^{n^d \cdot \Psi} \tag{5.19}$$

and

$$M^b = M \cdot e^{-n^b \cdot \Psi} \tag{5.20}$$

of which both n^d and n^{-b} are positive material constants and Ψ is a state parameter defined by Been and Jefferies (1985) as the difference between the current void ratio and the void ratio at critical state, namely $\Psi = e - e_c$. Note that as the void ratio approaches the critical one, both M^d and M^b approaches the critical line (M) as part of the CSSM framework (Manzari and Dafalias, 1997).

Soil fabric of sands may be described as the pattern of soil grains being of various size, shape and arrangement (Brewer and Sleeman, 1988). Dafalias and Manzari (2004) simulated triaxial tests with cyclic loading without taking into account the effect on dilatancy of the change in soil fabric, and suggested that the pore water pressure buildup was simulated too low. The effect of change in soil fabric on dilatancy is then incorporated, and a larger pore water pressure buildup is simulated. A fabric-dilatancy variable z is introduced, which changes incrementally according to:

$$dz = -c_z \langle -d\varepsilon_v^p \rangle (s \cdot z_{max} + z) \tag{5.21}$$

of which c_z is related to the rate of change of z and z_{max} controls the maximum possible value of z. The angle brackets are MacCauley brackets, which introduce a condition that in this case imply that if $-d\varepsilon_v^p > 0$ then $\langle -d\varepsilon_v^p \rangle = -d\varepsilon_v^p$ and if $-d\varepsilon_v^p \leq 0$ then $\langle -d\varepsilon_v^p \rangle = 0$. I.e., a change of z only occurs during dilation, due to the MacCauley bracket condition of $d\varepsilon_v^p < 0$ giving non-zero input of $d\varepsilon_v^p$ in Equation 5.21. $s = \pm 1$ follows the sign of m in $\eta = \alpha \pm m$. These conditions imply that $dz < 0$ for dilation in triaxial compression and $dz > 0$ for dilation in triaxial extension.

The change of z (dz) is related to the dilatancy parameter (d) by:

$$A_d = A_0(1 + \langle s \cdot z \rangle) \tag{5.22}$$

of which A_d in Equation 5.15 is updated.

5.2.2 Multiaxial Stress Space

The formulations of the SANISAND material model are also defined for a multiaxial stress space. Figure 5.4 shows the yield, dilatancy, critical and bounding surfaces in the π plane, of which the three axes are defined by respectively $r_1 = \frac{s_1}{p'}$, $r_2 = \frac{s_2}{p'}$ and $r_3 = \frac{s_3}{p'}$, called deviatoric stress ratios, which are generalisations of the stress ratio in the triaxial space ($\eta = \frac{q}{p'}$) (Dafalias and Manzari, 2004).

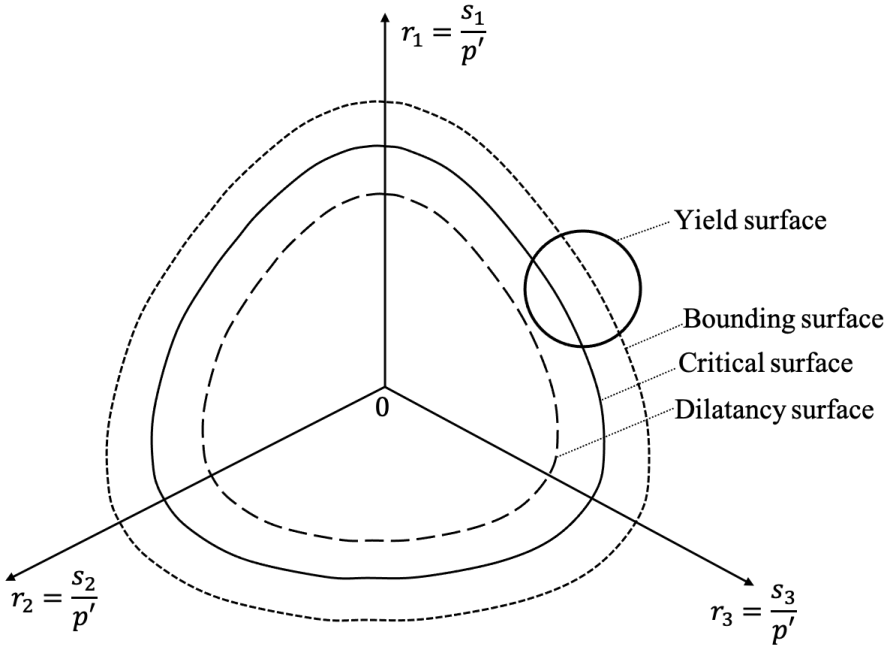

Figure 5.4: SANISAND material model: π plane with dilatancy, critical, bounding and yield surfaces indicated. Note that not all symbols describing the soil behaviour in the π plane are included in this figure. Redrawn, with modifications, after Dafalias and Manzari (2004) and Manzari and Dafalias (1997).

Table 5.1: SANISAND material model equations for triaxial and multiaxial stress space, and model constants used as input for the material model. After Dafalias and Manzari (2004).

Triaxial equations	Multiaxial equations	Constants
	Critical state line	
–	$e_c = e_0 - \lambda_c(\frac{p'_c}{p_{atm}})^{\xi}$	e_0, λ_c, ξ
	Elastic deviatoric strain increment	
$d\varepsilon^e_q = \frac{dq}{3 \cdot G}$	$d\boldsymbol{e}^e = \frac{d\boldsymbol{s}}{2 \cdot G}$	–
–	$G = G_0 \cdot p_{atm} \cdot \frac{(2.97-e)^2}{1+e} \cdot \sqrt{\frac{p'}{p_{atm}}}$	G_0
	Elastic volumetric strain increment	
–	$d\varepsilon^e_v = \frac{dp'}{K}$	
	$K = \frac{2(1+\nu)}{3(1-2 \cdot \nu)} \cdot G$	ν
	Yield surface	
$f_{yield} = \lvert\eta - \alpha\rvert - m = 0$	$f_{yield} = \sqrt{[(\boldsymbol{s} - p'\boldsymbol{\alpha}) : (\boldsymbol{s} - p'\boldsymbol{\alpha})]} - \sqrt{\frac{2}{3}} \cdot p' \cdot m = 0$	m
	Plastic deviatoric strain increment	
$d\varepsilon^p_q = \frac{d\eta}{H}$	$d\boldsymbol{e}^p = \langle L \rangle \boldsymbol{R'}$	
$H = h(M^b - \eta)$	$K_p = (\frac{2}{3})p' \cdot h(\boldsymbol{\alpha}^b_\theta - \boldsymbol{\alpha}) : \boldsymbol{n}$	
$M^b = M^{-n^b \cdot \Psi}$	$\boldsymbol{\alpha}^b_\theta = \sqrt{\frac{2}{3}}[g(\theta, c)M^{-n^b \cdot \Psi} - m]\boldsymbol{n}$	M, c, n^b
$h = \frac{b_0}{\lvert\eta - \eta_{in}\rvert}$	$h = \frac{b_0}{(\boldsymbol{\alpha} - \boldsymbol{\alpha}_{in}) : \boldsymbol{n}}$	
–	$b_0 = G_0 \cdot h_0(1 - c_h \cdot e)(\frac{p'}{p_{atm}})^{-\frac{1}{2}}$	h_0, c_h
	Plastic volumetric strain increment	
$d\varepsilon^p_v = d\lvert\varepsilon^p_q\rvert$	$d\varepsilon^p_v = \langle L \rangle D$	
$d = A_d(M^d - \eta)$	$D = A_d(\boldsymbol{\alpha}^d_\theta - \boldsymbol{\alpha}) : \boldsymbol{n}$	
$M^d = M^{n^d \cdot \Psi}$	$\boldsymbol{\alpha}^d_\theta = \sqrt{\frac{2}{3}}[g(\theta, c)M^{n^d \cdot \Psi} - m]\boldsymbol{n}$	n^d
$A_d = A_0(1 + \langle s \cdot z \rangle)$	$A_d = A_0(1 + \langle \boldsymbol{z} : \boldsymbol{n} \rangle)$	A_0
	Fabric-dilatancy tensor update	
$dz = -c_z\langle -d\varepsilon^p_v \rangle (s \cdot z_{max} + z)$	$d\boldsymbol{z} = -c_z\langle -d\varepsilon^p_v \rangle (z_{max}\boldsymbol{n} + \boldsymbol{z})$	c_z, z_{max}
	Back-stress ratio tensor update	
$d\alpha = d\eta$	$d\boldsymbol{\alpha} = \langle L \rangle (\frac{2}{3})h(\boldsymbol{\alpha}^b_\theta - \boldsymbol{\alpha})$	

The equations listed in Table 5.1 describes the SANISAND model of Dafalias and Manzari (2004) in both triaxial and multiaxial stress space, and lists the associated material model constants specifying the soil properties.

5.2.3 Implementation in PLAXIS 2D

SANISAND is not a material model available by default in PLAXIS 2D, however, it may be implemented as a user-defined material model. This requires a .dll file to be added into the PLAXIS directory on the computer. The PLAXIS implementation for the SANISAND version presented in Dafalias and Manzari (2004) is available at *SoilModels.com* (2021) for registered users.

The input parameters for the material model may be calibrated for a given sand, and is done on Toyoura sand by Dafalias and Manzari (2004), and are the parameters to be used in the numerical simulations presented in Chapter 6.

Chapter 6

Numerical Simulation of Pile Driving

Vibratory and impact pile driving is to be numerically simulated. PLAXIS 2D is used for the simulations, which is a two dimensional (2D) finite element analysis (FEA) software for geotechnical applications. The version is PLAXIS 2D CONNECT Edition V20 Update 4 (20.04.00.790).

This chapter describes the modelling of the soil, pile and the load applied to simulate vibratory and impact pile driving. The calculation parameters and the phases of the simulations are also described. The number of different simulations performed are 7, of which 6 are vibratory driving and 1 impact driving. The driving parameters and soil parameters are altered for the vibratory driving simulations to investigate the effect of these. The vibratory driving frequencies simulated are 12 Hz, 18 Hz and 23.33 Hz.

The monopile is wished-in-place at final depth, before the dynamic loading is applied to the top of the pile. This is one of the limitations of the simulations, as this excludes the possible effects on soil behaviour due to pile penetration of the soil for the embedded length. In addition, only a short time of pile driving is simulated, limiting the results to only a portion of the total installation time.

It is important to note that PLAXIS 2D defines compression by negative values of stress. The same counts for strain, of which negative volumetric strains are considered compaction. The results to be presented in Chapter 7 follows the same notation.

6.1 Modelling

This section describes the numerical model used for the simulations. Results from a FEM analysis may strongly depend on model selections, and it is desirable that the decisions made regarding creating the model are presented to allow replication of the simulations. The whole model and pile driving situation is not based on any specific performed vibratory or impact driven pile installation.

6.1.1 Project Properties

The model is axisymmetric and the elements are 15-noded triangles. Figure 6.1 shows the principle of axisymmetric models in PLAXIS 2D, and Figure 6.2 shows the nodes and stress points for 15-noded triangle elements and the other option of 6-noded. The model is made solely by volume elements, i.e. the soil, pile and hammers are all modelled by soil clusters.

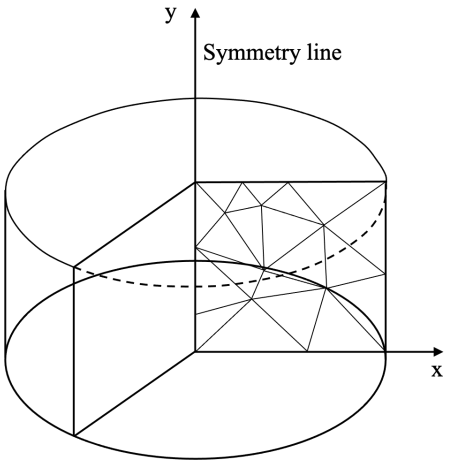

Figure 6.1: Example of an axisymmetrical model in PLAXIS 2D. The x-y plane with triangular elements represents the 2D modelling plane. Redrawn, with modifications, after *PLAXIS 2D - Reference Manual* (2020).

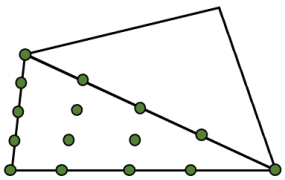

(a) Nodes of 15-noded triangle element.

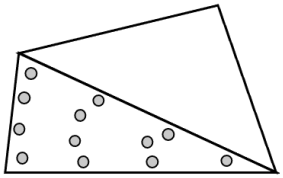

(b) Stress points of 15-noded triangle element.

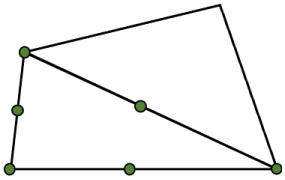

(c) Nodes of 6-noded triangle element.

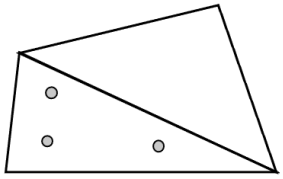

(d) Stress points of 6-noded triangle element.

Figure 6.2: Visualisation of nodes and stress points for 15- and 6-noded triangle elements. Redrawn, with modifications, after *PLAXIS 2D - Reference Manual* (2020).

The geometric size of the project is defined by minimum and maximum boundaries in x- and y-direction, listed in Table 6.1

Table 6.1: PLAXIS 2D Simulations: Geometric size of project

x_{min}	0.00 m
x_{max}	20.00 m
y_{min}	-45.00 m
y_{max}	22.00 m

Seabed is modelled at $y = 0\,\text{m}$, and the sand ranges from seabed to y_{min}, and from x_{min} to x_{max} horizontally. The earth gravity and the specific weight of water is by default set to $g = 9.810\,\text{m/s}^2$ and $\gamma_{water} = 10.00\,\text{kN/m}^3$ respectively.

6.1.2 Pile

The simulated monopile is a hollow, open-ended steel pile with an outer diameter of $D_{outer,pile} = 5000\,\text{mm}$.

Pile Geometry
The thickness of the pile wall ($t_{wall,pile}$) is calculated by (API, 2010):

$$t_{wall,pile} = 6.35 + \frac{D_{outer,pile}}{100} \tag{6.1}$$

of which $t_{wall,pile}$ and $D_{outer,pile}$ are given in [mm]. Equation 6.1 gives $t_{wall,pile} \approx 56.4\,\text{mm}$. The cross section are of the pile is uniform along the pile length, and is calculated to $A_{pile} \approx 0.876\,\text{m}^2$.

The total pile length ($L_{total,pile}$) and the embedded length ($L_{embedded,pile}$) of the modelled pile are selected based on equations suggested by Negro et al. (2017), which are developed after a regression analysis of already installed piles with the following dimensions: pile diameter in the range of $3 - 7\,\text{m}$, total length of pile between $30 - 80\,\text{m}$, total pile weight $200 - 800\,\text{ton}$ and at water depths in the range of $5 - 30\,\text{m}$. Installation method is not taken into account. The suggested equation for the total pile length is (Negro et al., 2017):

$$L_{total,pile} = 14 \cdot D_{outer,pile} - 17 \tag{6.2}$$

and for the embedded pile length:

$$L_{embedded,pile} = 8 \cdot D_{outer,pile} - 5 \tag{6.3}$$

of which $L_{total,pile}$, $L_{embedded,pile}$ and $D_{outer,pile}$ are given in [m]. These equations give $L_{total,pile} = 53\,\text{m}$ and $L_{embedded,pile} = 35\,\text{m}$.

Table 6.2: PLAXIS 2D Simulations: Pile geometry. After Eiesland (2020) with some modifications.

Parameter	Symbol	Value	Unit
Outer pile diameter	$D_{outer,pile}$	5000	mm
Inner pile diameter	$D_{inner,pile}$	4887.2	mm
Pile wall thickness	$t_{wall,pile}$	56.4	mm
Total pile length	$L_{total,pile}$	53.0	m
Driven pile length	$L_{embedded,pile}$	35.0	m
Area of pile cross section	A_{pile}	0.876	m^2

The selected pile geometry parameters are listed in Table 6.2.

Pile Material

The steel pile is modelled by volume elements with a *Linear elastic* soil material model with drainage type set to *Non-porous*, of which the latter automatically sets $\gamma_{unsat} = \gamma_{sat}$. The properties selected for the pile is summarised in Table 6.3.

Table 6.3: PLAXIS 2D Simulations: Pile material parameters. After Eiesland (2020).

Parameter	Symbol	Value	Unit
Unsaturated specific weight	$\gamma_{pile,unsat}$	77	kN/m^3
Elastic modulus	E_{pile}	$200 \cdot 10^6$	kN/m^2
Poisson's ratio	ν_{pile}	0.3	-

The coefficient of the pressure at rest (K_0) is set to be determined *Automatic*, giving $K_{0,x} = K_{0,z} = 0.5$ for a linear elastic material model in PLAXIS 2D (*PLAXIS 2D - Reference Manual*, 2020). Note that no material damping is added to the pile material. However, the real pile behaviour may be assumed to lead to some energy dissipation during driving. Hence, this introduces an uncertainty related to the results to be obtained.

6.1.3 Soil

The soil is modelled as a sand with the user-defined soil model (UDSM) Simple Anisotropic Sand constitutive model (SANISAND).[10] The SANISAND version used is presented by Dafalias and Manzari (2004). This material model is used for the simulations since it is capable of simulating cyclic loading and is available at SoilModels.com (*SoilModels.com*, 2021) with implementations for PLAXIS 2D. The availability of the material model allows replication of the simulations.

[10]The PLAXIS implementation file of SANISAND is received by main supervisor Prof. Gudmund Eiksund, and is available for registered users on *SoilModels.com* (2021).

SANISAND Parameters

Dafalias and Manzari (2004) presents a set of calibrated parameters for the SANISAND material model of Toyoura sand, which are to be used directly for the simulations. These are listed in Table 6.4.

Table 6.4: PLAXIS 2D Simulations: SANISAND input parameters for Toyoura sand. After Dafalias and Manzari (2004), with some alterations in symbol notation.

Description	Parameter symbol	Value
Elasticity	G_0	125
	ν	0.05
Critical state	M_c	1.25
	c	0.712
	λ_c	0.019
	e_0	0.934
	ξ	0.7
Yield surface	m	0.01
Plastic modulus	h_0	7.05
	c_h	0.968
	n^b	1.1
Dilatancy	A_0	0.704
	n^d	3.5
Fabric-dilatancy tensor	z_{max}	5 [11]
	c_z	600

Note that c is defined as the ratio between the critical state lines (CSLs) of extension and compression in the $p' - q$ space (Mašín, 2015):

$$c = \frac{M_e}{M_c} \tag{6.4}$$

In the PLAXIS implementation of this SANISAND version there are 19 parameters available for input. Mašín (2015) presents an overview and description of these parameters, shown in Table 6.5. Note that not all of the 19 input parameters are suggested by Table 6.4.

[11] Dafalias and Manzari (2004) presents a value of 4, while 5 is used for some of the simulations presented in the paper

Table 6.5: PLAXIS 2D Simulations: Description of input parameters of SANISAND implementation to PLAXIS 2D. After Mašín (2015), with some alterations in symbol notation.

Parameter	Parameter symbol	Description
Parameter 1	p_{atm}	atmospheric pressure
Parameter 2	e_0	void ratio on CSL at $p' = 0$
Parameter 3	λ_c	CSL parameter in $p' - e$ plane
Parameter 4	ξ	CSL parameter in $p' - e$ plane
Parameter 5	M_c	slope of CSL in $p' - q$ plane in triaxial compression
Parameter 6	M_e	slope of CSL in $p' - q$ plane in triaxial extension
Parameter 7	m	opening of yield surface cone
Parameter 8	G_0	shear modulus constant
Parameter 9	ν	Poisson's ratio
Parameter 10	h_0	plastic modulus constant
Parameter 11	c_h	plastic modulus constant
Parameter 12	n^b	plastic modulus constant
Parameter 13	A_0	dilatancy constant
Parameter 14	n^d	dilatancy constant
Parameter 15	z_{max}	fabric index constant
Parameter 16	c_z	fabric index constant
Parameter 17	K_w	pore water bulk modulus
Parameter 18	p_{tmult}	shift of mean stress, calculated by $p_t = p_{tmult} \cdot p_{atm}$
Parameter 19	e_{init}	initial void ratio

An overview of the input parameters to be used in the soil material model, both the parameters from Dafalias and Manzari (2004) and those selected by the author, is presented in Table 6.6.

Table 6.6: PLAXIS 2D Simulations: SANISAND implementation parameters. After Dafalias and Manzari (2004) and Mašín (2015), with some alterations in symbol notation.

Parameter	Symbol	Dafalias and Manzari (2004)	Selected by author
Parameter 1	p_{atm}		101.3
Parameter 2	e_0	0.934	
Parameter 3	λ_c	0.019	
Parameter 4	ξ	0.7	
Parameter 5	M_c	1.25	
Parameter 6	M_e	0.89	
Parameter 7	m	0.01	
Parameter 8	G_0	125	
Parameter 9	ν	0.05	
Parameter 10	h_0	7.05	
Parameter 11	c_h	0.968	
Parameter 12	n^b	1.1	
Parameter 13	A_0	0.704	
Parameter 14	n^d	3.5	
Parameter 15	z_{max}	5	
Parameter 16	c_z	600	
Parameter 17	K_w		0
Parameter 18	p_{tmult}		0
Parameter 19	e_{init}		0.734

The initial void ratio is set to $e_{init} = 0.734$ based on the trial and error performed by Dahl and Løyland (2017) to find the initial void ratio of the simulations performed by Dafalias and Manzari (2004).

Specific Weight, Rayleigh Damping and Drainage Type

The drainage type is set to *Drained* to simulate the possible partly drained behaviour during pile driving.

SANISAND is capable of simulating plastic strains during several loading cycles, and is therefore capable of simulating dissipation of energy due to plasticity. Rayleigh damping is added to introduce a material damping at small strains with elastic behaviour. However, this may lead to an exaggerated total material damping compared to real soil behaviour. This introduces an uncertainty regarding realistically simulating the soil behaviour.

The Rayleigh damping coefficients (α, β) are estimated based on the following formulas

by PLAXIS (*PLAXIS 2D - Reference Manual*, 2020):

$$\alpha = 2\omega_1\omega_2\frac{\omega_1\xi_2 - \omega_2\xi_1}{\omega_1^2 - \omega_2^2} \tag{6.5}$$

$$\beta = 2\frac{\omega_1\xi_1 - \omega_2\xi_2}{\omega_1^2 - \omega_2^2} \tag{6.6}$$

of which ω and ξ, denoted 1 and 2, are the target angular frequency [rad/s] and target damping ratio [%/100] respectively. The target frequencies (ω_1, ω_2) are selected to be 10π rad/s above and under the driving frequencies for the vibratory hammer. The damping ratios for the target frequencies are selected to be $\xi_1 = \xi_2 = 6\%$.[12]

The frequency of 50 Hz is used to calculate the damping coefficients for the sand for the impact driving simulation, which is the frequency of the sinusoidal curve modelling the impact load, as further discussed in Section 6.1.8. The damping ratios are kept similar as for the soil during vibratory driving and the range for the target angular frequencies are set 10π rad/s above and under the frequency of 50 Hz.

Table 6.7: PLAXIS 2D Simulations: Sand properties

Parameter	Symbol	Value	Unit
Unsaturated specific weight	$\gamma_{sand,unsat}$	17.0	kN/m^3
Saturated specific weight	$\gamma_{sand,sat}$	20.0	kN/m^3
Rayleigh damping, alpha ($f = 12$ Hz)	α_{12}	3.738	-
Rayleigh damping, beta ($f = 12$ Hz)	β_{12}	$0.7958 \cdot 10^{-3}$	-
Rayleigh damping, alpha ($f = 18$ Hz)	α_{18}	6.262	-
Rayleigh damping, beta ($f = 18$ Hz)	β_{18}	$0.5305 \cdot 10^{-3}$	-
Rayleigh damping, alpha ($f = 23.33$ Hz)	$\alpha_{23.33}$	8.391	-
Rayleigh damping, beta ($f = 23.33$ Hz)	$\beta_{23.33}$	$0.4093 \cdot 10^{-3}$	-
Rayleigh damping, alpha ($f = 50$ Hz)	α_{50}	18.66	-
Rayleigh damping, beta ($f = 50$ Hz)	β_{50}	$0.1910 \cdot 10^{-3}$	-

The selection of other input parameters that are not specific for the SANISAND model, amongst others specific weight of the sand, are listed in Table 6.7. Note the different sets of Rayleigh damping coefficients calculated for the different frequencies.

Flow Parameters

The hydraulic conductivity for the sand is relevant in order to evaluate the build-up and dissipation of excess pore water pressure, both during pile driving and the subsequent consolidation. The soil characteristics of the sand regarding grain size, minimum and maximum void ratio are presented in Table 6.8, and are based on the description of a fine

[12]Target frequencies and target damping ratios suggested by main supervisor Prof. Gudmund Eiksund, and are adopted from Eiesland (2020).

Toyoura sand by Verdugo and Ishihara (1996). Note that the minimum and maximum void ratios are not implemented in the material model.

Table 6.8: PLAXIS 2D Simulations: Toyoura sand characteristics (Verdugo and Ishihara, 1996).

Description	Symbol	Value	Unit
Mean grain diameter	D_{50}	0.17	mm
Uniformity coefficient	U_c	1.7	-
Minimum void ratio	e_{min}	0.597	-
Maximum void ratio	e_{max}	0.977	-

$D_{50} = 0.17\,\text{mm}$ indicates that 50% of the grains are smaller than 0.17 mm, and the uniformity coefficient is given by the relation:

$$U_c = \frac{D_{60}}{D_{10}} \tag{6.7}$$

of which D_{60} and D_{10} indicate the grain diameter which respectively 60% and 10% of the grains are smaller than.

The USDA data set with the Van Genuchten model is selected in PLAXIS. The USDA data set is based on regression analysis of hydraulic conductivity (Carsel and Parrish, 1988), and the Van Genuchten model describes the characteristics of unsaturated soils with respect to its capacity to retain water at different stresses (*PLAXIS 2D - Material Models Manual*, 2020). The soil type *Sand* is selected, and the associated grain size distribution is listed in Table 6.9.

Table 6.9: PLAXIS 2D Simulations: Grain size distribution

Description	Grain size range	Distribution
Clay	$< 2\,\mu m$	4%
Silt	$2\,\mu m - 50\,\mu m$	4%
Sand	$50\,\mu m - 2\,mm$	92%

This grain size distribution in Table 6.9 may fit the characteristics of the Toyoura sand with respect to D_{50} and U_c. According to the selected grain size distribution 8% of the grains are either classified as silt or clay, i.e. D_{10} is in the range classified as sand, hence must also D_{60}. This implies that D_{50}, D_{60} and D_{10} are all in the range classified as sand for the suggested grain size distribution in Table 6.9. This suggests a relatively uniform sand, also being a description used by Verdugo and Ishihara (1996). If the *Loamy sand* type were to be selected, which is the type considered second most coarse in the data set after *Sand*, the grain size distribution would give a $D_{60} = D_{10} \cdot U_c$ lower than the given $D_{50} = 0.17\,\text{mm}$, which is contradictory.

The flow parameters are selected based on grain size distribution, giving $k_x = k_y =$

1.492 m/day. Note that this estimate is with a relatively high level of uncertainty. Both relatively fine and coarse sands may be fitted to the selected grain size distribution, hence the hydraulic conductivity is not necessarily specifically for fine sand.

Interface Tabsheet
No interface elements are used in the model. The interfaces tabsheet in PLAXIS requires input of values, however, these are not presented here.

Coefficient of Soil Pressure at Rest
The coefficient of the pressure from the soil at rest (K_0) is selected based on Jaky's formula (*PLAXIS 2D - Reference Manual*, 2020):

$$K_0 = 1 - \sin(\varphi) \tag{6.8}$$

The friction angle (φ) is estimated based on the given slope of the triaxial compression and extension critical state line in the $p' - q$ space ($M_c = 1.25$ and $M_e = 0.89$ from Table 6.6) by the following equations (Nordal, 2020):

$$M_c = \frac{6 \cdot \sin(\varphi_c)}{3 - \sin(\varphi_c)}; \quad M_e = \frac{6 \cdot \sin(\varphi_e)}{3 + \sin(\varphi_e)} \tag{6.9}$$

of which it is assumed that the friction angle is equal to the mobilised friction angle, i.e. $\rho = \varphi$. This gives $\varphi_c = 31.1474°$ and $\varphi_e = 31.5004°$ for triaxial compression and extension respectively. The average is used as input, being $\varphi = 31.3239° \approx 31.32°$. K_0 is assumed equal in both x- and z-direction, giving $K_{0,x} = K_{0,z} = 0.4802$.

6.1.4 Pile-soil Interface

No interface elements are modelled at the contact between the pile and soil. It is then assumed that possible failure does not occur at the interface, but in the soil. The occurrence of failure is then based on the parameters of the soil surrounding the pile.

6.1.5 Global Water Level

The numerical simulation aims at simulating an offshore pile, of which the top of the pile is located $L_{total,pile} - L_{embedded,pile} = 53\,\text{m} - 35\,\text{m} = 18\,\text{m}$ above seabed. The global water level is set to 15 m above seabed.

6.1.6 1 m Mohr-Coulomb Sand

Seabed is located at $y = 0\,\text{m}$, and from there to 1 m beneath there is a layer of a sand with the Mohr-Coulomb (MC) material model, with a non-zero effective cohesion and

dilatancy angle equal to zero. This is to avoid numerical issues if possibly approaching zero effective stresses at the free surface of the seabed. The material properties for the MC sand are similar to the ones of the SANISAND material model, with exception of the SANISAND specific input parameters being replaced with the ones for MC. Different MC models are created based on the different Rayleigh damping inputs for the different simulations, similarly as for the SANISAND soil model. The MC specific inputs are listed in Table 6.10.

Table 6.10: PLAXIS 2D Simulations: 1 m MC sand layer properties

Parameter	Symbol	Value	Unit
Effective elastic modulus	E'	$25 \cdot 10^3$	kN/m^2
Effective Poisson's ratio	ν'	0.250	-
Effective reference cohesion	c'_{ref}	1.0	kN/m^2
Effective friction angle	φ'	31.32	$\circ$
Dilatancy angle	ψ	0	$\circ$

Note that the effective friction angle is set equal the friction angle calculated from the triaxial compression and extension critical state lines.

6.1.7 Vibratory Driving

It is desirable to select a realistic set of input parameters regarding modelling of the vibratory hammer with respect to the size of the pile. The hammer selection and modelling is presented in this section.

Hammer Selection

DFI (2015) presents a list of some previously performed pile installations with vibratory driving.[13] The diameter of some of the piles are listed, in addition to eccentric moment and max frequency of the vibratory driver.[14] The piles with this information available are plotted, with pile diameter ($D_{outer,pile}$) against the calculated maximum amplitude of the vertical sinusoidal force generated by the hammers ($F^A_{v,vib}$). Figure 6.3 presents the plot, with a linear regression line and its associated function.

[13] Note that some of these installed piles were finished with an impact hammer (DFI, 2015).

[14] Note that one pile is listed with a diameter ranging from 1.2-1.5 m, of which 1.2 m is used in the linear regression presented.

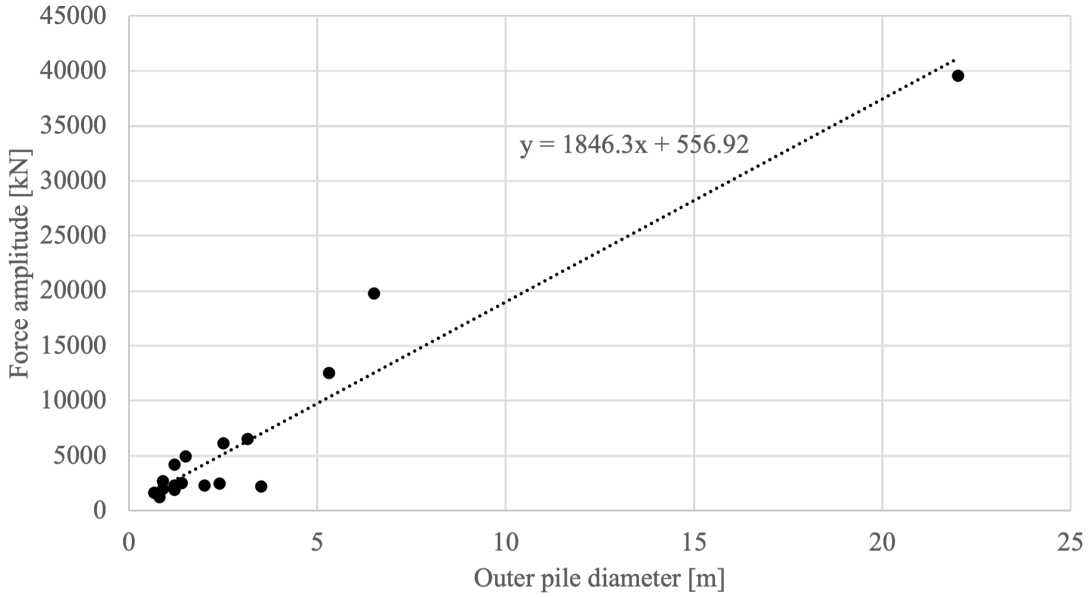

Figure 6.3: Linear regression of outer pile diameter ($D_{outer,pile}$) vs. maximum force amplitude generated by vibratory hammer ($F^A_{v,vib}$). Data from DFI (2015).

The linear regression line in Figure 6.3 suggests an amplitude of the vertical sinusoidal force equal to $F^A_{v,vib} = 9788.42\,\text{kN}$ for a pile with $D_{outer,pile} = 5\,\text{m}$. Note that this is a simplified estimation of necessary driving amplitude that does not take into account, amongst others, the specific soil conditions or pile length.

The vibratory hammer PVE 500M may provide $F^A_{v,vib} = 10748\,\text{kN}$ according to *PVE - Dutch Masters in Vibro Technology* (2021), and the properties of this hammer are used as reference when selecting input parameters regarding masses of different hammer components and driving parameters for the simulations. The reference properties are adopted from the websites of *PVE - Dutch Masters in Vibro Technology* (2021) and *Foundation Equipment — PVE Equipment USA* (2021).

Modelling of $m_{vib,dyn}$, Elastomer Pads and m_{ib}

Three different soil materials are created in order to model the dynamic mass of the vibratory hammer ($m_{vib,dyn}$), elastomer pads and mass of isolator block (m_{ib}) respectively. Note that $m_{vib,dyn} = m_{eb} + m_{cl}$, and is interpreted as the dynamic part of the vibratory hammer (see Figure 2.3b). The soil clusters modelling $m_{vib,dyn}$, elastomer pads and m_{ib} are modelled with the same width as the pile. 1 m soil cluster directly on top of the pile is assigned with the dynamic mass material, followed by 0.5 m of the elastomer pads and finally 1 m of the isolator block material on top, visualised in Figure 6.4.

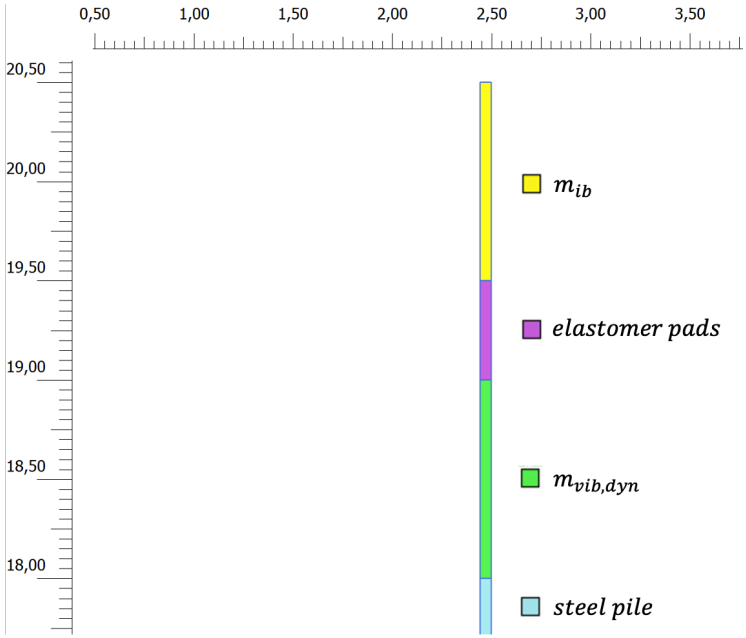

Figure 6.4: Visualisation of the soil clusters modelling the vibratory hammer masses and elastomer pads. Figure from PLAXIS 2D with modifications.

The inputs and selections for the material model of the masses and the spring are similar the ones for the steel pile, with exception of the specific weights and, for the elastomer pads, the elastic modulus. The masses, specific weights and elastic moduli selected are listed in Table 6.13. Note that the spring, i.e. elastomer pads, have zero mass.

Table 6.11: PLAXIS 2D Simulations: Parameters of soil modelling the vibratory hammer masses

Description	Mass [kg]	Specific weight (γ_{unsat}) [kN/m^3]	Elastic modulus [kN/m^2]
Dynamic mass ($m_{vib,dyn}$)	56640.033	634.3	$200.0 \cdot 10^6$
Static mass (m_{ib})	15000.287	168.0	$200.0 \cdot 10^6$
Elastomer pads (spring)	0.000	0.0	1679.8

The specific weight of $m_{vib,dyn}$ is calculated by:

$$\gamma_{unsat} = \frac{m_{vib,dyn} \cdot g}{1000 \frac{\mathrm{N}}{\mathrm{kN}} \cdot A_{pile} \cdot 1\,\mathrm{m}} \tag{6.10}$$

of which the division of 1 m and A_{pile} indicate the masses are modelled in the 2D (x-y) space with a height of 1 m and an area equal to A_{pile}. The substitution of $m_{vib,dyn}$ with m_{ib} in Equation 6.10 gives the specific weight of m_{ib}.

The elastomer pads are modelled as a spring between the dynamic vibratory masses and the isolator block, and a lower elastic modulus is used for the material compared to

$m_{vib,dyn}$ and m_{ib}. The elastomer pads (spring) are assumed to respond linearly elastic, and its elastic modulus (E_{spring}) is estimated by the following formula:

$$\delta_{spring} = \frac{m_{ib} \cdot g \cdot L_{spring}}{E_{spring} \cdot A_{pile}} \tag{6.11}$$

of which $g = 9.810\,\mathrm{m/s^2}$ is the earth gravity and L_{spring} =0.5 m is the length of the spring. E_{spring} is preliminary estimated by limiting the static deflection of the spring, induced by the overlying m_{ib}, to $\delta_{spring} = L_{spring}/10 = 0.05\,\mathrm{m}$. This gives $E_{spring} \approx 1679.8\,\mathrm{kN/m^2}$.

Load Input

The load induced by the vibratory driver is modelled by input of a dynamic multiplier, assigned to an evenly distributed reference load acting in negative y-direction on the top of the pile, i.e. at the transition between $m_{vib,dyn}$ and *steel pile* in Figure 6.4. Note that positive values for the multiplier subjects load in negative y-direction. The static load component of the linear load is removed. The load multiplier is added as a harmonic, sinusoidal, function of time. The inputs are stress amplitude (σ_v^A) [$\mathrm{kN/m^2}$] and frequency (f) [Hz]. The load multiplier may be interpreted as the load subjected to the top of the pile, not the force generated by the rotating eccentric moments.

The hammer of reference (PVE 500M) works at up to a frequency of 23.33 Hz. Three different frequencies are simulated, namely 12 Hz, 18 Hz and 23.33 Hz. The load amplitude produced by the vibratory hammer depends on the driving frequency of the eccentric masses, and the difference between generated force by the hammer and the load subjected to the top of the pile may depend on a load transfer ratio. The vibratory hammer and pile system is assumed rigid, hence the force transfer ratio from the vibratory hammer to the top of the pile may be given by combining Equations 2.12 and 2.13, presented in Section 2.3, giving:

$$\eta_F^{rigid} = \frac{1}{1 + \frac{m_{vib,dyn}}{m_p}} \tag{6.12}$$

of which m_p may be calculated by:

$$m_p = \gamma_{pile,unsat} \cdot L_{total,pile} \cdot A_{pile} \cdot \frac{1}{g} \tag{6.13}$$

giving $m_p \approx 364.42 \cdot 10^3\,\mathrm{kg}$.

Equation 6.12 then gives $\eta_F^{rigid} \approx 0.865$.

The sum of eccentric moments ($M_{ecc,sum}$) of the vibratory hammer is 500 kg·m. The amplitude of the dynamic multipliers acting on the top of the pile ($\sigma_{v,vib,p}^A$) for the different

driving frequencies are estimated by:

$$\sigma^{A}_{v,vib,p} = \frac{F^{A}_{v,vib} \cdot \eta^{rigid}_{F}}{A_{pile}} = \frac{M_{ecc,sum} \cdot \omega^2 \cdot \eta^{rigid}_{F}}{A_{pile}} \tag{6.14}$$

of which the angular frequency relates to the frequency in terms of Hz [1/s] with the following relation $\omega = 2\pi \cdot f$.

Table 6.12: PLAXIS 2D Simulations: Vibratory driving load parameter inputs

Parameter	Symbol	Value	Unit
Frequency	f_{12}	12.00	Hz $= 1/s$
Frequency	f_{18}	18.00	Hz $= 1/s$
Frequency	$f_{23.33}$	23.33	Hz $= 1/s$
Amplitude ($f = 12\,\text{Hz}$)	$\sigma^{A}_{v,vib,p,12}$	2 806.75	kN/m^2
Amplitude ($f = 18\,\text{Hz}$)	$\sigma^{A}_{v,vib,p,18}$	6 315.19	kN/m^2
Amplitude ($f = 23.33\,\text{Hz}$)	$\sigma^{A}_{v,vib,p,23.33}$	10 608.92	kN/m^2

Frequencies and associated stress amplitudes for the sinusoidal function modelling the dynamic loading of vibratory driving are listed in Table 6.12.

6.1.8 Impact Driving

The impact hammer selection and modelling is presented in this section.

Hammer Selection

The hammer selection is based on estimating the energy needed to subject the pile in order to drive the pile a permanent settlement of $s_{plastic}$ each blow (E^{i}_{pile}), and select a hammer able to deliver the needed amount of energy. The so-called impact formula may provide an estimation of this energy, previously presented in Equation 2.6 in Section 2.2.

The permanent settlement of the pile each blow of the impact hammer is set to $s_{plastic} = 1/\text{blow per meter} = 1/100\,\text{m} = 0.01\,\text{m}$ and the load distribution factor is set to $\alpha_{distr} = 0.7$.[15] The axial bearing capacity of the pile in compression (Q_u) is for simplicity assumed equal its static axial bearing capacity, and is estimated by (*Peleveiledningen*, 2019) (*Geoteknikk Beregningsmetoder*, 2020):

$$Q_u = Q_{shaft} + Q_{toe} - W_p + F_b \tag{6.15}$$

of which Q_{shaft} and Q_{toe} are the contributions from the shaft and toe bearing respectively, W_p is the weight of the pile and F_b is the upward force due to buoyancy. The approach

[15] Selection of $s_{plastic}$ and α_{distr} are proposed by main supervisor Prof. Gudmund Eiksund.

and formulas related to estimating Q_u are adopted from *Peleveiledningen* (2019) and *Geoteknikk Beregningsmetoder* (2020).

The pile is an open-ended and hollow steel pile, hence there are contributions from both the internal and external pile wall to the total shaft resistance. The contribution from the shaft resistance may be estimated by:

$$Q_{shaft} = \beta_{friction} \cdot p'_{v,average} \cdot A_{shaft} \tag{6.16}$$

of which $\beta_{friction}$ is a factor for the side friction, $p'_{v,average}$ is the average value, from seabed to pile toe, for the vertical effective stress from the overlying soil along the pile shaft and A_{shaft} is the total area of the internal and external pile wall. $\beta_{friction}$ is interpreted to $\beta_{friction} = 0.22$.[16] $p'_{v,average}$ is estimated by assuming a linear increase of effective overburden stress with depth along the pile, giving:

$$p'_{v,average} = \frac{1}{2}(\gamma_{sand,sat} - \gamma_{water}) \cdot L_{embedded,pile} \tag{6.17}$$

of which $\gamma_{sand,sat} = 20\,\mathrm{kN/m^3}$ and $\gamma_{water} = 10\,\mathrm{kN/m^3}$ are the specific weight of the saturated sand and for water respectively. $L_{embedded,pile} = 35\,\mathrm{m}$ is the embedded length of the pile. Equation 6.17 then gives $p'_{v,average} = 175.0\,\mathrm{kN/m^2}$. The area of the internal and external pile wall may be estimated by:

$$A_{shaft} = \pi \cdot L_{embedded,pile} \cdot (D_{outer,pile} + D_{inner,pile}) \tag{6.18}$$

of which $D_{outer,pile}$ and $D_{inner,pile}$ is the outer and inner pile diameter respectively. Equation 6.18 gives $A_{shaft} \approx 1087.2\,\mathrm{m^2}$. The contribution from the shaft resistance may then be estimated by Equation 6.16, giving:

$$Q_{shaft} = 0.22 \cdot 175.0\,\mathrm{kN/m^2} \cdot 1087.2\,\mathrm{m^2} \approx 41.9 \cdot 10^3\,\mathrm{kN} \tag{6.19}$$

The contribution from the toe bearing of the pile may be estimated by:

$$Q_{toe} = N_q \cdot p'_v \cdot A_{pile} \tag{6.20}$$

of which N_q is a toe bearing capacity factor, p'_v is vertical effective stress from overlying soil at same depth as pile toe and A_{pile} is the area of the pile toe cross section. The value for the toe bearing capacity factor is set to $N_q = 22$,[17] and the effective overburden pressure is calculated to be $p'_v = 350\,\mathrm{kN/m^2}$. Equation 6.20 then gives:

$$Q_{toe} = 22 \cdot 350\,\mathrm{kN/m^2} \cdot 0.876\,\mathrm{m^2} = 6745.2\,\mathrm{kN} \tag{6.21}$$

[16] From *Peleveiledningen* (2019), as a function of embedded pile length and soil density.

[17] Interpreted from *Geoteknikk Beregningsmetoder* (2020) by assuming $\tan\rho = \tan\varphi$ and angle of plasticity $\beta_{angle} \approx 0°$.

The weight of the pile may be calculated by the following equation:

$$W_p = \gamma_{pile,unsat} \cdot L_{total,pile} \cdot A_{pile} \tag{6.22}$$

which by input of previously presented parameters and geometries of the pile gives:

$$W_p = 77\,\mathrm{kN/m^3} \cdot 53.0\,\mathrm{m} \cdot 0.876\,\mathrm{m^2} \approx 3575.0\,\mathrm{kN} \tag{6.23}$$

The contribution to the axial bearing capacity due to buoyancy may be estimated by:

$$F_b = \gamma_{water} \cdot L_{w,pile} \cdot A_{pile} \tag{6.24}$$

of which $L_{w,pile}$ is the submerged length of the pile. Equation 6.24 gives:

$$F_b = 10\,\mathrm{kN/m^3} \cdot 50\,\mathrm{m} \cdot 0.876\,\mathrm{m^2} = 438.0\,\mathrm{kN} \tag{6.25}$$

Equation 6.15 then gives the static axial bearing capacity of the pile:

$$Q_u = 41.9 \cdot 10^3\,\mathrm{kN} + 6745.2\,\mathrm{kN} - 3575.0\,\mathrm{kN} + 438.0 \approx 45.5 \cdot 10^3\,\mathrm{kN} \tag{6.26}$$

The energy needed of the impact hammer in order to obtain a permanent settlement of $s_{plastic}$ per blow may be calculated by Equation 2.6, giving $E^i_{pile} \approx 674.2\,\mathrm{kJ}$.

The hydraulic hammer IHC IQIP S-2000 may provide a maximum net energy of 2000 kJ (*Hydrohammer –The hydraulic impact hammer*, 2021), and the parameters regarding weight of ram, weight of hammer and the range of blows per minute that the hammer may deliver are selected based on this hammer.

Modelling of $m_{impact,static}$

The static mass of the impact hammer $m_{impact,static}$ is modelled by a soil cluster on top of the pile, and the inputs are equal the ones of the steel pile with exception of specific weight. Note that the ram is not included in the static mass. The mass and elastic modulus for the material of $m_{impact,static}$ is listed in Table 6.13. The specific weight is calculated by the same method as for the vibratory hammer components (Equation 6.10 in Section 6.1.7).

Table 6.13: PLAXIS 2D Simulations: Parameters of soil modelling the static impact hammer mass

Description	Mass [kg]	Specific weight (γ_{unsat}) [kN/m^3]	Elastic modulus [kN/m^2]
Static mass ($m_{impact,static}$)	$125.0 \cdot 10^3$	1399.8	$200.0 \cdot 10^6$

The soil cluster is the same width as the pile and extends 1 m upwards from the top of the pile, similar as for $m_{vib,dyn}$ for the vibratory hammer as seen in Figure 6.4. Note that neither the elastomer pads nor m_{ib} are included for the modelling of the impact hammer.

Load Input

The load subjected to the top of the pile at each blow of the impact hammer is modelled by assigning a dynamic multiplier to an evenly distributed reference load, as described for the vibratory driving load input in Section 6.1.7. However, this load is created by table values due to the discontinuous load applied by the impact hammer. The blow rate at maximum energy for this particular hammer is listed to be 24-35 blows per minute by *Hydrohammer –The hydraulic impact hammer* (2021), and is for the simulation set to 30 blows per minute.

The load inflicted by an impact hammer may be modelled differently, amongst others depending on the masses of the hammer components and their stiffness. Deeks and Randolph (1993) presents differences in the analytical modelling of a dimensionless force applied on the top of the pile vs. time with various dimensionless cushion stiffness, of which the latter amongst others depend on the actual cushion stiffness and mass of the ram. With infinite dimensionless cushion stiffness the dimensionless force starts at unity and exponentially decays, while for a reduced stiffness the amplitude is reduced and the curves to a larger degree approach the shape of a half sinusoidal curve (Deeks and Randolph, 1993).

For simplicity the load input in the simulation is modelled by half a sinusoidal curve, with $f = 50\,\text{Hz}$, indicating a duration of 0.01 s per impact. This simplification may not give a realistic simulation of the stresses in the pile during driving. However, the soil behaviour is of focus and the estimation of the load amplitude is based on an equilibrium between the energy estimated from the so-called impact formula ($E^i_{pile} \approx 674.2\,\text{kJ}$) and the energy simulated to be transferred to the top of the pile obtained by results from preliminary simulations ($E^i_{pile,sim.}$). The latter is estimated by the integral of the resulting force vs. vertical displacement of top of the pile.

The preliminary simulations are performed on the same model as the main simulations, however, with a coarser mesh and simulating only one impact, i.e. simulating for 0.01 seconds.[18]. Due to the latter the load may be modelled by a harmonic sinusoidal function with $f = 50\,\text{Hz}$ for the preliminary simulations. *Max steps* is set to 8, and *Number of sub steps* set to 1, indicating a total of 8 calculation steps for the simulated impact.

The initial value of the load amplitude for the preliminary simulations is estimated by an equilibrium between impulse subjected by the ram to the top of the pile and the integral of the half sinusoidal curve modelling the impact load, of which it is assumed that the velocity of the ram is zero the moment after impact:

$$m_{ram} \cdot \mathrm{v}^i_{ram} = \int_0^{0.01} F^A_{v,impact,p} \cdot \sin(f \cdot 2\pi \cdot t)\, dt \tag{6.27}$$

[18]Element distribution is set to *Medium* with no mesh refinements.

of which $F^A_{v,impact,p}$ is the force amplitude of the dynamic multiplier, f is the frequency of the sinusoidal curve used to model the dynamic multiplier for the impact loading ($f = 50\,\text{Hz}$) and t is the time in seconds. The mass of the ram is $m_{ram} = 100 \cdot 10^3\,\text{kg}$. The velocity of the ram the moment before impact may be estimated by the equilibrium between kinetic energy ($E^i_{k,ram}$) and the impact formula (E^i_{pile}), giving the equation:

$$\text{v}^i_{ram} = \sqrt{\frac{2}{m_{ram}} \cdot E^i_{pile}} \tag{6.28}$$

Note that an efficiency ratio of 95% for the energy transfer from hammer to pile is not included in Equation 6.28, since v^i_{ram} is in this case used to find the impulse subjected to the top of the pile, which is assumed lower compared to the impulse of the ram at impact. If, on the other hand, the necessary velocity of the ram to be used in field was to be estimated the efficiency ratio of energy transfer from hammer to pile would be necessary to include. This means that the v^i_{ram} calculated in this case will have a slightly lower value than would be necessary to use in the field.

Equation 6.28 gives $\text{v}^i_{ram} \approx 3.7\,\text{m/s}$. The remaining unknown in Equation 6.27 is $F^A_{v,impact,p}$:

$$F^A_{v,impact,p} = \frac{m_{ram} \cdot \text{v}^i_{ram}}{\int_0^{0.01} \sin(f \cdot 2\pi \cdot t)\,dt} \tag{6.29}$$

giving $F^A_{v,impact,p} \approx 58.1 \cdot 10^3\,\text{kN}$. The amplitude may be expressed in terms of stress acting on top of the pile by:

$$\sigma^A_{v,impact,p,} = \frac{F^A_{v,impact,p}}{A_{pile}} \tag{6.30}$$

giving $\sigma^A_{v,impact,p} \approx 66.3 \cdot 10^3\,\text{kN/m}^2$, which is used as an initial value for the preliminary simulations.

The resulting vertical displacement of the top of the pile is plotted against the dynamic load applied in terms of force [kN], of which the enclosed area of the graph is the energy transferred to the top of the pile, seen in Figure 6.5. The initial value indicated an energy transferred to the top of the pile of 288.7 kJ, being too low compared to the estimated necessary energy equal to $E^i_{pile} \approx 674.2\,\text{kJ}$. The amplitude is then doubled to $\sigma^A_{v,impact,p} \approx 132.6 \cdot 10^3\,\text{kN/m}^2$. However, this indicates a transfer of energy to the top of the pile equal to 1154.9 kJ, i.e. too high. The stress amplitudes and the associated energy transferred to the top of the pile for these two preliminary simulations are plotted in GeoGebra, and a polynomial line of second degree is fitted to the two coordinate points, and the origin, by the *FitPoly* command. This is shown in Figure 6.6, and the suggested stress amplitude is seemingly 101 314.5 kN/m^2. This gives a transferred energy to the top of the pile equal to 674.2 kJ for the preliminary simulation, seen by the enclosed area in Figure 6.5, which is the desired magnitude. Table 6.14 lists the stress amplitudes and associated energy transferred to the top of the pile for the preliminary simulations.

Table 6.14: PLAXIS 2D Simulations: Stress amplitude applied in preliminary simulations and energy subjected to the top of the pile calculated from results of force vs. vertical displacement of top of the pile.

Stress amplitude ($\sigma^{A}_{v,impact,p}$) [kN/m^2]	Energy subjected to top of the pile ($E^{i}_{pile,sim.}$) [kJ]
66 300	288.7
132 600	1154.9
101 314.5	674.2

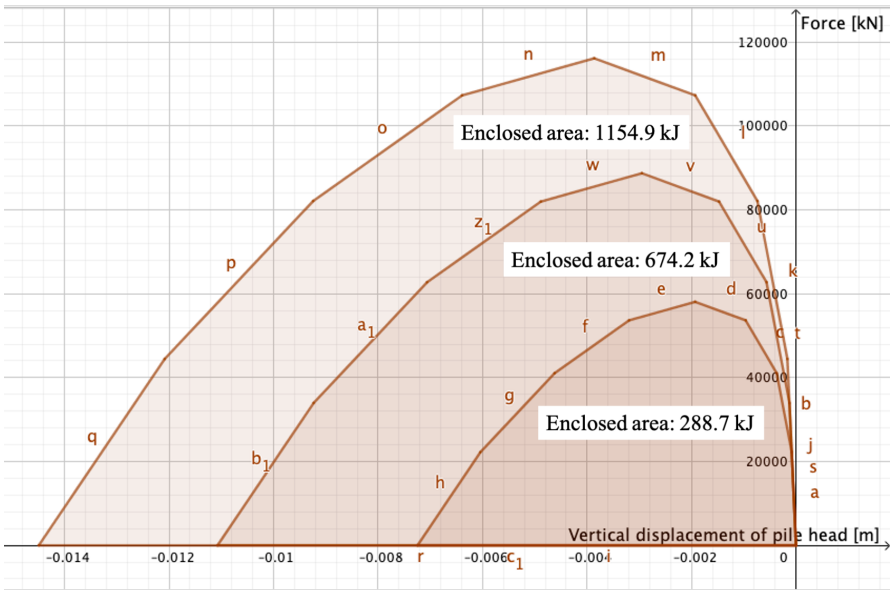

Figure 6.5: Energy transferred to pile during one impact, estimated by the resulting vertical displacement of top of the pile vs. the vertical force applied during driving in the preliminary simulations. Element distribution of mesh is set to *Medium*, and no mesh refinements applied. Data from PLAXIS plotted in GeoGebra.

Based on the presented results and interpretations from the preliminary simulations the amplitude for the stress is set to $\sigma^{A}_{v,impact,p} = 101314.5\,\mathrm{kN/m^2}$. The table values are then created, consisting of repetitive half sinusoidal curves with the aforementioned stress amplitude. The time between the initiation of each impact is set to 2 s to simulate the rate of 30 blows per minute. The frequency of the sinusoidal function determines the duration of each blow, indicating a duration of each impact of 0.01 s for $f = 50\,Hz$. Only the first half of the sinusoidal function is calculated, and the values are calculated with a time step of 0.0001 s. This indicates 100 calculation steps for each impact.

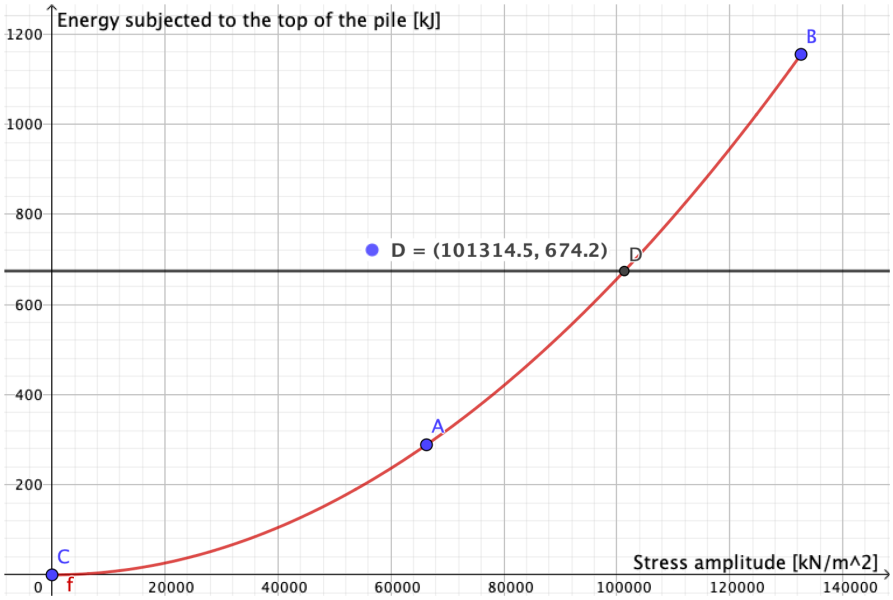

Figure 6.6: Visualisation of the interpolation to find necessary stress amplitude in order to subject $E^i_{pile} \approx 674.2\,\text{kJ}$ to the top of the pile. *FitPoly* command used to fit a polynomial line of second degree to points A, B and C. Data from preliminary simulations in PLAXIS 2D plotted in GeoGebra.

6.1.9 Mesh Generation

The mesh is generated with a *Very fine* element distribution, giving a relative element size factor of 0.5, compared to 1.0 being the value of the default element distribution *Medium* (*PLAXIS 2D - Reference Manual*, 2020). Local mesh refinement is introduced in an enclosed area surrounding the pile, horizontally ranging from symmetry line ($x = 0\,\text{m}$) to $x = 5\,\text{m}$ and vertically from seabed ($y = 0\,\text{m}$) to 0.5 m below the pile toe ($y = -35.5\,\text{m}$). The option of *Enhanced mesh refinements* is selected, which introduces mesh refinement in the model that are automatically performed by PLAXIS 2D in the vicinity of structural elements, modelled loads and prescribed displacements (*PLAXIS 2D - Reference Manual*, 2020). After generating the mesh PLAXIS 2D is reporting the model to contain a total of 11544 elements and 93529 nodes. The mesh for model is shown in Figure 6.7. The mesh at the centre of the embedded pile length ($y = -17.5\,\text{m}$), near the pile wall, is shown in Figure 6.8 while Figure 6.9 shows the mesh at the pile toe. Note the blue lines at $x = 5\,\text{m}$ and $y = -35.5\,\text{m}$) enclosing the area of local refinement.

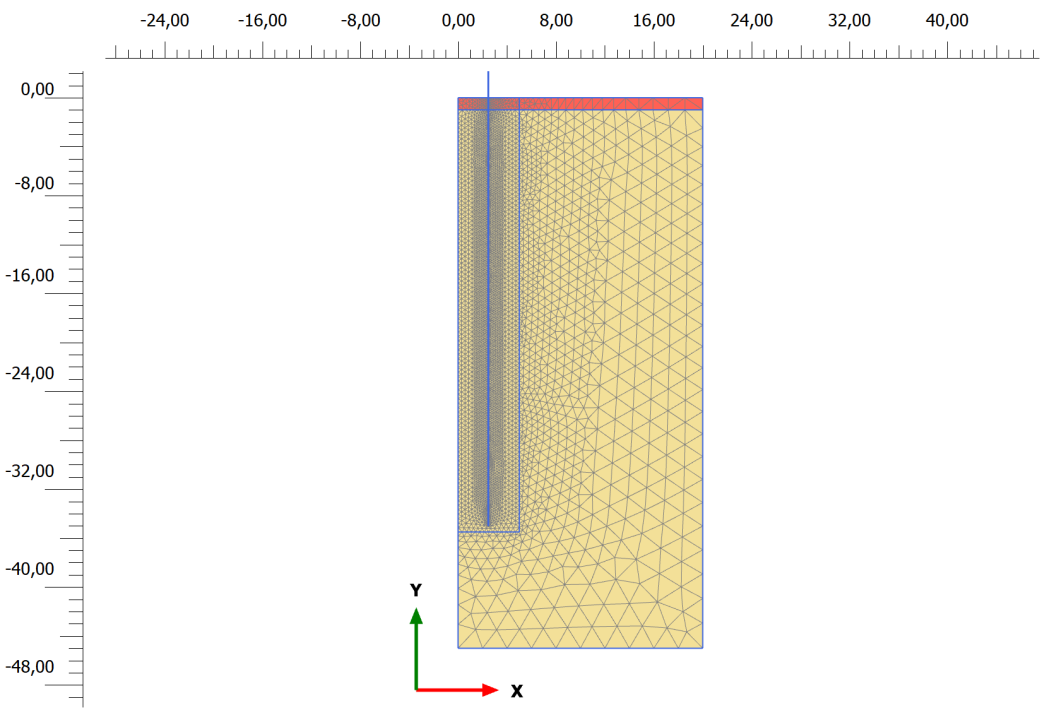

Figure 6.7: Mesh of the numerical model. Full length of pile not included in the figure. Figure exported from PLAXIS 2D Output.

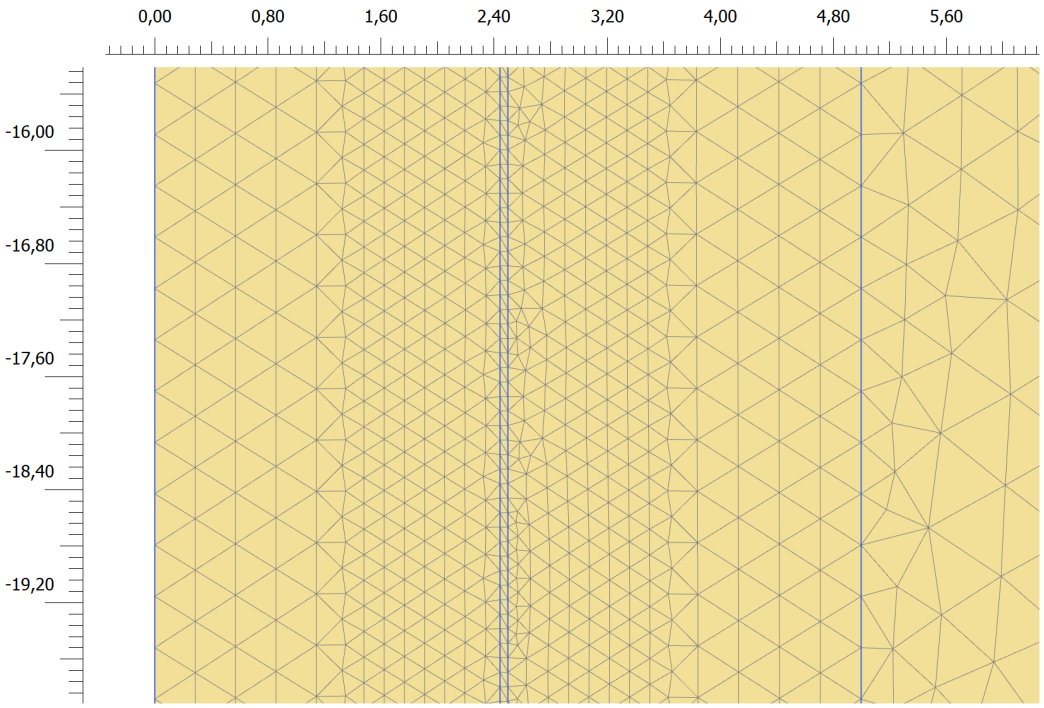

Figure 6.8: Mesh of the numerical model, zoomed in at pile wall at depth 17.5 m. Figure exported from PLAXIS 2D Output.

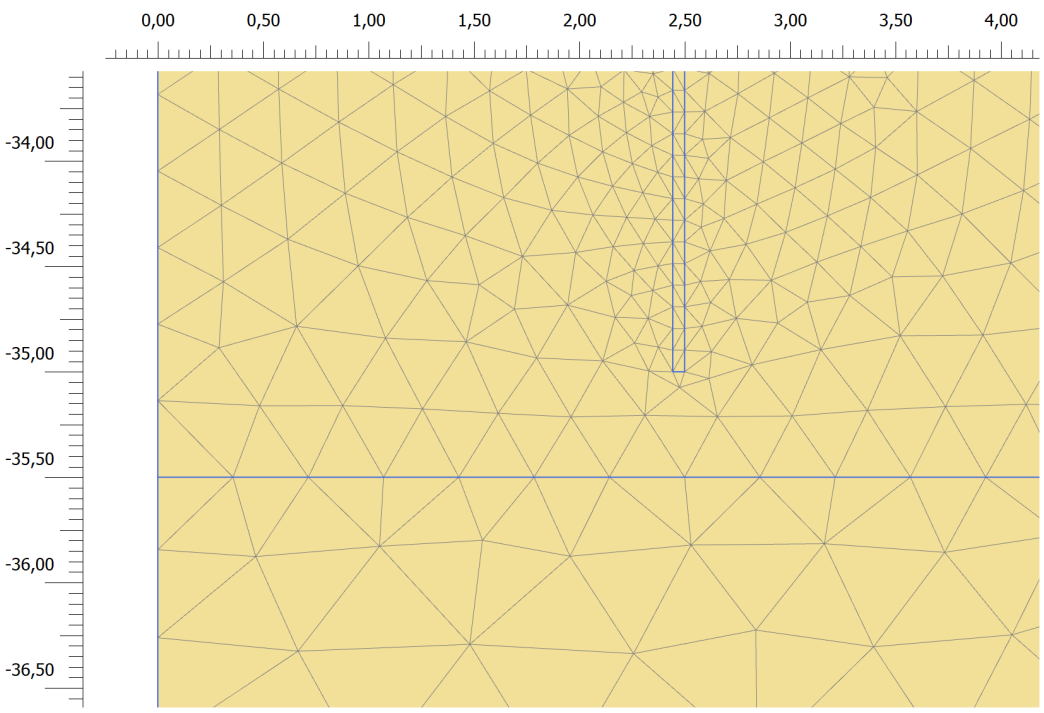

Figure 6.9: Mesh of numerical model, zoomed in at pile toe. Figure exported from PLAXIS 2D Output.

Nodes and Stress Points Selected

Nodes and stress points are selected to extract data from these points after the numerical simulations. Figure 6.10 shows a visualisation of the nodes and stress points selected. The green circles indicate nodes while the grey indicate stress points, and the x- and y-coordinates respectively are shown for each point.

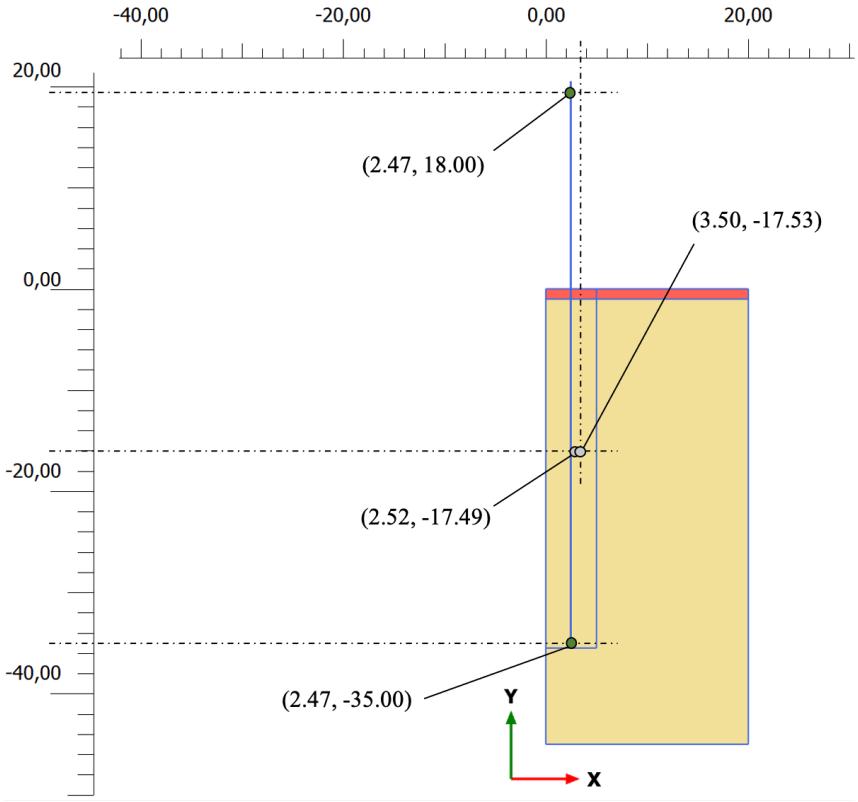

Figure 6.10: Visualisation of nodes and stress points selected to extract data. Green circles are nodes and grey are stress points. The location of each point is indicated by the x- and y-coordinates respectively. Figure exported from PLAXIS 2D Output with modifications.

Table 6.15: PLAXIS 2D Simulations: Reference names for nodes and stress points selected in the model, with associated coordinates.

Reference name	Point type	x-coordinate [m]	y-coordinate [m]
Top of the pile	node	2.47	18.00
Pile toe	node	2.47	-35.00
Depth 17.5 m, near exterior pile wall	stress point	2.52	-17.49
Depth 17.5 m, 1 m from exterior pile wall	stress point	3.50	-17.53

The reference names and coordinates for the nodes and stress points visualised in Figure 6.10 are listed in Table 6.15.

6.1.10 Boundary Conditions

Since the model is enclosed by a finite sized project the boundaries need to be defined according to certain boundary conditions.

Groundwater Flow
The groundwater flow boundary conditions are specified and activated in order to simulate the consolidation both during and after the dynamic loading. The groundwater flow boundaries are specified to *Closed* at the symmetry line and bottom of the model, i.e. respectively the x-min and y-min lines. This is chosen due to the possibility of having a less permeable material beneath this boundary. The boundary conditions at seabed and x-max are set to *Seepage*, which allow water flow through the boundary freely (*PLAXIS 2D - Reference Manual*, 2020). This is chosen as it is assumed that the similar sand material exceeds in x-direction outside the model boundaries. The groundwater flow for the model conditions are at the boundaries x-min and y-min set to *Closed* and at x-max and y-max set to *Open*.

Dynamic Boundary Conditions
The dynamic boundary conditions at model conditions x-max and y-min are set to *Viscous*. This option activates absorption of wave energy passing through these boundaries (*PLAXIS 2D - Reference Manual*, 2020). The boundaries at x-min and y-max are set to *None*.

6.2 Calculation

A total of 7 simulations are performed with the presented model. Table 6.16 lists the different simulations. Simulation A (referred to as sim.A) is the base simulation, being vibratory driving with load and frequency input previously described in Section 6.1.7. The other vibratory driving simulations are alterations of the base simulation. One simulation of impact driving is performed (sim.F), of which the modelling decisions are described in Section 6.1.8. The differences between sim.A and the other simulations are emphasised by bold text in Table 6.16.

Table 6.16: PLAXIS 2D Simulations: Overview of simulations performed. Main differences from base simulation (sim.A) indicated in bold text.

Description	Vibratory driving						**Impact driving**
Reference	sim.A	sim.A*	sim.B	sim.C	sim.D	sim.E	sim.F
Driving frequency, f [Hz]	23.33	23.33	**18**	**12**	**12**	23.33	-
Blow rate [blow/min.]	-	-	-	-	-	-	**30**
Dynamic time interval [s]	0.8573	**1.667**	**1.111**	**1.667**	**1.667**	0.8573	**12.01**
Number of cycles/impacts	20	**38.9**	20	20	20	20	**7**
Stress amplitude, σ_v^A [kN/m^2]	10 608.92	10 608.92	**6 315.19**	**2 806.75**	10 608.92	10 608.92	**101 314.5**
Initial void ratio, e_{init} [-]	0.734	0.734	0.734	0.734	0.734	**0.650**	0.734
Rayleigh damping of soil (α)	8.391	8.391	**6.262**	**3.738**	**3.738**	8.391	**18.66**
Rayleigh damping of soil (β) ($\cdot 10^{-3}$)	0.4093	0.4093	**0.5305**	**0.7958**	**0.7958**	0.4093	**0.1910**

The simulations are performed through several *Phases*, and every simulation consists of 5 phases. *Phase 0 - Initial phase* is the first phase, of which every simulation starts from. Figure D.2 in Appendix D shows a visualisation of the calculation phases for the simulations listed in Table 6.16. Note that some of the simulations also share other phases than the initial phase. A visualisation of the axisymmetric model in PLAXIS 2D in the dynamic loading phase for sim.A is presented in Figure D.1 in Appendix D.

The 5 phases are to be presented for all simulations (A-F), however, only explained in detail for sim.A. The alterations made for the others will be stated in the following.

6.2.1 sim.A - Vibratory Driving, $f = 23.33$ Hz

Phase 0 - Initial Phase

The initial stresses in the soil are calculated by the K_0 *procedure*. Neither the soil clusters of the pile nor the hammer materials are yet activated.

Phase 1 - Activate Pile and Hammer Material and Select 23.33 Hz Soil
The pile and hammer materials (m_{ib}, elastomer pads (spring) and $m_{vib,dyn}$), as well as the soils with the Rayleigh damping coefficients associated to the driving frequency in the dynamic loading phase are activated in this phase. Note that this includes the 1 m layer of MC soil. Both *Reset displacements to zero* and *Reset small strain* are selected.

Phase 2 - Plastic Nil-phase
Nothing additional is activated in the model at this phase. A plastic nil-phase may be introduced in order to achieve equilibrium after performing the initial phase with the calculation of initial stresses (*PLAXIS 2D - Reference Manual*, 2020). Neither *Reset displacements to zero* nor *Reset small strain* are selected.

Phase 3 - Dynamic Loading 23.33 Hz
The dynamic load acting on the top of the pile is activated in this phase, i.e. this is the phase of simulating the pile driving. The calculation type used is the *Dynamic with consolidation*. This calculation type allows dynamic load input, and is able to calculate the generation of excess pore pressure in soils with a predefined drained behaviour, as opposite of *Dynamic* calculation type which may only calculate generation of excess pore pressure if the drainage type is set to *Undrained (A)* or *Undrained (B)* (*PLAXIS 2D - Reference Manual*, 2020). *Dynamic with consolidation* calculation type hence utilises the input of soil permeability and the boundary conditions regarding groundwater flow (*PLAXIS 2D - Reference Manual*, 2020). The loading type is *Staged construction*. The *Dynamic time interval* is set to 0.8573 s in order to simulate approximately 20 load cycles of the vibratory driving. Both *Reset displacements to zero* and *Reset small strain* are selected, which resets the displacements and strains to zero at the beginning of this phase. This is to not include any possible displacements or strains from previous phases in this or the subsequent phases.

The total number of calculation steps is the multiplication of *Max steps* with *Number of sub steps*, of which *Max steps* defines the number of steps that stores data that may be used to plot data in the predefined nodes and stress points (*PLAXIS 2D - Reference Manual*, 2020). The time step used in the dynamic calculation (δt) is given by (*PLAXIS 2D - Reference Manual*, 2020):

$$\delta t = \frac{Dynamic\,time\,interval}{Max\,steps \cdot Number\,of\,sub\,steps} \tag{6.31}$$

The number of steps per cycle of the sinusoidal function is set to 40, giving a total of 800 calculation steps for 20 cycles. *Max steps* is set to 800 and *Number of sub steps* is set to 1. This gives a time step of $\delta t \approx 1.07 \cdot 10^{-3}$ s for this phase. The tolerance for global errors in the calculation is 0.01000.

Phase 4 - Dynamic Damping 23.33 Hz
The dynamic load is deactivated, and also this phase is performed with calculation type

Dynamic with consolidation. This phase is added in order to damp out vibrations induced by the dynamic load before initiating the consolidation. Note that vibrations causing elastic strain may not be damped out if the wave frequency is not within the targeted damping range for the implemented Rayleigh damping in the soil material. The *Dynamic time interval*, *Max steps* and *Number of sub steps* are equal the ones in the dynamic loading phase, i.e. 0.8573 s, 800 and 1 respectively. This is to keep the same time step for the calculations as in the dynamic loading phase. Note that neither *Reset displacements to zero* nor *Reset small strain* are selected in this phase.

Phase 5 - Consolidation 23.33 Hz
This phase simulates the dissipation of possible excess pore pressure generated during the dynamic loading phase. Note that the materials modelling the hammer are still activated. The calculation type is set to *Consolidation* with loading type *Minimum excess pore pressure*, which consolidates until the maximum absolute value of excess pore pressure present in the model is below a predetermined absolute value. The absolute value of 1.0 kPa is set as target value. *Use default iter parameters* are selected, indicating *Max steps* of 1000 and an automatic *Time step determination*. However, for the *Minimum excess pore pressure* loading type the consolidation phase may not reach the number of *Max steps* if the predetermined target value for the excess pore pressure is reached first (*PLAXIS 2D - Reference Manual*, 2020).

6.2.2 sim.A* - Vibratory Driving, $f = 23.33$ Hz, Longer Duration

This simulation is similar as sim.A, however, with a longer *Dynamic time interval* (1.667 s) for the dynamic loading phase to be able to see evolution of soil behaviour beyond 20 cycles, i.e. 0.8573 s. The time interval of 1.667 s indicates simulation of 38.9 loading cycles for the frequency of 23.33 Hz. Still 40 calculation steps are used per cycle, i.e. *Max steps* is set to 1556 and *Number of sub steps* are set to 1.

6.2.3 sim.B - Vibratory Driving, $f = 18$ Hz

All phases and their selections are similar the ones presented for sim.A in Section 6.2.1, with exception of the dynamic loading and damping phase. In this simulation the load multiplier with $f = 18$ Hz is assigned the dynamic load. The *Dynamic time interval* is set to 1.111 s in order to simulate approximately 20 cycles, and is also the *Dynamic time interval* for the dynamic damping phase. Note that *Max steps* and *Number of sub steps* remains unchanged, i.e. 800 and 1 respectively.

6.2.4 sim.C - Vibratory Driving, $f = 12$ Hz

All phases and their selections are similar the ones presented for sim.A in Section 6.2.1, with exception of the dynamic loading and damping phase. In this simulation the load

multiplier with $f = 12\,\text{Hz}$ is assigned the dynamic load. The *Dynamic time interval* is set to 1.667 s in order to simulate approximately 20 cycles, and is also the *Dynamic time interval* for the dynamic damping phase. Note that *Max steps* and *Number of sub steps* remains unchanged, i.e. 800 and 1 respectively.

6.2.5 sim.D - Vibratory Driving, $f = 12\,\text{Hz}$, with Similar Load Amplitude as sim.A

This simulation has a driving frequency of $f = 12\,\text{Hz}$, but the same load amplitude as sim.A ($f = 23.33\,\text{Hz}$). This is to investigate the effect of frequency on soil behaviour.

Note that sim.D is identical to sim.C, but with an increased load amplitude of the dynamic load applied to the top of the pile..

6.2.6 sim.E - Vibratory Driving, $f = 23.33\,\text{Hz}$, Denser Sand

This simulation is identical to sim.A, with exception of the initial void ratio in the sand being set to $e_{init} = 0.650$, instead of $e_{init} = 0.734$. This indicates a denser sand in sim.E compared to sim.A. This is to investigate the effect of initial void ratio on soil behaviour during vibratory driving. Note that all other inputs are unchanged. Both flow parameters and specific weight may depend on the void ratio, however, these are kept equal the ones used in sim.A. Hence, the flow parameters are not estimated based on grain size distribution, but set equal to $k_x = k_y = 1.492\,\text{m/day}$ for sim.E.

6.2.7 sim.F - Impact Driving

All phases and their selections are similar the ones stated for sim.A, with exception of activation of hammer materials, loading and damping phases.

In this simulation only the lower soil cluster on top of the top of the pile is activated, and is assigned the material of $m_{static,impact}$ (replacing $m_{vib,dyn}$ shown in Figure 6.4). The dynamic load is assigned the load modelling impact driving and the *Dynamic time interval* is set to 12.01 s, simulating 7 impacts. Note that the time between impacts is not included after the last impact in the dynamic loading phase. The number of steps in the dynamic loading phase is based a the selection of 8 steps per impact, which has a duration of 0.01 s. An even number of steps each impact is selected to better capture the peak amplitude of the dynamic multiplier. The number of 8 steps per impact implies a number of *Max steps* of 9608 with *Number of sub steps* set to 1. An increased number of steps per impact could increase calculation accuracy, however, this could considerably increase calculation time due to the relatively long time between impacts compared to the duration of the impact itself. For the damping phase *Dynamic time interval* is set to 2 s, number of *Max steps* is set to 1600 and *Number of sub steps* is set to 1, keeping the same time step as for the dynamic loading phase.

Chapter 7

Results and Discussion

The results from the numerical simulations, along with interpretations and discussion of these are to be presented. Output data in PLAXIS defines stress in pressure by negative values, and the same for volumetric contraction. The results presented uses the same notation as PLAXIS. Results regarding, amongst others, Cartesian stresses are to be presented, and Figure 7.1 visualises the directions stress notations in three-dimensions (3D).

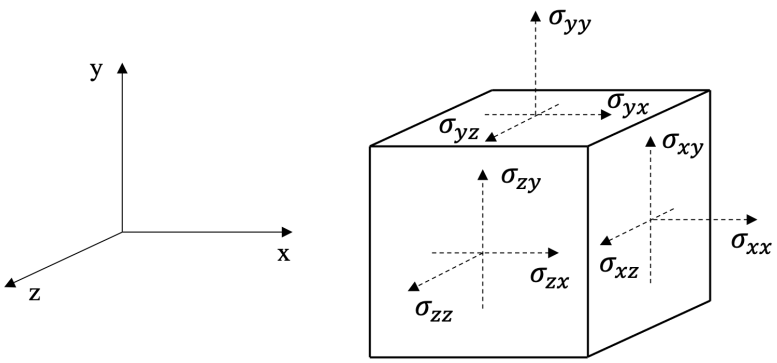

Figure 7.1: Cartesian stress directions in 3D. Redrawn, with modifications, after *PLAXIS 2D - Reference Manual* (2020).

Note that *Use result smoothing* is selected by default in PLAXIS 2D Output, which aims at reducing possible numerical noise occurred during extrapolation of nodal data from stress point data (*PLAXIS 2D - Reference Manual*, 2020). The contour plots to be presented may be scaled for better visibility, hence, the who range between minimum and maximum values may not be included in the plot.

The indicators on the graphs, i.e. the dots, represent the calculation points, or steps, during the simulation. Note that seabed is modelled at $y = 0\,\text{m}$, hence $y = -17.5\,\text{m}$ may be referred to as at depth 17.5 m. *Vibratory driving* may in figure captions be referred to by *vibro*, while *impact* refers to *Impact driving*.

7.1 Vibratory vs. Impact Driving

Results from the simulated vibratory driving at 23.33 Hz, with a longer duration, (sim.A*) are compared to the simulated impact driving (sim.F). See Table 6.16 in Section 6.2 for the main differences in simulation parameters between sim.A* and sim.F.

Vertical Displacement of the Top of the Pile During Loading, Damping and Consolidation Phases

The vertical displacement (u_y) of the top of the pile during loading, damping and consolidation phases is plotted against a logarithmic time scale, shown in Figure 7.2. The relatively large fluctuations of vertical displacement indicate the dynamic loading phase, followed by a damping phase until consolidation is initiated. The latter is indicated by the increased horizontal spacing between the calculation points.

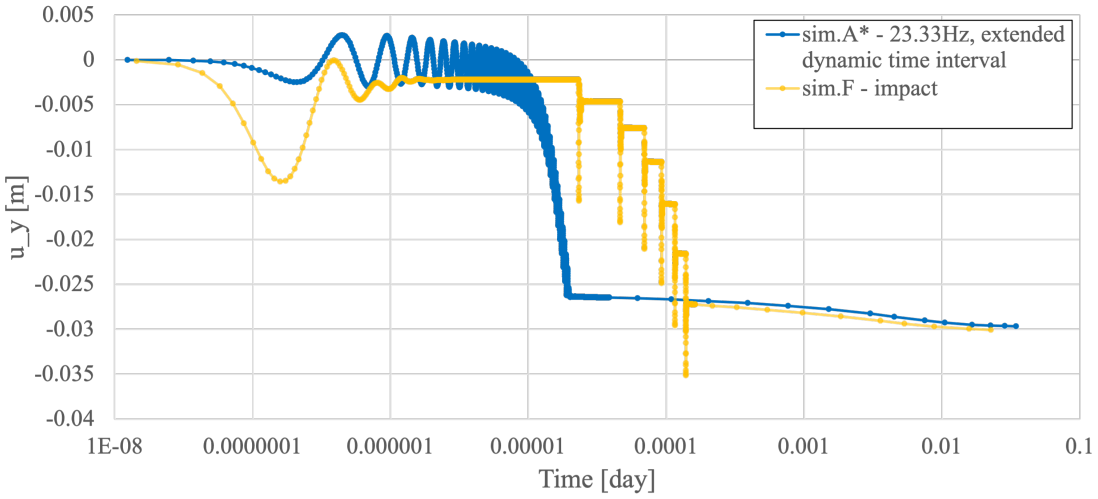

Figure 7.2: sim.A* (vibro 23.33 Hz, 38.9 cycles) and sim.F (impact): vertical displacement of top of the pile during loading, damping and consolidation phases against a logarithmic time scale. Initiation of consolidation phase is indicated by the increased horizontal spacing between calculation points. Data from PLAXIS 2D plotted in Excel.

The vertical displacements of the top of the pile during driving and consolidation for sim.A* and sim.F (Figure 7.2) indicate an almost equal final settlement for both simulations, being approximately 30 mm. This was not intended prior the simulations, however, this may allow a better comparison of the soil behaviour during driving between the two methods.

Excess Pore Pressure

The contour plots in Figures 7.3 and 7.4 show the excess pore pressure (p_{excess}) at end of the loading phase, hence before consolidation phase. Note that for the impact driving the dynamic damping phase is added to include the effect of the vibrations from the last impact. Negative values for the stress is pressure.

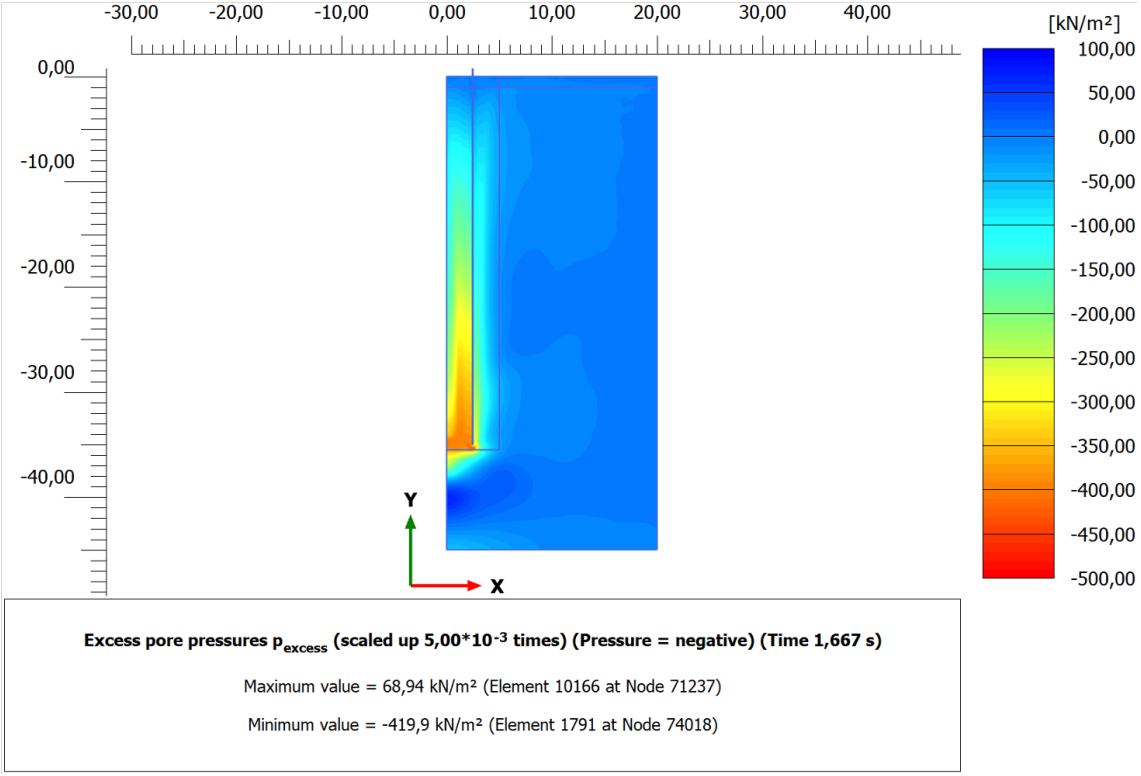

Figure 7.3: sim.A* (vibro 23.33 Hz, 38.9 cycles): p_{excess} contour plot of soil at the end of dynamic loading phase. File exported from PLAXIS 2D Output.

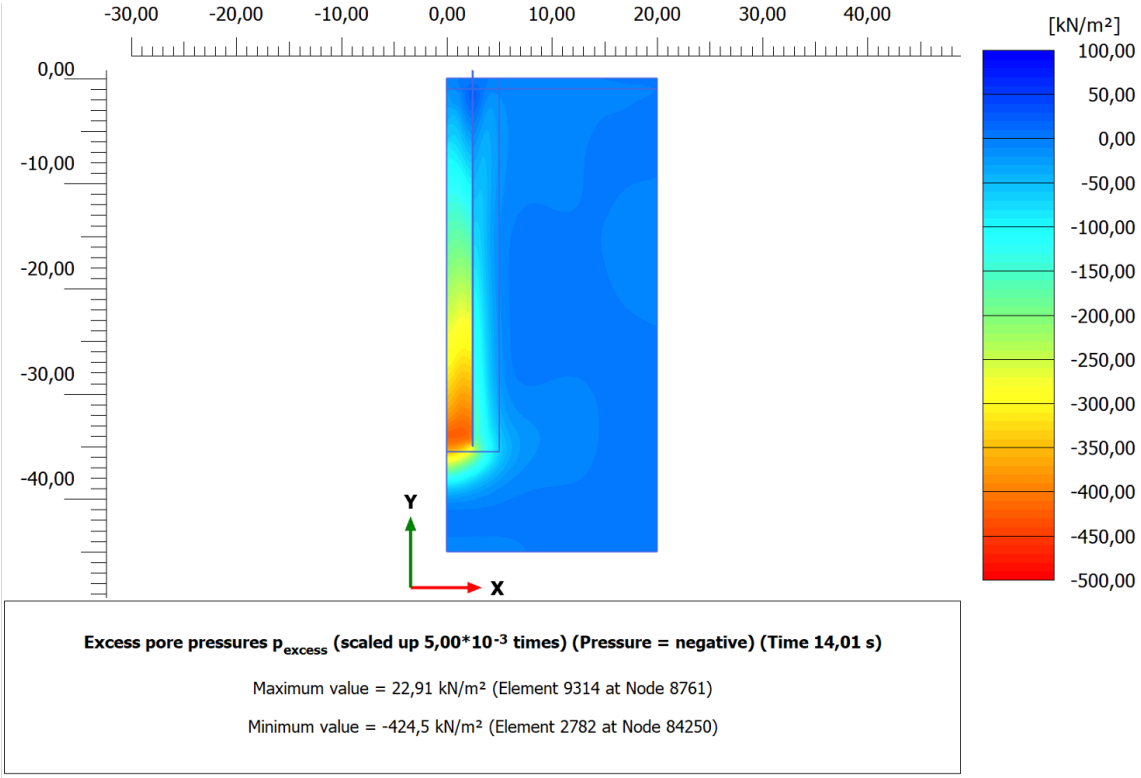

Figure 7.4: sim.F (impact): p_{excess} contour plot of soil at the end of dynamic damping phase. File exported from PLAXIS 2D Output.

The build-up of excess pore pressure is present after both pile driving methods, however, the contour plots in Figures 7.3 and 7.4 indicate slightly greater p_{excess} in pressure (i.e. greater negative values of p_{excess}) after vibratory driving along the exterior pile wall and at the upper part of the pile at the interior of the pile wall compared to impact driving. While at the interior of the pile at the pile toe and below pile toe the generated excess pore pressure is slightly larger after impact driving.

Figure 7.5 shows the evolution of p_{excess} in a point at the centre of the embedded pile length (depth 17.5 m) near the exterior pile wall during driving for sim.A* and sim.F (including the damping phase for the latter). Figure 7.6 shows the evolution of p_{excess} at the same depth, but 1 m from the exterior pile wall.

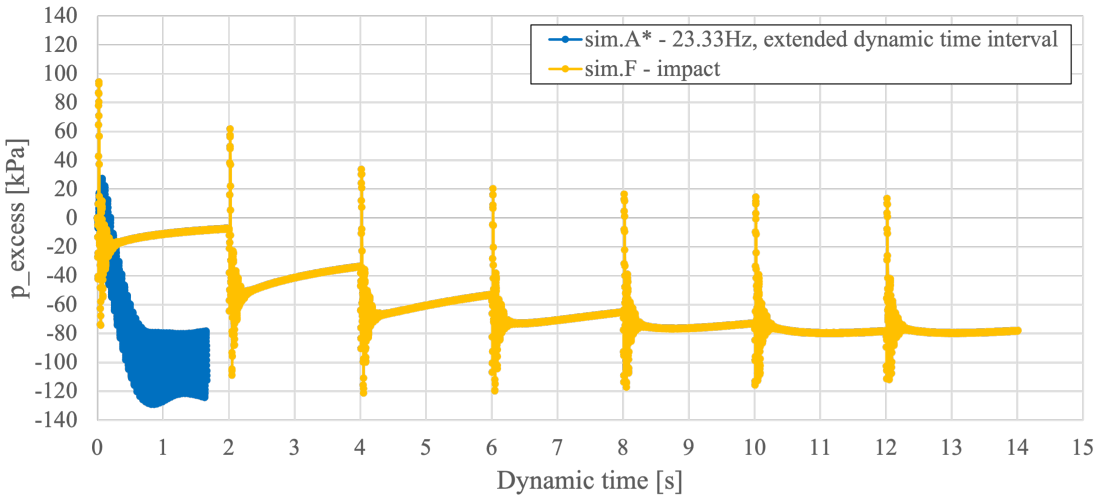

Figure 7.5: sim.A* (vibro 23.33 Hz, 38.9 cycles) and sim.F (impact): p_{excess} during dynamic loading phase (damping phase included for sim.F). At depth 17.5 m, near exterior pile wall. Data from PLAXIS 2D plotted in Excel.

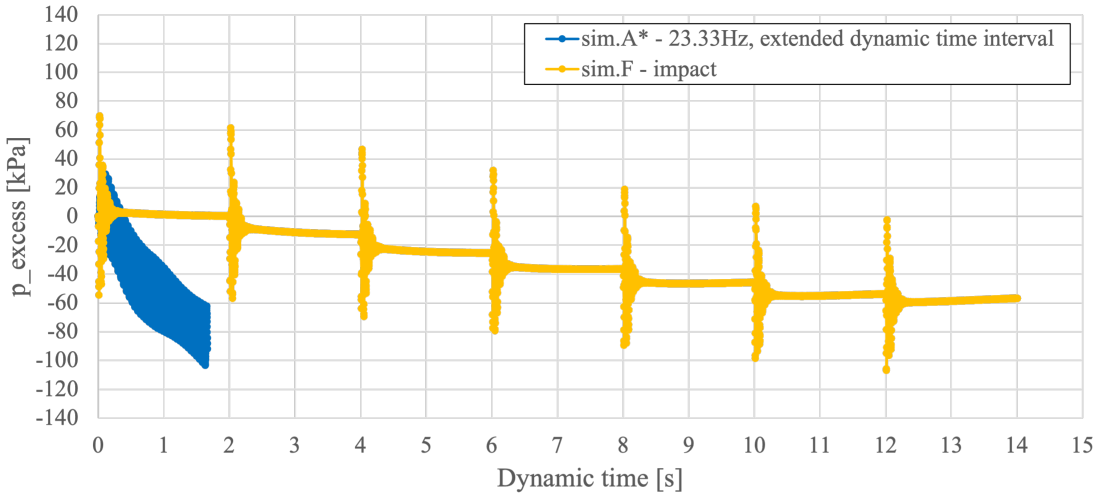

Figure 7.6: sim.A* (vibro 23.33 Hz, 38.9 cycles) and sim.F (impact): p_{excess} during dynamic loading phase (damping phase included for sim.F). At depth 17.5 m, 1 m from exterior pile wall. Data from PLAXIS 2D plotted in Excel.

The same graphs of p_{excess} during vibratory driving (sim.A*) seen in Figures 7.5 and 7.6 are also plotted for a smaller time scale, presented in Figures 7.7 and 7.8 respectively.

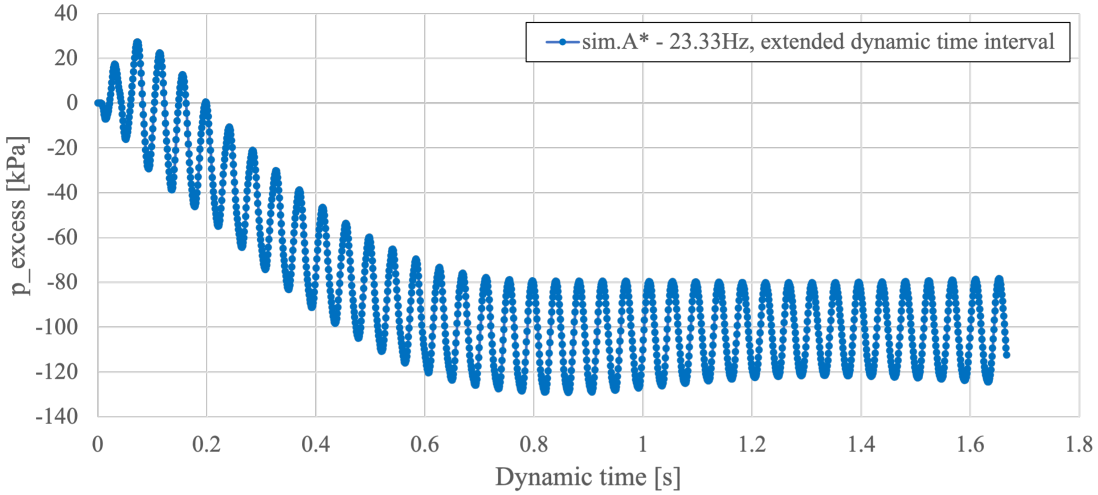

Figure 7.7: sim.A* (vibro 23.33 Hz, 38.9 cycles): p_{excess} during dynamic loading phase. At depth 17.5 m, near exterior pile wall. Data from PLAXIS 2D plotted in Excel.

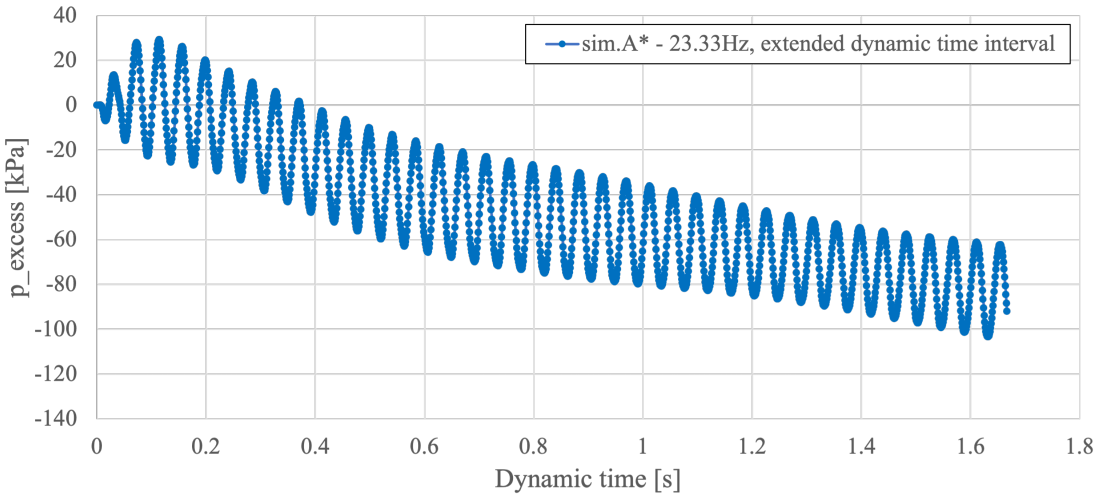

Figure 7.8: sim.A* (vibro 23.33 Hz, 38.9 cycles): p_{excess} during dynamic loading phase. At depth 17.5 m, 1 m from exterior pile wall. Data from PLAXIS 2D plotted in Excel.

Excerpts of the evolution of excess pore pressure at depth 17.5 m, near the exterior pile wall and 1 m further out, during the first loading cycle and a short subsequent dynamic time of impact driving (sim.F) may be found in Figures B.1 and B.2 in Appendix B.1.

By evaluating the graphs presenting the evolution of p_{excess} at depth 17.5 m, near the exterior pile wall and 1 m further out, it is seen that the rate, with respect to time, of excess pore pressure build-up is significantly higher during vibratory driving. SANISAND incorporates kinematic hardening, and vibratory driving may induce several more fluctuations of the stress ratio ($\eta = q/p'$) in the soil above and below the yield lines for the $p' - q$ stress space, possibly leading to the more rapid generation of excess pore pressure compared to impact driving.

The hydraulic conductivity parameters used for the simulation affects the magnitude of p_{excess} build-up since the calculation type is set to *Dynamic with consolidation*, which allows p_{excess} build-up for soils being considered to have a drained behaviour prior to applying a rapid load. A slight reduction of p_{excess} in pressure is seen near the exterior pile wall during the time between the first impacts during impact driving (Figure 7.5), which may be suggested not seen during vibratory driving at 23.33 Hz frequency possibly due to the continuous loading (Figure 7.7). Near the exterior pile wall, at depth 17.5 m, the excess pore pressure seem to approach a steady-state during vibratory driving and possibly during impact driving, however, at a seemingly lower pressure for the latter. This may be related to the drainage between impacts, leading to an equilibrium of p_{excess} build-up at a lower pressure. However, the number of simulated impacts are relatively few, and the further evolution of p_{excess} for an increased number of loading cycles is uncertain. It may be suggested that selecting the input parameters for hydraulic conductivity with caution is important, as these may affect the pore pressure generation, hence also the shear stiffness degradation, during partly drained loading situations.

Effective Mean Stress

The effective mean stress (p') is plotted in 7.9 and 7.10 at the same data points presented for p_{excess}, amongst others, to visualise the dependency between evolution of excess pore pressure and effective mean stress. Negative values for the stress is pressure.

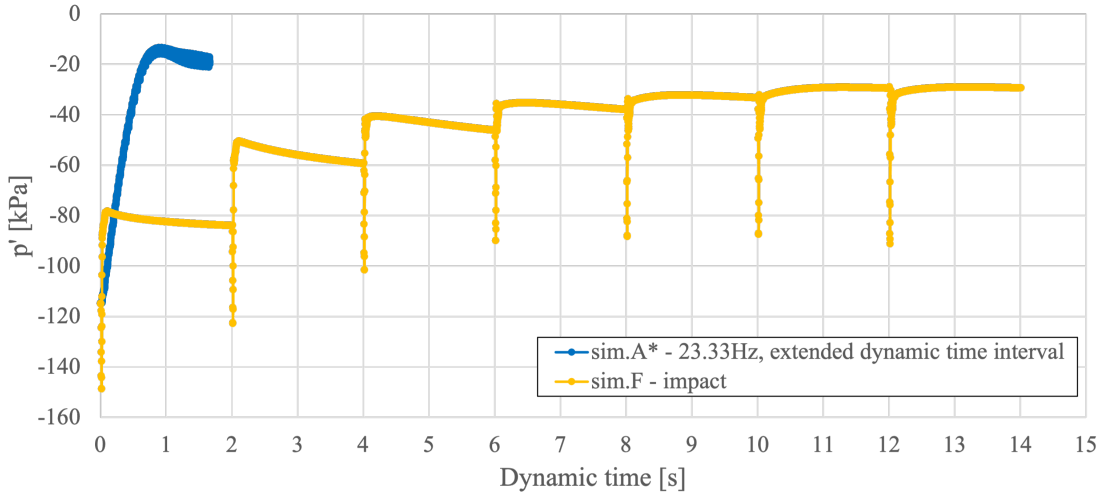

Figure 7.9: sim.A* (vibro 23.33 Hz, 38.9 cycles) and sim.F (impact): p' during dynamic loading phase (damping phase included for sim.F). At depth 17.5 m, near exterior pile wall. Data from PLAXIS 2D plotted in Excel.

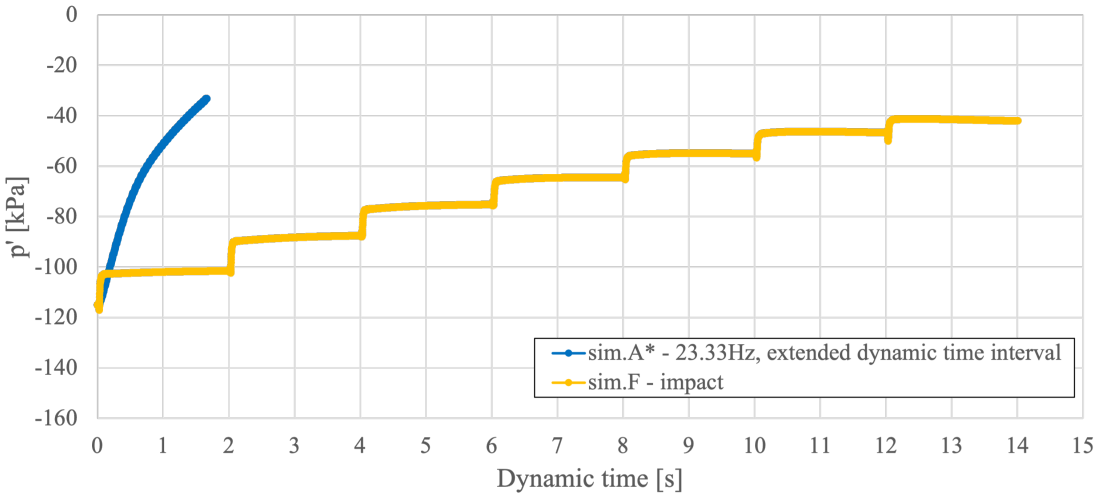

Figure 7.10: sim.A* (vibro 23.33 Hz, 38.9 cycles) and sim.F (impact): p' during dynamic loading phase (damping phase included for sim.F). At depth 17.5 m, 1 m from exterior pile wall. Data from PLAXIS 2D plotted in Excel.

The evolution of p' seen in Figures 7.9 and 7.10 for sim.A* are plotted for a smaller time scale, and may be found in Figures B.5 and B.6 in Appendix B.2. Excerpts of the evolution of effective mean stress at depth 17.5 m, near the exterior pile wall and 1 m further out, during the first loading cycle and a short subsequent dynamic time of impact driving (sim.F) may be found in Figures B.3 and B.4 in Appendix B.2.

During vibratory driving the effective mean stress at depth 17.5 m near the exterior pile wall approaches approximately −15 kPa, before a slight increase of pressure is seen towards −20 kPa (Figure 7.9). 1 m further out from the pile wall the value of p' is approximately −33 kPa, without showing signs of approaching a steady-state (Figure 7.10). During impact driving the value of p' approaches approximately −29 kPa near the exterior pile wall and −42 kPa 1 m further out, with slight indications of possibly approaching a steady-state at the point near the pile wall. Note that at both distances from the pile wall the effective mean stress is approaching a smaller value in pressure during vibratory driving, suggesting the soil to be liquefied to a larger degree compared to impact driving.

Figures 7.11 and 7.12 show the evolution of p' for the same simulations and in the same data points as Figures 7.9 and 7.10 respectively, but with data from dynamic loading, damping and consolidation phases. Note the logarithmic time scale.

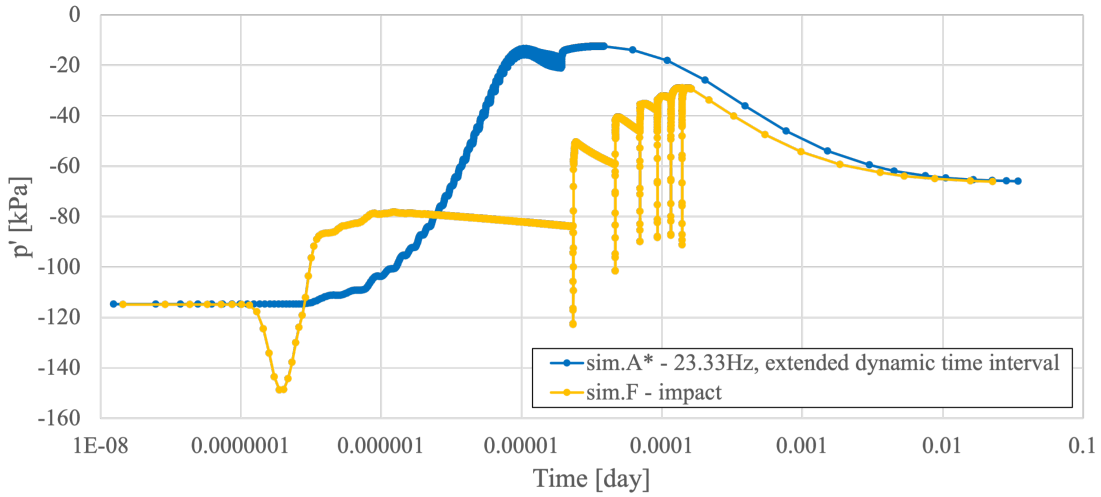

Figure 7.11: sim.A* (vibro 23.33 Hz, 38.9 cycles) and sim.F (impact): p' during loading, damping and consolidation phases against a logarithmic time scale. At depth 17.5 m, near exterior pile wall. Data from PLAXIS 2D plotted in Excel.

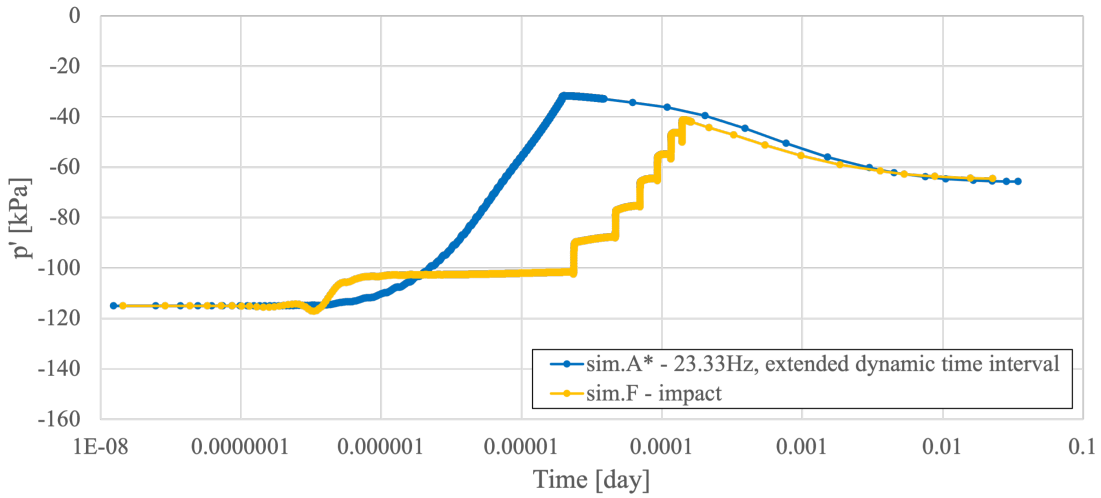

Figure 7.12: sim.A* (vibro 23.33 Hz, 38.9 cycles) and sim.F (impact): p' during loading, damping and consolidation phases against a logarithmic time scale. At depth 17.5 m, 1 m from exterior pile wall. Data from PLAXIS 2D plotted in Excel.

Figures 7.11 and 7.12 indicate that p' is initially similar at both distances from the pile and for both driving methods (approximately -115 kPa), and approaches seemingly the same value after consolidation for both vibratory and impact driving, in the range of approximately -65 kPa and -66 kPa. However, the evolution of p' during driving is different. After the first impact there is a relatively large decrease of pressure, but this is surpassed during vibratory driving after a certain number of cycles. Since the excess pore pressure is dissipated to an absolute value of maximum of 1 kPa during consolidation the reduction of effective mean stress in pressure from initial to after consolidation to this degree is not due to a present p_{excess}.

$\sigma_{xy} - \gamma_{xy}$ Hysteresis Loops

Shear stress (σ_{xy}) is plotted against shear strain (γ_{xy}) during pile driving, referred to as $\sigma_{xy} - \gamma_{xy}$ hysteresis loops, of which the slope of the loops visualises the evolution of shear modulus (G). The data is from points at the centre of the embedded length of the pile (depth 17.5 m), at two different horizontal locations (near exterior pile wall and 1 m from exterior pile wall). Note the difference in scale in both x- and y-axes for the different distances from the exterior pile wall. The hysteresis loops indicate start of the dynamic loading by the colour purple and evolves to yellow during the dynamic loading. The damping phase is included for the impact driving simulation (sim.F), i.e. including 2 s after the end of the last impact, to include the immediate evolution of strains and stresses after the last impact.

The secant shear modulus ratio between first cycle and cycle number N ($G_{s,N}/G_{s,1}$) is interpreted by the one-way amplitudes for the first cycle of both driving methods, and for cycle number N of impact driving, while cycle number N for vibratory driving is interpreted by the last two-way amplitudes of the hysteresis loops. This method of interpretation is presented in Appendix C.

In the point near the exterior pile wall, at depth 17.5 m there are clear indications of shear modulus degradation during both impact and vibratory driving. The secant shear modulus degradation is significantly lower due to vibratory driving, with a secant shear modulus ratio between first cycle and cycle number 39 being $G_{s,39}/G_{s,1} = 0.13$, compared to $G_{s,7}/G_{s,1} = 0.54$ during impact driving at load cycle number 7. The vibratory driving is simulated for 1.667 s, while impact driving for 12.01 s, suggesting the rate of soil degradation to be considerably higher during vibratory driving. However, it may be noted that the secant shear modulus during the first cycle is significantly lower during impact driving compared to vibratory driving. This may partly be explained by the relatively large decrease of p' in pressure after the first cycle of impact driving to a lower value compared to after the first cycle of vibratory driving, seen in the graph in Figure 7.15. Taking into account the seemingly approach of a steady-state for the graphs of both p_{excess} and p' it may be suggested that the stiffness ratio near the exterior pile wall during vibratory driving approaches a steady-state of 0.13, and possibly a steady-state of 0.54 during impact driving.

Note that the hysteresis loop of the first loading cycle during vibratory driving indicate the same tendency of variation in shear modulus as seen in Figure 4.3, in Section 4.3, i.e. largest shear modulus at load initiation, followed by a softening, before the stiffness increases after load reversals and then decreases again. The simulation of this behaviour by the SANISAND material model may be attributed to its ability of simulating kinematic hardening. Initially, both at the beginning of a cycle and at load reversal, the soil strains are elastic before plastic strain may occur.

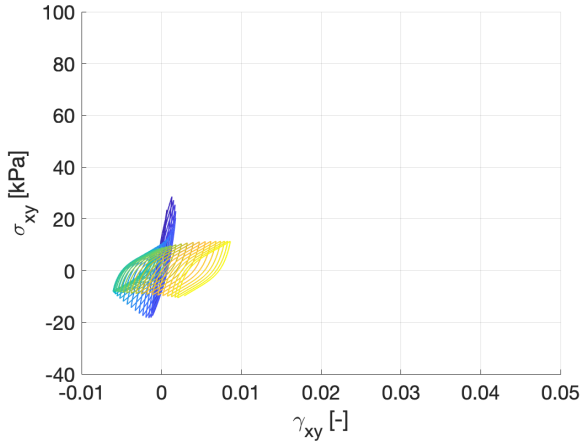

(a) sim.A* (vibro 23.33 Hz): 38.9 loading cycles. $G_{s,39}/G_{s,1} = 0.13$.

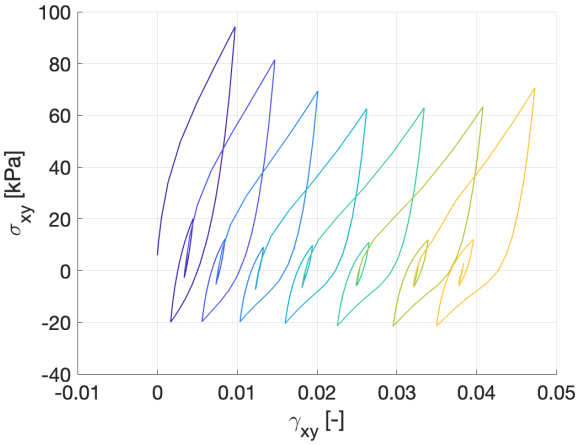

(b) sim.F (impact): 7 loading cycles. $G_{s,7}/G_{s,1} = 0.54$.

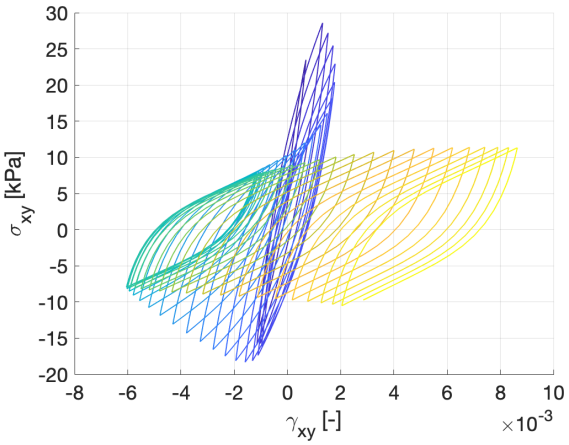

(c) sim.A* (vibro 23.33 Hz): 38.9 loading cycles. $G_{s,39}/G_{s,1} = 0.13$.

Figure 7.13: sim.A* (vibro 23.33 Hz, 38.9 cycles) and sim.F (impact) (two graphs for sim.A*, one at same scale as sim.F for reference): $\sigma_{xy} - \gamma_{xy}$ hysteresis loops during dynamic loading phase (damping phase included for sim.F). At depth 17.5 m, near exterior pile wall. Colour shades indicate calculation points, from purple to yellow. $G_{s,N}/G_{s,1}$ is ratio of shear modulus between first cycle and cycle number N. Data from PLAXIS 2D plotted in MATLAB.

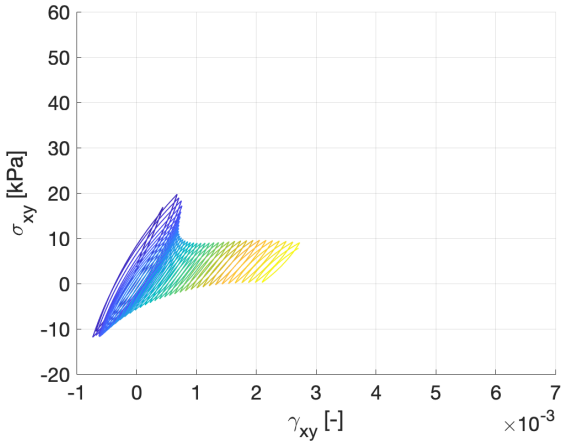

(a) sim.A* (vibro 23.33 Hz): 38.9 loading cycles. $G_{s,38}/G_{s,1} = 0.47$.

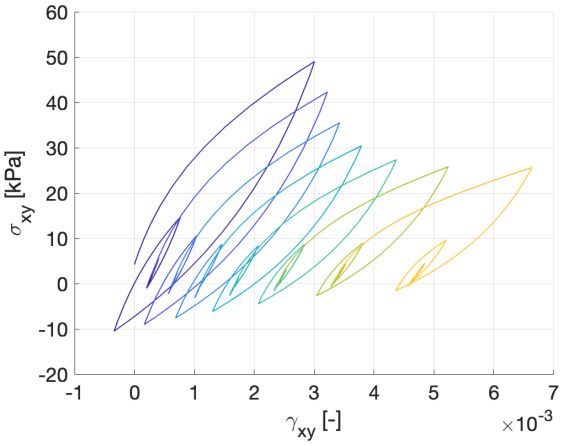

(b) sim.F (impact): 7 loading cycles. $G_{s,7}/G_{s,1} = 0.50$.

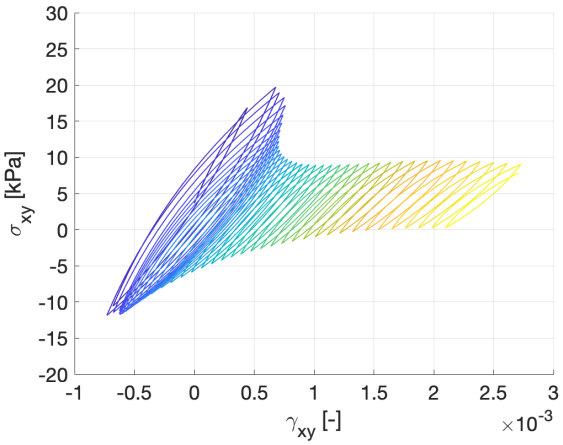

(c) sim.A* (vibro 23.33 Hz): 38.9 loading cycles. $G_{s,38}/G_{s,1} = 0.47$.

Figure 7.14: sim.A* (vibro 23.33 Hz, 38.9 cycles) and sim.F (two graphs for sim.A*, one at same scale as sim.F for reference): $\sigma_{xy} - \gamma_{xy}$ hysteresis loops during dynamic loading phase (damping phase included for sim.F). At depth 17.5 m, 1 m from exterior pile wall. Colour shades indicate calculation points, from purple to yellow. $G_{s,N}/G_{s,1}$ is ratio of shear modulus between first cycle and cycle number N. Data from PLAXIS 2D plotted in MATLAB.

Considering the point further out from the exterior pile wall, i.e. 1 m from the pile wall and at depth 17.5 m, the secant shear modulus ratio ($G_{s,N}/G_{s,1}$) is relatively similar for both driving methods. However, $G_{s,1}$ is considerably lower during impact driving, compared to $G_{s,1}$ during vibratory driving. The shear modulus ratio during impact driving is 0.54 near the exterior pile wall and 0.50 at 1 m further out. During vibratory driving the ratios are 0.13 and 0.47 respectively. This may suggest that the rate of degradation of G_s in the soil decays to a larger degree for an increased distance from the driven pile during vibratory driving compared to impact driving.

Note that the secant shear modulus 1 m from the exterior pile wall during the last impact is

estimated to be lower than during the last cycle of vibratory driving. As previously pointed out, the evolution of p' in the same point may suggest a larger degree of liquefaction during vibratory driving compared to impact driving. The combination of having an indication of a larger degree of liquefaction for the p' graph and the less degradation of secant shear modulus at the last cycle may partly be due to the different method of estimating G_s of the last cycles, which is presented in Appendix C, and/or partly due to the considerably larger shear strain amplitude during the load cycles of impact driving, seen in Figure 7.14.

Table 7.1: Overview of interpreted secant shear modulus ratio between first cycle and cycle number N ($G_{s,N}/G_{s,1}$), for sim.A* and sim.F. From points at depth 17.5 m. Note that the method of estimating the secant shear modulus for the last cycle is different for vibratory and impact driving, see Appendix C.

	Vibratory driving (sim.A*)		Impact driving (sim.F)	
	near exterior pile wall	1 m from exterior pile wall	near exterior pile wall	1 m from exterior pile wall
$G_{s,1}$ [kPa]	26389.39	29789.88	9076.60	14892.53
$G_{s,7}$ [kPa]	-	-	4905.89	7428.22
$G_{s,7}/G_{s,1}$ [-]	-	-	0.54	0.50
$G_{s,39}$ [kPa]	3312.96	13986.06	-	-
$G_{s,39}/G_{s,1}$ [-]	0.13	0.47	-	-

An overview of the the estimated secant shear moduli during impact and vibratory driving at depth 17.5 m near and 1 m from the exterior pile wall are listed in Table 7.1.

Stress Path in $p' - \sigma_{xy}$ Space

Figure 7.14 shows the $p' - \sigma_{xy}$ stress paths for a point at depth 17.5 m, near the exterior pile wall, during vibratory driving (sim.A*) and impact driving (sim.F). The damping phase is additionally included in the stress path for the latter.

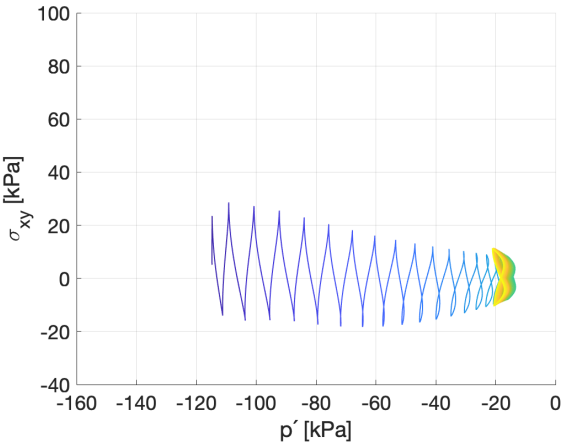

(a) sim.A* (vibro 23.33 Hz): 38.9 loading cycles.

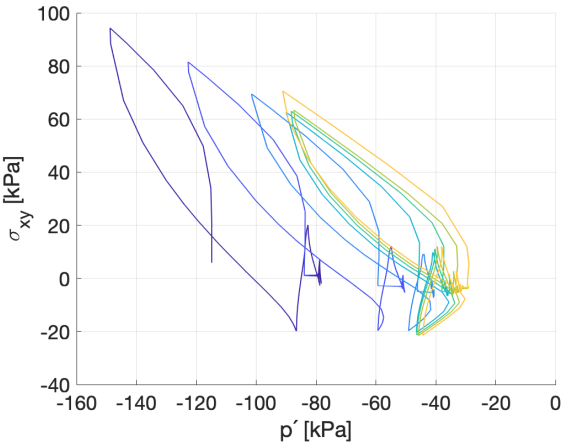

(b) sim.F (impact): 7 loading cycles.

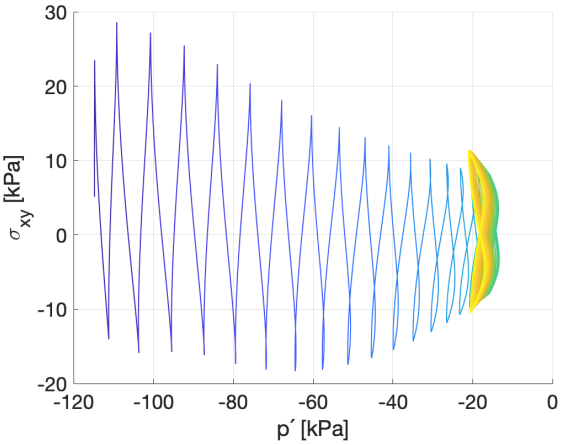

(c) sim.A* (vibro 23.33 Hz): 38.9 loading cycles.

Figure 7.15: sim.A* (vibro 23.33 Hz, 38.9 cycles) and sim.F (two graphs for sim.A*, one at same scale as sim.F for reference): stress path in $p' - \sigma_{xy}$ space during dynamic loading phase (damping phase included for sim.F). At depth 17.5 m, near the exterior pile wall. Colour shades indicate calculation points, from purple to yellow. Data from PLAXIS 2D plotted in MATLAB.

Note the difference in magnitude of both p' and σ_{xy} within each cycle between vibratory and impact driving. It may also be noted that the p' has a noticeable increase in pressure during the first loading cycle of impact driving, to a higher value than the one prior loading. The stress path during impact driving seem to indicate cyclic mobility already during the first cycle for positive values of σ_{xy}, and for both positive and negative values after the second or third loading cycle. It may be suggested that this cyclic mobility is also visible during the last cycles of the $\sigma'_{xy} - \gamma_{xy}$ loops seen in Figure 7.13b, by the slight increase of the slope (shear modulus) before load reversal. This may suggest that some

of the energy inflicted on the pile from the hammer is distributed over both contributions towards increasing and decreasing driving resistance during each impact, while during vibratory driving the slight indications of phase transformation occurs only after several cycles, and at a lower value for p' in pressure. This may indicate, for the point at depth 17.5 m near the exterior pile wall, that the vibratory driving method is a more energy efficient driving method in terms of a larger amount of the inflicted energy on the pile is dissipated into contributions towards reducing the driving resistance.

The $p' - \sigma'_{xy}$ paths at depth 17.5 m, near the exterior pile wall, during impact driving does not show as clear indications of a approaching a steady state during the 7 loading cycles compared to vibratory driving. Neither driving methods seem to cause full liquefaction ($p' = 0\,\text{kPa}$) of the sand at this depth near the exterior pile wall during the considered number of loading cycles with an initial void ratio in the soil equal to $e_{init} = 0.734$ and the particular flow parameters used as input for the soil. Based on a comparison between the stress paths in Figure 4.5, in Section 4.3, and the stress path during vibratory driving the sand may be suggested somewhere between medium dense and dense. The $p' - \sigma'_{xy}$ stress path at depth 17.5 m, near the exterior pile wall, during vibratory driving seem to almost solely exhibit a decreased pressure of p', possibly suggesting that the lack of cap hardening in the material model not being decisive of modelling the soil behaviour in this data point. During impact driving, however, the magnitude of p' is greater, and there is an increase of p' in pressure during the first two cycles to a value greater than the initial before loading. This may suggest that cap hardening is of importance for simulating soil behaviour during impact driving, since the possible plastic strains at large effective mean stresses in pressure are not simulated without this cap. This may, amongst others, lead to less settlement of the pile during each simulated impact of the hammer for the SANISAND material model used. Note, however, that the lack of cap hardening may affect also the simulated vibratory driving in other points of the soil not investigated, e.g. below the pile toe, during the loading phase.

Void Ratio after Consolidation

The void ratio after consolidation is presented in Figures 7.16 and 7.17 for sim.A* and sim.F respectively. Note that the scale for the colour shades may not include the extreme values in the plot, to increase the visibility of the other values. The plots are slightly zoomed in for better visualisation of the void ratio near the pile wall. The build-up of excess pore pressure is dissipated to an absolute value of maximum 1 kPa during consolidation. The consolidation phase lasts approximately 49.6 minutes and 32.4 minutes for sim.A* and sim.F respectively.

PLAXIS 2D Output allows plotting of state parameters, and number 7 is void ratio for the SANISAND implementation. There are slight differences between the void ratio from the state parameters and the void ratio from the standard void ratio plot through total strains. It may be suggested to be because of not selecting *Reset state variables* for the calculation phases in addition to the *Reset displacements to zero* and *Reset small strain*. The void ratio plotted here is the one obtained through the standard plotting of void ratio in PLAXIS, not through the state parameters of the user-defined soil model SANISAND.

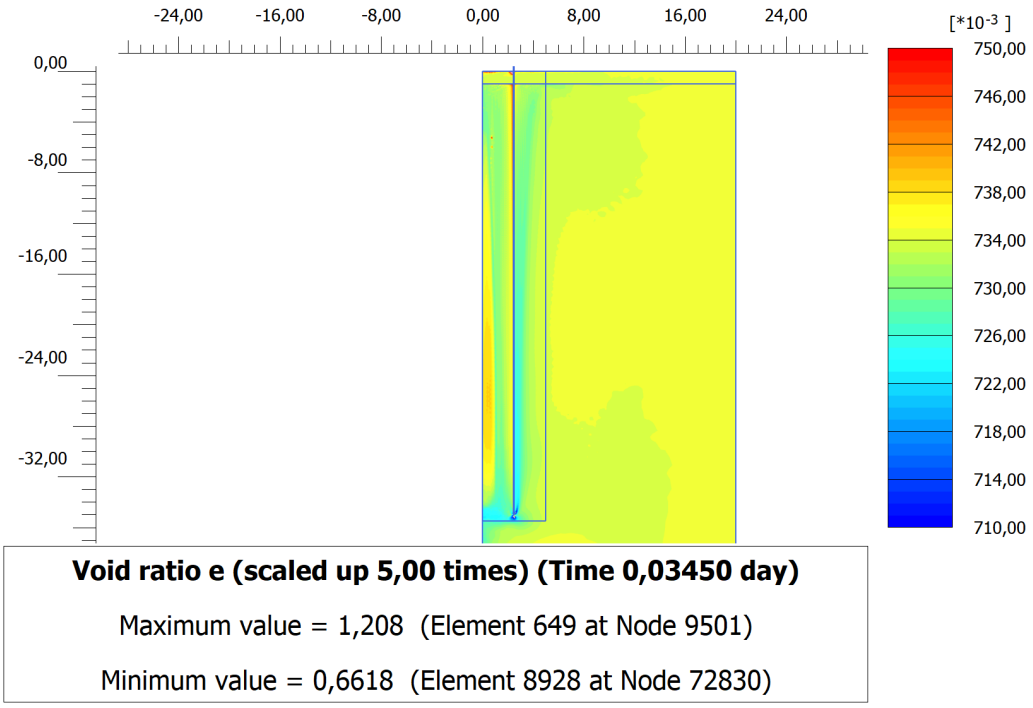

Figure 7.16: sim.A* (vibro 23.33 Hz, 38.9 cycles): contour plot of void ratio in soil at the end of consolidation phase. $e_{init} = 0.734$. File exported from PLAXIS 2D Output.

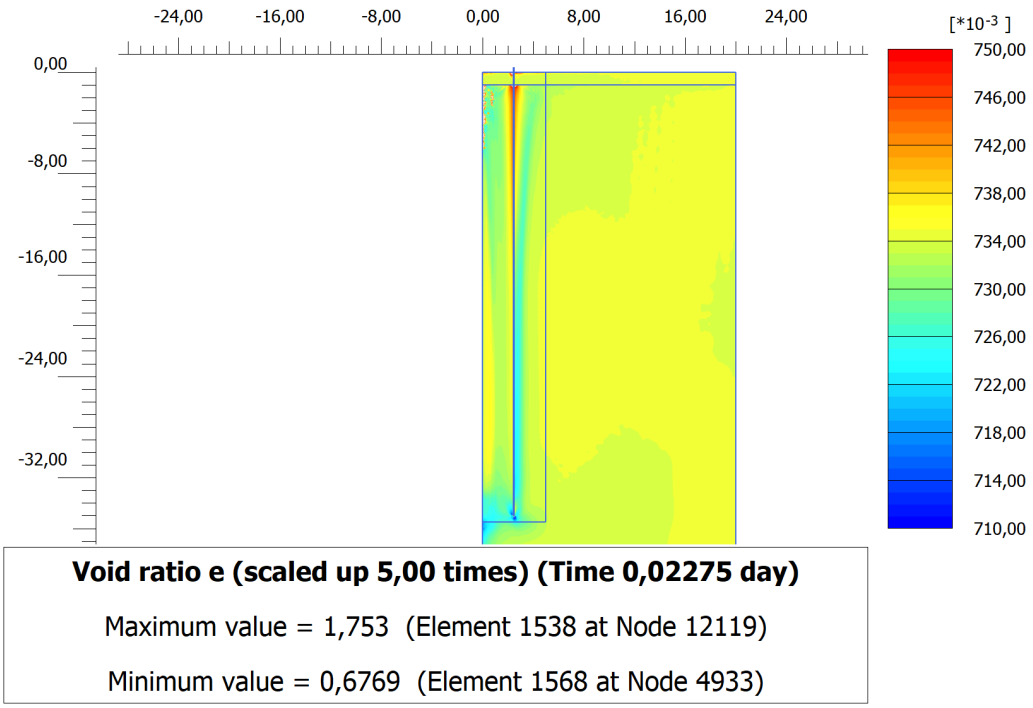

Figure 7.17: sim.F (impact): contour plot of void ratio in soil at the end of consolidation phase. $e_{init} = 0.734$. File exported from PLAXIS 2D Output.

The contour plots showing void ratio after consolidation indicate a relatively small change of void ratio compared to the initial value ($e_{init} = 0.734$). This could partly be due to the relatively short time of pile driving simulated, since an increased pile driving duration might lead to a generally greater increase in excess pore pressures throughout the model. It may additionally be due to the absence of cap hardening in the soil model. However, both vibratory and impact driving seem to indicate the same tendency of a lower void ratio (compaction) near the exterior pile wall, especially at the middle and lower part of the pile. Loosening is seen near the upper part of the exterior pile wall and along the interior pile wall in both simulations. However, the contour plot of impact driving shows a larger loosening at the upper part of the pile, both at the interior and exterior pile wall, compared to vibratory driving.

Effective Cartesian Stresses

The effective Cartesian stresses (σ'_{xx}, σ'_{yy} and σ'_{zz}) after consolidation are presented for both sim.A* and sim.F in the contour plots of Figures 7.18 to 7.22. Note that the scale of the shades may not include the extreme values of the stresses, and is due to better visibility for the stress values between the extremes. The stress states at plastic nil-phase, i.e. before dynamic loading phase, of the effective Cartesian stresses may be found in Appendix A.3.

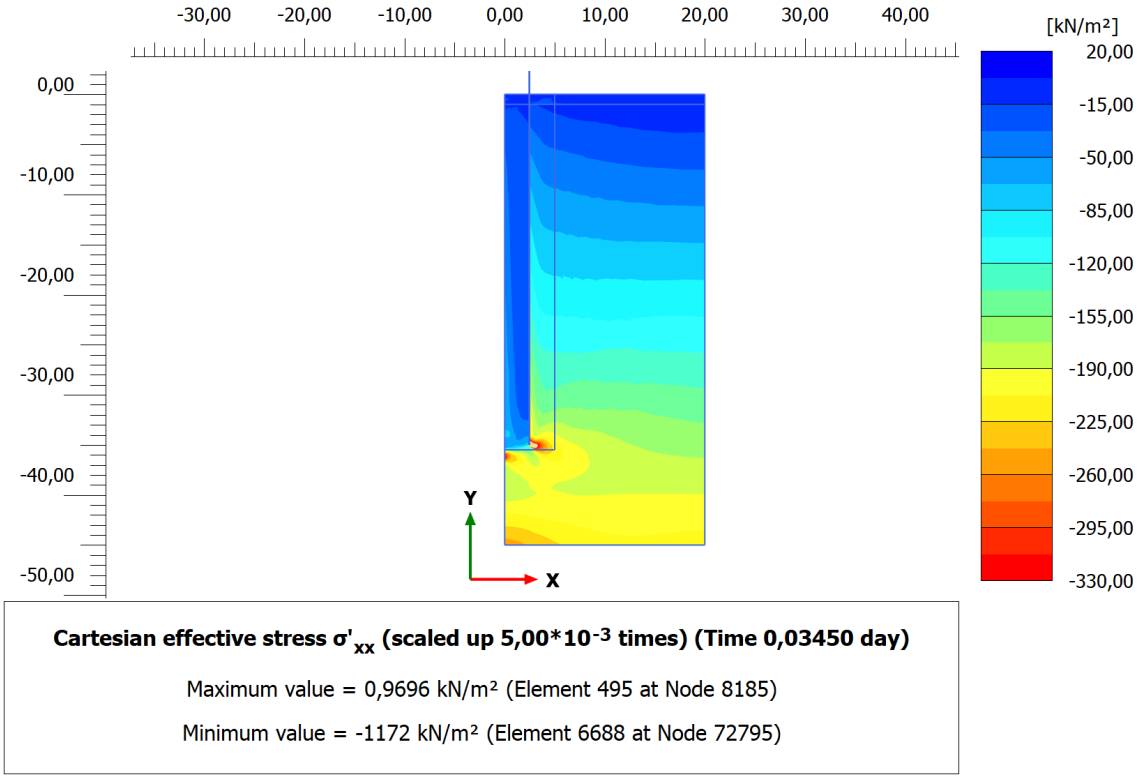

Figure 7.18: sim.A* (vibro 23.33 Hz, 38.9 cycles): σ'_{xx} contour plot of soil at the end of consolidation phase. File exported from PLAXIS 2D Output.

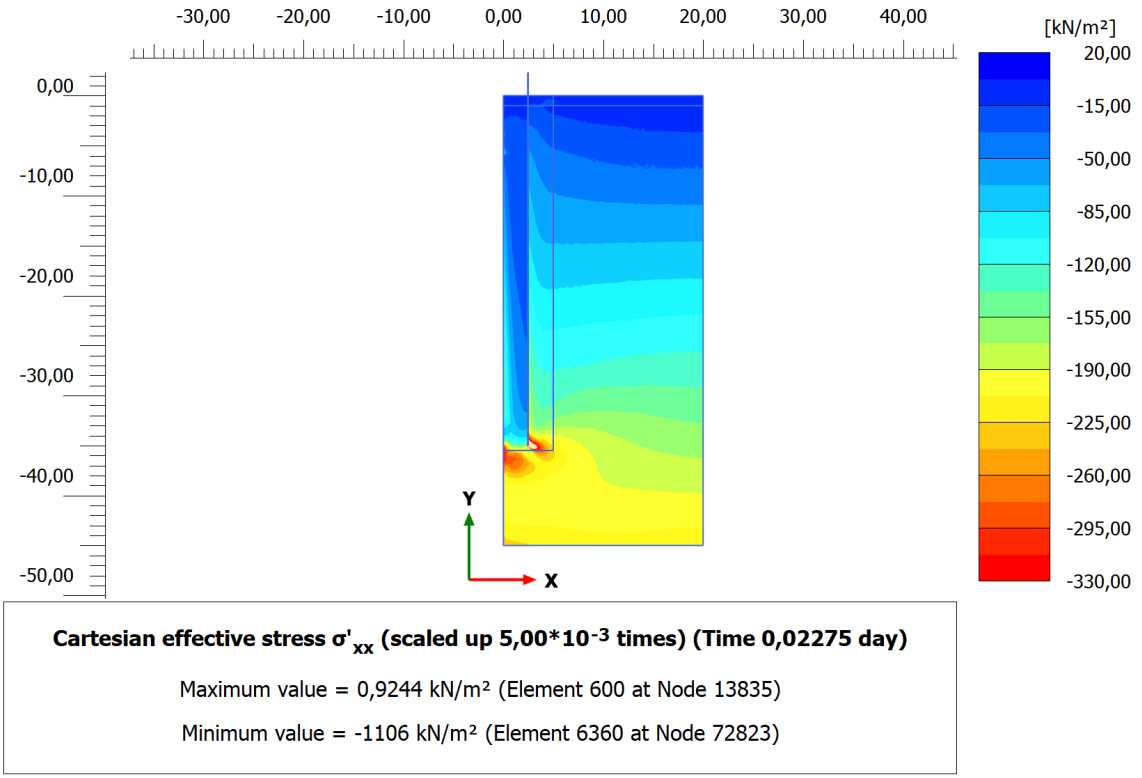

Figure 7.19: sim.F (impact): σ'_{xx} contour plot of soil at the end of consolidation phase. File exported from PLAXIS 2D Output.

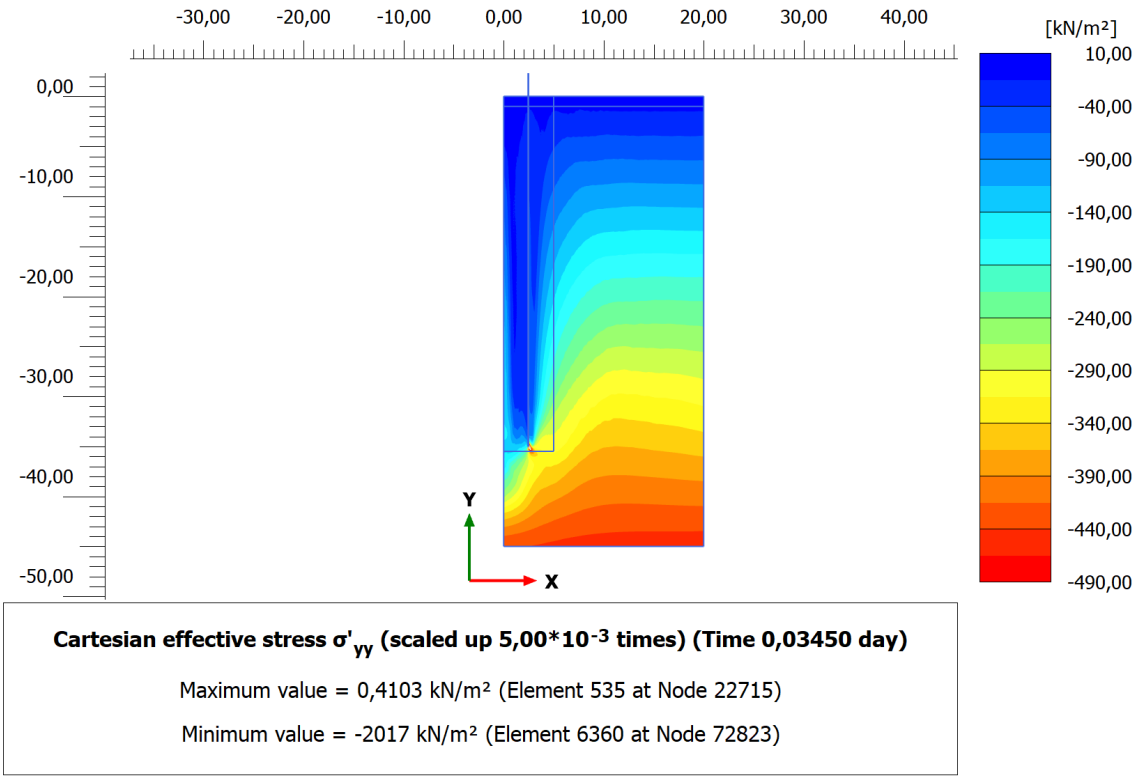

Figure 7.20: sim.A* (vibro 23.33 Hz, 38.9 cycles): σ'_{yy} contour plot of soil at the end of consolidation phase. File exported from PLAXIS 2D Output.

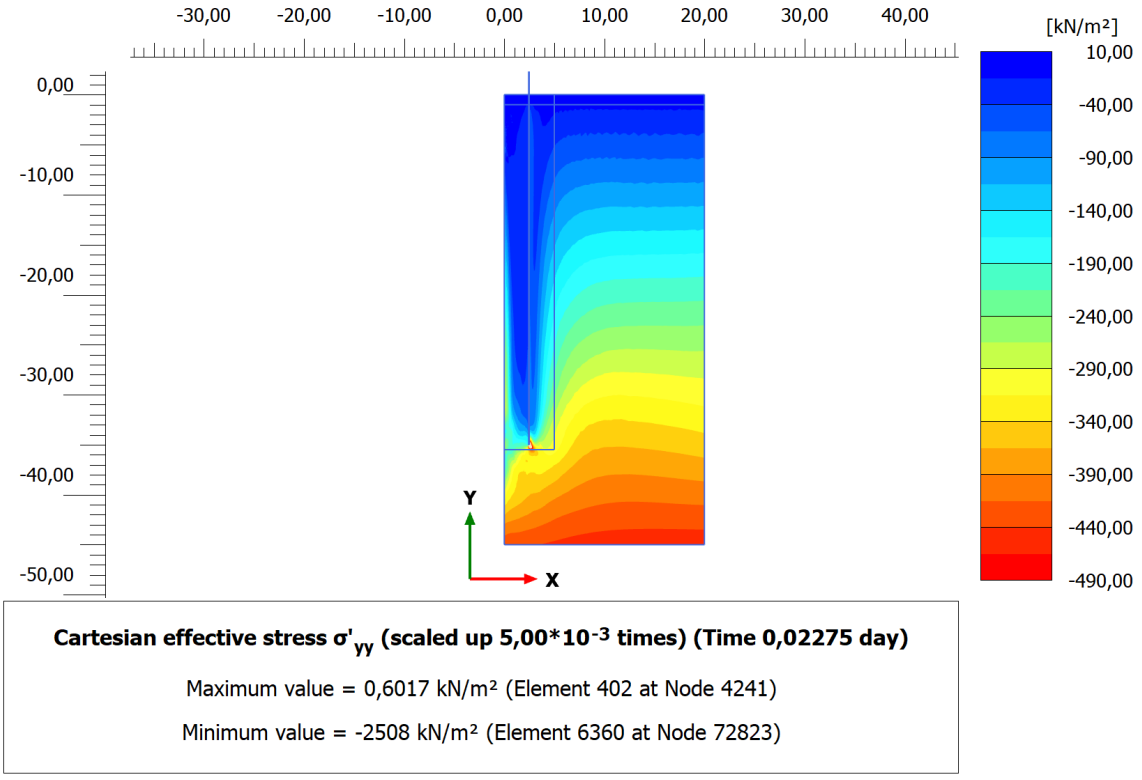

Figure 7.21: sim.F (impact): σ'_{yy} contour plot of soil at the end of consolidation phase. File exported from PLAXIS 2D Output.

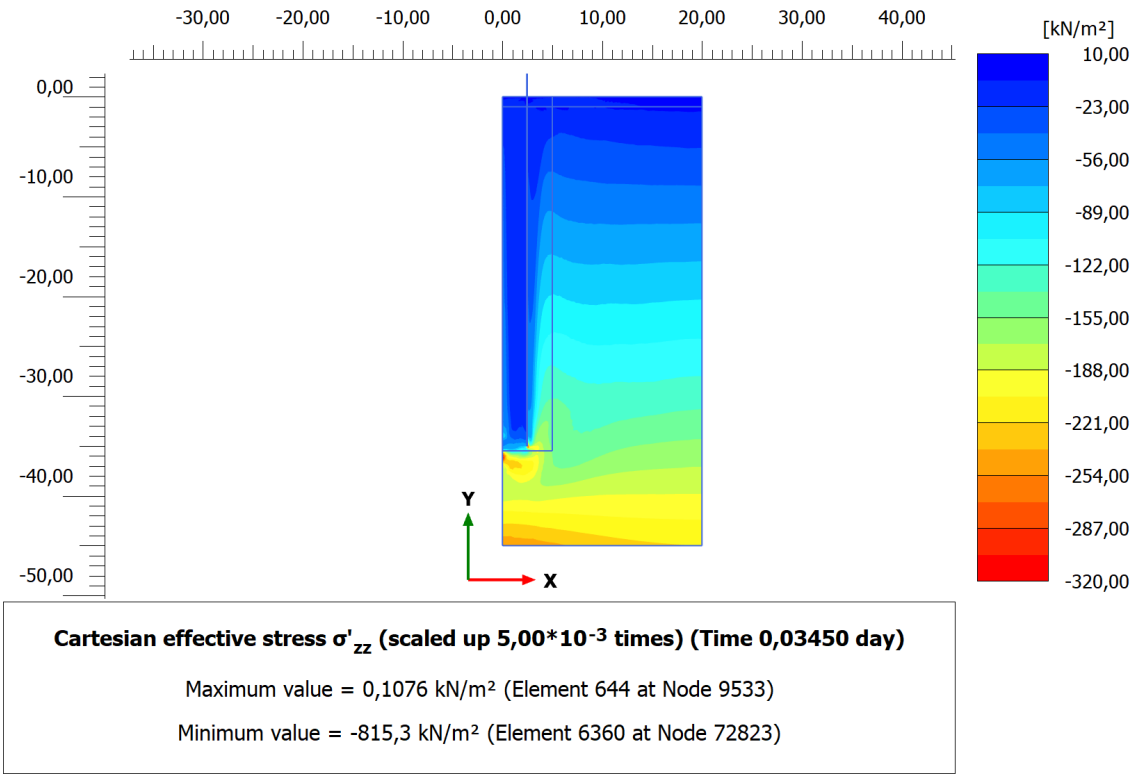

Figure 7.22: sim.A* (vibro 23.33 Hz, 38.9 cycles): σ'_{zz} contour plot of soil at the end of consolidation phase. File exported from PLAXIS 2D Output.

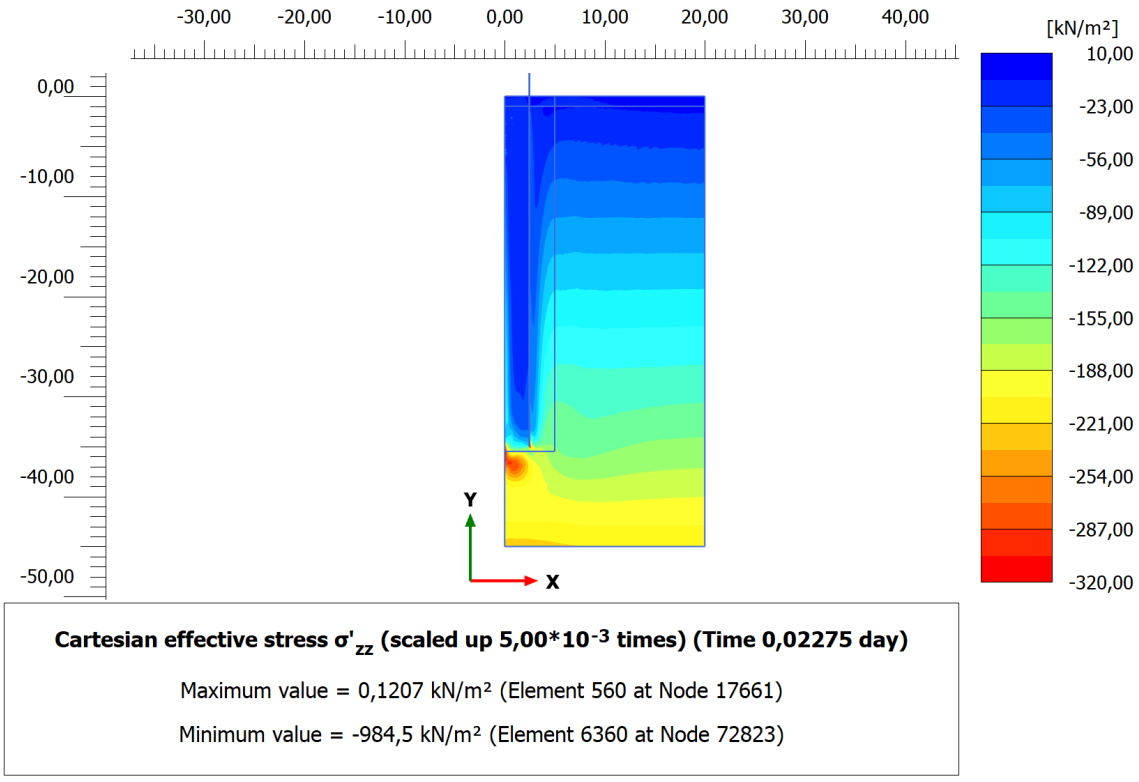

Figure 7.23: sim.F (impact): σ'_{zz} contour plot of soil at the end of consolidation phase. File exported from PLAXIS 2D Output.

The contour plots showing the effective vertical stress (σ'_{yy}) after consolidation suggest a significant decrease of pressure, compared to before dynamic loading phase, near both the interior and exterior pile wall after both vibratory and impact driving. This may indicate that the pile carries a considerable portion of the vertical effective stresses, which at the interior of the pile may indicate the presence of a soil plug. This may partly be a result of not modelling interface elements. The same tendency of reduced pressure near the exterior pile wall is seen for σ'_{zz}, after both driving methods. σ'_{zz} may be interpreted as the effective hoop stress of the soil, due to the axisymmetric model. The contour plots of σ'_{xx} indicate, on the other hand, a noticeable increase in pressure near the pile wall for both driving methods. σ'_{xx} may be interpreted as the effective radial stresses.

The evolution of the effective Cartesian stresses during dynamic loading, damping and consolidation phases at depth 17.5 m, near the exterior pile wall, are plotted against a logarithmic time scale for vibratory (sim.A*) and impact driving (sim.F) in Figures 7.24 and 7.25 respectively. Note the coincident of σ'_{xx} and σ'_{yy} during the last part of the dynamic loading phase of vibratory driving.

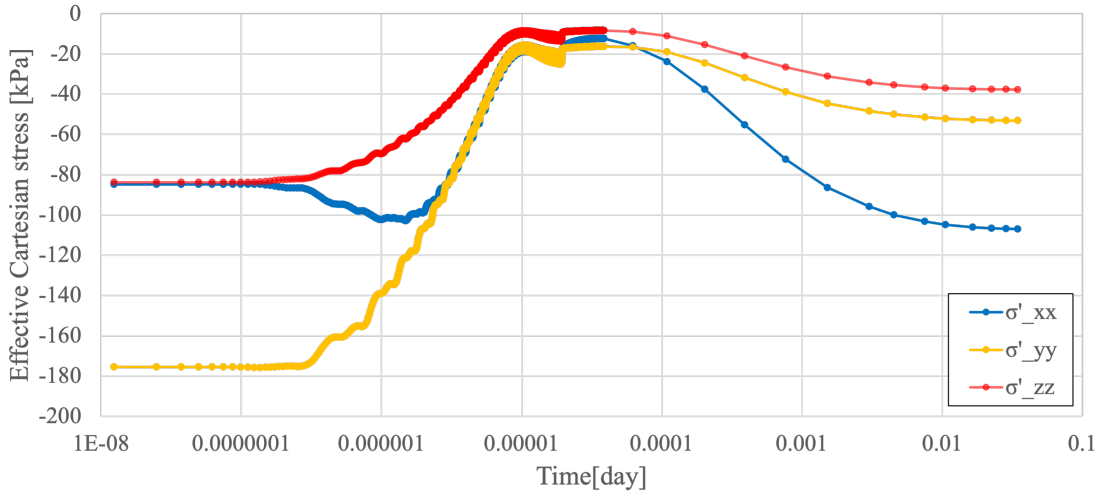

Figure 7.24: sim.A* (vibro 23.33 Hz, 38.9 cycles): Effective Cartesian stresses during loading, damping and consolidation phases against a logarithmic time scale. At depth 17.5 m, near exterior pile wall. Initiation of consolidation phase is indicated by the increased horizontal spacing between calculation points. Data from PLAXIS 2D plotted in Excel.

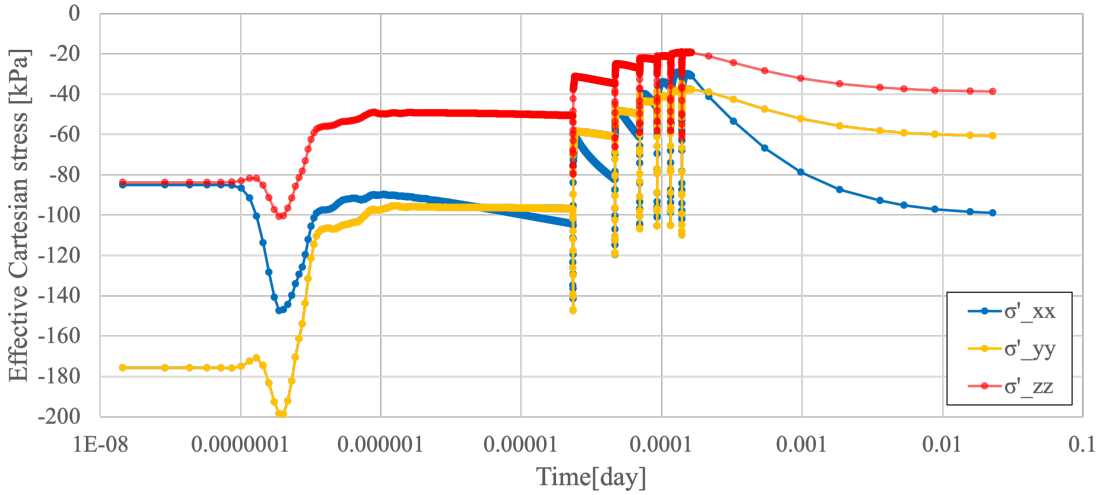

Figure 7.25: sim.F (impact): Effective Cartesian stresses during loading, damping and consolidation phases against a logarithmic time scale. At depth 17.5 m, near exterior pile wall. Initiation of consolidation phase is indicated by the increased horizontal spacing between calculation points. Data from PLAXIS 2D plotted in Excel.

It is seen that σ'_{xx} and σ'_{yy} coincides after a certain number of cycles during vibratory driving, approaching the same pressure before damping and consolidation is initiated. This indicates a ratio close to 1 between the effective radial and vertical stresses during the last part of the loading phase. Figure 7.24 also shows the increase of σ'_{xx} during consolidation to a noticeably larger pressure compared to initial value. The reason for this increased effective radial stress near the exterior pile wall is currently uncertain. However, it could be suggested that during consolidation the soil tries to contract towards the axisymmetric line, but due to the presence of the significantly stiffer pile this is to a large degree prevented, increasing the pressure on the exterior pile wall from the soil. This may possibly also explain the reason for the compaction of the soil seen along the middle and upper part of the exterior pile wall. Figure 7.25 shows the evolution of the effective Cartesian stresses, in the same point of the soil, but for impact driving. The same tendencies are seen for this driving method regarding a larger value for σ'_{xx} in pressure after consolidation compared to initial value, and that both σ'_{yy} and σ'_{zz} regains only parts of the initial pressure during consolidation.

Effective Principal Stress Directions

Figures 7.26 and 7.27 show the contour plot of the centre principal stress directions near the pile wall at the centre of the embedded length of the pile (depth 17.5 m). The longest line in each cross visualise the direction of σ'_1 while the perpendicular and shorter cross visualises σ'_3. Note that the lines in a cross may also be of almost equal length, hence $\sigma'_1 \approx \sigma'_3$. *Centre* effective principal stress directions indicates values at the soil element centre, and is selected to plot fewer points for better visibility.

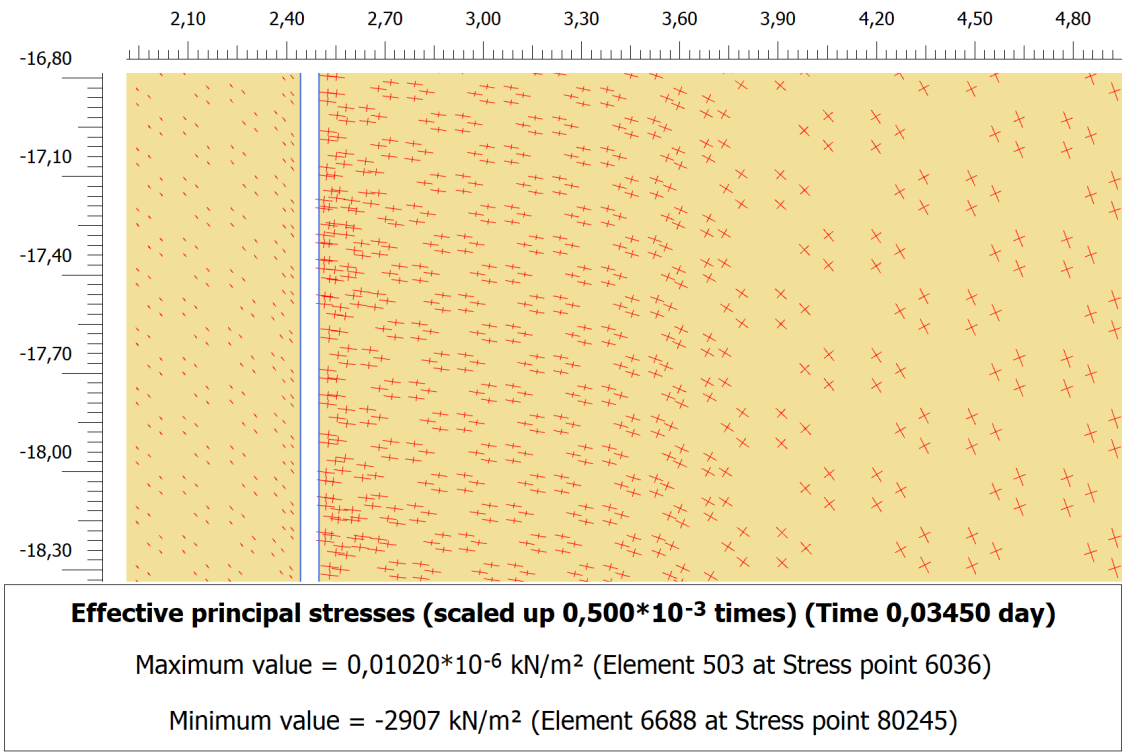

Figure 7.26: sim.A* (vibro 23.33 Hz, 38.9 cycles): Centre effective principal stress directions contour plot of soil at the end of consolidation phase. Zoomed in at pile wall at depth 17.5 m. File exported from PLAXIS 2D Output.

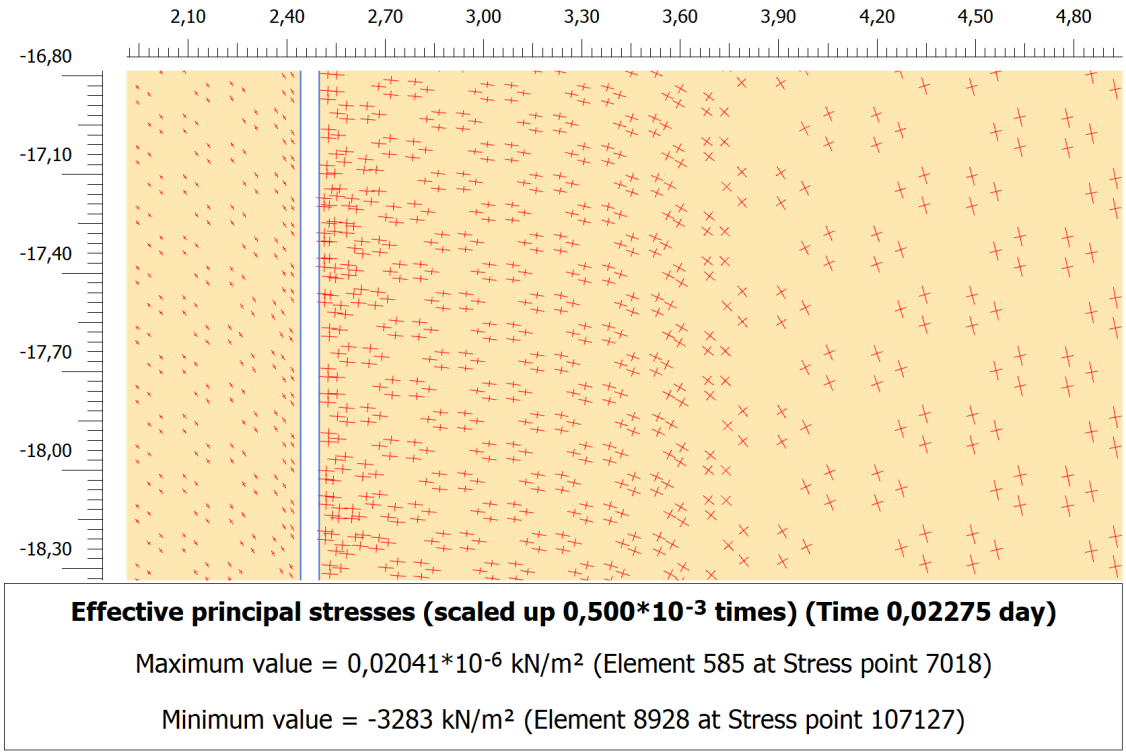

Figure 7.27: sim.F (impact): Centre effective principal stress directions contour plot of soil at the end of consolidation phase. Zoomed in at pile wall at depth 17.5 m. File exported from PLAXIS 2D Output.

Figures 7.26 and 7.27 indicate that the direction of σ'_1, at depth 17.5 m, is rotated from an initially approximately vertical direction to perpendicular to the exterior pile wall after consolidation for both driving methods. This may suggest that a large part of the dissipated excess pore pressure is regained in the effective radial stresses. The contour plots showing the centre effective principal stress directions at depth 3 m and at pile toe may be found in Appendix A.4.

The vertical displacements of the top of the pile shown in Figure 7.2 suggest both driving methods reach an approximately similar settlement before consolidation begins. Vibratory driving reaches this depth at a significantly faster time, suggesting a shorter installation time for this method, which is also suggested in the literature (see e.g. Section 1.1). The presented results and the following interpretation and discussion may suggest this faster installation time to be attributed the higher rate of shear modulus degradation, and higher rate of reduction of p' in pressure, near the exterior pile wall. However, the absence of cap hardening in the model may be suggested to affect the permanent settlement of the pile after each impact during impact driving, to a larger degree than vibratory driving, based on the previous discussion of the $p' - \sigma_{xy}$ stress path at depth 17.5 m near the exterior pile wall.

7.2 Vibratory Driving: Effect of Lower Driving Frequency with Associated Smaller Load Amplitude

sim.A is the base simulation, with a driving frequency of 23.33 Hz. sim.B and sim.C have a driving frequency of 18 Hz and 12 Hz respectively, and the load amplitudes are estimated based on the driving frequencies. See e.g. Equation 2.9 in Section 2.3 for this relation. Hence, the three simulations all have different load amplitudes associated to the frequencies. The combination of sim.A, sim.B and sim.C may replicate the start-up of vibratory pile driving, since the rotating masses needs to start at a frequency of 0 Hz and accelerate to reach the desired driving frequency (e.g. 23.33 Hz, sim.A).[19] 20 load cycles are simulated for all three simulations.

Vertical Displacement of the Top of the Pile During Loading, Damping and Consolidation Phases

The vertical displacement of the top of the pile during loading, damping and consolidation phases is plotted against a logarithmic time scale, shown in Figure 7.28.

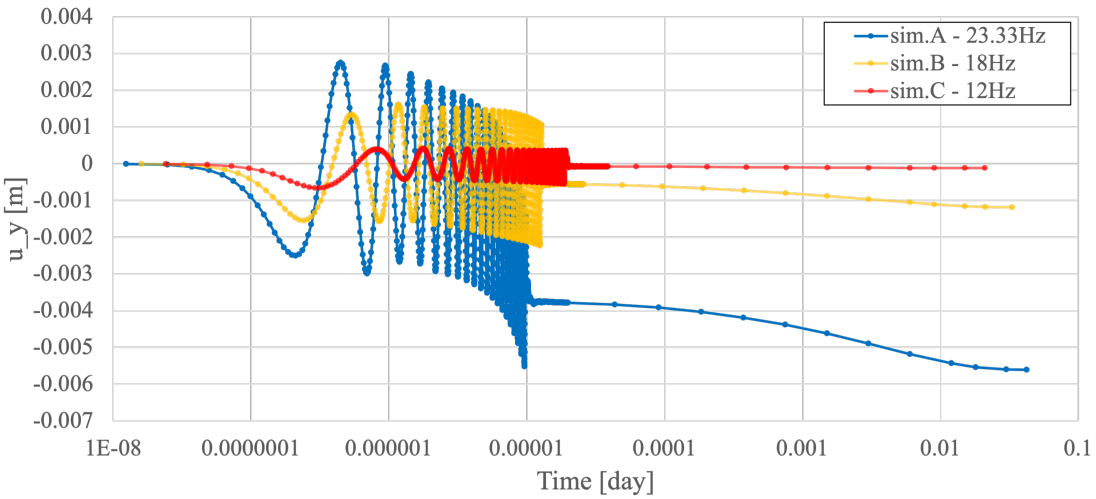

Figure 7.28: sim.A, sim.B and sim.C (vibro 23.33-, 18- and 12 Hz respectively): vertical displacement of top of the pile during loading, damping and consolidation phases against a logarithmic time scale. Initiation of consolidation phase is indicated by the increased horizontal spacing between calculation points. Data from PLAXIS 2D plotted in Excel.

Note that vibratory driving at 12 Hz (sim.C) shows almost no vertical settlement after consolidation compared to prior the loading phase, seen in Figure 7.28. The pile settlement is considerably larger during driving at 23.33 Hz compared to 18 Hz, and the difference is greater than the different settlement between 18 Hz and 12 Hz. The dependency between simulated pile penetration and driving frequency, with associated load amplitude, may therefore be suggested to be non-linear.

[19] Unless the vibratory hammer is equipped with variable moments, as discussed in Section 2.3.

Excess Pore Pressure

Figures 7.29, 7.30 and 7.31 show the contour plots of excess pore pressure (p_{excess}) at the end of the dynamic loading phase for sim.A, sim.B and sim.C respectively.

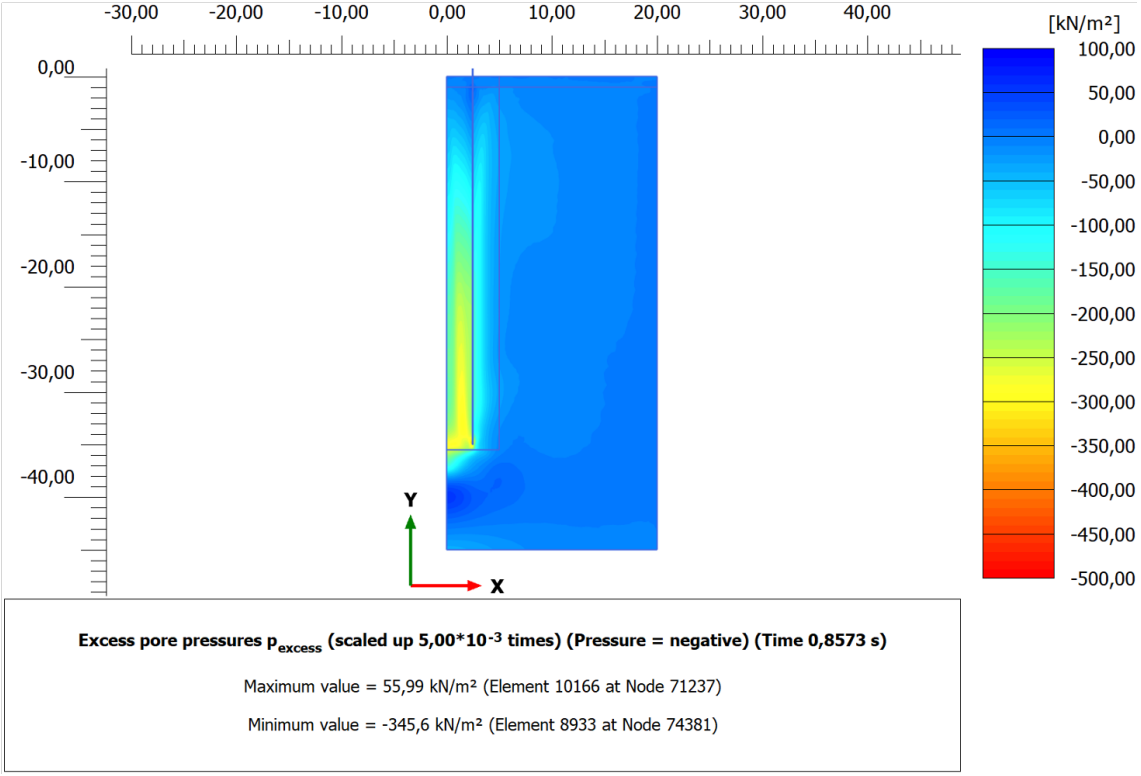

Figure 7.29: sim.A (vibro 23.33 Hz): p_{excess} contour plot of soil at the end of dynamic loading phase. File exported from PLAXIS 2D Output.

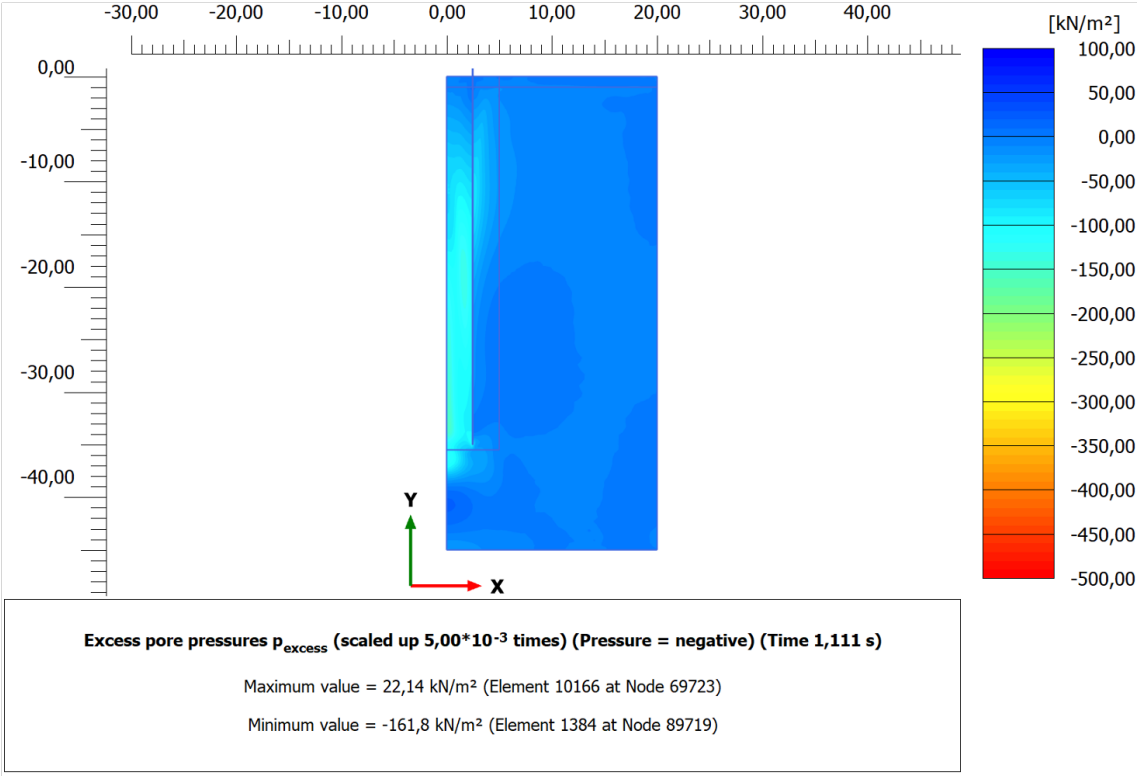

Figure 7.30: sim.B (vibro 18 Hz): p_{excess} contour plot of soil at the end of dynamic loading phase. File exported from PLAXIS 2D Output.

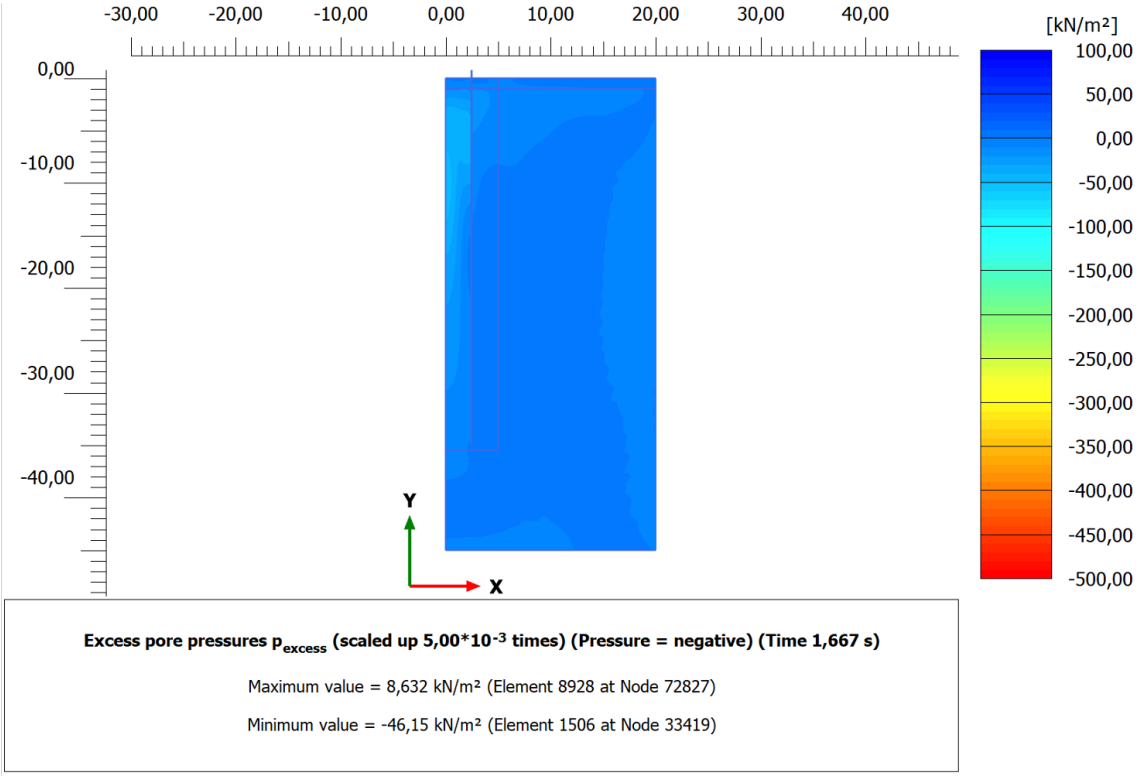

Figure 7.31: sim.C (vibro 12 Hz): p_{excess} contour plot of soil at the end of dynamic loading phase. File exported from PLAXIS 2D Output.

The evolution of p_{excess} in a point at the centre of the embedded pile length (depth 17.5 m) near the exterior pile wall is shown in Figure 7.32.

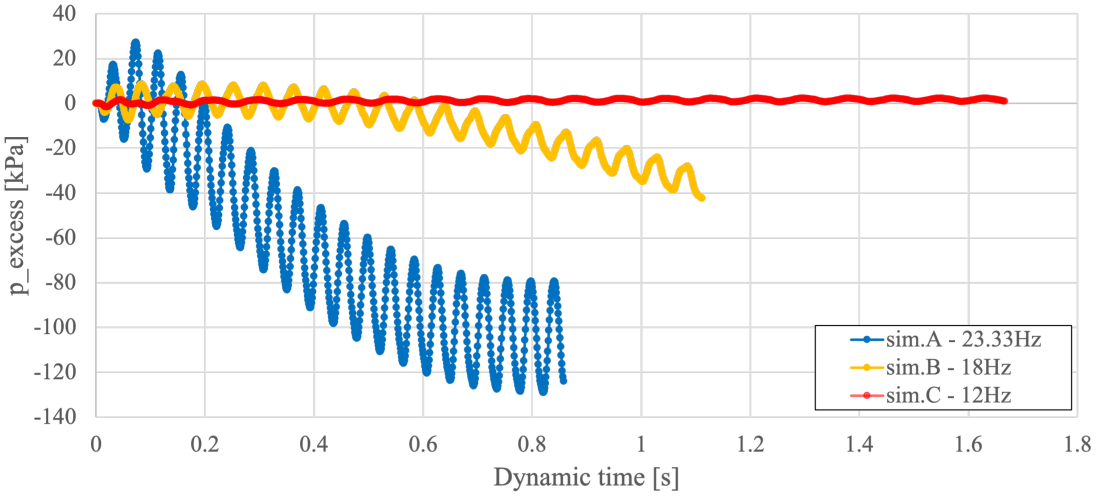

Figure 7.32: sim.A, sim.B and sim.C (vibro 23.33-, 18- and 12 Hz respectively): p_{excess} during dynamic loading phase. At depth 17.5 m, near exterior pile wall. Data from PLAXIS 2D plotted in Excel.

Figure 7.32 indicates a clear difference in evolution of excess pore pressure for the different driving frequencies with associated different load amplitudes. Note that by the end of driving of with 23.33 Hz the excess pore pressure seem to approach a steady-state during the dynamic time considered. In the point at depth 17.5 m, near the exterior pile wall, p_{excess} during driving at 12 Hz seems to fluctuate around 0 kPa, indicating close to zero excess pore pressure build-up. The contour plot in Figure 7.30 suggests a noticeable build-up of p_{excess} during driving at 18 Hz, which is also seen in the point near the exterior pile wall at depth 17.5 m (Figure 7.32). This may suggest that the threshold of excess pore pressure build-up lies between the frequency of 12-18 Hz for the simulated soil condition and the other vibratory hammer parameters considered. Determining this threshold could be of interest if it is desirable to drive a pile at a relatively low frequency. As presented in Section 4.4, the review of the results presented by Achmus et al. (2020) suggests the vibratory driven pile to be driven at both 15 Hz and 22.5 Hz to to have a stiffer response to lateral loading compared to the piles vibratory driven at 22.5 Hz, however, note that these results are related to the given soil conditions at that given site. If it is desirable to minimise the installation time, the graph showing the vertical displacement of the top of the pile (Figure 7.28) evidently suggests the most favourable frequency to be 23.33 Hz. Note, however, that this is limited to the soil condition and duration of pile driving simulated.

The contour plots of p_{excess} after driving at 23.33 Hz (sim.A) and at 18 Hz (sim.B) show a larger generation of excess pore pressure at the internal of the pile compared to the soil at the vicinity of the external pile wall. Shear waves from the vibrating pile propagate towards the axisymmetric line, from the internal pile wall at all radial directions. This may lead to an increased amount of shearing, compared to at the external of the pile, at

which the waves are propagating outwards over an increased area, leading to damping of the waves. This, in addition to the possibility of reduced water dissipation during driving at the internal of the pile, due to impermeable pile walls, may possibly be part of the reason for the increased p_{excess} internally of the pile.

Effective Mean Stress

The effective mean stress (p') is plotted for the same point as p_{excess} in Figure 7.32 (depth 17.5 m, near the exterior pile wall), and is shown in Figure 7.33.

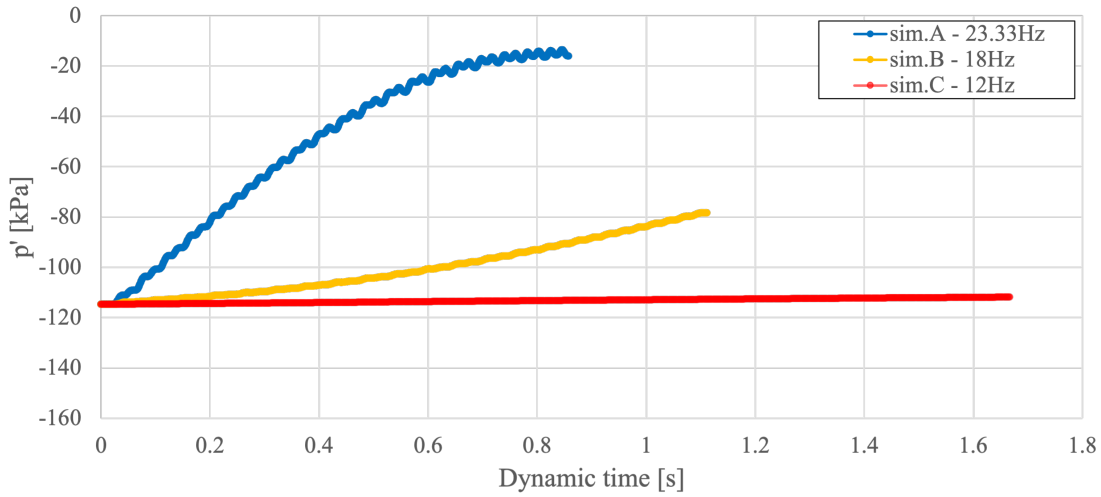

Figure 7.33: sim.A, sim.B and sim.C (vibro 23.33-, 18- and 12 Hz respectively): p' during dynamic loading phase. At depth 17.5 m, near exterior pile wall. Data from PLAXIS 2D plotted in Excel.

In the point at depth 17.5 m, near the exterior pile wall, the values of p' are initially similar for the three simulations, but is reduced to a considerably lower pressure during driving at 23.33 Hz compared to 12- and 18 Hz. This indicates a considerably larger degree of liquefaction in this point during driving at 23.33 Hz, with the associated load amplitude. The magnitude of p', at the same point in the soil, during driving at 12 Hz remains relatively unaffected throughout the vibratory driving.

Cartesian Shear Strains During Driving

Figures 7.34, 7.35 and 7.36 show the total Cartesian shear strains (γ_{xy}) during the dynamic loading phase of sim.A, sim.B and sim.C respectively. Note the different scale in y-direction for the graphs.

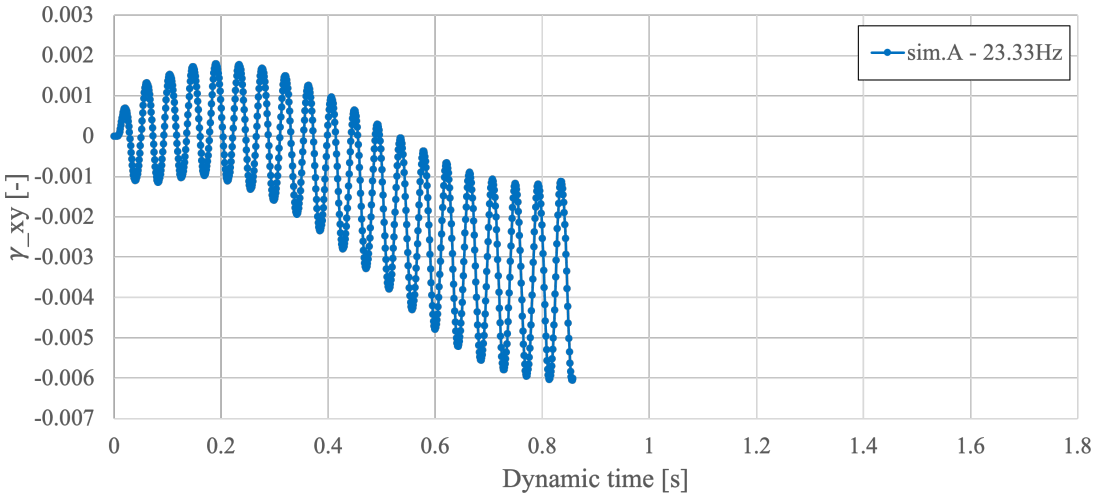

Figure 7.34: sim.A (vibro 23.33 Hz): Cartesian shear strain (γ_{xy}) during dynamic loading phase. At depth 17.5 m, near exterior pile wall. Data from PLAXIS 2D plotted in Excel.

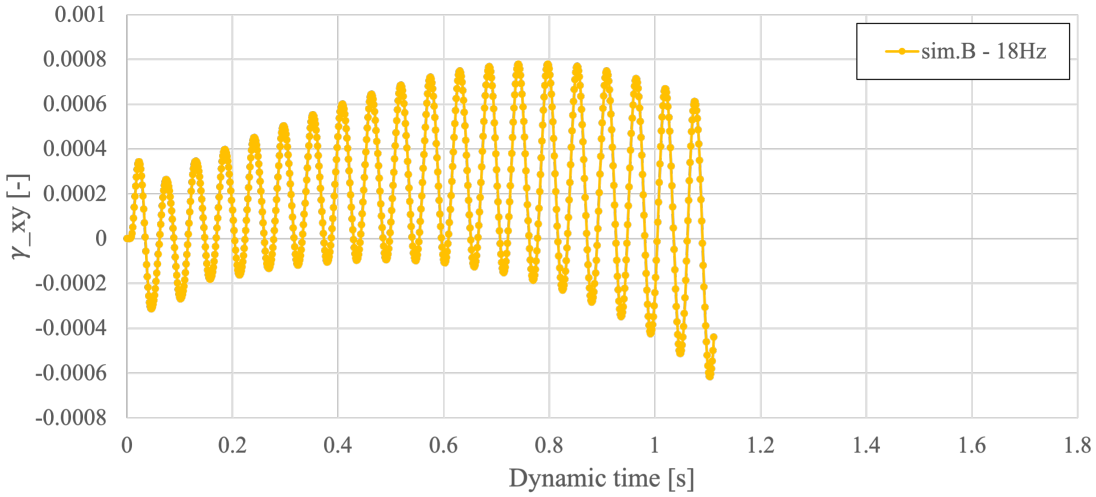

Figure 7.35: sim.B (vibro 18 Hz): Cartesian shear strain (γ_{xy}) during dynamic loading phase. At depth 17.5 m, near exterior pile wall. Data from PLAXIS 2D plotted in Excel.

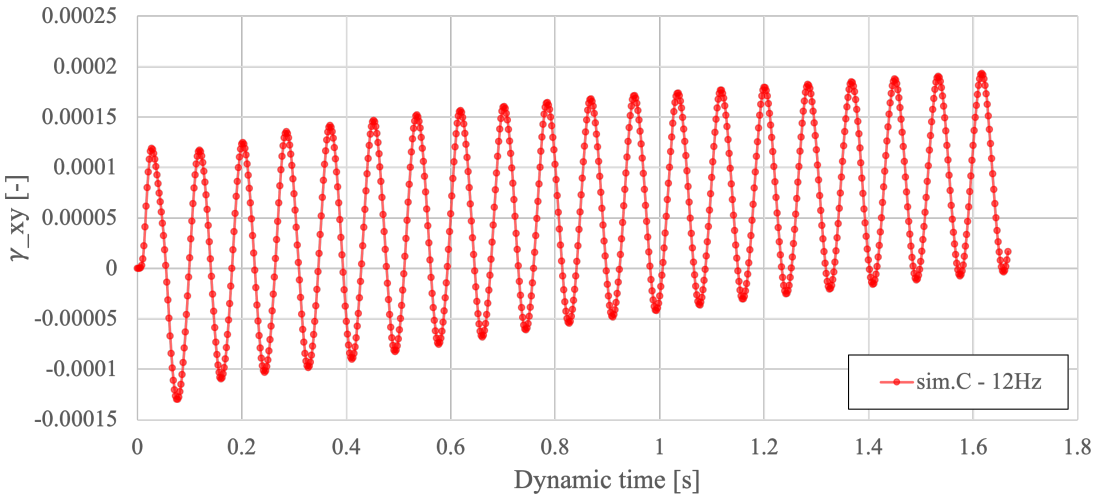

Figure 7.36: sim.C (vibro 12 Hz): Cartesian shear strain (γ_{xy}) during dynamic loading phase. At depth 17.5 m, near exterior pile wall. Data from PLAXIS 2D plotted in Excel.

The amplitude of the Cartesian shear strains (γ_{xy}) at depth 17.5 m, near the exterior pile wall, during driving at 12 Hz seem to fluctuate with an amplitude between approximately $1-1.25\cdot10^{-4}$, seen in Figure 7.36, while the shear strains during driving at 18 Hz seem to fluctuate with an amplitude in the range of approximately $3-6\cdot10^{-4}$, seen in Figure 7.35. Therefore, based the threshold for excess pore pressure build-up seemingly being between driving at 12- and 18 Hz, the simulated cyclic threshold amplitude of γ_{xy} could be suggested to lie between these two ranges of shear strain amplitudes. This could be in compliance with the suggested cyclic threshold shear strain amplitude of $\gamma_{c,t} \approx 1\cdot10^{-4}$ for a water-saturated sand (Dobry et al., 1982).

$\sigma_{xy} - \gamma_{xy}$ Hysteresis Loops

The shear stress (σ_{xy}) and shear strain (γ_{xy}) hysteresis loops are plotted for the point at depth 17.5 m near the exterior pile wall. The slope of the loops visualises the evolution of shear modulus (G) during the dynamic loading phase. The hysteresis loops indicate start of the dynamic loading by the colour purple and evolves to yellow during the dynamic loading.

The secant shear modulus ratio between first cycle and cycle number N ($G_{s,N}/G_{s,1}$) is interpreted by the one-way amplitudes for the first cycle while by the last two-way amplitudes for cycle number N. This method of interpretation is presented in Appendix C.

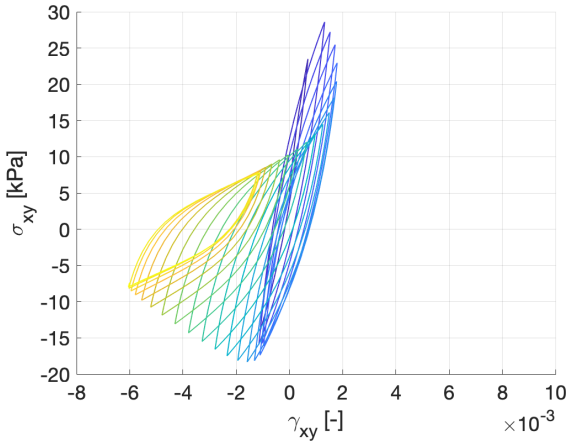

(a) sim.A (vibro 23.33 Hz): 20 loading cycles. $G_{s,20}/G_{s,1} = 0.12$.

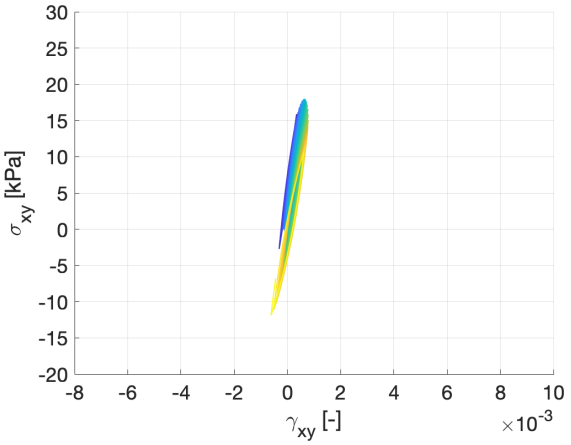

(b) sim.B (vibro 18 Hz): 20 loading cycles. $G_{s,20}/G_{s,1} = 0.59$.

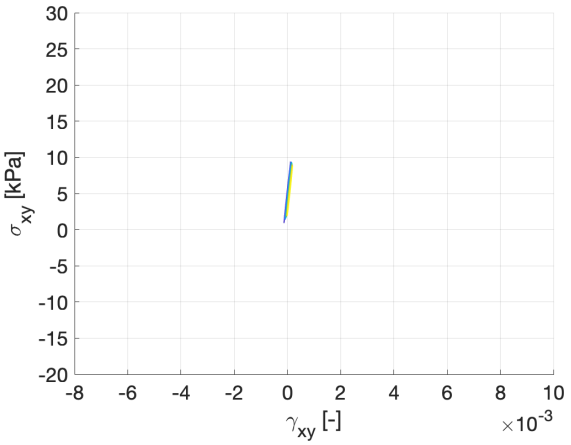

(c) sim.C (vibro 12 Hz): 20 loading cycles. $G_{s,20}/G_{s,1} = 0.96$.

Figure 7.37: sim.A, sim.B and sim.C (vibro 23.33-, 18- and 12 Hz respectively): $\sigma_{xy} - \gamma_{xy}$ hysteresis loops during dynamic loading phase. At depth 17.5 m, near exterior pile wall. Colour shades indicate calculation points, from purple to yellow. $G_{s,N}/G_{s,1}$ is ratio of shear modulus between first cycle and cycle number N. Data from PLAXIS 2D plotted in MATLAB.

The $\sigma_{xy} - \gamma_{xy}$ hysteresis loops of data from the point at depth 17.5 m, near the exterior pile wall, during driving at 12 Hz (sim.C) suggest a close to linear cyclic behaviour, with a secant shear modulus ratio of 0.96. The ratio during driving at 18 Hz and 23.33 Hz are interpreted to 0.59 and 0.12 respectively. This suggests a considerably higher rate of secant shear modulus degradation during driving at 23.33 Hz compared to driving at 18 Hz and 12 Hz. This may be suggested in compliance with the seemingly higher pile penetration rate during driving at 23.33 Hz, seen in Figure 7.28.

Table 7.2: Overview of interpreted secant shear modulus ratio between first cycle and cycle number N ($G_{s,N}/G_{s,1}$), for sim.A, sim.B and sim.C (vibro 23.33-, 18- and 12 Hz respectively). From point at depth 17.5 m, near exterior pile wall.

	Vibratory driving		
	sim.A	sim.B	sim.C
$G_{s,1}$ [kPa]	26389.00	31336.48	36215.96
$G_{s,20}$ [kPa]	3192.06	18345.51	34707.82
$G_{s,20}/G_{s,1}$ [-]	0.12	0.59	0.96

An overview of the interpreted secant shear moduli during sim.A, sim.B and sim.C at depth 17.5 m near the exterior pile wall are listed in Table 7.2. It may be noted that the higher frequencies, with associated larger load amplitudes, show a lower secant shear stiffness already at the first cycle. Note also that during 20 load cycles of driving with 12 Hz (sim.C) there is relatively little secant shear modulus degradation (secant shear modulus ratio close to 1.0).

7.3 Vibratory Driving: Effect of Lower Driving Frequency with Similar Load Amplitude

To evaluate the effect of altering the driving frequency on the soil behaviour, sim.D simulates vibratory driving with a frequency of 12 Hz while the load amplitude is equal the one driving at 23.33 Hz (sim.A). This is a modification is made for comparative purposes, since the vibratory hammer selected may not produce the same load amplitude for two different driving frequencies due to the direct relation between driving frequency and load amplitude, unless the sum of eccentric moments for the hammer is additionally altered (see e.g. Equation 2.9 in Section 2.3). Both sim.A and sim.D simulates 20 load cycles.

Vertical Displacement of the Top of the Pile During Loading, Damping and Consolidation Phases

The vertical displacement of the top of the pile during loading, damping and consolidation phases is plotted against a logarithmic time scale, shown in Figure 7.38.

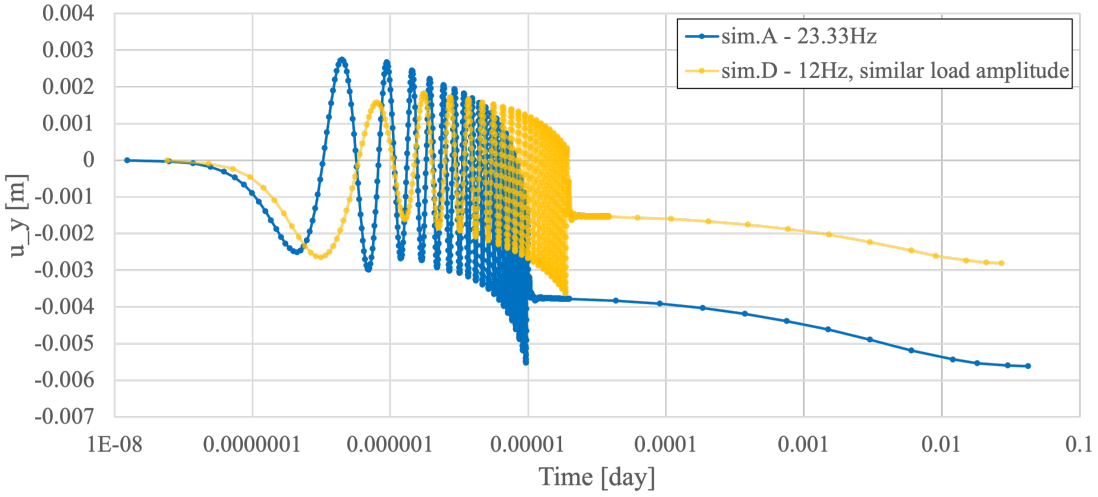

Figure 7.38: sim.A (vibro 23.33 Hz) and sim.D (vibro 12 Hz, similar load amplitude as 23.33 Hz): vertical displacement of top of the pile during loading, damping and consolidation phases against a logarithmic time scale. Initiation of consolidation phase is indicated by the increased horizontal spacing between calculation points. Data from PLAXIS 2D plotted in Excel.

There is a significant difference in the final settlement of the top of the pile after consolidation between driving at 23.33 Hz (sim.A) and at 12 Hz for the same load amplitude as 23.33 Hz (simD). During consolidation sim.A and sim.D approaches approximately a final settlement at top of the pile equal to 0.0056 m and 0.0028 m respectively.

Excess Pore Pressure

Figures 7.39 and 7.40 show the contour plots of excess pore pressure (p_{excess}) at the end of the dynamic loading phase for sim.A and sim.D respectively.

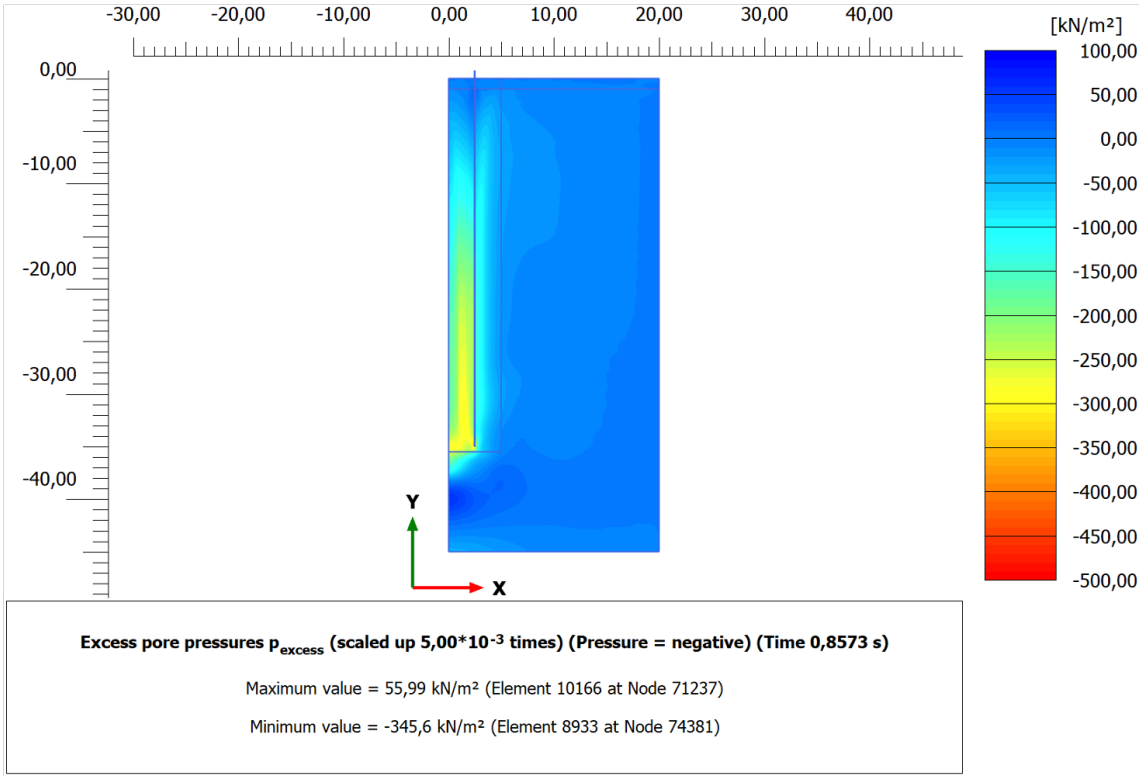

Figure 7.39: sim.A (vibro 23.33 Hz): p_{excess} contour plot of soil at the end of dynamic loading phase. File exported from PLAXIS 2D Output.

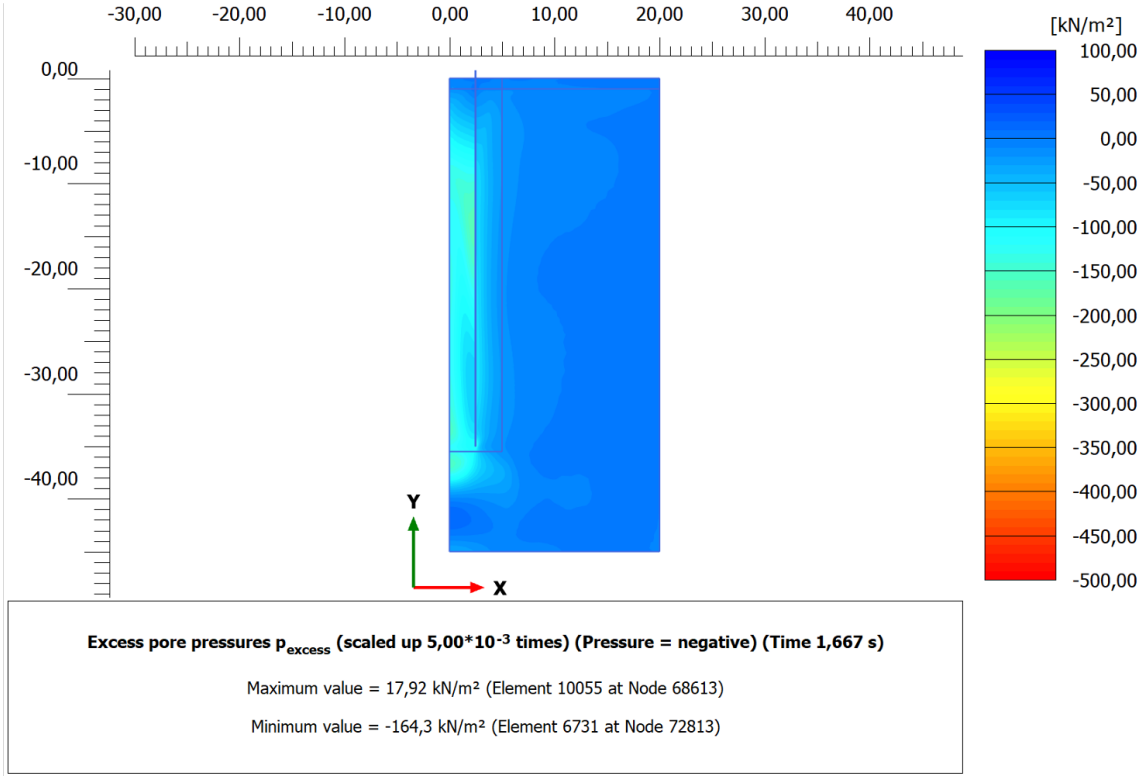

Figure 7.40: sim.D (vibro 12 Hz, similar load amplitude as 23.33 Hz): p_{excess} contour plot of soil at the end of dynamic loading phase. File exported from PLAXIS 2D Output.

The evolution of p_{excess} in the point at the centre of the embedded pile length (depth 17.5 m) near the exterior pile wall is shown in Figure 7.41.

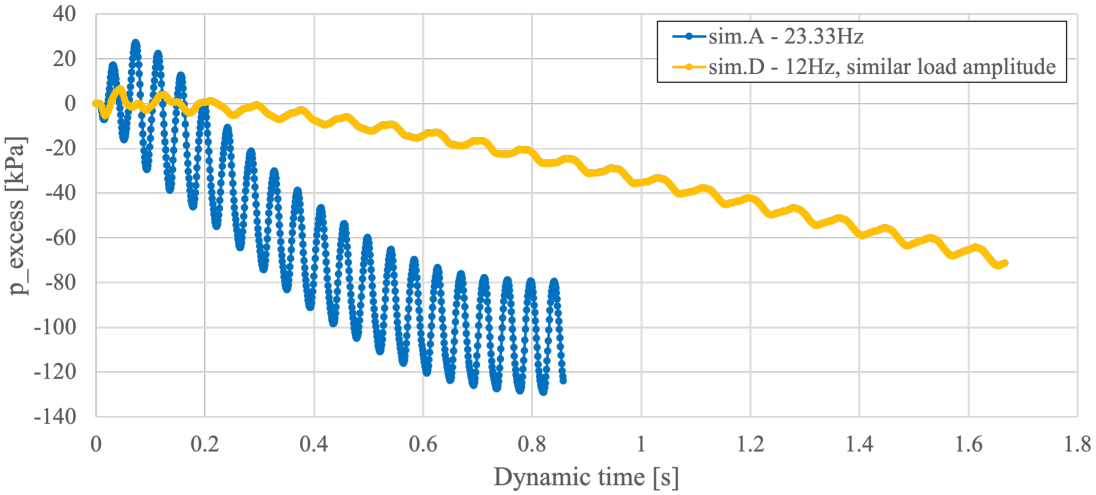

Figure 7.41: sim.A (vibro 23.33 Hz) and sim.D (vibro 12 Hz, similar load amplitude as 23.33 Hz): p_{excess} during dynamic loading phase. At depth 17.5 m, near exterior pile wall. Data from PLAXIS 2D plotted in Excel.

The build-up of excess pore pressure is present during driving at 12 Hz with the increased amplitude, however, still considerably lower than driving at 23.33 Hz. The greatest difference in p_{excess} is seemingly at the interior of the pile at depths between $y = -25$ m and $y = -35$ m and along the exterior pile wall, according to the contour plots. This emphasises the effect of increased loading frequency on pore pressure build-up for the situation considered. The graphs showing the evolution of p_{excess} at depth 17.5 m, near the exterior pile wall, show that sim.D does not approach a steady-state during 20 load cycles, while it seemingly does for sim.A. The rate of p_{excess} build-up in pressure is considerably higher for sim.A compared to sim.D.

Effective Mean Stress

The effective mean stress (p') during dynamic loading is plotted for the same point as p_{excess} in Figure 7.41 (depth 17.5 m and near the exterior pile wall), seen in Figure 7.42.

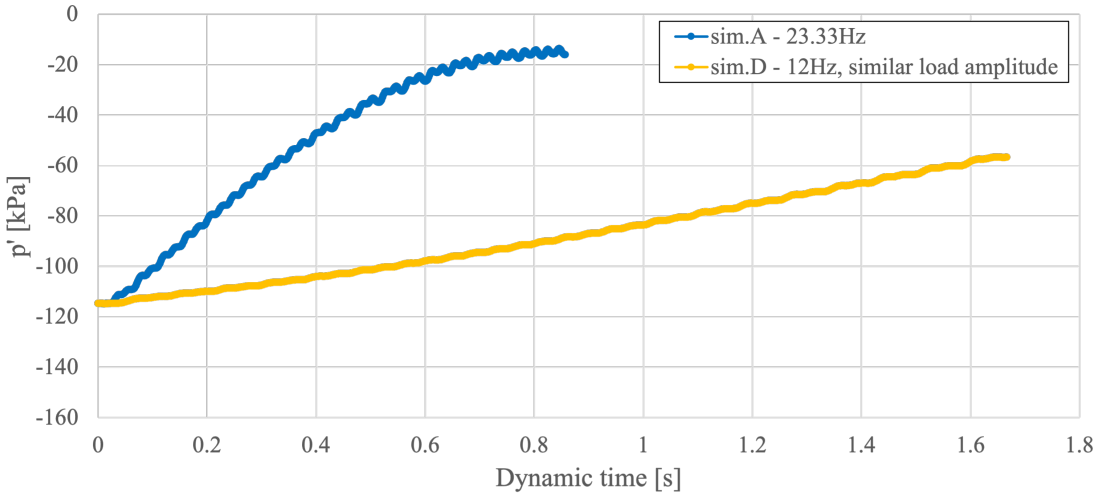

Figure 7.42: sim.A (vibro 23.33 Hz) and sim.D (vibro 12 Hz, similar load amplitude as 23.33 Hz): p' during dynamic loading phase. At depth 17.5 m, near exterior pile wall. Data from PLAXIS 2D plotted in Excel.

Note the tendency of approaching a steady-state in p' during sim.A, while this is not seen during sim.D. The latter simulation has indications of a less degree of liquefaction compared to sim.A for during the 20 load cycles simulated, due to the higher value of p' in pressure.

$\sigma_{xy} - \gamma_{xy}$ Hysteresis Loops

The shear stress (σ_{xy}) and shear strain (γ_{xy}) hysteresis loops are plotted for the point at depth 17.5 m near the exterior pile wall. The slope of the loops visualises the evolution of shear modulus (G) during the dynamic loading phase. The hysteresis loops indicate start of the dynamic loading by the colour purple and evolves to yellow during the dynamic loading.

The secant shear modulus ratio between first cycle and cycle number N ($G_{s,N}/G_{s,1}$) is interpreted by the one-way amplitudes for the first cycle while by the last two-way amplitudes for cycle number N. This method of interpretation is presented in Appendix C.

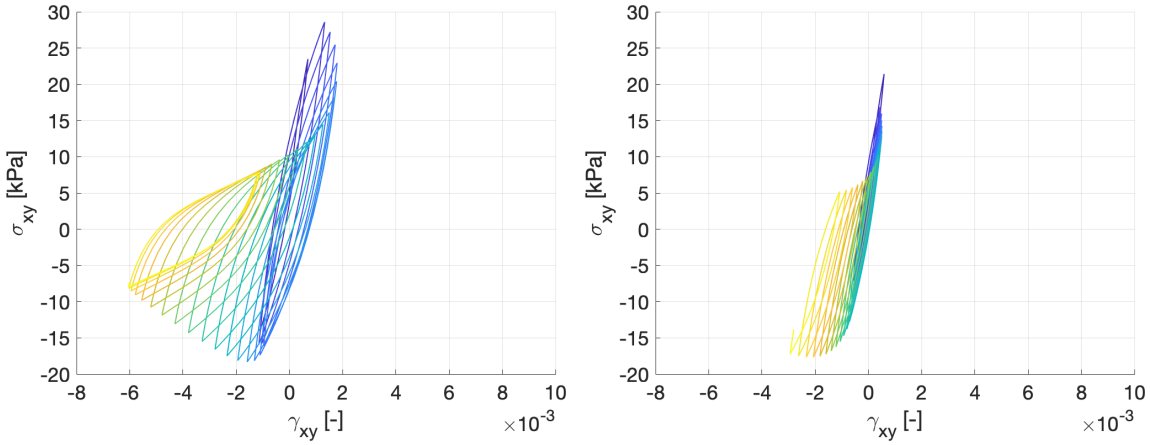

(a) sim.A (vibro 23.33 Hz): 20 loading cycles. $G_{s,20}/G_{s,1} = 0.12$.

(b) sim.D (vibro 12 Hz, similar load amplitude as 23.33 Hz): 20 loading cycles. $G_{s,20}/G_{s,1} = 0.44$.

Figure 7.43: sim.A (vibro 23.33 Hz) and sim.D (vibro 12 Hz, similar load amplitude as 23.33 Hz): $\sigma_{xy} - \gamma_{xy}$ hysteresis loops during dynamic loading phase. At depth 17.5 m, near exterior pile wall. Colour shades indicate calculation points, from purple to yellow. $G_{s,N}/G_{s,1}$ is ratio of shear modulus between first cycle and cycle number N. Data from PLAXIS 2D plotted in MATLAB.

The $\sigma'_{xy} - \gamma_{xy}$ hysteresis loops indicate a larger reduction of shear modulus during the cyclic loading. The secant shear modulus ratio is significantly lower due to driving at 23.33 Hz, compared to 12 Hz, being interpreted to 0.12 and 0.44 respectively.

Table 7.3: Overview of interpreted secant shear modulus ratio between first cycle and cycle number N ($G_{s,N}/G_{s,1}$), for sim.A and sim.D. From point at depth 17.5 m, near exterior pile wall

	Vibratory driving	
	sim.A	sim.D
$G_{s,1}$ [kPa]	26389.00	27619.35
$G_{s,20}$ [kPa]	3192.06	12045.61
$G_{s,20}/G_{s,1}$ [-]	0.12	0.44

An overview of the interpreted secant shear moduli during sim.A and sim.D (vibratory driving), at depth 17.5 m near the exterior pile wall, is listed in Table 7.3. Note the relatively similar secant shear modulus at the first cycle between the two simulations, followed by a greater difference at cycle number 20.

7.4 Vibratory Driving: Effect of Initial Void Ratio

sim.A is the base simulation, with a driving frequency of 23.33 Hz and initial void ratio in the soil equal to $e_{init} = 0.734$. sim.E simulates the same frequency and load amplitude, but a denser soil with an initial void ratio equal to $e_{init} = 0.650$.

Initial void ratio is suggested to affect the soil behaviour when subjected to shearing, amongst others, affecting the potential of contractive behaviour and soil liquefaction during undrained loading, reviewed in Sections 4.2 and 4.3.

Vertical Displacement of the Top of the Pile During Loading, Damping and Consolidation Phases

The vertical displacement of the top of the pile during loading, damping and consolidation phases is plotted against a logarithmic time scale, shown in Figure 7.44.

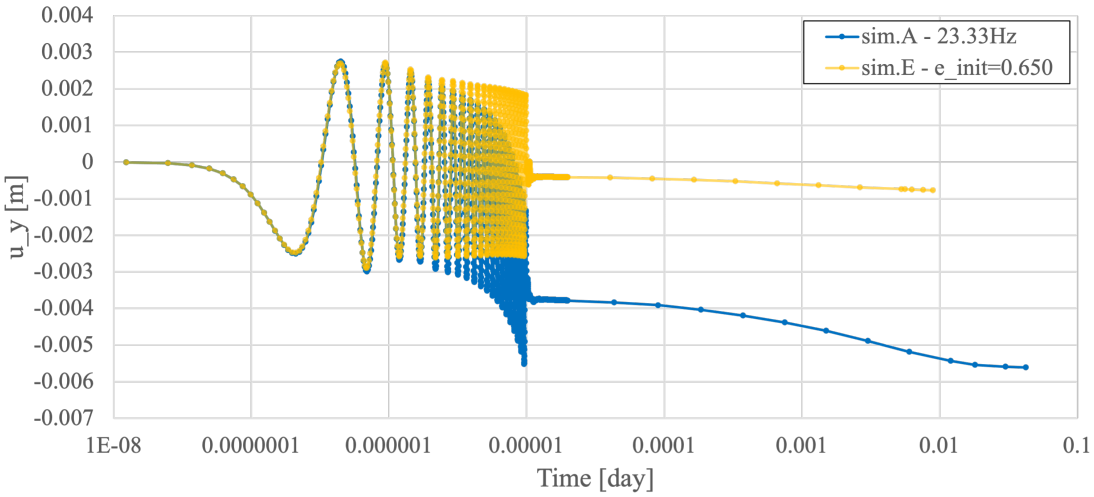

Figure 7.44: sim.A (vibro 23.33 Hz) and sim.E (vibro 23.33 Hz, initially denser sand): vertical displacement of top of the pile during loading, damping and consolidation phases against a logarithmic time scale. Initiation of consolidation phase is indicated by the increased horizontal spacing between calculation points. Data from PLAXIS 2D plotted in Excel.

The final settlement of the top of the pile is considerably lower due to driving in the denser sand, being approximately 0.0008 m, while 0.0056 m for the looser sand, seen in Figure 7.44. Note that both sim.B (18 Hz) and sim.D (12 Hz, similar load amplitude as 23.33 Hz) have a greater final settlement than the denser sand in sim.E.

Excess Pore Pressure

The contour plot of the excess pore pressure (p_{excess}) is shown for sim.A and sim.E in Figures 7.45 and 7.46 respectively.

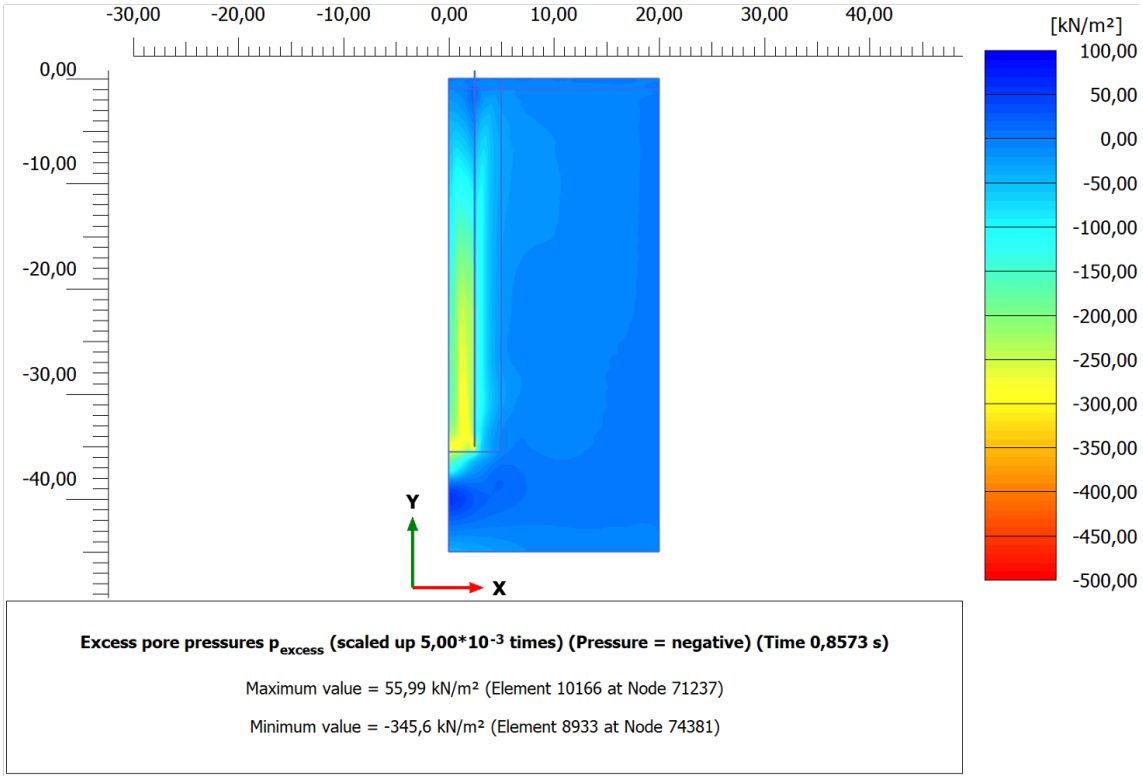

Figure 7.45: sim.A (vibro 23.33 Hz): p_{excess} contour plot of soil at the end of dynamic loading phase. File exported from PLAXIS 2D Output.

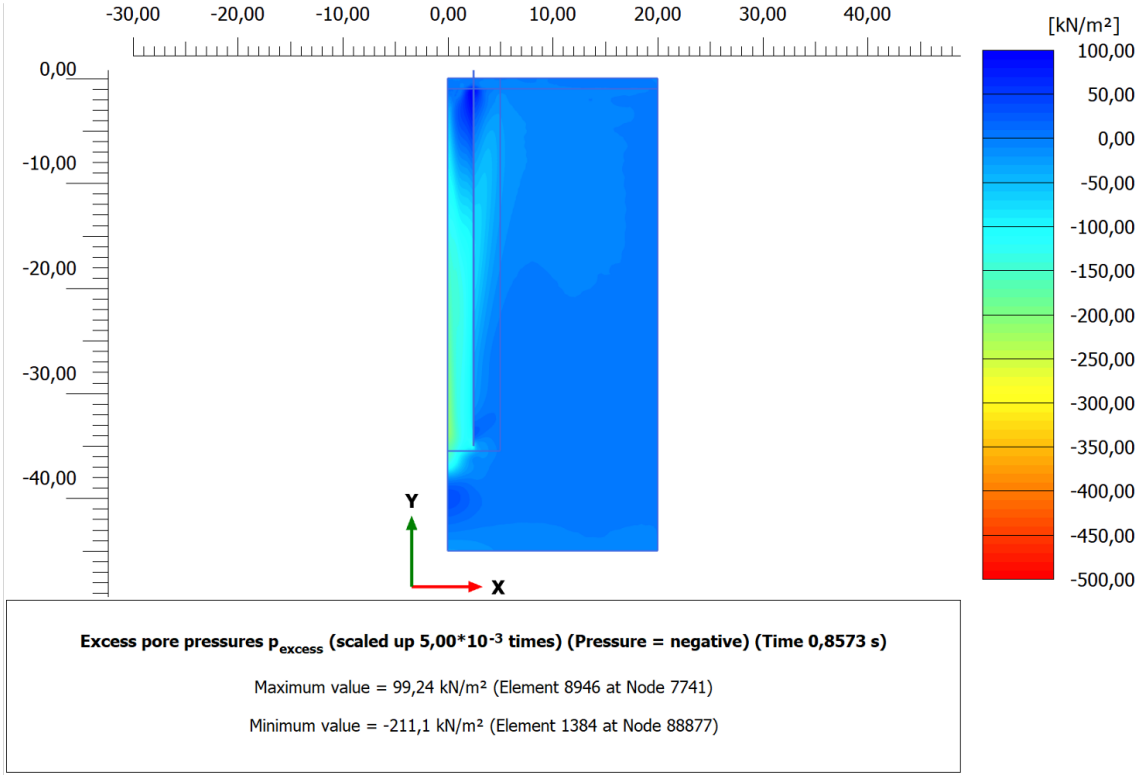

Figure 7.46: sim.E (vibro 23.33 Hz, initially denser sand): p_{excess} contour plot of soil at the end of dynamic loading phase. File exported from PLAXIS 2D Output.

The evolution of p_{excess} in a point at the centre of the embedded pile length (depth 17.5 m) near the exterior pile wall is shown in Figure 7.47.

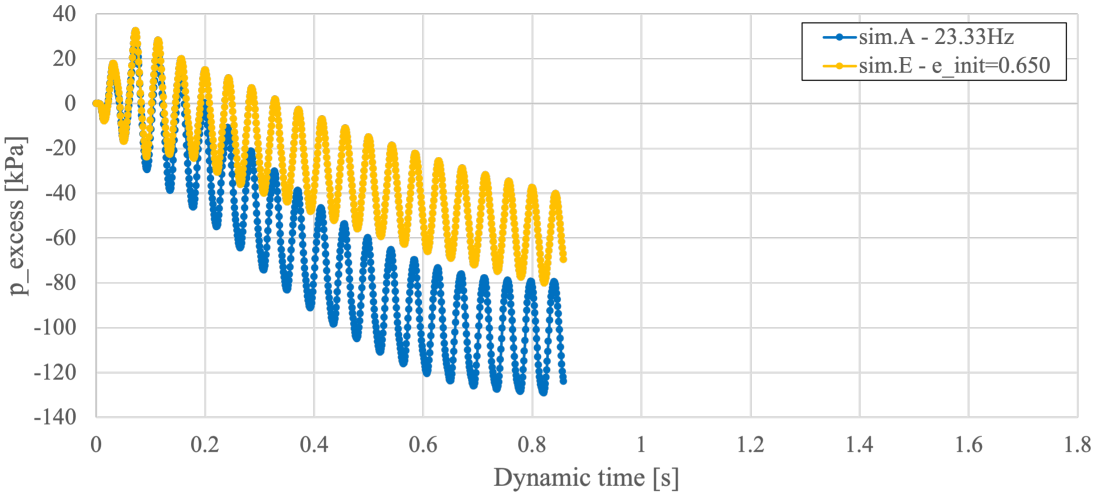

Figure 7.47: sim.A (vibro 23.33 Hz) and sim.E (vibro 23.33 Hz, initially denser sand): p_{excess} during dynamic loading. At depth 17.5 m, near exterior pile wall. Data from PLAXIS 2D plotted in Excel.

The initially denser sand indicates less build-up of p_{excess} after the loading phase, seen in the contour plots in Figures 7.45 and 7.46. The same tendency of less p_{exess} build-up in pressure for the denser sand is seen in the point at depth 17.5 m, near the exterior pile wall (Figure 7.47).

Effective Mean Stress

The effective mean stress (p') is plotted for the same point as p_{excess} in Figure 7.47 (depth 17.5 m and near the exterior pile wall), is presented in Figure 7.48.

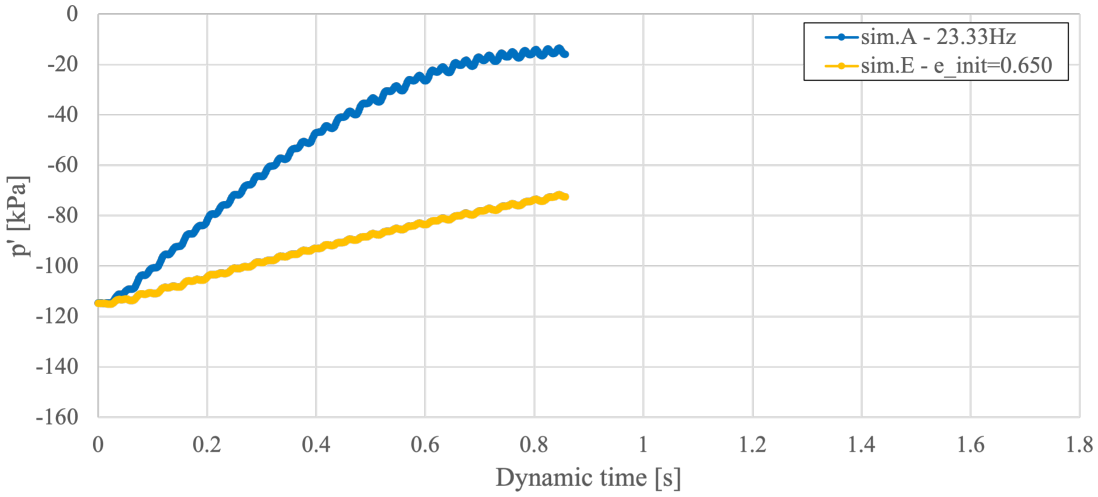

Figure 7.48: sim.A (vibro 23.33 Hz) sim.E (vibro 23.33 Hz, initially denser sand): p'during dynamic loading. At depth 17.5 m, near exterior pile wall. Data from PLAXIS 2D plotted in Excel.

The denser sand shows a considerably lower reduction of effective mean stress in pressure (Figure 7.48), indicating a lower degree of soil liquefaction during 20 simulated load cycles.

$\sigma_{xy} - \gamma_{xy}$ Hysteresis Loops

The shear stress (σ_{xy}) and shear strain (γ_{xy}) hysteresis loops are plotted for the point at depth 17.5 m near the exterior pile wall. The slope of the loops visualises the evolution of shear modulus (G) during the dynamic loading phase. The hysteresis loops indicate start of the dynamic loading by the colour purple and evolves to yellow during the dynamic loading.

The secant shear modulus ratio between first cycle and cycle number N ($G_{s,N}/G_{s,1}$) is interpreted by the one-way amplitudes for the first cycle while by the last two-way amplitudes for cycle number N. This method of interpretation is presented in Appendix C.

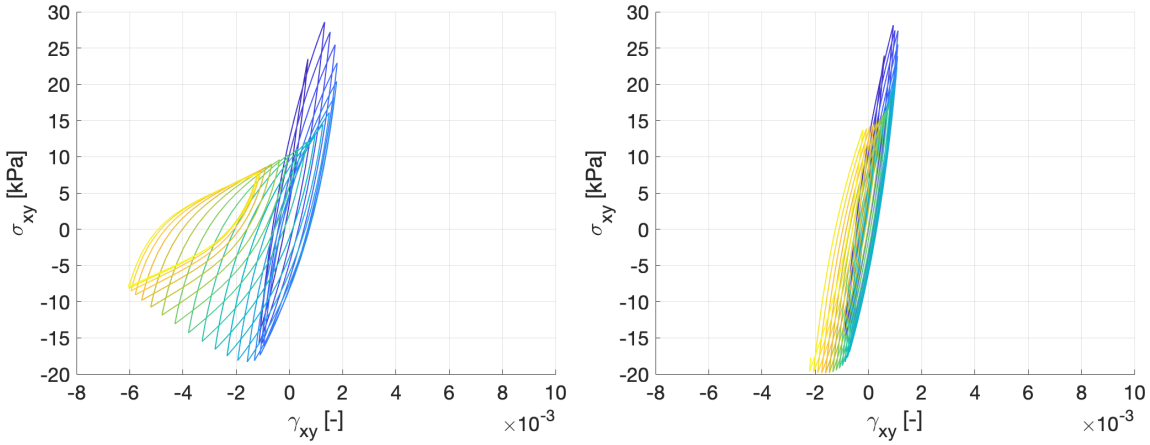

(a) sim.A (vibro 23.33 Hz): 20 loading cycles. $G_{s,20}/G_{s,1} = 0.12$.

(b) sim.E (vibro 23.33 Hz, initially denser sand): 20 loading cycles. $G_{s,20}/G_{s,1} = 0.52$.

Figure 7.49: sim.A (vibro 23.33 Hz) and sim.E (vibro 23.33 Hz, initially denser sand): $\sigma_{xy} - \gamma_{xy}$ hysteresis loops during dynamic loading. At depth 17.5 m, near exterior pile wall. Colour shades indicate calculation points, from purple to yellow. Data from PLAXIS 2D plotted in MATLAB.

The implemented SANISAND material model incorporates the effect of different void ratios, amongst other, by adjusting the dilatancy and bounding lines in the $p' - q$ stress space, as seen in Equations 5.19 and 5.20 respectively in Section 5.2.1. The equation of shear modulus in SANISAND also varies with current void ratio, seen in Equation 5.10, of which the $(2.97 - e)^2/(1 + e)$ factor of the equation is approximately 2.88 and 3.26 for $e_{init} = 0.734$ and $e_{init} = 0.650$ respectively. The same equation also shows the dependency of effective mean stress, of which a reduced p' in pressure leads to a reduced G. The initially denser sand (sim.E) indicates a higher secant shear modulus during the first cycle compared to the simulation with $e_{init} = 0.734$ (sim.A). The ratio of secant shear modulus degradation is 0.12 for the looser sand and 0.52 for the denser.

Table 7.4: Overview of interpreted secant shear modulus ratio between first cycle and cycle number N ($G_{s,N}/G_{s,1}$), for sim.A and sim.E (vibro 23.33 Hz, initially denser sand). From point at depth 17.5 m, near exterior pile wall

	Vibratory driving	
	sim.A	sim.E
$G_{s,1}$ [kPa]	26389.00	31596.57
$G_{s,20}$ [kPa]	3192.06	16547.57
$G_{s,20}/G_{s,1}$ [-]	0.12	0.52

An overview of the interpreted secant shear moduli during sim.A and sim.E (vibratory driving), at depth 17.5 m near the exterior pile wall, is listed in Table 7.4. Note that the secant shear stiffness is lower for sim.A already during the first cycle.

7.5 Overview of Secant Shear Modulus Ratios at Centre of Embedded Pile Length, Near the Exterior Pile Wall

Table 7.5: Overview of interpreted secant shear modulus ratio between first cycle and cycle number N ($G_{s,N}/G_{s,1}$), for sim.A to sim.F. From point at depth 17.5 m, near exterior pile wall. Note that the method of estimating the secant shear modulus for the last cycle is different for vibratory and impact driving, see Appendix C.

	Vibratory driving						Impact driving
	sim.A	sim.A*	sim.B	sim.C	sim.D	sim.E	sim.F
$G_{s,7}/G_{s,1}$ [-]	-	-	-	-	-	-	0.54
$G_{s,20}/G_{s,1}$ [-]	0.12	-	0.59	0.96	0.44	0.52	-
$G_{s,39}/G_{s,1}$ [-]	-	0.13	-	-	-	-	-

An overview of the interpreted secant shear modulus ratios for sim.A to sim.F in the soil at depth 17.5 m, near the exterior pile wall, are listed in Table 7.5. It may be noted that during sim.A and sim.A* the secant shear modulus ratio is significantly lower compared to all the other simulations listed. Note that these estimations of secant shear modulus ratios are from only one point in the soil.

7.6 Pile Response During Driving

The results regarding pile behaviour during the dynamic loading phases of the vibratory and impact driving simulations are to be presented and discussed.

7.6.1 Vibratory Driving

The pile behaviour during the dynamic loading phases of the vibratory driving simulations (sim.A to sim.E) are in the following presented and discussed.

Vertical Acceleration of the Top of the Pile

Figures 7.50 and 7.51 show the vertical acceleration (a_y) of the top of the pile during the dynamic loading phases of the vibratory driving simulations, with the exception of sim.A*.

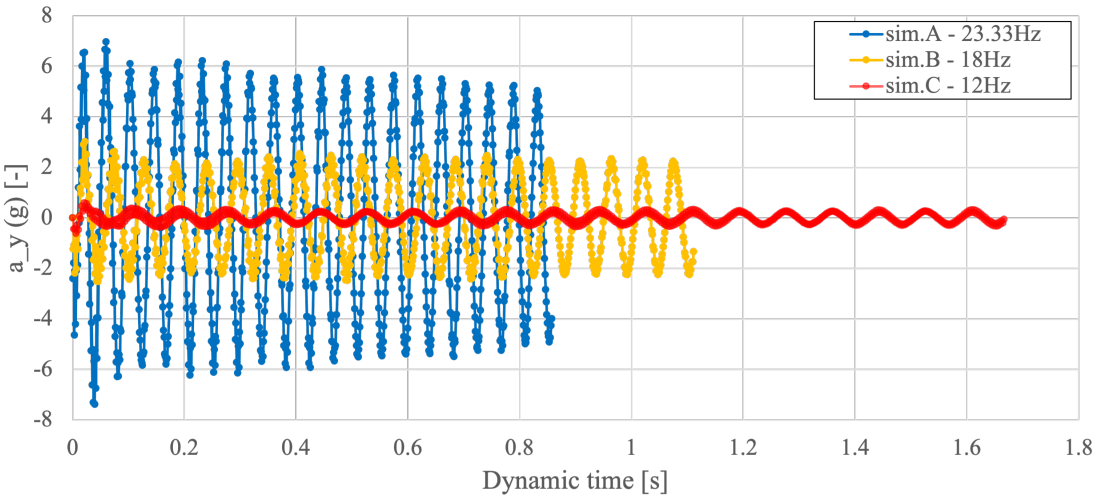

Figure 7.50: sim.A, sim.B and sim.C (vibro 23.33-, 18- and 12 Hz respectively): vertical acceleration of top of the pile during dynamic loading phase. Data from PLAXIS 2D plotted in Excel.

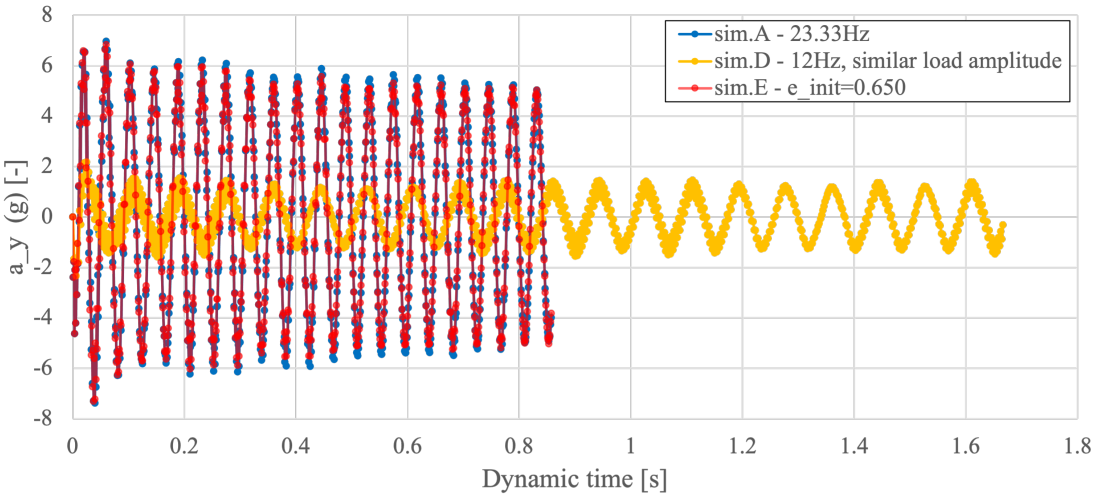

Figure 7.51: sim.A (vibro 23.33 Hz), sim.D (vibro 12 Hz, similar load amplitude as 23.33 Hz) and sim.E (vibro 23.33 Hz, initially denser sand): vertical acceleration of top of the pile during dynamic loading phase. Data from PLAXIS 2D plotted in Excel.

A comparison of the recommended driving parameters by Rodger and Littlejohn (1980), presented in Table 2.2 in Section 2.3, to the simulated pile behaviour during vibratory driving is presented in the following. Driving at 23.33 Hz (sim.A and sim.E) shows close to similar vertical acceleration amplitudes of the top of the pile, ranging between approximately 5-7 g, while the other simulations (sim.B, sim.C and sim.D) show amplitudes below 4 g. The recommended driving parameters by Rodger and Littlejohn (1980) suggest a vertical acceleration in the range of 5-15 g for pile driving in both dense and loose non-cohesive soils of which the side resistance of the pile is predominant. The latter may be initially assumed for the modelled hollow monopile with an outer diameter of 5 m, and a relatively thin wall thickness. All simulations are within the recommended range of driving frequency, namely $10 - 40$ Hz. The recommended range of displacement amplitude is $1 - 10$ mm, which is seen during sim.A, sim.B, sim.D and sim.E. Hence, only sim.C (12 Hz) is not within this recommended range. It may be suggested that only the simulations driving at 23 Hz (sim.A and sim.E) meet the recommended driving parameters by Rodger and Littlejohn (1980). However, the results may indicate that driving at 23.33 Hz with the initial void ratio of $e_{init} = 0.650$ (sim.E) may not be sufficient, depending on the requirement of installation time, since the rate of vertical displacement of the top of the pile seemingly is relatively low. However, note that the driving parameters of the simulation lies generally in the lower range of the recommended parameters by Rodger and Littlejohn (1980), hence, increasing the driving parameters within the suggested ranges for the simulation during driving of the denser sand (sim.E) could lead to an increased rate of settlement of the top of the pile.

The load amplitudes are similar for sim.A and sim.D, while the driving frequencies are 23.33- and 12 Hz respectively. Figure 7.51 indicates a considerably higher vertical acceleration amplitude at the top of the pile for sim.A. Due to the mass of the pile being equal in sim.A and sim.D, this indicates that a larger force is acting on the top of the pile during

driving. In general, the increased force subjected to the top of the pile may induce larger shear stresses and strains in the surrounding soil during driving, which in turn may lead to greater excess pore pressure build-up for contractive soils. Seen in Table 7.3 the secant shear modulus ratio is lower during vibratory driving at 23.33 Hz (sim.A) compared to driving at 12 Hz with the same load amplitude (sim.D). This emphasises the dependency of stiffness degradation on the rate of loading, i.e. driving frequency. It may be suggested that the dependency between excess pore pressure build-up and loading rate is more predominant for relatively permeable materials, since the drainage behaviour may be highly affected of the loading rate.

Vertical Displacement of the Top of the Pile and Pile Toe for sim.A* During Dynamic Loading Phase

The vertical displacement of the top of the pile and pile toe are plotted for sim.A* during the dynamic loading phase, presented in Figure 7.52.

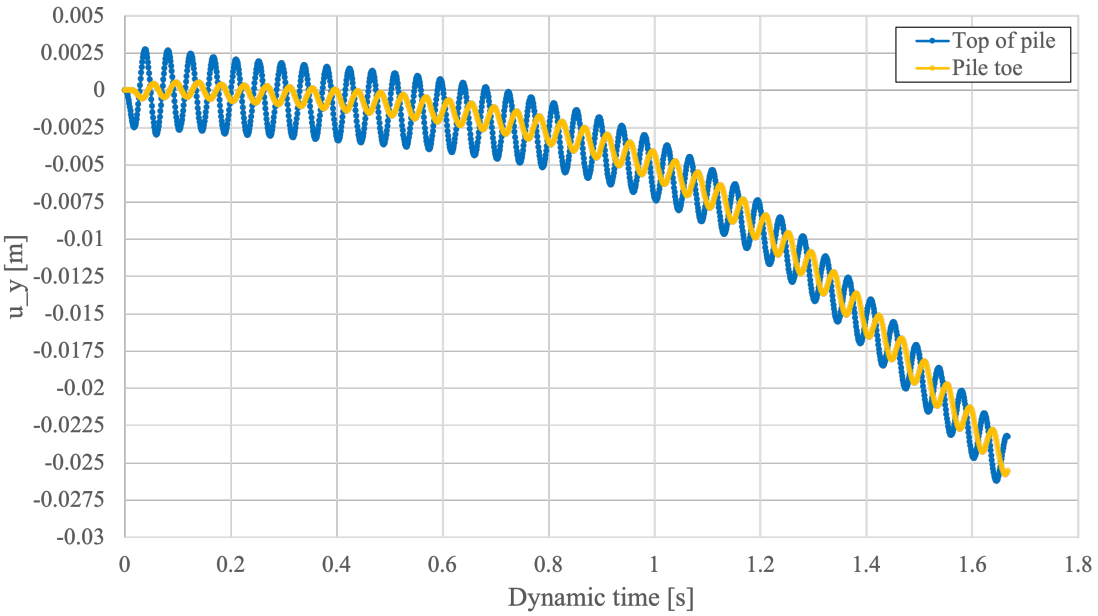

Figure 7.52: sim.A* (vibro 23.33 Hz, 38.9 cycles): vertical displacement of top of the pile and pile toe during dynamic loading phase. Data from PLAXIS 2D plotted in Excel.

The graph showing the vertical displacements of the top of the pile and pile toe for sim.A* (23.33 Hz, 38.9 loading cycles) indicates a non-rigid pile behaviour during driving, since the displacement amplitude of the top of the pile is considerably larger than at the pile toe. This would be expected, since the pile is modelled by a linear elastic material model. However, the difference between the vertical displacement amplitudes are seemingly reduced during the dynamic loading, and may be due to the reduced shear modulus along the pile walls. Note, however, the delay between the displacement amplitudes between the top of the pile and pile toe, visualising the elastic behaviour of the pile. During the modelling of the load transfer between hammer and pile the latter was assumed to behave as a rigid body, for simplicity. Note also the seemingly approach of a steady-state with respect to

vertical displacement rate of the pile for the last cycles, seen in Figure 7.52. The slope at this seemingly steady-state, i.e. the rate of settlement, is interpreted to approximately 0.036 m/s for both the top of the pile and pile toe.

7.6.2 Impact Driving

The pile behaviour during the dynamic loading phase of the impact driving simulation (sim.F) is in the following presented and discussed.

Vertical Displacement of the top of the Pile During Dynamic Loading and Damping Phases of sim.F

Figure 7.53 shows the vertical displacement during dynamic loading and damping phases of sim.F (impact driving).

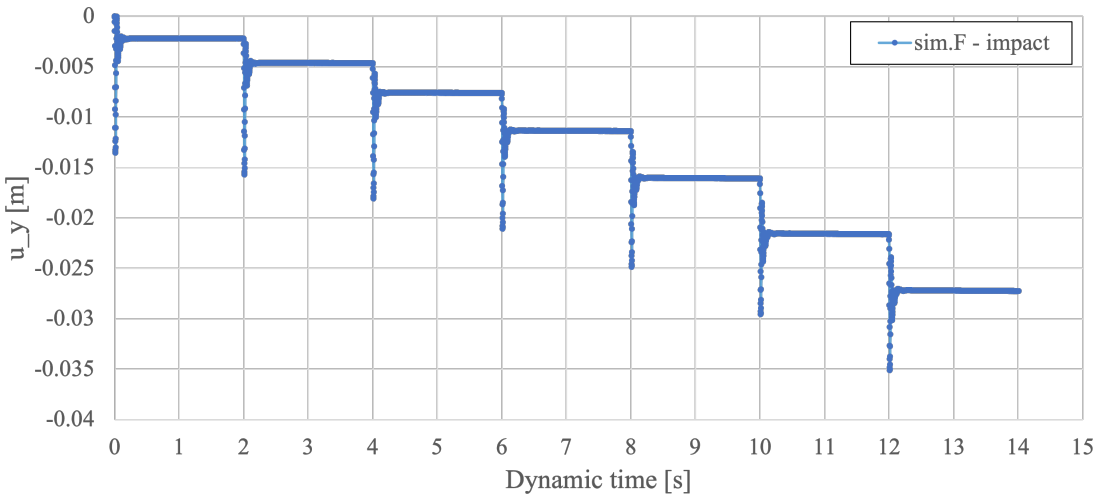

Figure 7.53: sim.F (impact): vertical displacement of top of the pile during dynamic loading and damping phases. Data from PLAXIS 2D plotted in Excel.

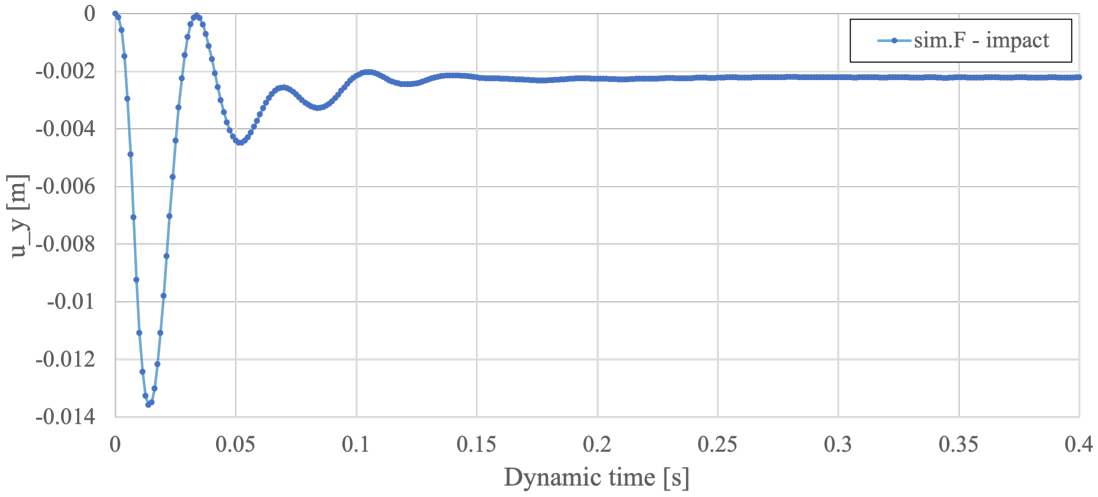

Figure 7.54: sim.F (impact): excerpt of vertical displacement of top of the pile during dynamic loading phase. Showing first impact and some subsequent dynamic time. Data from PLAXIS 2D plotted in Excel.

During the selection of an appropriate impact hammer the permanent settlement per impact of the hammer was set to $s_{plastic} = 0.01\,\text{m}$. The excerpt of the graph showing vertical displacement of the top of the pile (Figure 7.54) seemingly indicates a permanent settlement after the first impact equal to approximately 0.0022 m. This is in the magnitude of 1/5 of the selected plastic settlement during each blow ($s_{plastic} = 0.01\,\text{m}$). The simulated permanent settlement at each impact seem to increase during driving, seen in Figure 7.53, and is approximately 0.0056 m for the last impact (load cycle number 7). The SANISAND material model implemented is the one described in Dafalias and Manzari (2004), which does not include cap hardening. This indicate that the soil exhibits elastic behaviour for any value of p' as long as the stress ratio q/p' is within the yield lines in the $p' - q$ stress space. This may be suggested to affect the magnitude of permanent settlement during each impact. The $p' - \sigma_{xy}$ stress path in the point of the soil at depth 17.5 m, near the exterior pile wall, presented in Figure 7.15b shows an increase of p' in pressure during the first impact to a larger value than initial. With cap hardening implemented to the model this might exhibit plastic deformations, hence a larger permanent settlement during the impacts compared to the settlement obtained in sim.F. Note, however, that the selected permanent settlement each impact of $s_{plastic} = 0.01\,\text{m}$ is only one of several other selected parameters in the simplified estimation of necessary impact energy, hence the difference in simulated permanent settlement and $s_{plastic}$ may also be due to the selection of these.

7.7 Vibratory Driving: Additional Simulation with 6-noded Elements

An additional simulation is performed, of which the 6-noded elements are used for the modelling instead of 15-noded. Vibratory driving at 23.33 Hz with a longer duration is simulated (sim.A* with 6-noded elements).

The contour plots of the effective Cartesian stresses in x-, y- and z-direction (σ'_{xx}, σ'_{yy}, σ'_{zz}) at the end of consolidation are presented in Figures 7.55, 7.56 and 7.57 respectively. The simulation with 6-noded elements is primarily performed to investigate the reason for the increased effective radial stresses (σ'_{xx}) near the exterior pile wall after consolidation, seen for both impact and vibratory driving. The initial stress states, i.e. at the end of the plastic nil-phase, of the effective Cartesian stresses for the simulation may be found in Section A.5 in Appendix A.

The contour plots indicate the same tendency of increased effective radial stresses near the exterior pile wall, as seen for the simulation with 15-noded elements. This may suggest the explanation to not be related to the modelling of the elements.

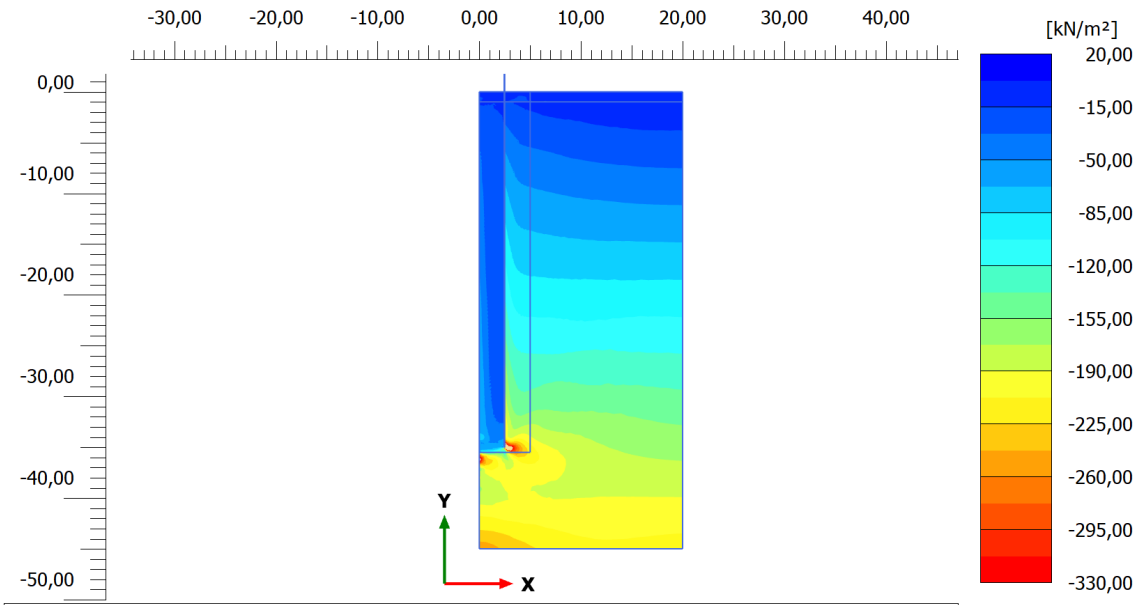

Figure 7.55: sim.A* (vibro 23.33 Hz, 38.9 cycles) with 6-noded elements: σ'_{xx} contour plot of soil at the end of consolidation phase. File exported from PLAXIS 2D Output.

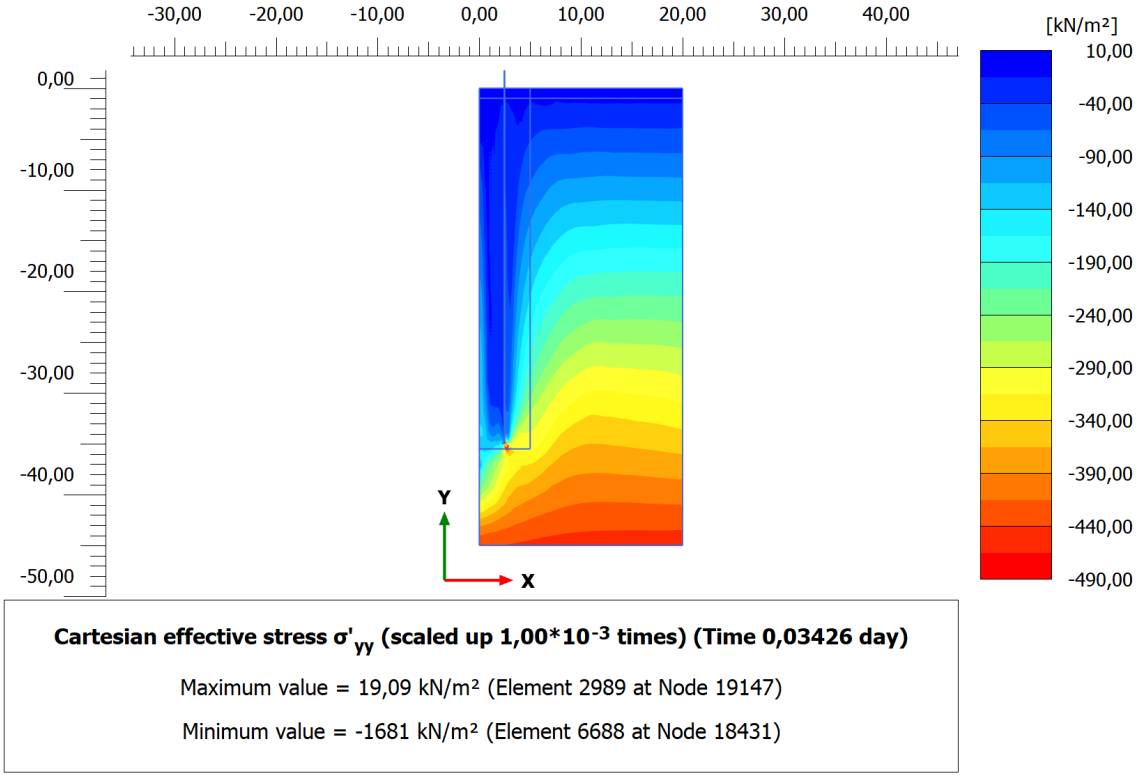

Figure 7.56: sim.A* (vibro 23.33 Hz, 38.9 cycles) with 6-noded elements: σ'_{yy} contour plot of soil at the end of consolidation phase. File exported from PLAXIS 2D Output.

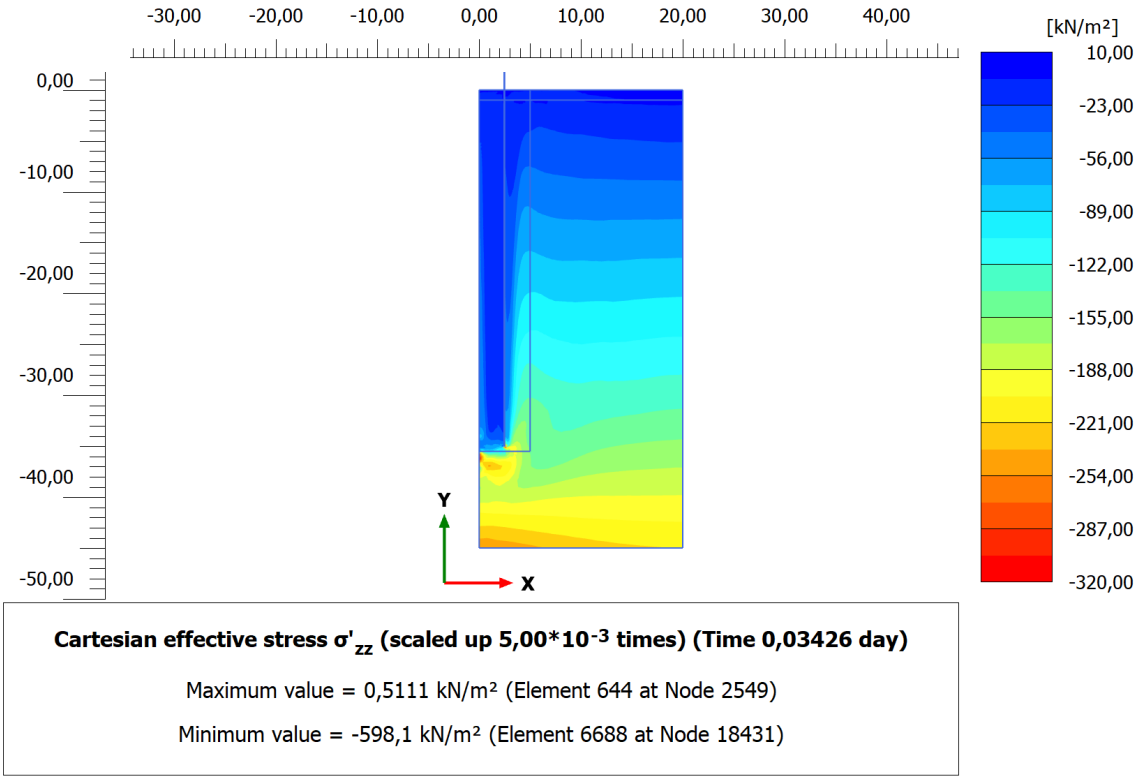

Figure 7.57: sim.A* (vibro 23.33 Hz, 38.9 cycles) with 6-noded elements: σ'_{zz} contour plot of soil at the end of consolidation phase. File exported from PLAXIS 2D Output.

Chapter 8

Conclusions

Numerical simulations of vibratory and impact pile driving have been carried out in PLAXIS 2D to investigate the research questions presented in Chapter 1. Based on the results and interpretations in Chapter 7 the research questions are answered as follows:

1. May the numerical simulations provide indications of different soil behaviour during vibratory driving compared to impact driving? To be evaluated in terms of excess pore pressure build-up and shear modulus degradation.

The results clearly show a different simulated soil behaviour during driving between the two assessed methods of pile installation. The rate of pile penetration and build-up of excess pore pressure for the investigated points in the soil are considerably higher during vibratory driving. At the centre of the embedded pile length (depth 17.5 m), near the exterior pile wall, the secant shear modulus ratio is significantly lower after 1.667 s of vibratory driving compared to 12.01 s of impact driving, while 1 m further out the ratios are almost equal. This suggests that the simulated secant shear ratio decays to a larger degree for an increased distance from the pile wall during vibratory driving compared to impact driving. This is, however, limited to the points in the soil investigated. Cyclic mobility is seen in the soil at depth 17.5 m, near the exterior pile wall, already during the first load cycle of impact driving. Only slight cyclic mobility is seen after several load cycles of vibratory driving. This may give indications of vibratory driving being more energy efficient in the simulations since a part of the energy inflicted to the soil in the evaluated point contributes to soil dilatancy, and an increased effective mean stress in pressure, already during the first load cycle during impact driving. Note that these remarks are limited to the point in the soil investigated and the comparison of vibratory driving with 38.9 load cycles and impact driving with 7 load cycles.

2. May the numerical simulations provide indications of different soil states after consolidation for vibratory driving compared to impact driving? To be evaluated in terms of stress state and void ratio.

Slightly different states of the soil after consolidation for the two driving methods are suggested by the results, however, the investigated behaviour of the soil during driving

may be suggested to show greater differences. The final settlements of the pile are close to similar after consolidation for both pile driving methods. At the centre of the embedded pile length (depth 17.5 m), near the exterior pile wall and 1 m further out, the evolution of the effective mean stresses (p') during driving are different for the two methods, while both the initial value and the one after consolidation are seemingly similar. The trend of an increase in effective radial stresses (σ'_{xx}) along the exterior pile wall after consolidation compared to initial state is similar for both installation methods. Both driving methods show the same trend of a decreased effective vertical stress (σ'_{yy}) and effective hoop stress (σ'_{zz}) near the exterior pile wall after consolidation compared to initial state. At the centre of the embedded pile length the effective principal stress directions of both driving methods indicate a rotation from an approximately vertical direction of effective major stress at initial state to a direction perpendicular to the exterior pile wall. The void ratio contour plots indicate soil compaction close to the middle and lower part of the exterior pile wall after consolidation for both driving methods. The void ratios in the soil near the exterior pile wall at the upmost part of the pile indicate a loosening after vibratory driving, while a greater loosening may be seen after impact driving and in a larger zone vertically along the pile.

3. How does the simulated soil behaviour during vibratory driving depend on driving parameters such as frequency and load amplitude, and initial void ratio of the soil? To be evaluated in terms of excess pore pressure build-up and shear modulus degradation.

The results clearly indicate lower rates of both pile penetration and excess pore pressure build-up, and a higher secant shear modulus ratio, when lowering the driving frequency with associated smaller load amplitude. The same tendencies are seen for the simulation with a lower frequency, while the load amplitude remains unchanged. The same tendencies are also seen for the initially denser soil compared to the looser. During vibratory driving of 38.9 loading cycles at 23.33 Hz, with the initially looser soil, (sim.A*) the excess pore pressure and effective mean stress, in the point at depth 17.5 m near the exterior pile wall, indicate an approach to a steady-state.

4. Are the results obtained indicating a close to real soil behaviour? Is the SANISAND material model, version by Dafalias and Manzari (2004), an appropriate material model to simulate vibratory and impact pile driving in PLAXIS 2D?

Neither the numerical modelling decisions nor the results are verified by data from field investigations. Hence, the reliability of the results is to a large degree evaluated conceptually. The results regarding soil and pile response during driving may indicate a closer to real soil behaviour during vibratory driving. During impact driving relatively small permanent settlements of the pile is simulated each blow of the hammer compared to the value used to estimate the energy needed per blow. This is suggested to be partly due to the absence of cap hardening in the SANISAND material model used. Cyclic mobility is seen at depth 17.5 m, near the exterior pile wall, already during the first loading cycle of impact driving with an increase of effective mean stress in pressure to a greater value than initial within the cycle. This might lead to plastic strains if cap hardening is present. In the same point in the soil, but during vibratory driving the absence of

cap hardening is suggested to affect the results to a less degree, based on the seemingly continuous decrease of effective mean stress until a slight cyclic mobility is seen after a certain number of cycles. The higher rate of pile penetration during vibratory driving is supported by suggestions in the literature of a faster installation time during this pile installation method. The threshold of generating excess pore pressure at depth 17.5 m, near the exterior pile wall, during vibratory driving for the loose sand seems to lie between the simulated driving at 12 Hz and 18 Hz, with their respective associated load amplitudes. The suggested cyclic threshold shear strain amplitude in the literature to generate excess pore pressure build-up lies between the shear strain amplitudes seen in the same point in the sand during driving of these two frequencies. There are uncertainties related to the simulated stress state after consolidation, however, the relatively large increase of effective radial stresses near the exterior pile wall, after consolidation for both vibratory and impact driving, may be suggested related to the pile restricting further compaction of the soil towards the axisymmetric line. The effective vertical stress at the interior of the pile after consolidation are considerably lower compared to prior dynamic loading phase, and is seen for vibratory (sim.A*) and impact driving (sim.F). This may be suggested partly attributed to the absence of interface elements along the pile wall.

8.1 Concluding Remarks

The global objective of the study is to grant enhanced knowledge regarding prediction of the axial and lateral bearing capacity of vibratory driven offshore monopiles. Particularly interesting may be the indications of a close to similar stress state after consolidation for the two different installation methods regardless of the considerably different soil behaviour during driving, presented in Section 7.1, Chapter 7. Note that, in addition to the general limitations of the numerical simulations (see Section 1.5), this is limited to the two investigated points of the soil. See particularly the graphs in Figures 7.11 and 7.12 regarding evolution of p', and e.g. graphs in Figures 7.2, 7.24 and 7.25 regarding evolution of vertical pile settlement and evolution of effective Cartesian stresses respectively. Slight differences of the void ratio in the soil are seen after consolidation between the two driving methods, seen in Figures 7.16 and 7.17. These results may suggest a relatively similar performance of the pile regarding bearing capacity after consolidation for both simulated installation methods.

Note that the assessments made remain conceptual, since neither the numerical model nor the results obtained are verified by field observations.

8.2 Recommendations for Further Work

To gain a better understanding of the soil behaviour during and after vibratory driving, and to grant enhanced knowledge regarding prediction of the bearing capacity of a vibratory driven pile used as foundation for an offshore wind turbine, several recommendations for further work can be made.

Neither the decisions made regarding the numerical model nor the results presented are verified by comparison with results from field studies of vibratory pile installations, hence, all the conclusions made are mainly conceptual. It may be recommended for further work to perform a study verifying a numerical model used for simulating vibratory pile driving. In addition to increase the reliability of the numerical model and the results, this may enhance the understanding of the relation between the soil behaviour during driving, e.g. shear modulus degradation and excess pore pressure build-up, and the alteration of soil state after installation. Hence, possibly allowing better prediction of axial and lateral bearing capacity based on data assessed during vibratory driving.

Replicating a field experiment in the numerical simulations would possibly require calibration of new soil parameters if the SANISAND material model is used. Hence, another recommendation for further work may be the calibration of these.

Several simplifications and other assumptions are made regarding the numerical modelling, and further work may consist of evaluating the effect of these. This is, amongst others, related to the modelling of the hammer masses and the load applied replicating the pile driving force. The effect of modelling interface elements along the pile wall and below the pile toe may also be evaluated, to investigate the seemingly high magnitude of adhesion of soil along the pile wall after consolidation.

Further work may consist of including a larger part of the installation process to the numerical simulations to better replicate the effects of full pile installation on soil behaviour. This could include simulating pile driving while the pile is set at different depths. In addition, the duration of the dynamic loading simulating the pile driving may be extended to evaluate possible effects of a longer driving duration.

It is suggested to evaluate the use of other material models for further numerical simulations of vibratory pile driving, and the SANISAND material model with cap hardening implemented, presented by Taiebat and Dafalias (2008), is suggested evaluated. However, other effects observed in soils subjected to cyclic loading may not be included in this material model. It is suggested to perform a study evaluating which material models includes the decisive formulations regarding simulating soil behaviour during vibratory driving.

Bibliography

Achmus, M. et al. (2020). 'Lateral bearing behaviour of vibro- and impact-driven large-diameter piles in dense sand'. In: *geotechnik* 43.3, pp. 147–159.

API (2010). *Recommended Practice for Planning, Designing and Constructing Fixed Offshore Platforms - Working Stress Design*. (RP 2A-WSD) Twenty-first edition. American Petroleum Institute (API).

Arshad, M. and O'Kelly, B. C. (2013). 'Offshore wind-turbine structures: a review'. In: *Proceedings of the Institution of Civil Engineers - Energy* 166.4. Publisher: ICE Publishing, pp. 139–152.

Ashmawy, A. K. et al. (1995). 'Soil Damping and Its Use in Dynamic Analyses'. In: *Third International Conference on Recent Advantages in Geotechnical Earthquake Engineering and Soil Dynamics*. St. Louis, Missouri, pp. 35–41.

Bailey, H. et al. (2010). 'Assessing underwater noise levels during pile-driving at an offshore windfarm and its potential effects on marine mammals'. In: *Marine Pollution Bulletin* 60.6, pp. 888–897.

Bardet, J. P. (1986). 'Bounding Surface Plasticity Model for Sands'. In: *Journal of Engineering Mechanics* 112.11. Publisher: American Society of Civil Engineers, pp. 1198–1217.

Been, K. and Jefferies, M. G. (1985). 'A state parameter for sands'. In: *Géotechnique* 35.2. Publisher: ICE Publishing, pp. 99–112.

Brewer, R. and Sleeman, J. R. (1988). *Soil Structure and Fabric*. Csiro Publishing. 307 pp.

Carsel, R. F. and Parrish, R. S. (1988). 'Developing joint probability distributions of soil water retention characteristics'. In: *Water Resources Research* 24.5, pp. 755–769.

Chung, J., Wallerand, R. and Hélias-Brault, M. (2013). 'Pile Fatigue Assessment During Driving'. In: *Procedia Engineering*. Fatigue Design 2013, International Conference Proceedings 66, pp. 451–463.

Dafalias, Y. F. and Manzari, M. T. (2004). 'Simple Plasticity Sand Model Accounting for Fabric Change Effects'. In: *Journal of Engineering Mechanics* 130.6. Publisher: American Society of Civil Engineers, pp. 622–634.

Dahl, B. M. and Løyland, M. S. (2017). *Cyclic Behaviour of Water Saturated Dense Sand*. NTNU.

Deckner, F. (2013). *Ground vibrations due to pile and sheet pile driving : influencing factors, predictions and measurements*. KTH, Royal Institute of Technology.

Deeks, A. J. and Randolph, M. F. (1993). 'Analytical modelling of hammer impact for pile driving'. In: *International Journal for Numerical and Analytical Methods in Geomechanics* 17.5, pp. 279–302.

DFI (2015). *Comparison of impact versus vibratory driven piles: With a focus on soil-structure interaction*. Deep Foundations Institute (DFI) and Gavin & Doherty Geo Solutions (GDG).

Dobry, R. et al. (1982). *Prediction of Pore Water Pressure Buildup and Liquefaction of Sands During Earthquake by the Cyclic Strain Method*. NBS BSS 138. Washington, D. C. 20234: National Bureau of Standards. Department of Commerce, No. of printed pages: 168.

Drnevich, V. P. and Richart, F. E. (1970). 'Dynamic Prestraining of Dry Sand'. In: *Journal of the Soil Mechanics and Foundations Division* 96.2. Publisher: American Society of Civil Engineers, pp. 453–469.

EC (2020). *Boosting Offshore Renewable Energy for a Climate Neutral Europe*. European Commission - European Commission. URL: https://ec.europa.eu/commission/presscorner/detail/en/IP_20_2096 (visited on 16th Apr. 2021).

Eiesland, H. (2020). 'Vibratory Driven Pile Installation'. Project thesis (TBA4510) (unpublished work). Trondheim, Norway: Norwegian University of Science and Technology (NTNU).

Erbe, C. (2013). 'International Regulation of Underwater Noise'. In: *Acoustics Australia* 41.1. Publisher: Springer Nature, pp. 12–19.

Flynn, K. and McCabe, B. (2016). 'Energy transfer ratio of hydraulic pile driving hammers'. In: Civil Engineering Research in Ireland (CERI 2016).

Foundation Equipment — PVE Equipment USA (2021). URL: https://www.pveusa.com/ (visited on 23rd Feb. 2021).

Geoteknikk Beregningsmetoder (2020). Faggruppe for Geoteknikk, NTNU, Trondheim. Kompendiet benyttes som pensumlitteratur i emnet TBA4105 Geoteknikk Beregn-

ingsmetoder ved NTNU. Compendium is used in relation with the course TBA4105 at NTNU.

Gonin, H. (2006). 'Forces, deformations et vitesses particulaires en battage et en vibrofonçage'. In: *Proceedings of the international conference on vibratory pile driving and deep soil compaction*. Paris, France.

Holeyman, A. E. (2002). 'Soil Behavior under Vibratory Driving'. In: *International Conference on Vibratory Pile Driving and Deep Soil Compaction*. TRANSVIB2002. Belgium: Lisse.

Hydrohammer –The hydraulic impact hammer (2021). IHC IQIP. URL: https://www.ihciqip.com/en/products/piling-equipment/hydrohammer (visited on 14th Apr. 2021).

Idriss, I. M., Dobry, R. and Singh, R. D. (1978). 'Nonlinear Behavior of Soft Clays during Cyclic Loading'. In: *Journal of the Geotechnical Engineering Division* 104.12. Publisher: American Society of Civil Engineers, pp. 1427–1447.

Jonker, G. (1987). 'Vibratory Pile Driving Hammers for Pile Installations and Soil Improvement Projects'. In: Offshore Technology Conference. OnePetro.

Jonker, G. and Middendorp, P. (1988). 'Subsea Installations Using Vibratory Piling Hammers'. In: *IN: OTC 88 PROC., TWENTIETH ANNUAL OFFSHORE TECHNOL. CONF., (HOUSTON, U.S.A.: MAY 2-5, 1988)* 3.

Keaton, J. R. (2018). 'Noncohesive Soils'. In: *Encyclopedia of Engineering Geology*. Ed. by P. T. Bobrowsky and B. Marker. Cham: Springer International Publishing, pp. 689–690.

Ko, Y.-Y. (2020). 'A simplified structural model for monopile-supported offshore wind turbines with tapered towers'. In: *Renewable Energy* 156, pp. 777–790.

Li, X. S. and Dafalias, Y. F. (2000). 'Dilatancy for cohesionless soils'. In: *Géotechnique* 50.4. Publisher: ICE Publishing, pp. 449–460.

Li, X. S. and Wang, Y. (1998). 'Linear Representation of Steady-State Line for Sand'. In: *Journal of Geotechnical and Geoenvironmental Engineering* 124.12. Publisher: American Society of Civil Engineers, pp. 1215–1217.

Madsen, P. T. et al. (2006). 'Wind turbine underwater noise and marine mammals: implications of current knowledge and data needs'. In: *Marine Ecology Progress Series* 309, pp. 279–295.

Manzari, M. T. and Dafalias, Y. F. (1997). 'A critical state two-surface plasticity model for sands'. In: *Géotechnique* 47.2. Publisher: ICE Publishing, pp. 255–272.

Mašín, D. (2015). *Implementation of SANISAND model as ABAQUS umat and PLAXIS user defined subroutines*. README document.

Massarsch, K. R., Fellenius, B. H. and Bodare, A. (2017). 'Fundamentals of the vibratory driving of piles and sheet piles'. In: *geotechnik* 40.2, pp. 126–141.

Mewis, J. and Wagner, N. J. (2009). 'Thixotropy'. In: *Advances in Colloid and Interface Science*. Colloids, polymers and surfactants.Special Issue in honour of Brian Vincent 147-148, pp. 214–227.

Negro, V. et al. (2017). 'Monopiles in offshore wind: Preliminary estimate of main dimensions'. In: *Ocean Engineering* 133, pp. 253–261.

Nordal, S. (2019). *Lecture notes: PhD Course BA8305 Geodynamics*. Geotechnical Group, NTNU, Trondheim, Norway.

Nordal, S. (2020). *TBA4116 Geotechnical Engineering, Advanced Course, Lecture notes*.

O'Neill, M. W., Vipulanandan, C. and Wong, D. (1990). 'Laboratory Modeling of Vibro-Driven Piles'. In: *Journal of Geotechnical Engineering* 116.8. Publisher: American Society of Civil Engineers, pp. 1190–1209.

Peleveiledningen (2019). Den norske pelekomité. Norsk Geoteknisk Forening.

PLAXIS 2D - Material Models Manual (2020). Bentley. CONNECT Edition V20.04.

PLAXIS 2D - Reference Manual (2020). Bentley. CONNECT Edition V20.04.

Poulos, S. J., Castro, G. and France, J. W. (1985). 'Liquefaction Evaluation Procedure'. In: *Journal of Geotechnical Engineering* 111.6. Publisher: American Society of Civil Engineers, pp. 772–792.

PVE - Dutch Masters in Vibro Technology (2021). URL: https://www.pve-holland.com/ (visited on 23rd Feb. 2021).

Rausche, F. and Klesney, A. (2007). 'Hammer Types, Efficiencies and Models in GRLWEAP'. In: *PDCA 11th Annual International Conference and Exposition*. Nashville, TN, USA, pp. 97–118.

Remspecher, F. et al. (2019). 'Vibratory Driven Installation of Monopiles – An Experimental Investigation of the Soil-Pile Interaction'. In: *Proceedings of the 1st Vietnam Symposium on Advances in Offshore Engineering*. Ed. by M. Randolph et al. Lecture Notes in Civil Engineering. Singapore: Springer, pp. 171–176.

Richart, F. E., Hall Jr, J. R. and Woods, R. D. (1970). 'Vibrations of Soils and Foundations'. In: *Prentice-Hall*. International series in theoretical and applied mechanics.

Rodger, A. A. and Littlejohn, G. S. (1980). 'A study of vibratory driving in granular soils'. In: *Géotechnique* 30.3. Publisher: ICE Publishing, pp. 269–293.

Roscoe, K. H., Schofield, A. N. and Wroth, C. P. (1958). 'On The Yielding of Soils'. In: *Géotechnique* 8.1. Publisher: ICE Publishing, pp. 22–53.

Saleem, Z. (2011). *Alternatives and modifications of Monopile foundation or its installation technique for noise mitigation*. Commissioned by the North Sea Foundation. Delft University of technology, p. 68.

Sawicki, A. and Świdziński, W. (2007). 'Drained Against Undrained Behaviour of Sand'. In: *Archives of Hydro-Engineering and Environmental Mechanics* Vol. 54 (nr 3), pp. 207–222.

SoilModels.com (2021). SoilModels. URL: https://soilmodels.com/.

Taiebat, M. and Dafalias, Y. F. (2008). 'SANISAND: Simple anisotropic sand plasticity model'. In: *International Journal for Numerical and Analytical Methods in Geomechanics* 32.8, pp. 915–948.

Towhata, I. (2008). *Geotechnical Earthquake Engineering*. 1st ed. Springer Series in Geomechanics and Geoengineering. Springer, Berlin, Heidelberg.

Verdugo, R. and Ishihara, K. (1996). 'The Steady State of Sandy Soils'. In: *Soils and Foundations* 36.2, pp. 81–91.

Vibratory Hammers (2011). In collab. with H. V. Starre and J. Boor. Z. Saleem, interviewer. Reference to interview is made in "Alternatives and modifications of Monopile foundation or its installation technique for noise mitigation" by Saleem, Z. (2011).

Viking, K. (2002). 'Vibro-driveability - A field study of vibratory driven sheet piles in non-cohesive soils'. Doctoral thesis. Stockholm, Sweden: Royal Institute of Technology (KTH).

Vucetic, M. (1994). 'Cyclic Threshold Shear Strains in Soils'. In: *Journal of Geotechnical Engineering* 120.12. Publisher: American Society of Civil Engineers, pp. 2208–2228.

Vucetic, M. and Dobry, R. (1991). 'Effect of Soil Plasticity on Cyclic Response'. In: *Journal of Geotechnical Engineering* 117.1. Publisher: American Society of Civil Engineers, pp. 89–107.

Vucetic, M. and Mortezaie, A. (2015). 'Cyclic secant shear modulus versus pore water pressure in sands at small cyclic strains'. In: *Soil Dynamics and Earthquake Engineering* 70, pp. 60–72.

Whenham, V. and Holeyman, A. (2012). 'Load Transfers During Vibratory Driving'. In: *Geotechnical and Geological Engineering* 30.

WindEurope (2020). *Offshore wind in Europe - key trends and statistics 2019*. WindEurope. URL: https://windeurope.org/data-and-analysis/product/offshore-wind-in-europe-key-trends-and-statistics-2019 (visited on 22nd Feb. 2021).

WindEurope (2021). *Offshore wind in Europe – key trends and statistics 2020*. WindEurope. URL: https://windeurope.org/data-and-analysis/product/offshore-wind-in-europe-key-trends-and-statistics-2020 (visited on 22nd Feb. 2021).

Wood, D. M. (1990). *Soil Behaviour and Critical State Soil Mechanics*. Cambridge University Press.

Zhang, F. et al. (2007). 'Explanation of Cyclic Mobility of Soils: Approach by Stress-Induced Anisotropy'. In: *Soils and Foundations* 47.4, pp. 635–648.

Appendices

Appendix A

Contour Plots

A.1 Effective Mean Stress at Plastic Nil-phase

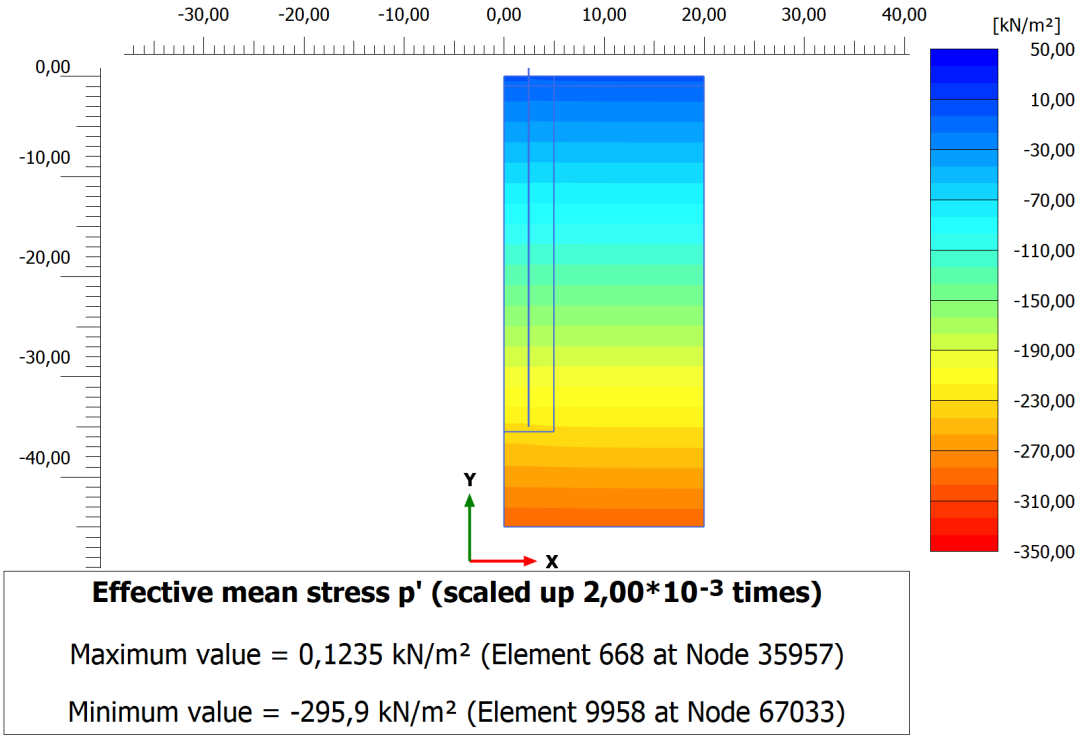

Figure A.1: sim.A* (vibro 23.33 Hz, 38.9 cycles): p' contour plot of soil at plastic nil-phase (before dynamic loading phase starts). File exported from PLAXIS 2D Output.

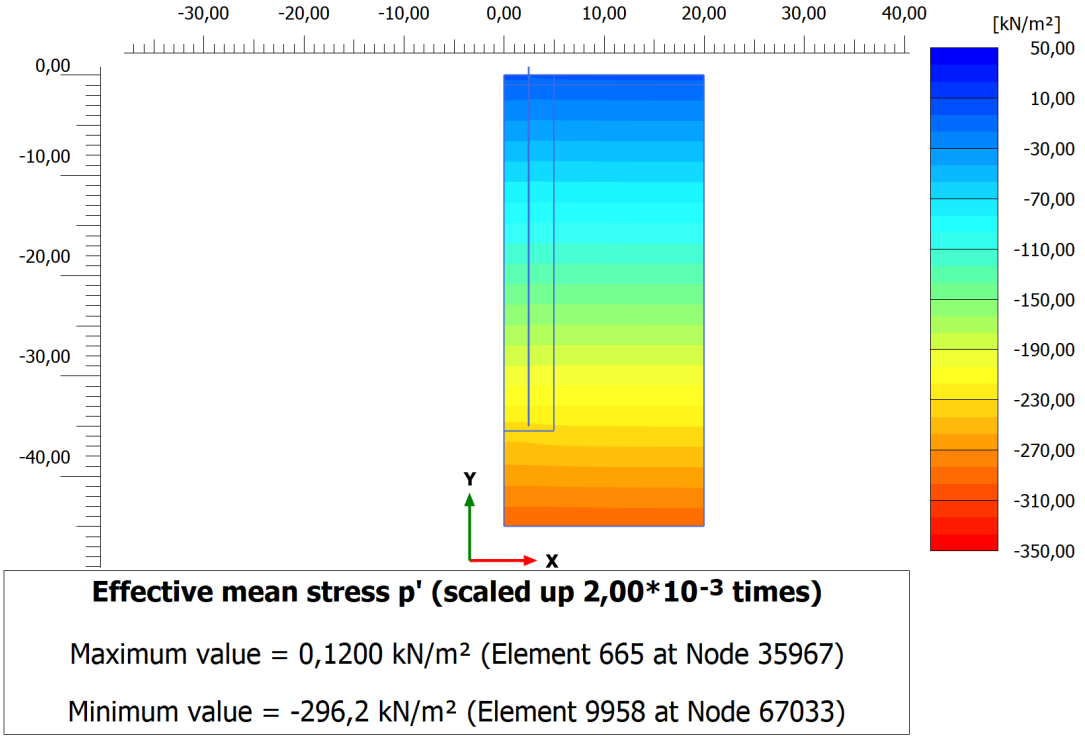

Figure A.2: sim.F (impact): p' contour plot of soil at plastic nil-phase (before dynamic loading phase starts). File exported from PLAXIS 2D Output.

A.2 Effective Mean Stress at the End of Consolidation Phase

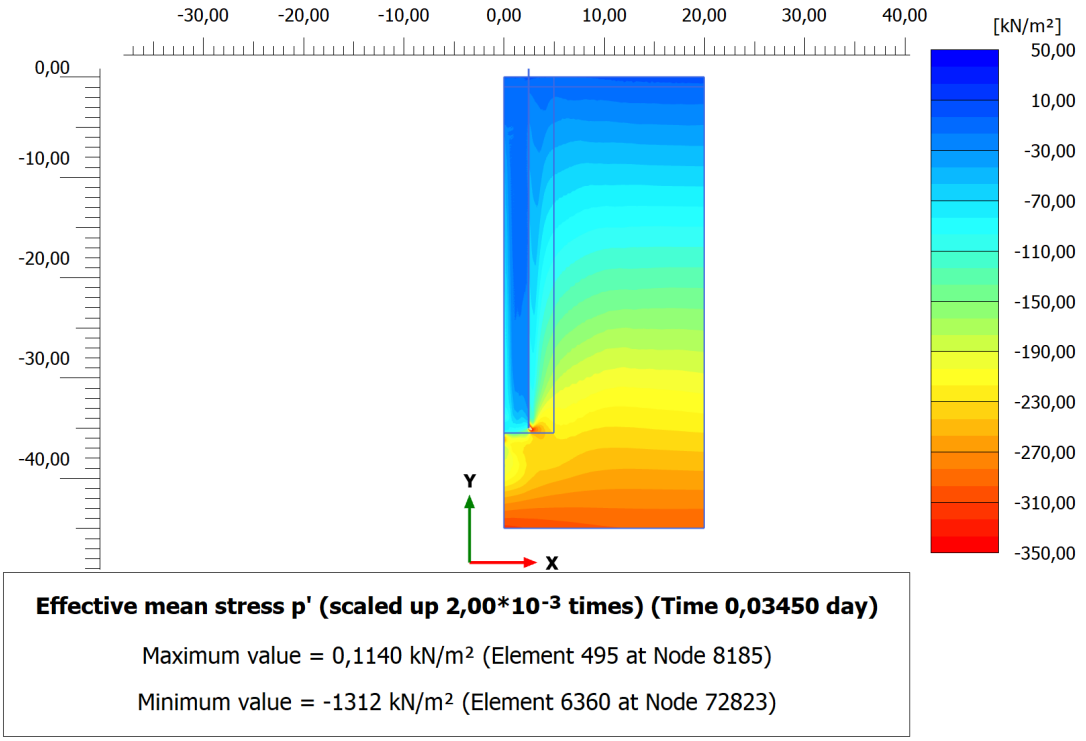

Figure A.3: sim.A* (vibro 23.33 Hz, 38.9 cycles): p' contour plot of soil at the end of consolidation phase. File exported from PLAXIS 2D Output.

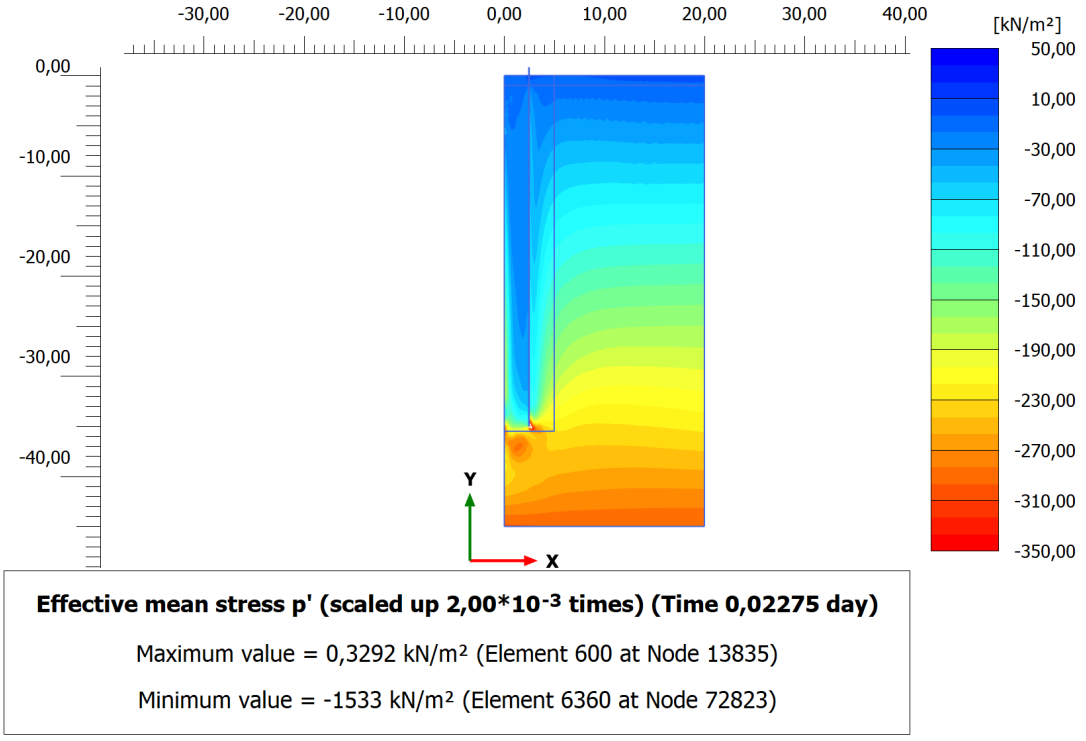

Figure A.4: sim.F (impact): p' contour plot of soil at the end of consolidation phase. File exported from PLAXIS 2D Output.

A.3 Effective Cartesian Stresses at Plastic Nil-phase

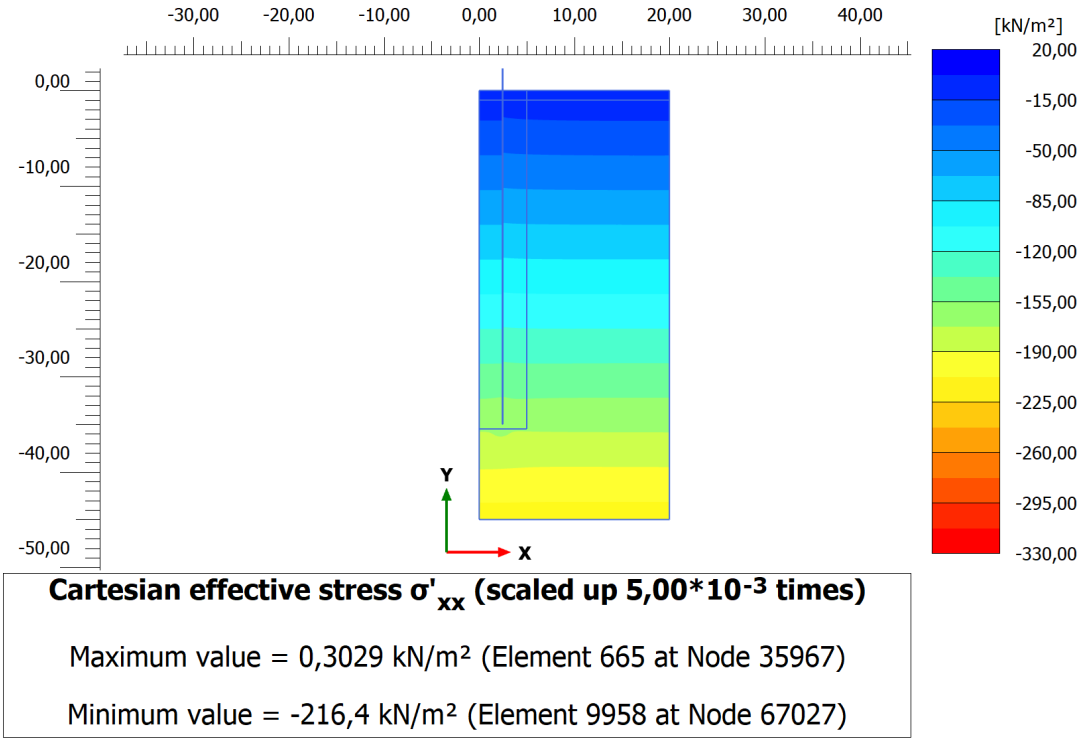

Figure A.5: sim.A* (vibro 23.33 Hz, 38.9 cycles): σ'_{xx} contour plot of soil at plastic nil-phase (before dynamic loading phase starts). File exported from PLAXIS 2D Output.

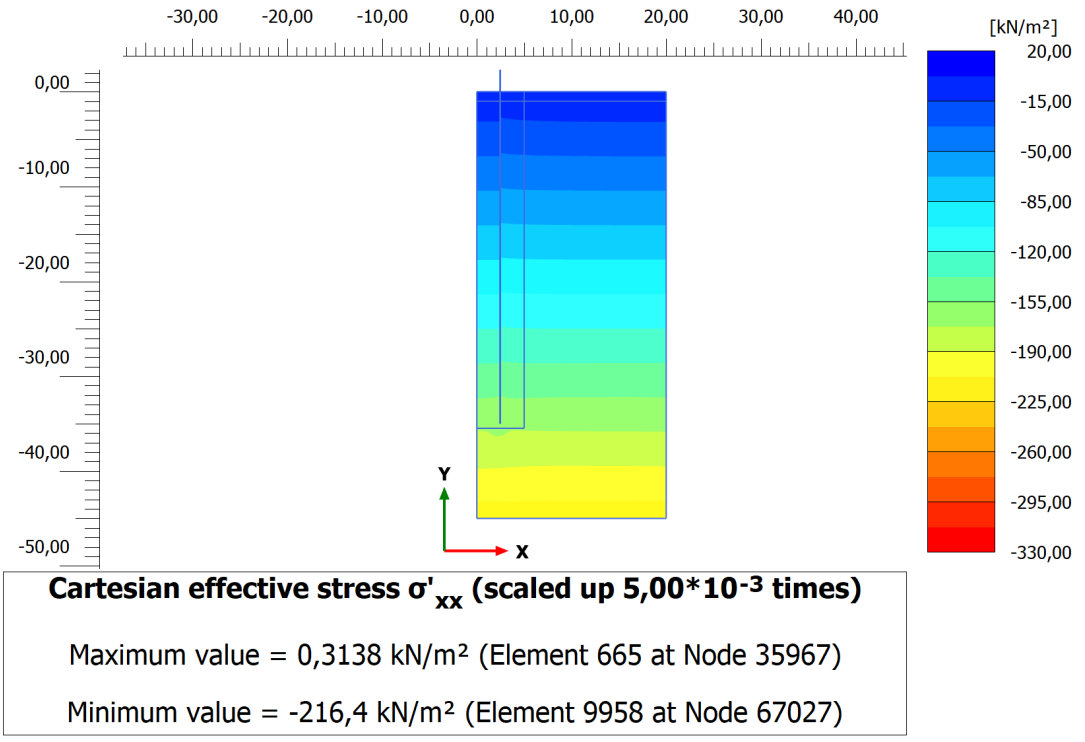

Figure A.6: sim.F (impact): σ'_{xx} contour plot of soil at plastic nil-phase (before dynamic loading phase starts). File exported from PLAXIS 2D Output.

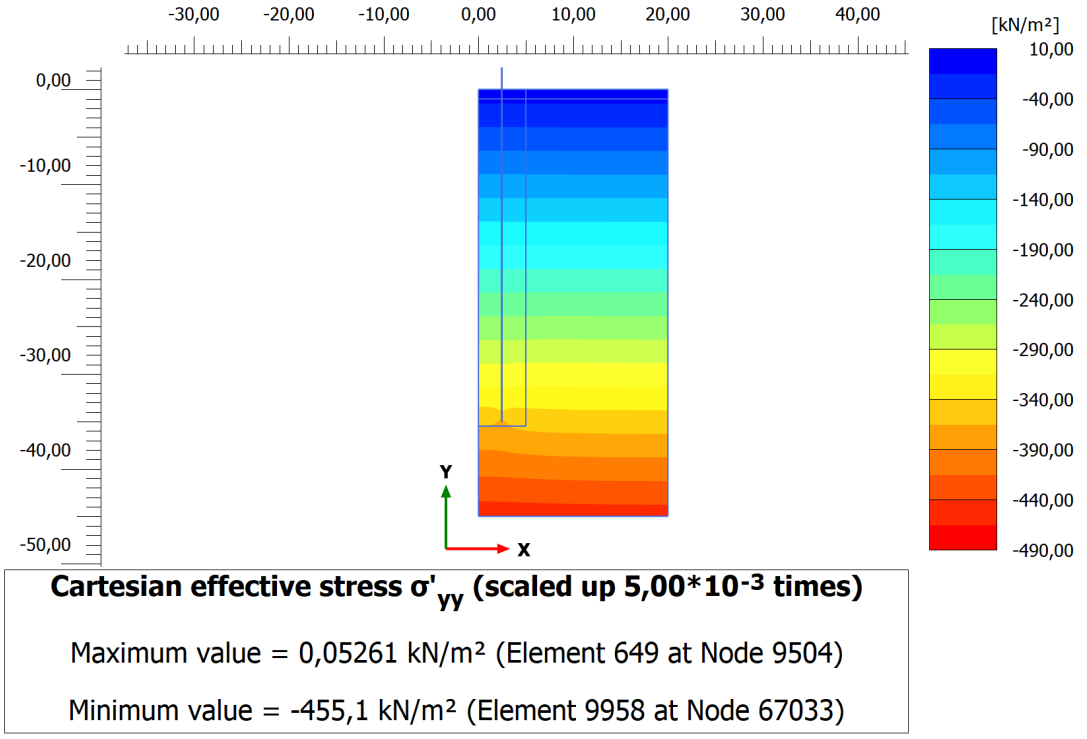

Figure A.7: sim.A* (vibro 23.33 Hz, 38.9 cycles): σ'_{yy} contour plot of soil at plastic nil-phase (before dynamic loading phase starts). File exported from PLAXIS 2D Output.

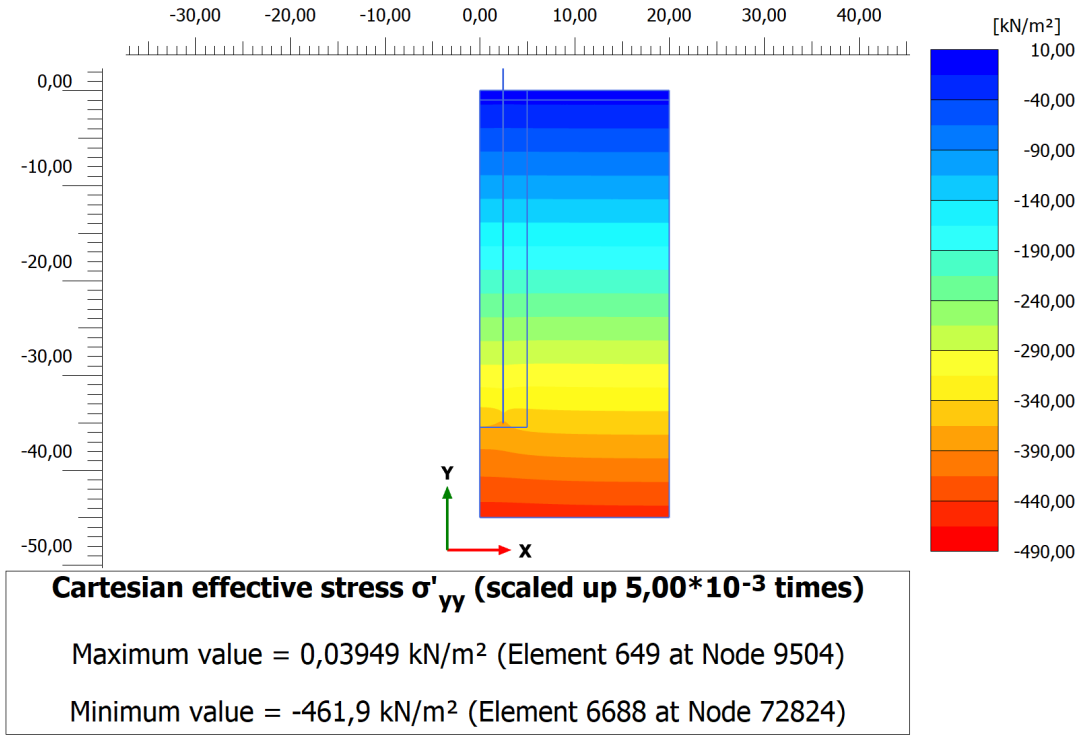

Figure A.8: sim.F (impact): σ'_{yy} contour plot of soil at plastic nil-phase (before dynamic loading phase starts). File exported from PLAXIS 2D Output.

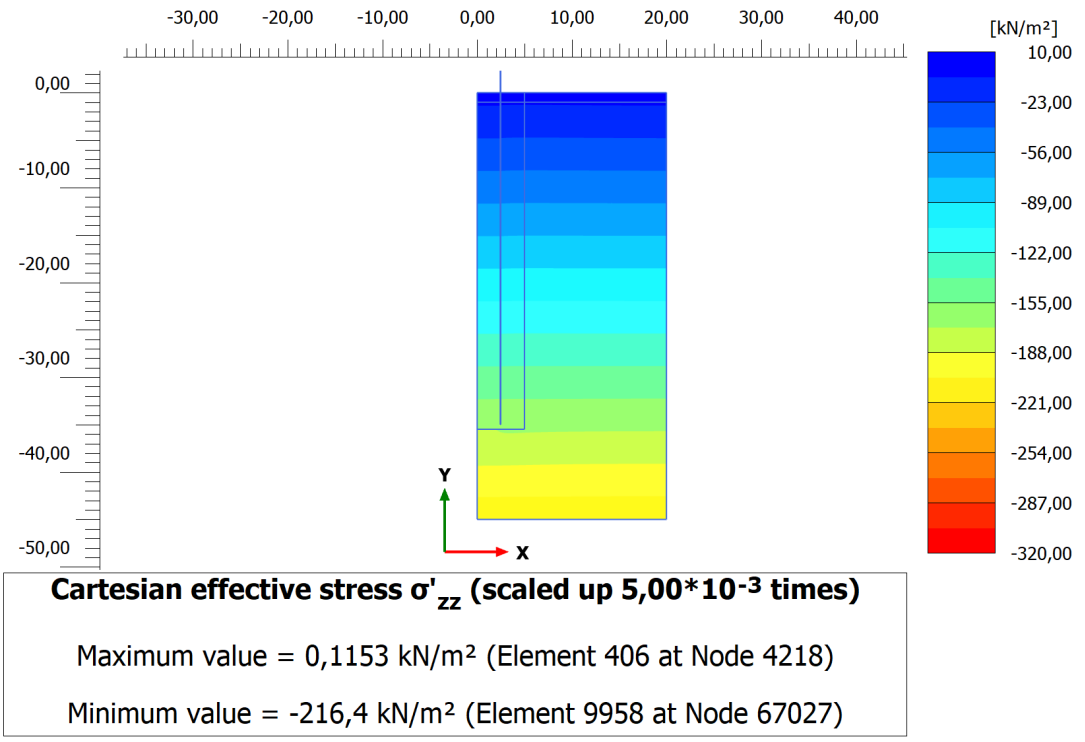

Figure A.9: sim.A* (vibro 23.33 Hz, 38.9 cycles): σ'_{zz} contour plot of soil at plastic nil-phase (before dynamic loading phase starts). File exported from PLAXIS 2D Output.

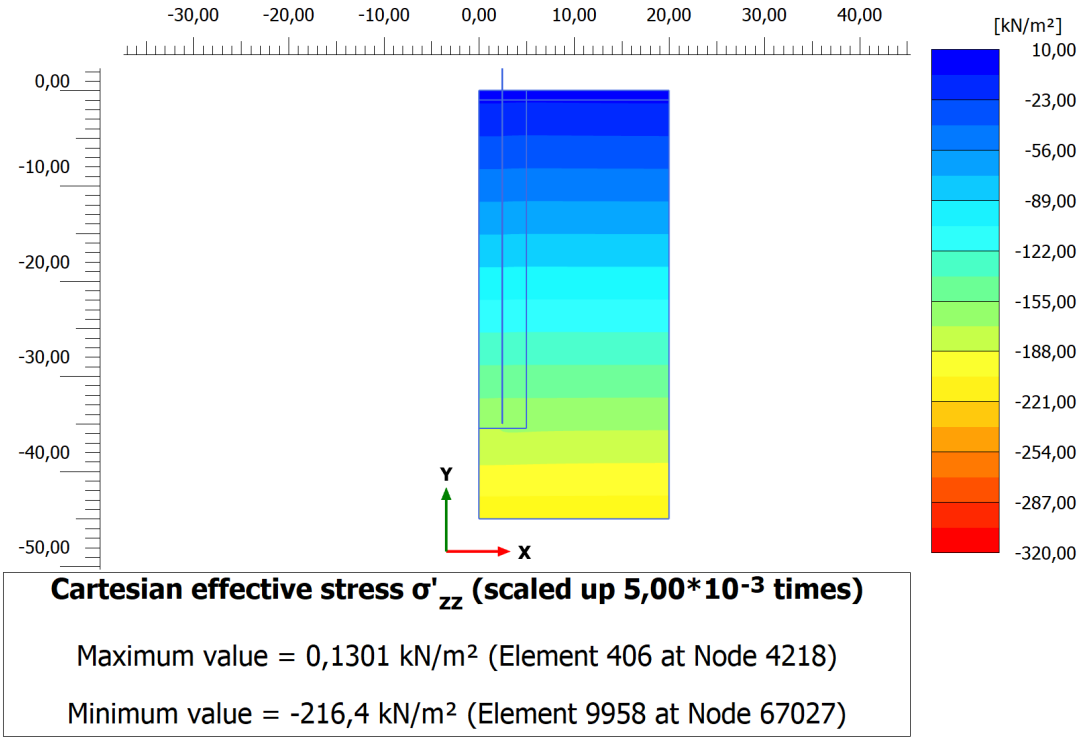

Figure A.10: sim.F (impact): σ'_{zz} contour plot of soil at plastic nil-phase (before dynamic loading phase starts). File exported from PLAXIS 2D Output.

A.4 Centre Effective Principal Stress Directions

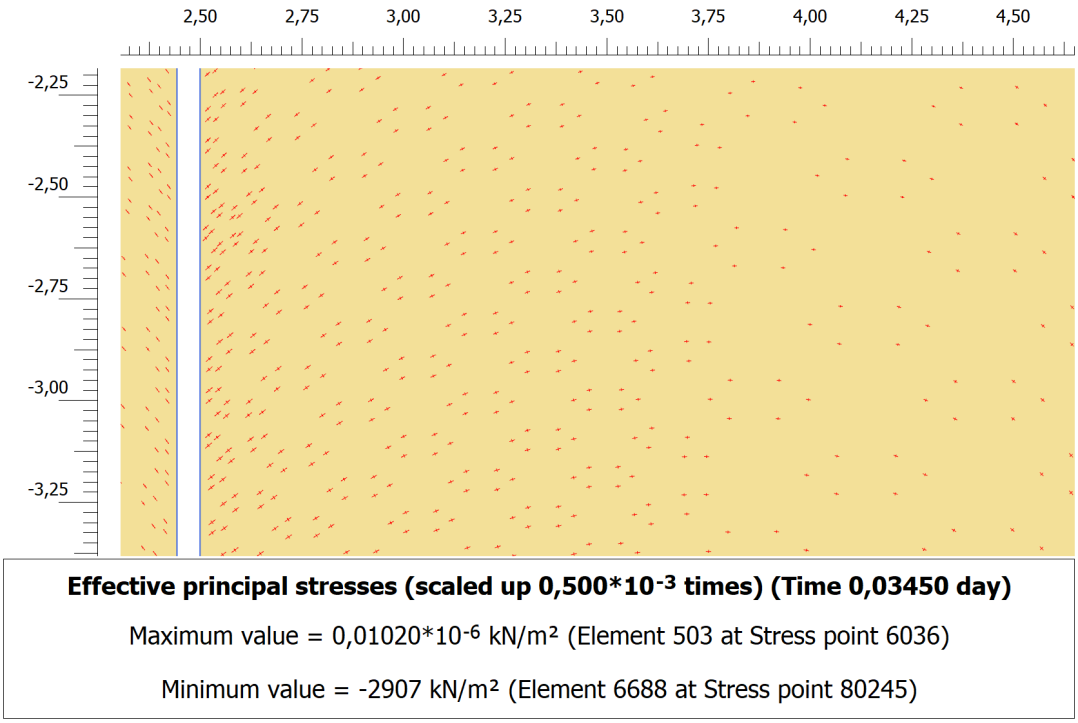

Figure A.11: sim.A* (vibro 23.33 Hz, 38.9 cycles): Centre effective principal stress directions contour plot of soil at the end of consolidation phase. Zoomed in at pile wall at depth 3 m ($y = -3$ m). File exported from PLAXIS 2D Output.

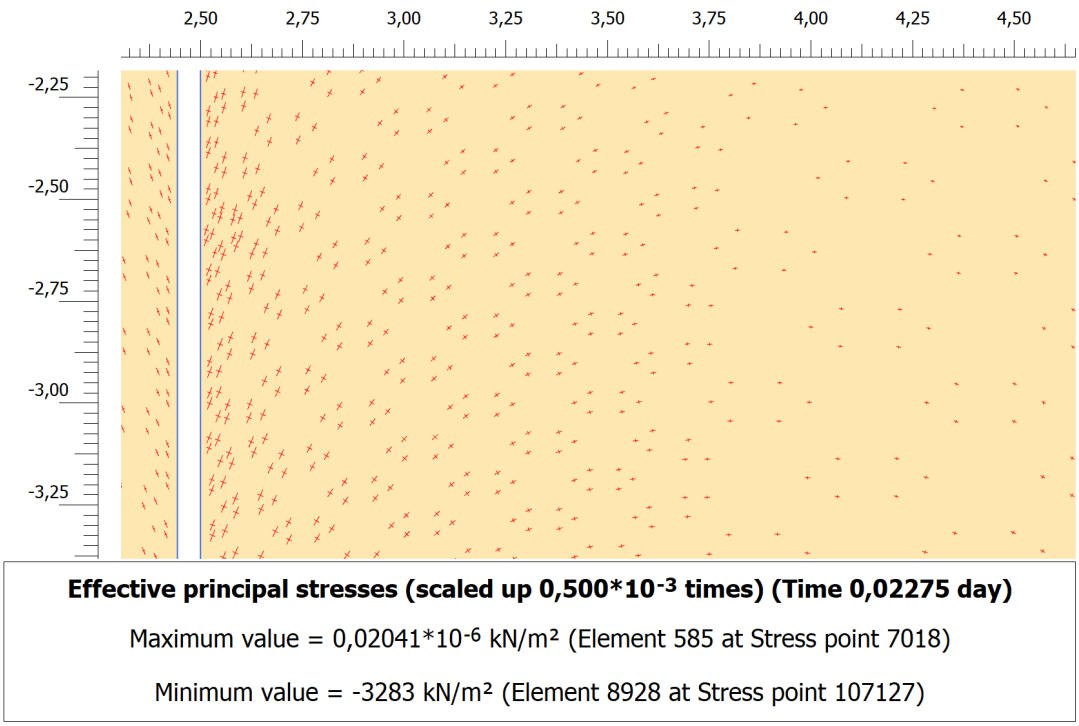

Figure A.12: sim.F (impact): Centre effective principal stress directions contour plot of soil at the end of consolidation phase. Zoomed in at pile wall at depth 3 m ($y = -3$ m). File exported from PLAXIS 2D Output.

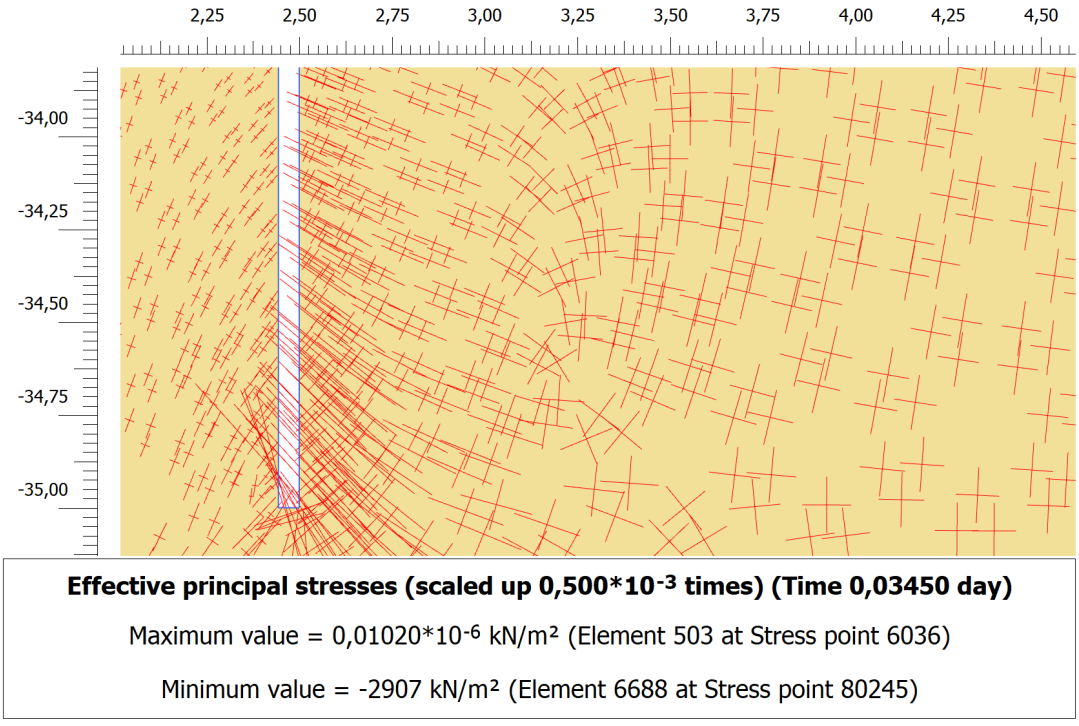

Figure A.13: sim.A* (vibro 23.33 Hz, 38.9 cycles): Centre effective principal stress directions contour plot of soil at the end of consolidation phase. Zoomed in at pile wall toe ($y = -35$ m). File exported from PLAXIS 2D Output.

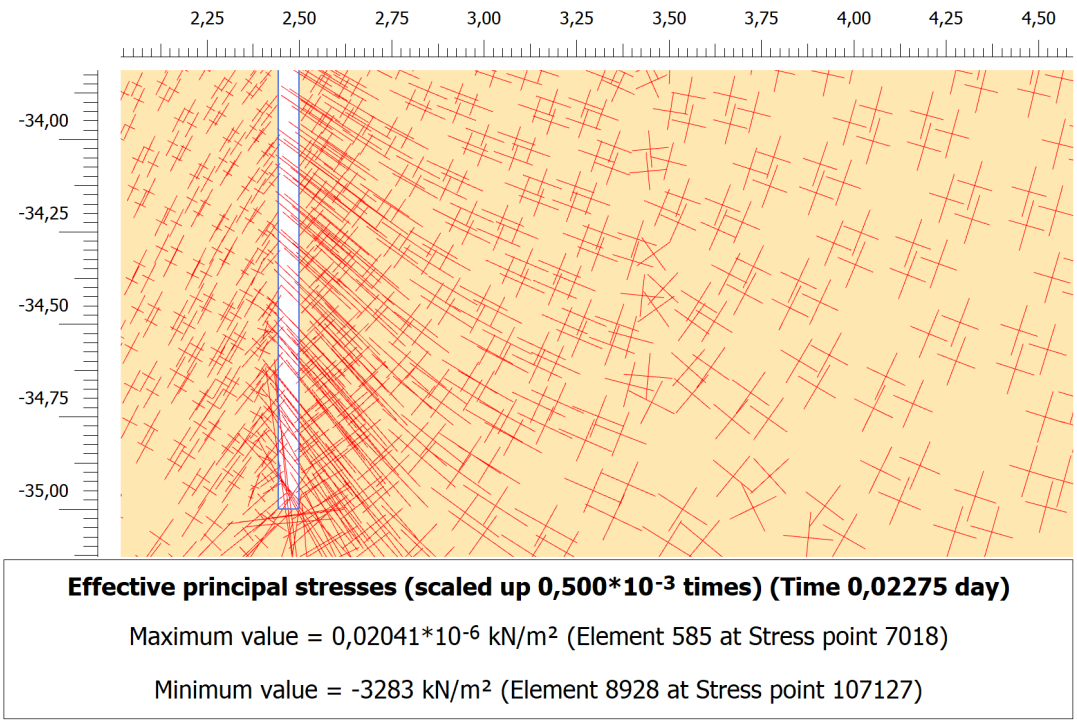

Figure A.14: sim.F (impact): Centre effective principal stress directions contour plot of soil at the end of consolidation phase. Zoomed in at pile wall toe ($y = -35\,\mathrm{m}$). File exported from PLAXIS 2D Output.

A.5 6-noded Elements: Effective Cartesian Stresses at Plastic Nil-phase

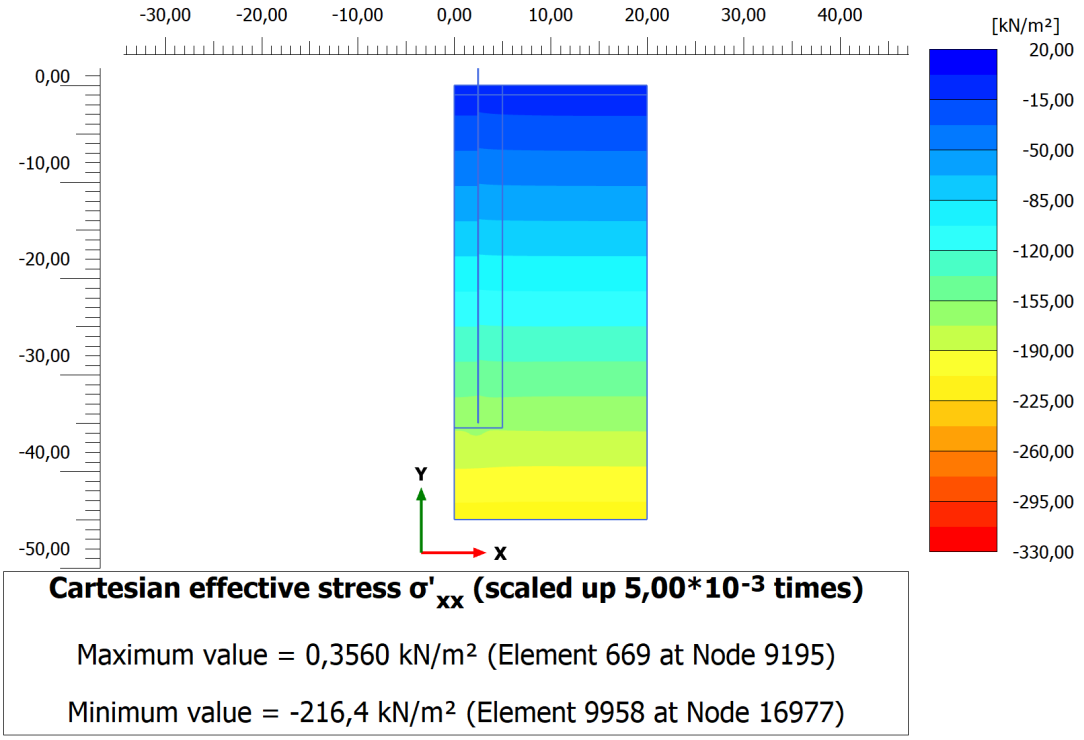

Figure A.15: sim.A* (vibro 23.33 Hz, 38.9 cycles) with 6-noded elements: σ'_{xx} contour plot of soil at plastic nil-phase (before dynamic loading phase starts). File exported from PLAXIS 2D Output.

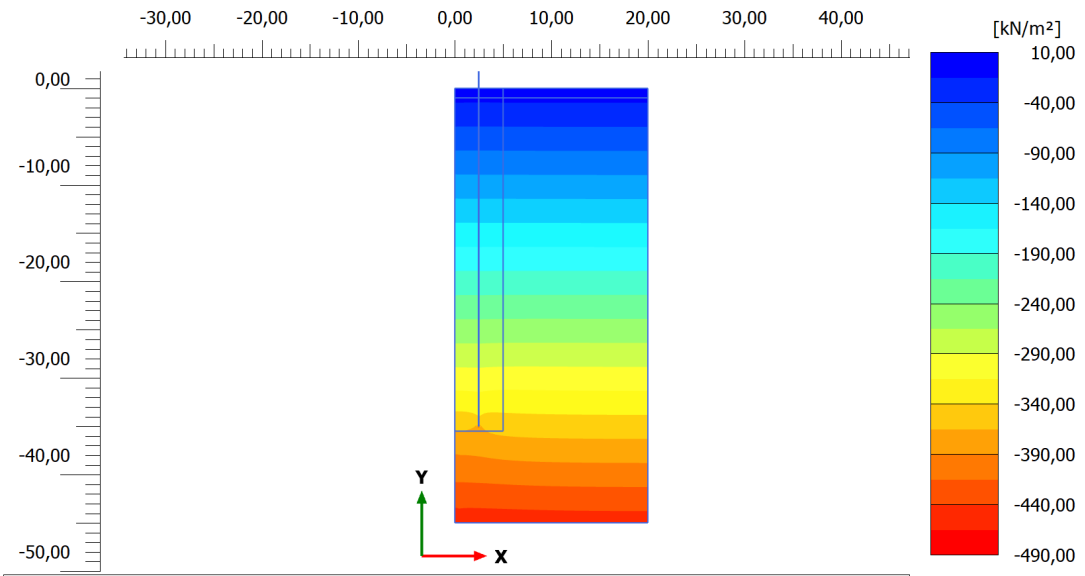

Figure A.16: sim.A* (vibro 23.33 Hz, 38.9 cycles) with 6-noded elements: σ'_{yy} contour plot of soil at plastic nil-phase (before dynamic loading phase starts). File exported from PLAXIS 2D Output.

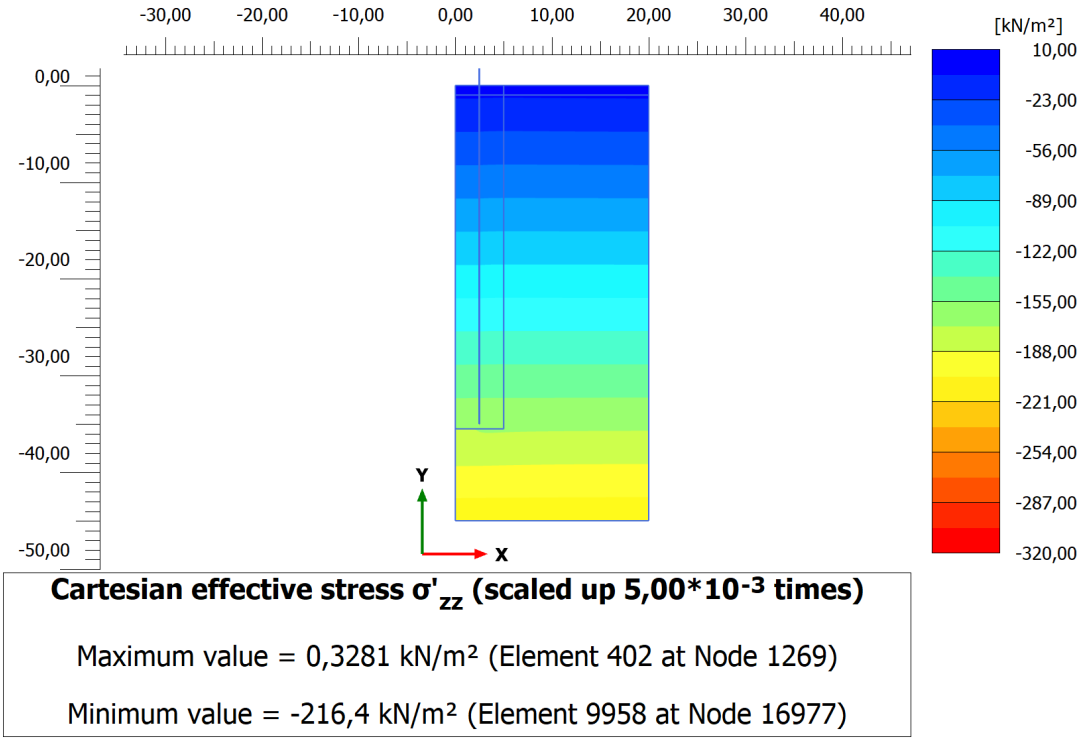

Figure A.17: sim.A* (vibro 23.33 Hz, 38.9 cycles) with 6-noded elements: σ'_{zz} contour plot of soil at plastic nil-phase (before dynamic loading phase starts). File exported from PLAXIS 2D Output.

Appendix B

Graphs

B.1 Excess Pore Pressure

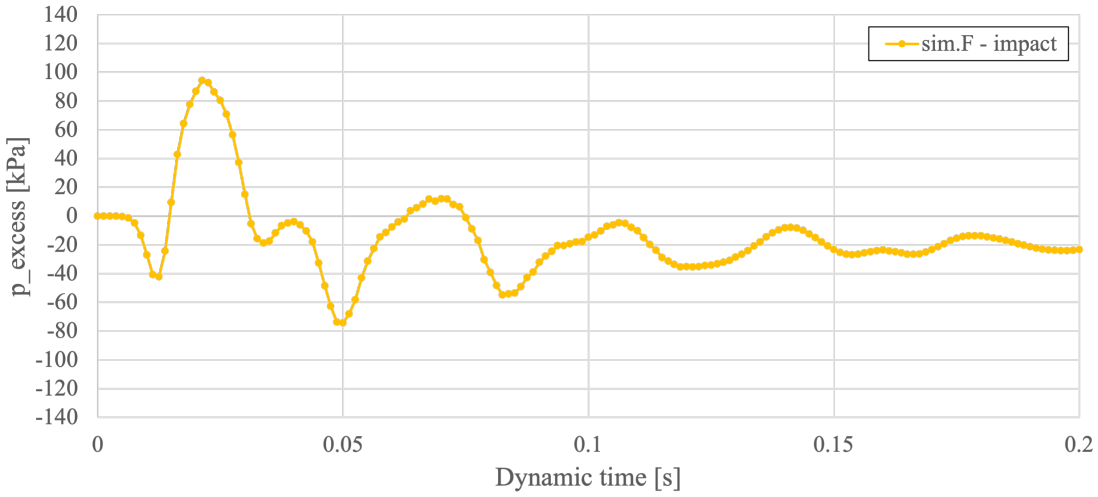

Figure B.1: sim.F (impact): p_{excess} during dynamic loading phase. At depth 17.5 m, near exterior pile wall. Showing first impact and some subsequent dynamic time. Data from PLAXIS 2D plotted in Excel.

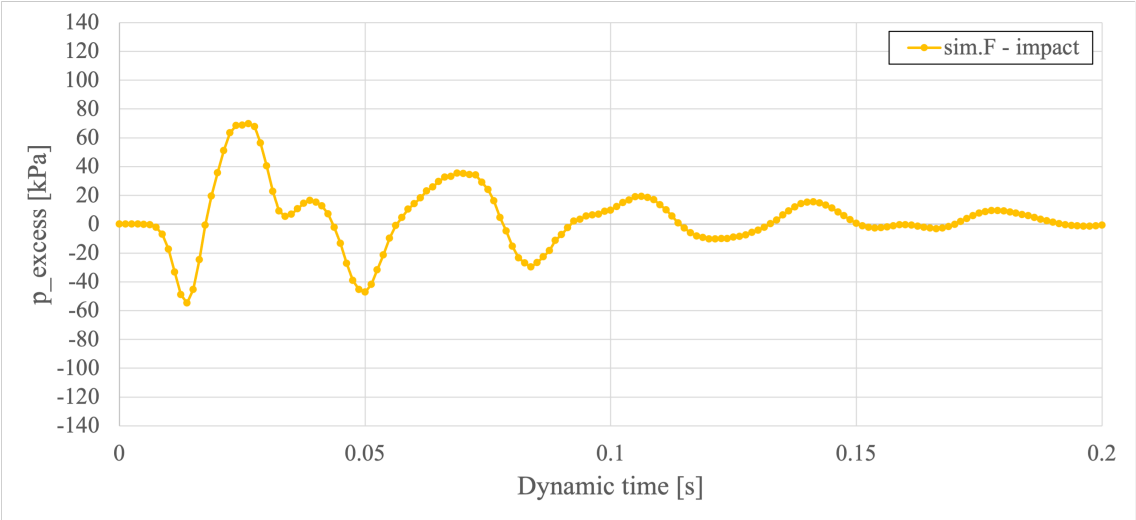

Figure B.2: sim.F (impact): excerpt of p_{excess} during dynamic loading phase. At depth 17.5 m, 1 m from exterior pile wall ($x = 3.5$ m). Showing first impact and some subsequent dynamic time. Data from PLAXIS 2D plotted in Excel.

B.2 Effective Mean Stress During Dynamic Loading Phase

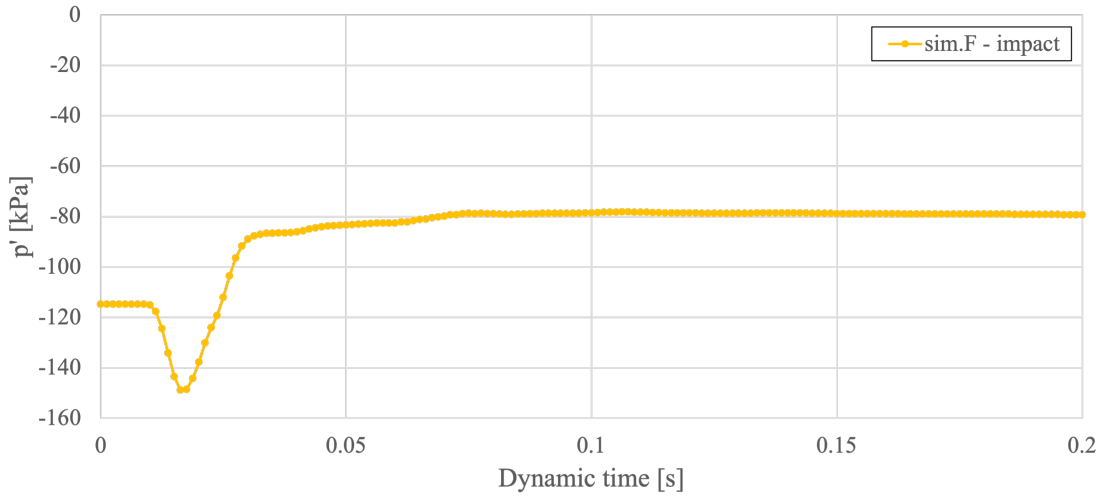

Figure B.3: sim.F (impact): excerpt of p' during dynamic loading phase. At depth 17.5 m, near exterior pile wall. Showing first impact and some subsequent dynamic time. Data from PLAXIS 2D plotted in Excel.

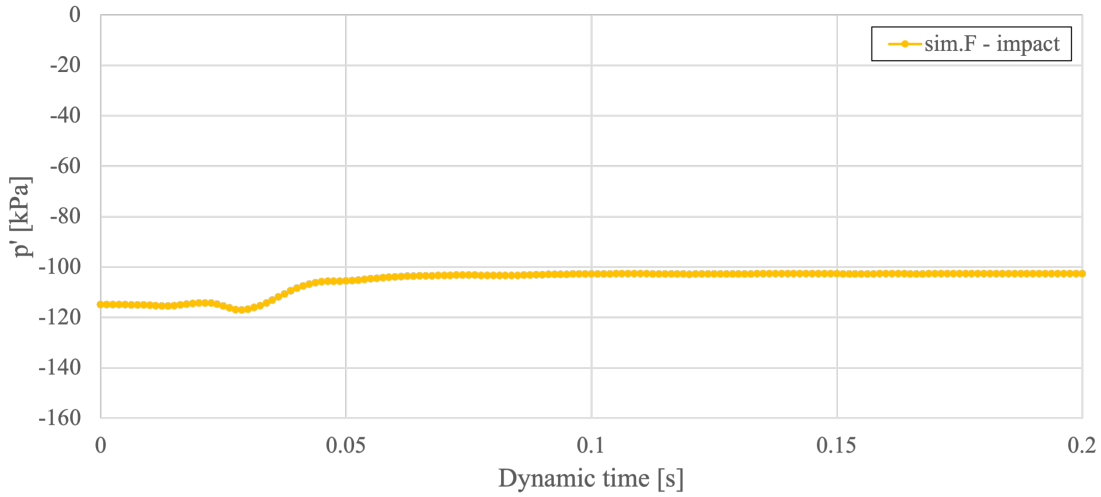

Figure B.4: sim.F (impact): excerpt of p' during dynamic loading phase. At depth 17.5 m, 1 m from exterior pile wall ($x = 3.5$ m). Showing first impact and some subsequent dynamic time. Data from PLAXIS 2D plotted in Excel.

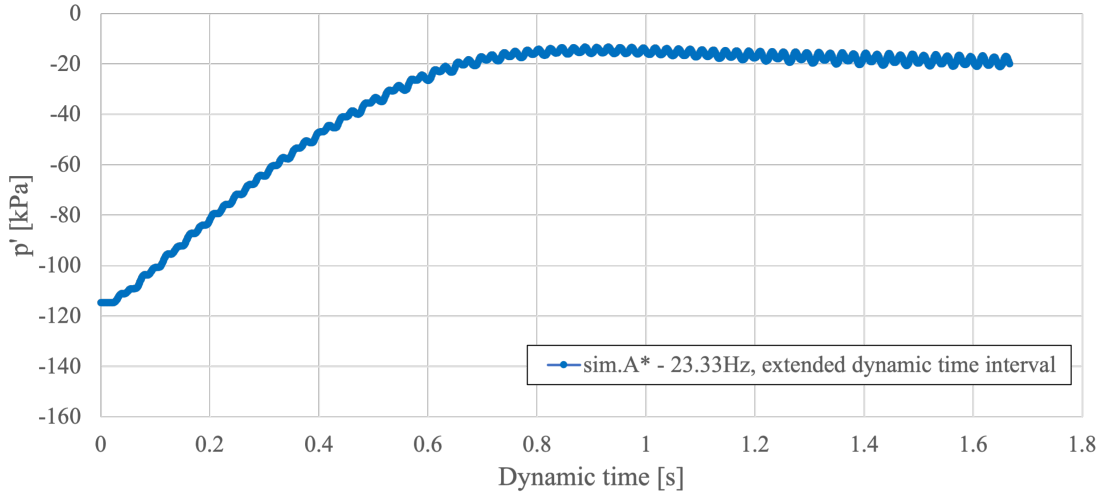

Figure B.5: sim.A* (vibro 23.33 Hz, 38.9 cycles): p' during dynamic loading phase. At depth 17.5 m, near exterior pile wall. Data from PLAXIS 2D plotted in Excel.

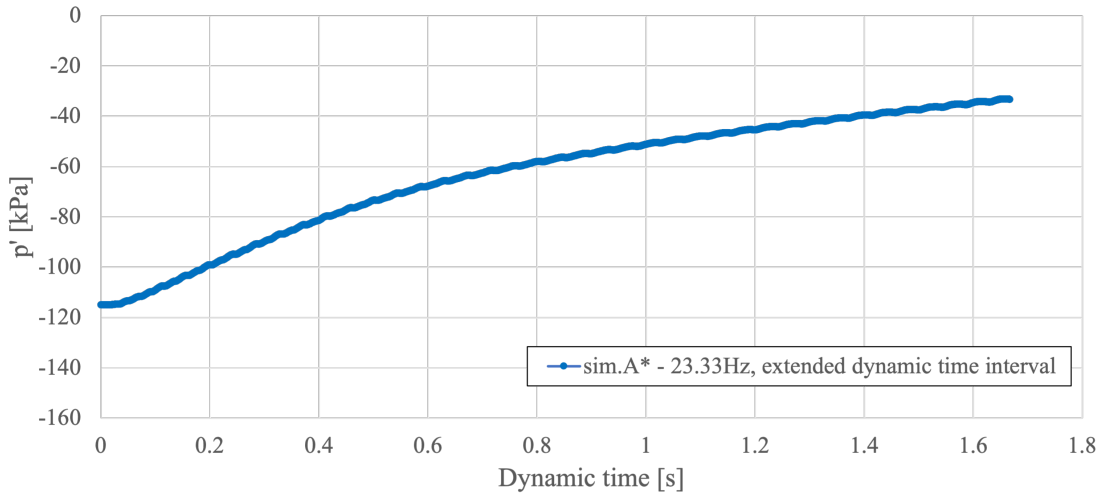

Figure B.6: sim.A* (vibro 23.33 Hz, 38.9 cycles): p' during dynamic loading phase. At depth 17.5 m, 1 m from exterior pile wall ($x = 3.5$ m). Data from PLAXIS 2D plotted in Excel.

Appendix C

Calculation of Secant Shear Modulus at Cycle N

The cyclic loading simulated in the soil during vibratory pile driving is neither strain nor stress controlled, and calculation of the secant shear modulus at cycle N is not calculated by the one-way cyclic shear stress amplitude (σ_{xy}) and one-way shear strain amplitude (γ_{xy}) as visualised in Figure 4.3 in Section 4.3, Chapter 4. Instead, the two-way amplitudes are used as visualised in Figure C.1. $\Delta\sigma_{xy}$ and $\Delta\gamma_{xy}$ are the two-way cyclic shear stress and shear strain amplitudes respectively. A two-way amplitude may be interpreted as the difference in value between the top and bottom amplitudes. Hence, the secant shear modulus calculated may be part of two cycles, e.g. cycle number 19 and 20. However, the estimated secant shear modulus are denoted $G_{s,20}$ and $G_{s,39}$ for the simulations consisting of 20 loading cycles and sim.A* (38.9 loading cycles) respectively. Note that the last possible two-way amplitudes of the hysteresis loops are used, regardless whether it is part of the last load reversal of the previous load to the first load reversal of the following cycle, or between the first and second load reversal of the same load cycle. However, the last two-way amplitudes are used for consistency of using the last possible values of the hysteresis loops. Note that the secant shear modulus for the first cycle ($G_{s,1}$) is calculated by the one-way cyclic amplitudes of shear stress and shear strain.

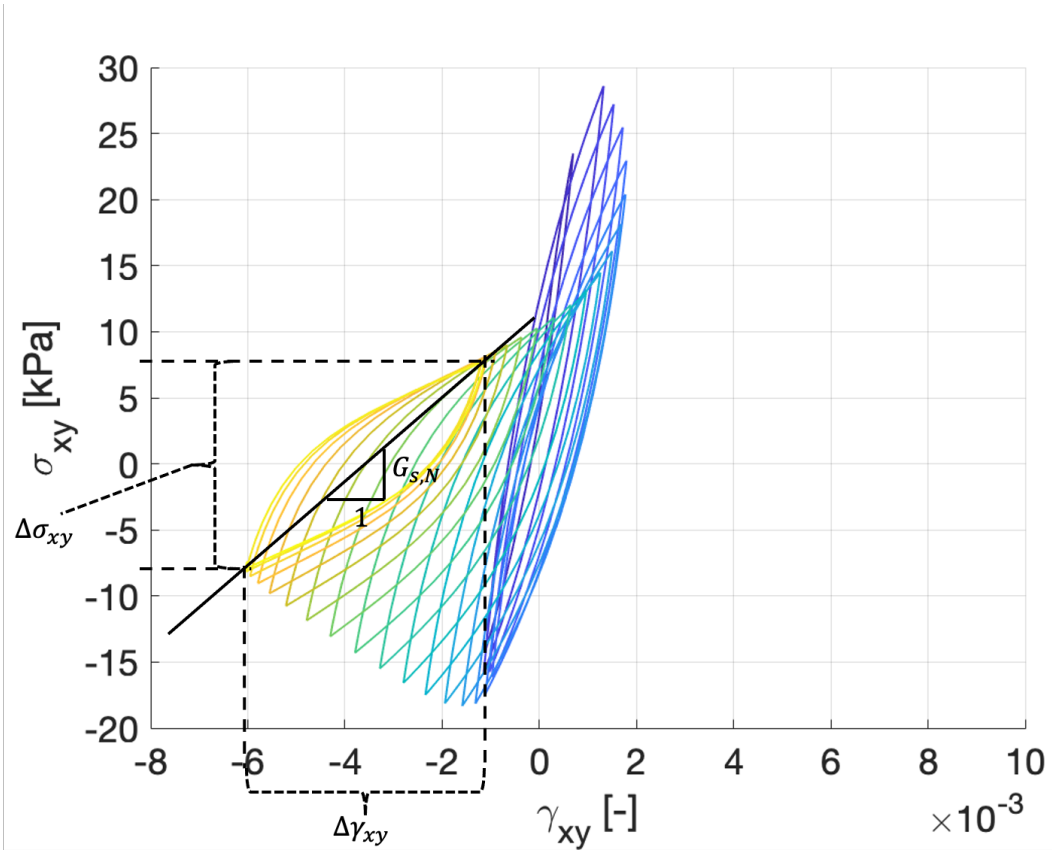

Figure C.1: Visualisation of method used to calculate the secant shear modulus during vibratory driving at cycle number N ($G_{s,N}$), of which $G_{s,N} = \Delta\sigma_{xy}/\Delta\gamma_{xy}$. The figure shows the $\sigma_{xy} - \gamma_{xy}$ hysteresis loops of sim.A, at depth 17.5 m near the exterior pile wall. Data from PLAXIS 2D plotted in MATLAB.

The one-way amplitudes are used to calculate the secant shear moduli at load cycle 7 during impact driving. However, the same secant shear moduli are calculated for two-way amplitudes to see whether there is a significant difference compared to the ones from one-way amplitudes. The interpreted values are listed in Table C.1. Note that the two-way amplitudes used during impact driving is one amplitude from the end of the previous impact, and the other amplitude is from the beginning of the next. Hence, there is a time of approximately 2 s between the amplitudes, which is considerably longer than the impact itself (0.01 s).

Table C.1: Different secant shear modulus ratio by using one-way or two-way amplitudes to calculate secant shear modulus at loading cycle number 7 ($G_{s,7}$) during impact driving (sim.F). Data from points at depth 17.5 m, near and 1 m from exterior pile wall.

	Amplitude	$G_{s,7}/G_{s,1}$
near exterior pile wall	one-way	0.54
	two-way	0.57
1 m from exterior pile wall	one-way	0.50
	two-way	0.53

Table C.1 shows the differences in the interpreted $G_{s,7}/G_{s,1}$ by using either one-way or two-way amplitudes for interpretation of $G_{s,7}$ for the impact driving simulation. Using two-way amplitudes leads to a slightly higher interpreted secant shear modulus at load cycle number 7, hence less stiffness degradation, for the considered hysteresis loops. This may partly be due to the time of approximately 2 s between the amplitudes, which is the duration between impacts, in which some excess pore pressure may be allowed to dissipate.

Appendix D

PLAXIS 2D Model

D.1 Visualisation of Axisymmetric Model in PLAXIS 2D

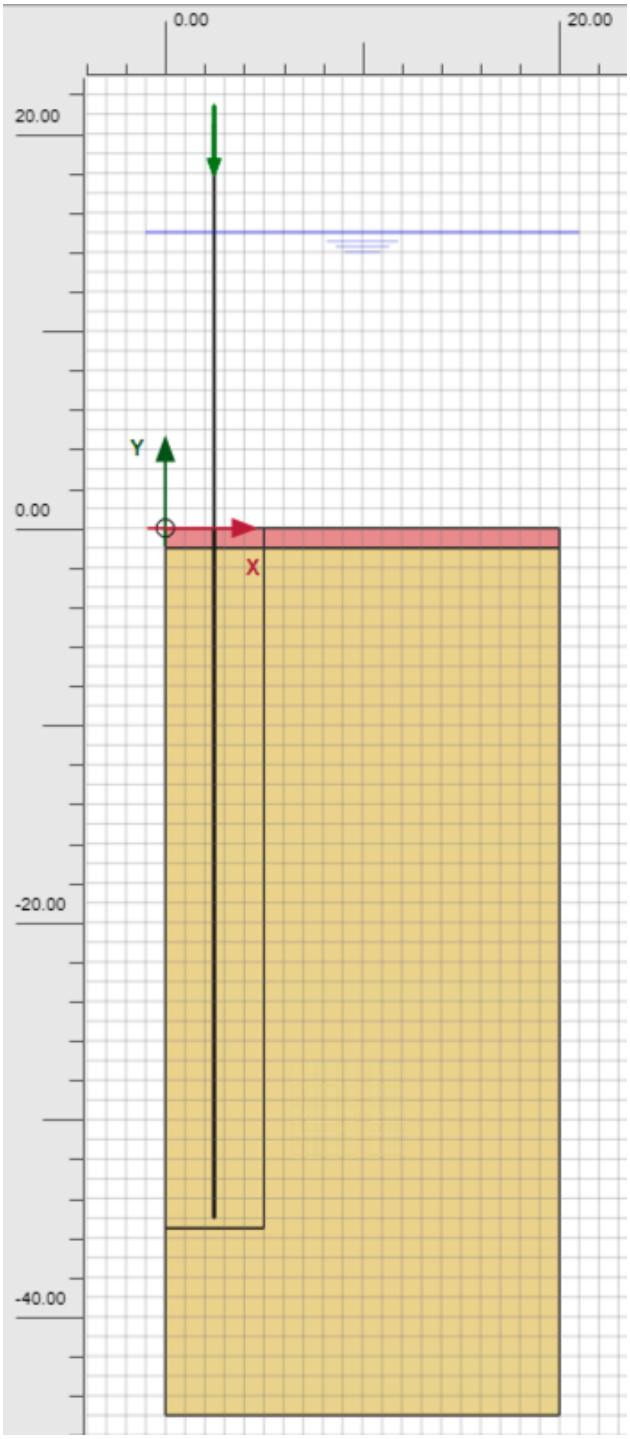

Figure D.1: Visualisation of the axisymmetric model in the dynamic loading phase for sim.A. Green arrow pointing in negative y-direction indicates the dynamic load applied to the top of the pile. Adopted from PLAXIS 2D.

D.2 Visualisation of Calculation Phases

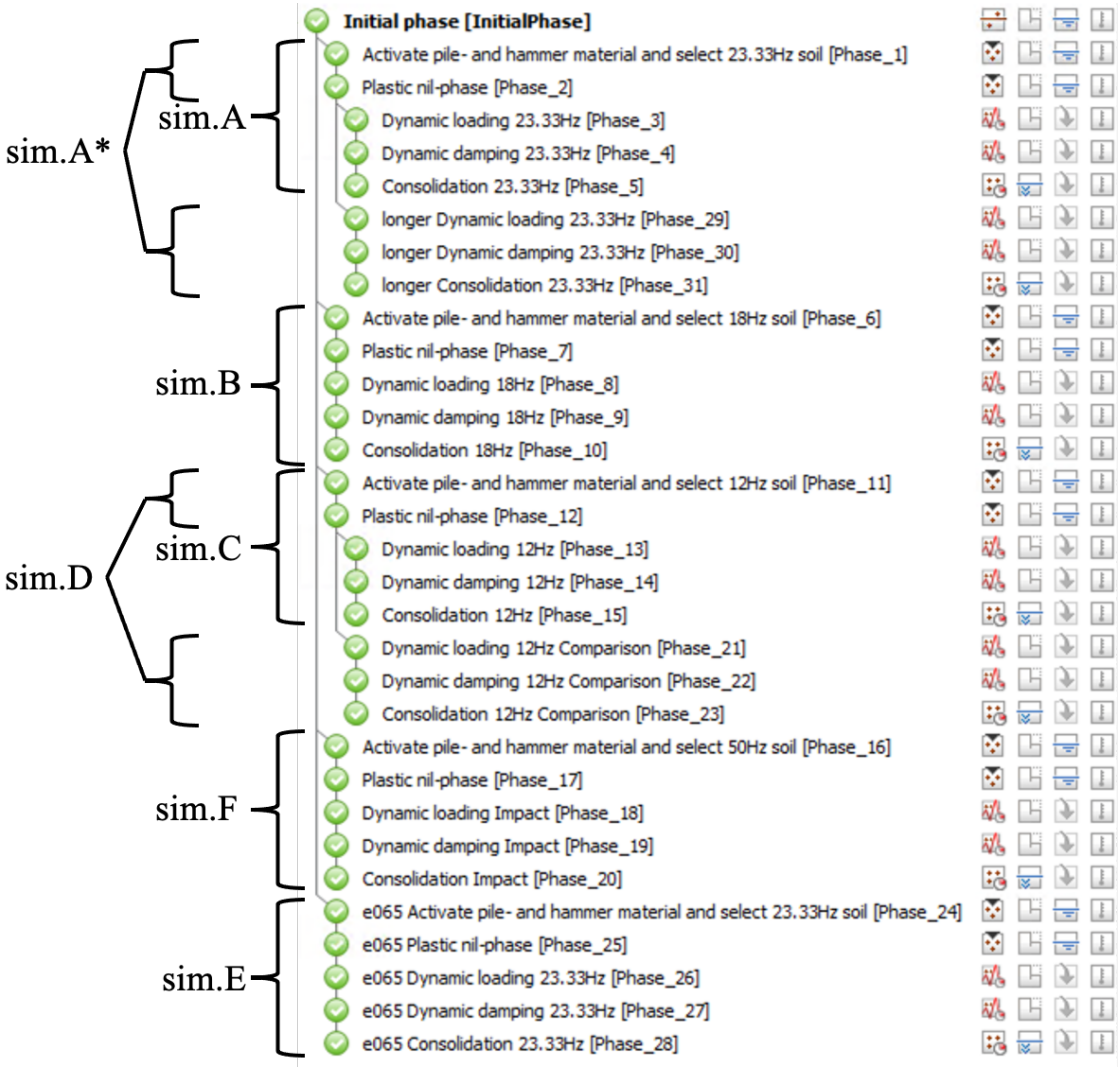

Figure D.2: Visualisation of calculation phases. All simulations starts at **Initial phase**. Adopted from PLAXIS 2D, with modifications.

Appendix E

Errors Encountered

Numerical errors were encountered during the building of the numerical model. One of these are to be presented as it may serve as an explanation regarding modelling decisions. In addition, a feedback by PLAXIS 2D is presented.

1 m MC Soil Layer at Seabed

The error "NaN found during calculation, probably severe divergence. [Error code: 39]" occurred during the consolidation phase with loading type *Minimum excess pore pressure* during simulation. It is suggested that this occurs due to approaching zero effective stresses at the free surface of the seabed. A layer of MC sand with an effective cohesion of $c' = 1\,\text{kPa}$ and a dilatancy angle of $\psi = 0°$ is added, ranging from the free surface of the seabed to 1 m below the free surface.

PLAXIS Feedback - Minor Issues Reading Project

A feedback was given by PLAXIS when opening the project, which reads "Some minor issues were encountered while reading this project. Typically these are caused by loading a project made with an older version and can be ignored safely. In case of doubt, back up the project and inspect it before further modifications. (...)" Followed by "Data for property "Multipliery" not found, keeping default value". It is currently uncertain what caused this feedback.

Halvard Eiesland

Numerical Simulation of Monopile Vibratory and Impact Installation in Saturated Sand

NTNU
Norwegian University of
Science and Technology